SISSA
Scuola
Internazionale
Superiore di
Studi Avanzati

Physics Area - PhD course in
Statistical Physics

Ergodicity breaking and restoring in disordered quantum systems

Thesis submitted for the degree of
Doctor Philosophiae

Candidate:
Giacomo Bracci Testasecca

Advisor:
Professor Antonello Scardicchio

Academic Year 2025-2026

Abstract

Understanding the effects of disorder in quantum many-body systems is one of the central challenges of contemporary statistical physics. Its interplay with interactions and quantum fluctuations profoundly modifies the nature of quantum states and their dynamics, giving rise to phenomena such as localization, ergodicity breaking, and the emergence of complex collective behavior. This thesis presents new results on two classes of disordered quantum systems.

The first part is devoted to the study of the many-body localization transition, a paradigmatic example of disorder-induced ergodicity breaking. The critical properties of the transition are investigated using a numerical renormalization-group approach, establishing a connection between its scaling behavior and that of the Anderson localization transition on tree-like graphs.

The second part focuses on the zero-temperature quantum spin-glass phase of the two-dimensional bond-disordered Heisenberg model. Combining large-scale numerical simulations with a semiclassical expansion, evidence is provided for the existence of the spin-glass phase. The effective model governing the semiclassical fluctuations is further analyzed to characterize the low-energy excitation spectrum and its localization properties. Finally, the weak-disorder regime is investigated and its implications for the ferromagnetic phase are discussed.

Overall, the results presented in this thesis contribute to the understanding of the effects of disorder in interacting quantum many-body systems, encompassing both localization phenomena and the collective behavior of disordered quantum magnets.

This thesis is dedicated to my grandfather,
who taught me the joy of solving problems.

Publications

This doctoral thesis work is based on the following publications and preprints

[1] Jacopo Niedda, Aldo Coraggio, **Giacomo Bracci Testasecca**, Antonello Scardicchio,
Vanishing spin stiffness in weakly disordered two-dimensional Heisenberg ferromagnets, arXiv:2607.20036

[2] **Giacomo Bracci Testasecca**, Jacopo Niedda, Aldo Coraggio, Roderich Moessner, Antonello Scardicchio
Semiclassical picture of the Heisenberg spin glass in two dimensions: from weak localization to hydrodynamics, arXiv:2603.22077

[3] Jacopo Niedda, **Giacomo Bracci Testasecca** , Giuseppe Magnifico, Federico Balducci, Carlo Vanoni, Antonello Scardicchio
Renormalization group analysis of the many-body localization transition in the random-field XXZ chain, Phys. Rev. B 112, 144201

[4] Luciano Loris Viteritti, Riccardo Rende, **Giacomo Bracci Testasecca**, Jacopo Niedda, Roderich Moessner, Giuseppe Carleo, Antonello Scardicchio
Quantum spin glass in the two-dimensional disordered heisenberg model via foundation neural-network quantum states, arXiv:2507.05073

[5] Federico Balducci, **Giacomo Bracci Testasecca**, Jacopo Niedda, Antonello Scardicchio, Carlo Vanoni
Scaling analysis and renormalization group on the mobility edge in the quantum random energy model , Phys. Rev. B 111, 214206

Contents

1. Introduction

1.1. Disorder in statistical physics

Nature is not always regular. Real condensed-matter and statistical-mechanical systems carry impurities, defects, and other sources of randomness, that in some cases may only quantitatively alter the description in terms of clean theoretical models, but in others drastically change the physical properties of the system, giving birth to novel and highly non-trivial phenomena. Throughout this thesis we consider *quenched* disorder: the random degrees of freedom evolve on timescales far longer than any other in the problem, so that for all practical purposes they can be treated as frozen. A system of this kind is described by a Hamiltonian

$$H(\boldsymbol{s}\,|\,\boldsymbol{\gamma})\,, \qquad \boldsymbol{\gamma} \sim p(\boldsymbol{\gamma})\,, \tag{1.1}$$

where $\boldsymbol{s}$ collects the dynamical degrees of freedom and $\boldsymbol{\gamma}$ the frozen disorder, drawn from a probability distribution p. Given a disorder distribution $p(\boldsymbol{\gamma})$, physical predictions follow from averaging observables over the disorder,

$$\overline{O} \equiv \int d\boldsymbol{\gamma}\, p(\boldsymbol{\gamma})\, O(\boldsymbol{\gamma})\,. \tag{1.2}$$

The presence of quenched disorder may drastically alter thermodynamical properties of the system, being responsible, for example, for the emergence of novel form of order. Beyond static properties, it reshapes significantly how a system evolves in time. Interference between randomly scattered paths, a rugged energy landscape, the proliferation of nearly degenerate configurations can slow relaxation dramatically and, in the extreme case, arrest it altogether, preventing the system from ever exploring its accessible states. When this happens the system fails to act as its own thermal bath: it retains memory of its initial condition and never reaches equilibrium. This breakdown of *ergodicity* is the phenomenon at the heart of this thesis.

Disorder can drive it in several ways, and in this thesis we focus on two cases. The first is *many-body localization*, where interference and interactions localize a quantum system, so that ergodicity and transport are lost *dynamically*, without any equilibrium

transition underlying it. The second is the *spin glass*, where frozen frustration fractures the equilibrium landscape into a multitude of long-lived states, giving rise to slow dynamics and eventually thermodynamic ergodicity breaking.
In the following pages, we briefly review the notion of ergodicity, both classical and quantum, and then we present an overview of the two classes of systems that are studied in this thesis.

1.2. The ergodic hypothesis

The ergodic hypothesis is the cornerstone of statistical physics: it is the instrument that allows one to move from the equations of motion of a many-body system – classical or quantum – to a description in terms of a statistical ensemble. While classical ergodic theory is a long and well-established subject [6–8], the question of how an isolated quantum system thermalizes under its own unitary dynamics was addressed only much later, through the eigenstate thermalization hypothesis (ETH), introduced by Deutsch and Srednicki in the 1990s [9, 10]. Several aspects of this picture remain open questions today, most notably the fate of thermalization in the presence of disorder, which will be the central theme of the following chapters.

1.2.1. Classical ergodic hypothesis

Consider a classical Hamiltonian system with phase space $\Gamma = (\boldsymbol{p}, \boldsymbol{q})$ and energy $E = H(\boldsymbol{p}, \boldsymbol{q})$. Liouville's theorem guarantees that the phase-space volume is conserved under the Hamiltonian flow, so that the microcanonical measure, i.e. uniform on the constant-energy shell $\Sigma_E = \{(\boldsymbol{p}, \boldsymbol{q}) : H(\boldsymbol{p}, \boldsymbol{q}) = E\}$, is invariant under time evolution. This invariant measure is the natural candidate for a statistical description of the system, but its use is justified only if time averages of observables along a single trajectory coincide with averages over this measure:

$$\lim_{T\to\infty} \frac{1}{T} \int_0^T dt\, O(\boldsymbol{p}(t), \boldsymbol{q}(t)) \;=\; \frac{1}{|\Sigma_E|} \int_{\Sigma_E} dV\, O(\boldsymbol{p}, \boldsymbol{q})\,. \tag{1.3}$$

This equality is what is meant by the *ergodic hypothesis*, originally introduced by Boltzmann to justify the foundations of statistical mechanics: a system is ergodic if a typical trajectory, given infinite time, visits the entire energy shell Σ_E (more precisely, comes arbitrarily close to every point of it, or equivalently spends a fraction of time in any subregion proportional to its measure), so that time averages become independent of the initial condition and equal to the microcanonical average.

The hypothesis was put on rigorous footing by Birkhoff and von Neumann in the 1930s, who proved that the time average of an integrable observable exists for almost every initial condition, and that it equals the phase-space average if and only if the energy shell cannot be split into invariant subsets of nonzero measure, that is, if the dynamics is *metrically indecomposable* [6, 7]. Ergodicity in this sense is a comparatively weak property: it guarantees the equivalence of time and ensemble averages, but says nothing about the rate at which this equivalence sets in, nor about the loss of correlations along the trajectory. Stronger notions – mixing, and further up the ergodic hierarchy, the Kolmogorov and Bernoulli properties – characterize increasingly chaotic dynamics and are typically what is required to justify the approach to equilibrium on physically relevant timescales, rather than only in the infinite-time limit [8].

We stress that ergodicity is a non-trivial dynamical property, not a generic feature of Hamiltonian systems: integrable systems, possessing as many conserved quantities as degrees of freedom, are manifestly non-ergodic, since their trajectories are confined to low-dimensional tori rather than covering the full energy shell. Whether and how ergodicity emerges as an integrable system is perturbed, and what remains of it in nearly integrable systems, is the subject of the Kolmogorov-Arnold-Moser (KAM) theorem [8].

1.2.2. The eigenstate thermalization hypothesis

Let us now address the problem of thermalization in closed quantum systems, which is made significantly harder due to the absence of the notion of phase space. Consider a quantum system with Hamiltonian $\hat{H}$, energy eigenstates $\{|n\rangle\}$ and eigenvalues $\{E_n\}$, prepared in a generic initial state $|\psi(0)\rangle = \sum_n C_n |n\rangle$. Under closed, unitary time evolution, the expectation value of a local (i.e. few-body) observable $\hat{O}$ reads

$$O(t) = \langle\psi(t)|\,\hat{O}\,|\psi(t)\rangle = \sum_n |C_n|^2 O_{nn} + \sum_{m\neq n} C_m^* C_n\, e^{i(E_m-E_n)t/\hbar}\, O_{mn}\,, \tag{1.4}$$

with $O_{mn} \equiv \langle m|\,\hat{O}\,|n\rangle$. For $\hat{O}$ to become thermal at late times, two conditions must hold: the infinite-time average of $O(t)$, given by the diagonal part $\sum_n |C_n|^2 O_{nn}$, must coincide with the microcanonical prediction $\mathrm{Tr}[\hat{\rho}_{\mathrm{ME}}\hat{O}]$; and the off-diagonal (oscillatory) part must become negligible at almost all times, rather than merely on average. Neither is guaranteed *a priori*. The diagonal sum depends on the full initial-state decomposition $\{C_n\}$ together with the individual matrix elements O_{nn}, and there is no obvious reason why it should reproduce a microcanonical average that, by construction, only depends on energy. The off-diagonal terms, in turn, dephase only as fast

as their smallest relevant frequency spacing allows and in a generic interacting system this can be as slow as the inverse Heisenberg time, exponentially long in system size. Resolving the controversy between the manifestly non-thermal, initial-state-dependent structure of Eq. (1.4) and the empirical fact that generic quantum systems do relax to thermal-looking states requires a statement about the structure of the matrix elements O_{mn} themselves, rather than about the dynamics in the abstract. This is precisely what the eigenstate thermalization hypothesis provides, and it is the result of two originally independent lines of inquiry.

The first traces back to 1929, when von Neumann proved what he called the *quantum ergodic theorem*: for a macroscopic quantum system prepared in a generic initial state, and for a suitably coarse-grained set of macroscopic observables, the system spends the vast majority of time in a state indistinguishable from the microcanonical prediction [11, 12]. This result already contains the ideas of quantum thermalization for isolated systems, but does not provide a practical criterion on how to construct such observables.

That criterion emerged from a second, seemingly unrelated line of development: Wigner's introduction of random matrix theory (RMT) to describe the statistics of highly excited nuclear energy levels [13]. The idea that fine-grained spectral properties of sufficiently complex quantum systems could be modeled by ensembles of random matrices, classified according to their underlying symmetries [14], turned out to be far more general than its original nuclear-physics motivation. This connection was made precise by Bohigas, Giannoni, and Schmit, who conjectured that the spectral statistics of any quantum system whose classical limit is chaotic should coincide with those of the corresponding Gaussian random matrix ensemble, while systems with an integrable classical limit instead display Poissonian, uncorrelated level statistics [15]. The Bohigas-Giannoni-Schmit conjecture provided, for the first time, a precise and computable diagnostic of quantum chaos, encoded not only in the statistics of energy levels, but, as would soon become clear, in the structure of the matrix elements of local observables between eigenstates as well. In the early 1990s, Deutsch proposed that in a chaotic system the matrix elements of physical observables in the energy eigenbasis should themselves resemble those of a random matrix drawn from the appropriate RMT ensemble [16]. Srednicki then developed this idea into a quantitative ansatz for O_{mn}, coining the term *eigenstate thermalization hypothesis* (ETH) [17]. The ETH ansatz states that

$$O_{mn} = \overline{O}(E)\,\delta_{mn} + e^{-S(E)/2} f_O(E,\omega)\,R_{mn}\,, \tag{1.5}$$

where $E = (E_m + E_n)/2$ and $\omega = E_m - E_n$. Here $\overline{O}(E)$ is a smooth function of energy, coinciding with the microcanonical average of $\hat{O}$ at that energy density; $S(E)$ is the entropy at energy E, so that $e^{-S(E)/2}$ is exponentially small in system size (of the order of the inverse square root of the Hilbert-space dimension); $f_O(E,\omega)$ is a smooth envelope function; and R_{mn} is an effectively random variable of zero mean and unit variance, encoding the RMT-like statistical fluctuations anticipated by the Bohigas-Giannoni-Schmit picture.

Equation (1.5) directly resolves the two conditions identified in Eq. (1.4). First, since $O_{nn} = \overline{O}(E_n)$ is a smooth function of energy alone, the diagonal contribution $\sum_n |C_n|^2 O_{nn}$ automatically reproduces the microcanonical average for any sufficiently narrow initial energy distribution, independently of the detailed structure of the coefficients C_n: a *single* energy eigenstate already encodes thermal expectation values for local observables, with no need to invoke an ensemble. This is the way in which "ergodicity" is realized in an isolated quantum system, replacing the classical notion of a trajectory visiting the entire energy shell. Second, the off-diagonal matrix elements are not merely small but effectively random, with a magnitude $e^{-S(E)/2}$ set by the Hilbert-space dimension and their random signs and phases cause the corresponding terms in Eq. (1.4) to dephase and cancel efficiently, driving $O(t)$ towards its microcanonical value with only exponentially small residual fluctuations at almost all times. In this sense, ETH is not only a statement about long-time averages, but also about the genuine loss of memory of the initial state at the level of local observables.

ETH is now understood to hold for a *generic* quantum many-body system that will serve as the reference "ergodic" case throughout this thesis, and it has been substantiated by extensive numerical evidence in interacting lattice models, as reviewed in detail in Ref. [18]. Its validity is not universal, however: integrable systems violate ETH due to the presence of an extensive number of local conservation laws, relaxing instead to generalized Gibbs ensembles [19]. This violation is, however, non-generic: integrability requires an extensive set of conservation laws in involution, a condition that is destroyed by essentially any local perturbation of the Hamiltonian. A more subtle exception was discovered in Rydberg-atom quantum simulators, where a small subset of anomalously non-thermal eigenstates, named *quantum many-body scars*, was observed to coexist with an otherwise ETH-obeying spectrum, giving rise to persistent, weakly-damped oscillations following certain special initial states [20, 21]. A far more drastic departure from ETH is provided by many-body localization (MBL), in which disorder is conjectured to produce an extensive number of local, quasi-conserved quantities, causing every eigenstate in a given spectral window to violate ETH, and generic initial states to retain local memory of their initial conditions indefinitely. Building up

to this discussion requires first revisiting the single-particle phenomenon from which MBL takes its name and much of its intuition – Anderson localization – which is the subject of the next section.

1.3. Anderson localization

Anderson localization [22] is the phenomenon by which disorder localizes the eigenstates of a quantum particle and suppress transport. In a clean lattice, the eigenstates of the Hamiltonian are extended Bloch waves, and a particle initially localized in space spreads ballistically through the system: the system is a metal, and its transport properties are well understood in terms of standard kinetic theory. The presence of disorder breaks translational invariance and introduces scattering between plane waves and lattice impurities. When these scattering processes are sufficiently strong, interference effects become important and can qualitatively modify the nature of the eigenstates, turning the system into an insulator.

The prototypical model in which this phenomenon appears is the Anderson Hamiltonian

$$H = -t \sum_{\langle i,j \rangle} \left(c_i^\dagger c_j + \text{h.c.} \right) + \sum_i \epsilon_i n_i \,, \tag{1.6}$$

where t is the hopping amplitude between neighboring sites and ϵ_i are random on-site energies drawn from a disorder distribution of width W, the disorder strength. For sufficiently large $W > W_c(E)$ the eigenstates at energy E are exponentially localized around localization centers r_0,

$$|\psi(r)|^2 \sim e^{-|r-r_0|/\xi} \,, \tag{1.7}$$

where ξ is the localization length. In the limit $W/t \to \infty$ the eigenstate structure becomes trivially localized, $\psi_n(i) = \delta_{ni}$, since the Hamiltonian is diagonal in the site basis. Localized and extended states, when both are present in the spectrum, are separated by a *mobility edge* $E_c(W)$ [23], marking the energy at which the nature of the eigenstates changes.

The physical mechanism underlying localization originates from quantum interference. When a particle scatters off multiple disorder configurations, the amplitudes of different scattering paths can interfere destructively, reducing the probability of transmission. This interference effect is present in every dimension, but its qualitative consequences are crucially dimension-dependent: the existence and location of the localization transition depend sharply on dimensionality. In one dimension, all

states are localized for any $W > 0$. The one-dimensional geometry admits only a single interference path, along which destructive interference is always effective, and the localization length diverges only in the clean limit $W \to 0$, as $\xi \propto W^{-2}$ [22]. Two dimensions represents a marginal case, sensitive to the symmetries of the system: in the absence of spin orbit coupling, all states remain localized for any $W > 0$, but the localization length becomes anomalously large and exhibits logarithmic scaling [24]. Only in three and higher dimensions, $d \geq 3$, a true localization transition exists at finite critical disorder $W_c > 0$: states are extended for $W < W_c$ and localized for $W > W_c$, separated in energy by the mobility edge $E_c(W)$, with extended states occupying the band center $|E| < E_c(W)$ and localized states the band tails [25–27]. The transition is critical in the usual sense of a continuous phase transition: at $W = W_c$ the system is scale invariant, and the localization length diverges upon approaching the transition from the localized side as

$$\xi \propto (W - W_c)^{-\nu}\,, \qquad W \to W_c^{+}\,, \tag{1.8}$$

with a critical exponent ν that is universal, depending only on the symmetry class and dimensionality of the problem, as expected for a transition governed by long-range critical fluctuations. Near $E_c(W)$, eigenfunctions are neither fully localized nor fully extended, but instead *multifractal*: they concentrate on a fractal set of sites across multiple length scales, characterized by a continuous spectrum of multifractal dimensions [28].

The distinction between localized and extended phases also manifests sharply in spectral statistics, providing a powerful diagnostic tool, particularly for numerical studies. In the extended phase, level repulsion dominates and the level-spacing distribution follows Wigner-Dyson statistics, as predicted by random matrix theory [29–31] and anticipated by the discussion of quantum chaos in the previous section. In the localized phase, by contrast, eigenstates are spatially separated and effectively decoupled from one another: level repulsion is suppressed, and the spacing distribution instead approaches Poisson statistics, precisely the signature expected of an integrable-like, non-chaotic spectrum.

Anderson localization has been observed directly in a variety of experimental platforms, most notably with ultracold atoms, where the disorder potential can be engineered and controlled with very high precision. Localization of a Bose-Einstein condensate released into a one-dimensional disordered optical potential was first observed in a speckle potential [32] and, independently and simultaneously, in a quasi-periodic (Aubry-André-type) potential [33]. These experiments were later extended to three

dimensions, where the existence of a genuine mobility edge could be probed directly: the first observations of a 3D Anderson transition in ultracold-atom systems were reported shortly after [34, 35], and a direct experimental measurement of the mobility edge itself was subsequently achieved [36] by mapping out the disorder and energy dependence of the transition. More recently, the two-dimensional case has also been investigated experimentally, with signatures of the anomalously large, logarithmically-corrected localization length reported in ultracold atoms [37]. Beyond cold atoms, Anderson localization has also been observed for classical waves, including light in disordered photonic lattices and microwaves in random media, providing complementary platforms in which disorder and interactions can be controlled independently [38].

1.4. Many body localization

The robustness of the Anderson insulating phase against interactions is a fundamental question for understanding localization in real materials, where Coulomb repulsion between electrons is ubiquitous and provides a natural channel for coupling otherwise-isolated localized states.

The first attempt to address this question is due to Fleishman and Anderson, who argued on perturbative grounds that a weakly interacting Anderson insulator should generically be destabilized by interactions [39]. Their argument, however, was based on low-order perturbation theory and could not settle the fate of localization at strong disorder, where a perturbative treatment in the interaction strength is uncontrolled.

A conclusive answer came with the work of Basko, Aleiner, and Altshuler [40], who went beyond the low-order perturbative treatment of Fleishman and Anderson by computing, within a self-consistent diagrammatic scheme, the decay rate of a local excitation to all orders in the interaction strength. Their key conceptual step was to reformulate the problem in Fock space: viewing the many-body eigenstates of $H = H_0 + V$ (with H_0 the localized single-particle Hamiltonian and V the interaction) as sites of an effective lattice, on which interactions act as an effective hopping. Because the Fock-space dimension grows exponentially with system size, this effective lattice is effectively infinite-dimensional, and the fate of localization is decided by a resonance-counting argument à la Anderson: a many-body state remains localized as long as the density of resonant, interaction-coupled configurations stays finite, and delocalizes once such resonances proliferate. This established, for the first time, that a disorder-localized phase can survive in the presence of generic, short-range interactions, at strong enough disorder and low enough temperature.

1.4.1. Ergodicity breaking in many-body localization

The Basko-Aleiner-Altshuler result can be rephrased directly in the language of the eigenstate thermalization hypothesis introduced earlier in this chapter: a vanishing decay rate for local excitations is precisely the statement that local observables retain memory of the initial state indefinitely, in flagrant violation of ETH. Many-body localization is understood as a genuine, many-body example of ETH breaking, one that, unlike integrability or quantum scars, is stable against generic (non-fine-tuned) local perturbations, and survives for *every* eigenstate in a given spectral window rather than an extensive set of conservation laws.

This identification was confirmed numerically through the same spectral diagnostic introduced earlier for the single-particle Anderson transition: Oganesyan and Huse showed that the level-spacing statistics of disordered spin chains cross over from the Wigner-Dyson distribution characteristic of the ergodic, ETH-obeying phase to Poisson statistics in the localized phase, directly mirroring the extended-versus-localized distinction familiar from single-particle Anderson localization [41], and this transition was subsequently mapped out in detail by Pal and Huse [42].

These numerical results motivated a phenomenological description of the localized phase in terms of an extensive set of local, quasi-conserved quantities – the local integrals of motion, or *l-bits* – in terms of which the many-body localized Hamiltonian can be written as an effectively non-interacting model,

$$H = \sum_i h_i \tau_i^z + \sum_{ij} J_{ij}\, \tau_i^z \tau_j^z + \dots \,, \tag{1.9}$$

with $\tau_i^z = \pm 1$ quasi-local operators, exponentially localized around site i [43–45]. This picture makes the violation of ETH manifest at the level of the eigenstate structure itself: because $[H, \tau_i^z] = 0$ for every i, an extensive number of local quantities are exactly conserved, eigenstates retain a memory of local initial conditions to arbitrarily long times, and entanglement entropy grows only logarithmically in time following a quench – in sharp contrast to the linear (volume-law) growth expected in an ergodic, ETH-obeying system – while individual many-body eigenstates obey an area law rather than the volume-law entanglement expected on the basis of ETH. This phenomenological picture was later put on rigorous mathematical footing, under suitable assumptions, by Imbrie [46].

On the experimental side, the defining signature of the localized phase—the failure of local observables to lose memory of their initial conditions—is remarkably direct to probe, and has been observed across several platforms. Cold atoms in quasiperiodic optical lattices retain a finite density imbalance imprinted on a charge-density-

wave initial state for arbitrarily long times above a critical disorder strength [47], an experiment subsequently extended to two dimensions [48]; trapped-ion chains with programmable random fields display the same persistence of local magnetization [49], and analogous signatures have been resolved spectroscopically in arrays of superconducting qubits [50]. More incisively, quantum-gas microscopes provide access to the entanglement structure predicted by the ℓ-bit picture: entropy measurements in a Bose–Hubbard chain reveal the characteristic logarithmic growth after a quench [51], and the same platform has been used to probe the critical behavior at the transition itself [52]. These experimental work suffer from limitation due to accessible times and sizes. What they establish beyond doubt is a robust localized regime; whether that regime survives as a genuine thermodynamic phase is a question that no finite experiment can answer on its own.

On the theoretical side, the very existence of the many-body localized phase remains contested. One dimension is the subtle case. Even granting Imbrie's proof and the subsequent work by De Roeck et al. [53], the picture is far from settled. Numerical studies pose the first problem: as the accessible chains grow, the apparent transition drifts steadily toward stronger disorder [54–56], with no sign of converging, so that the localization seen at reachable sizes may be nothing more than an unusually slow crossover. In two or more dimensions the question is settled by the avalanche argument [57, 58]. A rare region of anomalously weak disorder thermalizes on its own and acts as a bath for its surroundings: each spin it absorbs halves its many-body level spacing, while the matrix element coupling it to the next spin decays exponentially with the localization length. Whether the bath keeps growing is set by which of the two exponentials wins, and this depends only on how fast the absorbed volume grows with distance. Notice that the avalanche argument in one dimension gives a linearly growing volume and the two rates are commensurate, and the competition yields only a threshold. In two or more dimensions the volume grows faster than the distance, the level spacing always collapses first, and the bath grows without bound. No threshold exists, and the same conclusion holds whenever interactions decay slower than exponentially. The avalanche mechanism has been observed directly by coupling a thermal inclusion of controlled size to a localized region [59].

1.5. Spin glasses

Few problems in condensed-matter physics have proven as durably rich as that of spin glasses (SG), which for more than half a century have stimulated intense activity on both the theoretical and the experimental fronts [60–62]. First discussed in the

1970s in connection with dilute magnetic alloys hosting quenched impurities, such as CuMn and AuFe, [63, 64], these systems freeze, at low temperature, into a state that bears no resemblance to ferromagnetism, antiferromagnetism, or any of the more familiar patterns of magnetic order.

Two ingredients are responsible for this behavior: quenched disorder in the couplings and frustration, namely,the impossibility of simultaneously satisfying all competing pairwise interactions [65]. Their interplay produces a rugged free-energy landscape with a proliferation of nearly degenerate minima separated by large free-energy barriers. As a consequence, equilibration becomes exceedingly slow, and the system retains a long memory of its thermal history, giving rise to the characteristic aging and memory effects observed experimentally. [66, 67]

What at first sight appears as a random freezing of the spins in fact conceals a subtle form of long-range order, which manifests itself only through the spatio-temporal correlations of the local degrees of freedom. Unlike conventional magnets, no global order parameter associated with a broken spatial symmetry exists. Instead, the ordered phase is detected through the Edwards-Anderson order parameter, which measures the persistence of each spin along its own frozen direction [63].

A rigorous description of the spin-glass phase has been achieved within mean-field theory [68–72], whose paradigmatic realization is the fully-connected Sherrington–Kirkpatrick model [73]. There, the low-temperature phase is shown to consist of a multitude of equilibrium states, unrelated by any symmetry and organized hierarchically into an ultrametric structure. This remarkable solution, obtained through Parisi's replica-symmetry-breaking (RSB) ansatz, remains one of the landmark achievements of modern statistical mechanics. This wealth of states underlies a host of striking out-of-equilibrium phenomena [66], and has turned spin glasses into an archetype of complex systems, with ramifications extending well beyond magnetism, including optimization, neural networks, inference, and theoretical computer science [60, 62].

From a technical standpoint, describing spin glasses confronts one with obstacles that resist both analytical and numerical attack. Performing the quenched average of observables over the disorder analytically calls for either the replica trick or the introduction of auxiliary fermionic fields. The fermionic route appears better suited to capturing localization physics in disordered media [74], whereas the replica approach has been the workhorse behind the mean-field replica-symmetry-breaking description of the glassy phase [60]. Neither, however, provides an exact solution in finite dimensions.

This gap has fueled a long-standing debate between two competing scenarios. The RSB picture, inherited from mean-field theory, predicts infinitely many pure states

with a non-trivial overlap distribution, whereas the droplet picture argues that only a single pair of pure states, related by global spin reversal, survives in the thermodynamic limit [75, 76]. The two scenarios therefore make qualitatively different predictions for the nature of low-energy excitations, the overlap distribution, and the stability of the ordered phase under perturbations. The controversy bears directly on the applicability of mean-field ideas in low dimensions and on the values of both the upper and lower critical dimensions of the transition [77–81]. Despite decades of analytical work and increasingly large-scale numerical simulations, this question remains one of the central open problems in the theory of disordered systems.

1.5.1. Quantum spin glasses

Upon lowering the temperature of any system, quantum effects must be included in the description. They give rise to novel and rich phases of matter [82–84], and the classical understanding could be qualitatively modified. Before discussing quantum spin glasses, let us spend a few words on possible scenarios in quantum magnetism.

Classical magnetic systems are governed by a simple principle: the ground state minimizes the exchange energy by arranging the spins into an ordered pattern, possibly frustrated. In quantum systems, however, this picture becomes considerably richer. Because spin components do not commute, the ground state is no longer a static spin configuration but a quantum superposition of many classical states. Magnetic order must therefore compete with the zero-point fluctuations generated by the uncertainty principle, and this competition gives rise to an extraordinary variety of phases with no classical analogue.

The effectiveness of quantum fluctuations depends strongly on dimensionality. In three-dimensional magnets they are often too weak to qualitatively alter the classical picture, whereas in one and two dimensions they become increasingly important.

The simplest consequence of this competition is the formation of valence-bond solids (VBS). Instead of developing long-range magnetic order, neighboring spins bind into singlet pairs that arrange themselves periodically throughout the lattice, breaking lattice symmetries while preserving the global $SU(2)$ spin symmetry [83, 85]. The elementary degrees of freedom are therefore not ordered magnetic moments but quantum-mechanical singlet bonds. VBS phases constitute perhaps the clearest example of a state whose existence is entirely due to quantum fluctuations: classically they would simply reduce to an ordinary antiferromagnet. Whether the singlets crystallize or instead remain in a liquid superposition of coverings is a question already contained in quantum dimer models [86, 87], and, at the level of the spin models themselves, in the

choice of variational ansatz within projected-fermion approaches [88].

Quantum fluctuations may, however, be even more disruptive. In some highly frustrated magnets they remain sufficiently strong to prevent any kind of symmetry breaking, even at zero temperature. The resulting quantum spin liquids (QSLs), first envisioned by Anderson through the resonating-valence-bond (RVB) picture [89], possess neither magnetic order nor crystalline order. Instead, they are characterized by long-range quantum entanglement, fractionalized excitations and, in many cases, emergent gauge fields [90–93]. Variational Monte Carlo studies based on Gutzwiller-projected fermionic states have been instrumental in locating such phases in the paradigmatic frustrated models and in computing their spectral signatures [94–97]. During the last two decades, spin liquids have become one of the central paradigms of strongly correlated quantum matter, with candidate realizations in kagome antiferromagnets, organic Mott insulators, Kitaev materials and, more recently, synthetic Rydberg platforms [98–100]. The examples above illustrate a common theme: quantum fluctuations tend to suppress conventional magnetic order, replacing it with increasingly exotic phases. A natural question then arises. What becomes of the much subtler order found in spin glasses, where the ordered phase is already stabilized only through the combined effects of disorder and frustration? Does quantum mechanics eventually melt the frozen spin configuration, or can glassy order survive in the presence of coherent quantum dynamics?

These questions define the field of quantum spin glasses (QSG) [101]. Here, the transition into the glassy phase is driven not by temperature alone, but also by a non-thermal control parameter, typically a transverse magnetic field or a tunneling amplitude [83]. The resulting quantum phase transition separates a quantum paramagnet from a frozen glassy state whose properties are shaped simultaneously by disorder, frustration and quantum fluctuations.

At first sight, one might expect quantum fluctuations to destabilize the glassy order, just as they might suppress long-range magnetic order in frustrated antiferromagnets. Remarkably, experiments indicate that this intuition is only partially correct. The canonical testing ground is the diluted dipolar Ising magnet $LiHo_xY_{1-x}F_4$, in which the Ho^{3+} moments behave as effective Ising spins, random dilution supplies frustration and disorder, and a transverse field tunes quantum fluctuations independently of temperature [102]. There, spin-glass order survives well into the quantum regime, although the freezing temperature is suppressed and the characteristic relaxation times become substantially shorter [103–105]; the same platform has been used to demonstrate quantum annealing towards low-lying configurations [106], coherent spin oscillations [107] and entanglement between dipoles [108]. The interpretation is

not uncontroversial, however: some measurements report the absence of a conventional transition [109, 110], and it has been argued that the transverse field unavoidably generates random longitudinal fields through the off-diagonal dipolar couplings, possibly rendering the intrinsic quantum critical point experimentally inaccessible [111, 112].

Indeed, many hallmarks of the classical problem—including slow relaxation, aging and memory effects—persist [113–115], while entirely new quantum phenomena emerge.

Quantum spin glasses therefore occupy a particularly interesting position within the landscape of quantum matter. On one hand, they inherit the complex free-energy landscape and slow dynamics of classical glasses; on the other hand, they exhibit genuinely quantum features, including coherent tunneling between metastable configurations, quantum criticality, and competition with thermalization. The importance of quantum spin glasses extends well beyond disordered magnetism. Their rugged energy landscapes make them natural benchmark models for quantum optimization and quantum annealing [116–120], where the objective is precisely to navigate an exponentially complex landscape by exploiting quantum tunneling.

Almost everything that is understood with confidence in quantum spin glasses comes from the generalization of the classical mean-field theory. Making this construction quantum introduces one essential complication [121]: the frozen configuration is no longer static, since each spin keeps fluctuating in imaginary time, and the order parameter must therefore describe not only how strongly the spins are frozen but also how they move. The problem consequently loses its purely thermodynamic character and becomes dynamical.

For a long time the temporal structure was neglected altogether, an assumption that restores a classical-looking problem and predicts a discontinuous freezing transition [122]; retaining the dynamics gives instead a continuous quantum phase transition and a glassy phase whose low-energy excitations remain gapless, the quantum counterpart of marginal stability [123, 124]. Large M expansion of $SU(M)$ models shed new light on the problem: Sachdev and Ye found that a fully connected random Heisenberg magnet need not freeze at all, settling instead into a critical, strongly entangled liquid [125] that later seeded the SYK model and its role in the theory of strange metals [126]. At physical $SU(2)$ spin the glass eventually wins, but the liquid survives as an intermediate-energy regime [127–129], and treating the hierarchical replica structure and the quantum dynamics together confirms that glassy order does withstand quantum fluctuations [130].

The finite-dimensional problem remains considerably less understood. Quantum fluctuations become increasingly effective as the dimensionality is lowered, raising the

possibility that they may ultimately destabilize spin-glass order altogether. Already in the classical problem, the lower critical dimension plays a central role: for short-range Ising spin glasses it is believed to lie near $d \simeq 2.5$, precluding a finite-temperature glass transition in two dimensions while allowing one for $d \gtrsim 3$. Whether quantum fluctuations modify this picture, and in particular whether a genuine zero-temperature glass phase may exist in dimensions where thermal order is absent, remains one of the central open questions in the field.

Numerically, the finite-dimensional landscape is equally unsettled. The transverse-field Ising spin glass constitutes the notable exception: since the pioneering work of Rieger and Young [131], sign-problem-free quantum Monte Carlo simulations have demonstrated that spin-glass order survives up to sizable transverse fields [132–134]. This provides a clean existence proof that quantum fluctuations alone do not necessarily destroy glassiness. Whether the same conclusion holds for continuous $SU(2)$-symmetric quantum magnets is a far more difficult question. We will deal with this problem in Chapter 6.

1.5.2. Ergodicity breakings in spin glasses

To conclude this introduction, let us spend a few words on ergodicity breaking in spin glasses which, although it has not been directly addressed in this thesis, still provides physical motivation for the study of such intriguing systems.
The concept of ergodicity breaking is used in the field of quantum disordered systems for at least three distinct phenomena.

The first meaning is thermodynamic and is the one encoded in Parisi's solution [135–137]. Below the freezing temperature the Gibbs measure ceases to be a single object and fragments into an exponentially large number of pure states, mutually inaccessible in the thermodynamic limit and organized ultrametrically. The consequence is that the order parameter is no longer a number but a distribution, the overlap distribution $P(q)$, and that it fails to be self-averaging: two macroscopically identical samples, or two replicas of the same sample, need not agree. Ergodicity is broken here in the strict textbook sense, through a decomposition of configuration space into components separated by barriers that diverge with system size.

The second meaning is dynamical, and it is weaker and more subtle [138, 139]. A spin glass quenched below its freezing temperature never reaches a stationary state: correlation and response functions depend separately on the two times at which they are measured, not only on their difference, and the relaxation becomes slower the longer the sample has been waiting. This aging behavior, together with the memory

and rejuvenation effects that accompany it, is directly observable in the magnetic response of laboratory spin glasses [66, 67, 140], and in mean-field models it can be solved exactly, revealing a violation of the fluctuation–dissipation theorem that can be reinterpreted as an effective temperature for the slow degrees of freedom [141]. No infinite barriers are required: the system is not confined anywhere but its dynamics is so slow that the exploration of the whole configuration space is suppressed in the thermodynamical limit.

This last point deserves emphasis, because it is what distinguishes glassy ergodicity breaking from the integrable kind. An integrable system is genuinely forbidden from most of phase space, confined by its conservation laws to a manifold of vanishing measure, while a glass is free to visit any configuration, and the landscape only ensures that it will take a time growing without bound with the size of the system to do so. Ergodicity is lost not by constraint but by the divergence of the time scale on which it would be recovered.

Neither notion should be identified with the failure of thermalization discussed in the context of the eigenstate thermalization hypothesis [9, 10]. Aging is the relaxation of a system in contact with an environment, and this remains true in its quantum formulation, in which the bath is what allows the system to relax at all [113, 142, 143]; ETH concerns instead the fate of an isolated system evolving under its own unitary dynamics. For the same reason, many-body localization and quantum spin-glass order are conceptually independent phenomena [42, 144]. The first is a statement about the structure of individual eigenstates across the whole spectrum, the second about the structure of the low-energy Gibbs measure. Neither implies the other: glassy order is perfectly compatible with thermalizing eigenstates, and localization can occur with no glassy order whatsoever. The two coincide in certain models, where non-ergodic eigenstates and a many-body mobility edge appear together with the frozen phase [145, 146].

1.6. Outline of the thesis

The thesis is organized as it follows. The first part of the thesis is devoted to the numerical renormalization group study of the many body localization transition:

- In chapter 2, we discuss the scaling theory of Anderson localization. First we introduce the original work by Abrahams et al. and then we present a revised version of such work in terms of modern observables easily accessible in large numerical simulations and show how it is possible to have a renormalization group flow that depends on two independent scaling variables.

- In chapter 3, we apply the techniques developed in the previous chapter to the numerical renormalization group study of the random field XXZ spin 1/2 chain, a candidate model for the many body localization transition.

- In chapter 4, we consider the case of the quantum random energy model, a prototypical toy model for many body localized and quantum spin glass phases, and discuss its renormalization group flow.

The second part of the thesis focuses on the analysis of quantum and classical two dimensional disordered system with rotational invariance:

- In Chapter 5, we systematically describe how to construct semiclassical, low energy excitation on top of a classical energy minimum for a class of rotational invariant spin systems. We discuss how the symmetry of the classical states constrain the dynamics of the low energy, quantum excitations.

- In Chapter 6, we present novel numerical results on the zero temperature quantum phase diagram of the bond disordered, two dimensional, Heisenberg spin 1/2 model. The results are based on a state of the art, neural quantum states approach and are validated by a semiclassical expansion relying on the techniques discussed in the previous Chapter.

- In Chapter 7, we further investigate the properties of the low energy excitations in $SU(2)$ invariant, bond disordered spin models. We show that the tension between the gaplessness of the spectrum and the disorder produces a mobility edge if magnetic order is present and a weakly localized spectrum if absent. We discuss how ergodicity can be restored by the addition of interactions.

- In Chapter 8, we analyze in depth the case of a weakly disordered, two dimensional ferromagnet. The presence of weak disorder produces an abundance of low

energy modes, leading to an increase of the dynamical exponent. We propose a field theoretical based explanation to characterize such phenomenon.

Part I.

Scaling theory of the Many Body Localization phase transition

2. Scaling theory of localization

In this chapter we provide an introduction to the scaling theory of localization transitions. After reviewing the original formulation by Abrahams et al. , which assumes a single parameter scaling for the Anderson transition, we present a revised version of their theory, discussing also the case of a two-parameter-scaling. Then we give an overview of recent phenomenological approaches to investigate the renormalization group structure of the many body localization transition.

2.1. Scaling of the conductance

The use of renormalization group (RG) to study localization transitions goes back to the seminal work of Abrahams, Anderson, Licciardello, and Ramakrishnan [24]. The great achievement of the so called "gang of four" was to understand that a one-parameter scaling hypothesis explains the localization of non-interacting particles in $d \leq 2$ for any disorder strength, and the presence of a finite-disorder localization transition in $d \geq 3$. They considered the dimensionless conductance of a hypercube of size $L^d \gg a^d$, the lattice spacing, defined as

$$g(L) = \frac{G(L)}{e^2/2\hbar} = \frac{E_{Th}}{\delta} = \frac{2\hbar}{e^2}\sigma L^{d-2} \,, \tag{2.1}$$

where E_{Th} is the Thouless energy, defined as the geometric mean of the fluctuation in energy levels caused by replacing periodic by antiperiodic boundary conditions, and it is associated with the characteristic inverse diffusion time $\tau_D \sim L^2/D$, D being the diffusion constant, $\delta \equiv dE/dN = \rho(E)L^d$ is the mean level spacing, that scales as the volume times the density of states and $\sigma = e^2\rho D$ is the electrical conductivity.
The variation of the dimensionless conductance at a larger scale bL, $g(bL) = f(b, g(L))$ is described by the generic flow equation

$$\frac{d\ln g(L)}{d\ln L} = \beta(g(L)) \,, \tag{2.2}$$

where the crucial assumption, the so called *one parameter scaling* hypothesis, is that the β function depends only on $g(L)$ and it is continuous.
At very large and small values of the conductance it is possible to derive simple asymptotic forms of the β function only from physical considerations: for large g the system is diffusive, standard transport theory holds and the conductance is $G(L) = \sigma L^{d-2}$ so the β function is

$$\lim_{g\to\infty} \beta(g) = d - 2 \, . \tag{2.3}$$

In the localized phase g decays exponentially $g = g_0 e^{-\alpha L}$ and

$$\lim_{g\to 0} \beta(g) = \ln(g/g_0) \, . \tag{2.4}$$

The scaling analysis introduced by the gang of four describes correctly the Anderson phase structure and remarkably predicts in a very intuitive way the lower critical dimension of the transition. In the following we present a revised version of this theory, where we consider the scaling of a generic observable - then we specialize to quantities more easily accessed with modern computer libraries- and we introduce the possibility of another scenario, the *two parameter scaling* hypothesis, where the renormalization group flow is ruled by two coupled equations. Recently, the renormalization group scaling of the Anderson transition on d dimensional hypercubical lattices was studied [147], finding numerical evidence of the one parameter scaling in every dimension. Remarkably, increasing the spatial dimensionality, the critical point drifts towards the localized phase. On the regular random graphs [148]– a lattice alias of infinite dimensions – there is evidence of a two parameter scaling.

2.1.1. One parameter RG flow

Consider a generic observable A and define its beta function as

$$\beta \equiv \frac{d \ln A}{d \ln N}, \tag{2.5}$$

where N is the volume of the system. One can identify the volume either with the Hilbert space dimension $N \sim 2^L$, or with the spatial volume $N = L^d$. In the definition of the beta function, we have traded the RG parameter for the system size, which in the context of finite-size scaling can be thought of as a relevant operator of the renormalization group [149, 150]. We will use the convention $A \in [0, 1]$, with asymptotic values $A_{\text{loc}} = 0$ for the localized fixed point and $A_{\text{erg}} = 1$ for the ergodic one, which indeed agrees with the rescaled r-parameter ϕ.

If the one-parameter scaling hypothesis holds, the beta function is a function of A

alone, i.e.

$$\frac{d\ln A}{d\ln N} = \beta(A). \tag{2.6}$$

Therefore, the dependence of A on the system size $\ln N$ is obtained by solving the differential equation above by separation of variables:

$$\int_{A_0}^{A} \frac{dA'}{A'\beta(A')} = \ln\frac{N}{N_0}, \tag{2.7}$$

where A_0 is the value of A at $N = N_0$. If one is far from a zero of the beta function, one can integrate formally and find

$$G(A) - G(A_0) = \ln\frac{N}{N_0}, \tag{2.8}$$

where G is a primitive of the integral in Eq. (2.7). Inverting this equation for A, one finds

$$A = f(N/\tilde{N}_0), \tag{2.9}$$

where $f(x) = G^{-1}(\ln x)$ turns out to be a universal scaling function, in one-to-one correspondence with the function β_0, and $\tilde{N}_0 \equiv N_0 e^{-G(A_0)}$. Therefore, in a regular section of the flow and far from a critical point, the observables are functions of the volume N, whether this volume is the spatial or the Hilbert space volume.

If, instead, the RG trajectories—obtained by varying the values of the initial parameters (e.g. disorder strength)—do not always lie on a single curve, one needs to take into account corrections to the one-parameter scaling solution. For a fixed value of the initial parameters, let us assume that the curve starts close to the one-parameter curve $\beta_0(A)$

$$\left.\frac{d\ln A}{d\ln N}\right|_{N=N_0} = \beta_0(A) + c \qquad \text{with } c \ll \beta_0, \tag{2.10}$$

and quickly converges to it; see Fig. 2.1 for a sketch. One can then write a phenomenological set of equations, projecting the RG flow in the plane spanned by the relevant and the least irrelevant operator

$$\frac{d\ln A}{d\ln N} = \beta, \tag{2.11}$$

$$\frac{d\beta}{d\ln N} = -\omega\Big(\beta - \beta_0(A)\Big). \tag{2.12}$$

In the limit $\omega \to \infty$, one recovers the one-parameter scaling equation $d\ln A/d\ln N = \beta_0(A)$. Taking ω large but finite, and assuming to start sufficiently close to the one-parameter scaling curve, such that $\beta_0(A)$ can be considered a constant for a first part

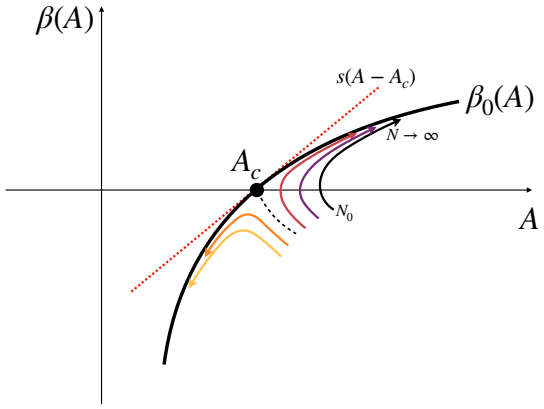

Figure 2.1.: Sketch of a one-parameter-scaling RG flow with irrelevant corrections, similar to what can be observed in the Anderson model in d-dimensional space [151]. The solid black curve represents the one-parameter-scaling beta function $\beta_0(A)$, which vanishes at the critical point A_c. The colored solid lines represent the beta function for different choices of the initial parameters, as described by Eq. (2.14). The starting point of these lines occurs at $N = N_0$ and N grows in the direction indicated by the arrows. Around the critical point A_c, the beta function can be linearized as described by Eq. (2.15).

of the RG flow, one can find the solution

$$\frac{d\ln A}{d\ln N} = \beta_0(A) + c\, e^{-\omega \ln(N/N_0)}. \tag{2.13}$$

Upon integration, in the approximation $c \ll 1$, one has

$$A(N, A_0) = f(N/\tilde{N}_0) + f_1(N/\tilde{N}_0)N^{-\omega}, \tag{2.14}$$

where ω corresponds to the dimension of the smallest irrelevant operator. Only rarely ω is so large that it can be ignored altogether. In particular, for the Anderson model in the limit of $d \to \infty$ — which corresponds to the model defined on the random regular graph (RRG) — it has been argued that actually $\omega \to 0$ [147, 151]. Let us mention that the limit $d \to \infty$ has to be taken with caution and cannot be obtained by simply setting $\omega = 0$ in Eq. (2.14). We comment more on this in Sec. 2.1.2.

2.1.2. Close to a critical point

Close to a critical point, if the beta function has a simple zero $\beta(A_c) = 0$ for some value $A_c \neq 0$ of the observable, then the dependence of A on N acquires the form of a scaling law. Let us write the Taylor expansion of $\beta(A)$ close to the fixed point as

$$\beta(A) = s(A - A_c) + \sum_{n\geq 2} \frac{c_n}{n!}(A - A_c)^n. \tag{2.15}$$

Going back to Eq. (2.7), it holds

$$\begin{aligned}\int_{A_0}^{A}\frac{dA'}{A'\beta(A')} &= \int_{A_0}^{A}dA'\frac{1}{A_c s(A'-A_c)}\\ &\quad+\int_{A_0}^{A}dA'\frac{A_c s(A'-A_c)-A'\beta(A')}{A_c s(A'-A_c)A'\beta(A')}\\ &= \frac{1}{A_c s}\ln\left|\frac{A-A_c}{A_0-A_c}\right|+\int_{A_0}^{A}dA' g(A'-A_c).\end{aligned} \tag{2.16}$$

The function

$$g(x)=\frac{A_c s x-(x+A_c)\beta(A_c+x)}{A_c s x(x+A_c)\beta(A_c+x)} \tag{2.17}$$

is regular close to $x=0$:

$$g(x)=-\frac{2s+c_2A_c}{2A_c^2s^2}+O(x)\equiv -a+O(x), \tag{2.18}$$

where again $c_n=d^n\beta/dx^n|_{x\to 0}$.

Putting everything together and defining the primitive $\int dx\, g(x)=G(x)=-ax+O(x^2)$ and the critical exponent $\nu=1/A_c s$, one has

$$\ln\frac{N}{N_0}=\nu\ln\left|\frac{A-A_c}{A_0-A_c}\right|+G(A-A_c)-G(A_0-A_c), \tag{2.19}$$

which can be inverted first as

$$|A-A_c|e^{G(A-A_c)/\nu}=\left(\frac{N}{N_0\xi(A_0)}\right)^{1/\nu}, \tag{2.20}$$

with $\xi(A_0)=|A_0-A_c|^{-\nu}e^{-G(A_0-A_c)}\simeq|A_0-A_c|^{-\nu}$ being a critical length. Consequently, by calling f the inverse of the function $x\mapsto xe^{G(x)/\nu}$, one gets

$$A(N,A_0)=A_c+f\left(\left(\frac{N}{N_0\xi(A_0)}\right)^{1/\nu}\right). \tag{2.21}$$

Notice that for small x it holds $xe^{G(x)/\nu}\simeq xe^{-\frac{a}{\nu}x}\simeq x-\frac{a}{\nu}\,x^2+O(x^3)$, therefore the function $f(x)\simeq x$ in the same region.

Under the hypothesis that, at $\ln N_0=O(1)$, A_0 is a smooth function of the microscopic parameters of the model, it is possible to collapse the data with a universal scaling function f, in one-to-one correspondence with the function β. In the context of localization transitions, the Anderson model in finite dimensions $d>2$ exhibits a phase transition which is characterized precisely by this kind of scaling theory. Including also

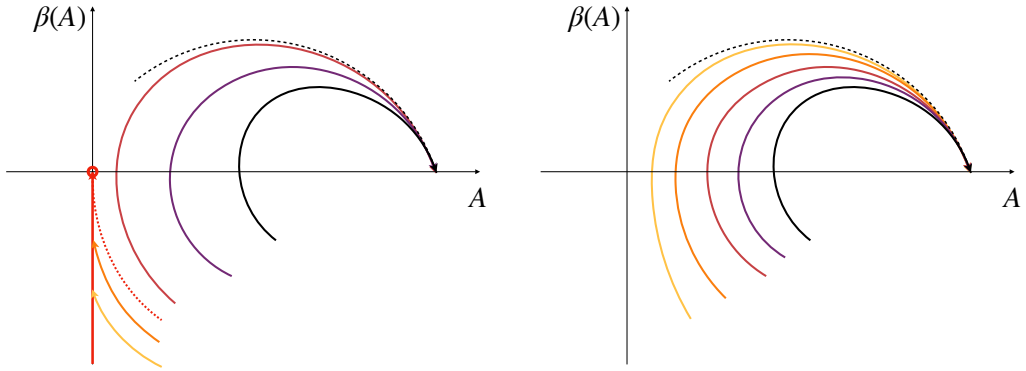

Figure 2.2.: *(Left)* Beta function for a two-parameter scaling transition scenario. In the localized phase, the RG flow reaches $A = 0$ at a finite and negative $\beta = -1/\xi_{\text{loc}}$, and its value depends on W, thus generating a line of fixed points (solid red). In the ergodic phase, instead, the curves flow to $A = 1$ as prescribed by random matrix theory. The RG flow around the ergodic fixed point is described by a one-parameter scaling, meaning that all the RG curves for $W < W_c$ ultimately approach a universal curve (dashed black). The red dotted line is the *critical* line for $W = W_c$, which separates the localized and ergodic phases. *(Right)* Beta function in the absence of a localized phase. For any finite value of W, the RG flow never reaches $A = 0$ and flows to the ergodic fixed point at large enough sizes.

the irrelevant corrections discussed in Sec. 2.1.1, one finds

$$A(N, A_0) = A_c + f(x) + N^{-\omega} f_1(x), \tag{2.22}$$

where ω is the scaling dimension of the least irrelevant operator [1] and $x \equiv (N/N_0\xi(A_0))^{1/\nu}$. Notice that Eq. (2.22) has a notation similar to Eq. (2.14), but the scaling functions involved are different, as an explicit linearization was performed around the critical point.

As mentioned previously, in the limit $d \to \infty$ of the Anderson model (corresponding to the RRG), the irrelevant exponent ω becomes marginal, but this does not correspond to simply setting $\omega = 0$ in Eq. (2.22). In fact, Eq. (2.22) has been derived for a critical point A_c isolated from the other "Gaussian" fixed points, while in the RRG $A_c = A_{\text{loc}} = 0$. One can show that, when these two limits are taken consistently, one obtains logarithmic corrections to Eq. (2.22), indicating the occurrence of a marginal direction [147].

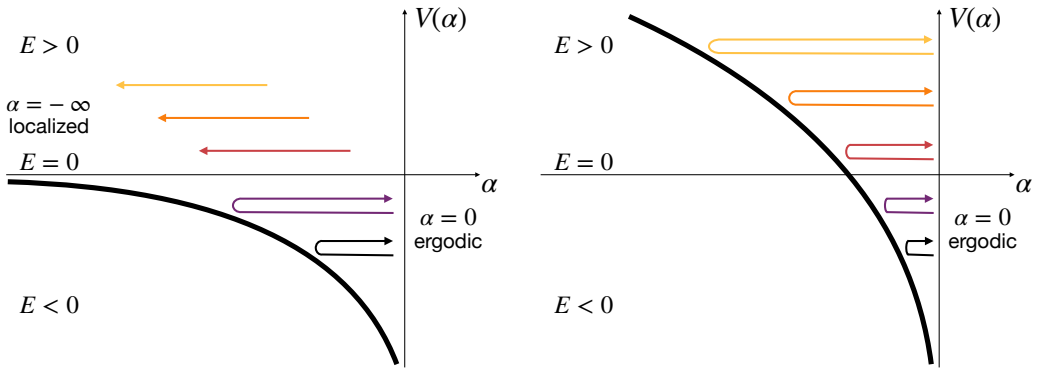

Figure 2.3.: *(Left)* Example of potential function for the one-dimensional dynamical model in the presence of a localization transition, similarly to what happens for the RRG. For small disorder, corresponding to energies $E < E_c$ ($E_c = 0$ in the sketch), the presence of the potential confines the trajectories, excluding the point $\alpha = -\infty$ (i.e. $A = 0$): the original system is ergodic. For large enough disorder, corresponding to energies $E > E_c$, the potential does not confine the classical trajectories, and $\alpha \to -\infty$ when $t \to \infty$: the localized phase is approached in the thermodynamic limit. Notice also that, at $t = 0$, particles move from right to left, since $\beta < 0$, being the beta function negative at small enough sizes. *(Right)* When the potential is such that $V(\alpha \to -\infty) \to +\infty$, the classical trajectories are always reflected and $\alpha \to 0$ (equivalently $A \to 1$) when $t \to \infty$. In this case there is no localized phase.

2.1.3. From one to two parameters

In the previous section, we considered the situation where there is only one relevant parameter in the Hamiltonian, and the lowest anomalous dimension is sufficiently large and negative that it can be included as a small correction to the one-parameter formulas. This occurs when the unstable fixed point A_c is well separated from the two other "Gaussian" fixed points, which in this case represent the localized and ergodic phases. When instead $A_c \to A_{\text{loc}}$ (like the Anderson model in $d \to \infty$) or $A_c \to A_{\text{erg}}$ (like the Anderson model as $d \to 2$), one of the parameters must necessarily become a flat direction or, in the language of RG, *marginal*. As a concrete example, this happens when the Wilson-Fisher critical point merges with the Gaussian fixed point in the Ising model at the upper critical dimension [152].

In order to go beyond one parameter scaling, let us define the RG time $t \equiv \ln N$ and

$$\alpha \equiv \ln A. \tag{2.23}$$

Let us also represent with a dot the derivatives with respect to RG time: $d\alpha/dt \equiv \dot{\alpha}$.

[1] It is possible to work not strictly in the limit $\omega \to \infty$, and analyze the flow close to the critical point to extract the correct relevant and irrelevant anomalous dimensions to $O(1/\omega)$.

The RG equations acquire the general form

$$\dot{\alpha} = \beta \tag{2.24a}$$

$$\dot{\beta} = \gamma(\alpha, \beta) \tag{2.24b}$$

for a certain function γ. This is the general system of equations describing a two-parameter scaling RG flow. In principle, the function γ depends also on β: this dependence is of particular importance also to model the adherence to the one-parameter scaling curve towards the ergodic fixed point as the overdamped limit of a dynamical system. However, in the region of A near zero it can be seen from the numerical data that γ is a function of α alone; therefore, one can reduce to the system of equations

$$\dot{\alpha} = \beta \tag{2.25a}$$

$$\dot{\beta} = \gamma(\alpha). \tag{2.25b}$$

The simplification $\gamma(\alpha, \beta) \to \gamma(\alpha)$ is crucial, because now the RG equations can be interpreted as Hamilton's equations of motion for an effective one-dimensional particle, living on the half-line $\alpha \leq 0$. Its Newton's equation reads: $\ddot{\alpha} = \gamma(\alpha)$, so $\gamma(\alpha)$ is the force field. RG equations that acquire Hamilton's (or Newton's) form are special because they admit an integral of motion, the energy:

$$E = \frac{1}{2}\dot{\alpha}^2 + V(\alpha), \tag{2.26}$$

where $V(\alpha) = -\int \gamma(\alpha) d\alpha$. The conservation of energy is a manifestation of the time/scale invariance which arises near the critical point $A = 0$.

In order to fix ideas, it is instructive to consider the illustrative example of the Anderson model on random regular graphs (RRG) [147]. There, the numerics for the fractal dimension are well described by $\gamma(\alpha) \propto e^{\alpha}$ in the region $\alpha \to -\infty$, giving rise to the Liouville equation

$$\ddot{\alpha} = ce^{\alpha} \tag{2.27}$$

for some constant c. The energy, in turn, reads

$$E = \frac{1}{2}\dot{\alpha}^2 - ce^{\alpha}. \tag{2.28}$$

The orbits of this dynamical system depend strongly on the value of E, which is fixed by the initial microscopic parameters. If $E > 0$, the particle can go all the way to $\alpha \to -\infty$, i.e. $A = A_{\text{loc}} = 0$; for $E < 0$, it bounces back with $\alpha \to 0$, i.e. $A \to A_{\text{erg}} = 1$.

Therefore, one can see that the presence of two stable phases, separated by a critical point $E = 0$, corresponds to whether the force field is *confining* or not: confining potentials correspond to the absence of localization, while non-confining ones admit a localized phase. This is shown by the sketches in Figs. 2.2 and 2.3.

In the case of the RRG — Eqs. (2.27) and (2.28) — the critical trajectory is $A_{\text{crit}}(t) \propto 1/t^2$, which describes well the numerical findings [147]. Notice that the existence of a localized region is universal for all $n > 0$ in $\gamma(\alpha) = e^{n\alpha}$. In fact, one can reabsorb n by rescaling $\alpha \to \alpha/n$, but this corresponds to $A \to A^{1/n}$ and therefore the critical line becomes $A_{\text{crit}}(t) \sim 1/t^{2/n}$. The value of the exponent n determines the power law behavior of observables near the critical point and thus "labels" different universality classes.

This example also clarifies the meaning of the second equation for $\dot{\beta}$: it describes the renormalization of the localization length ξ_{loc}, as a function of the distance from the localized critical point. This can be seen from the fact that observables (e.g. the r-parameter) decay exponentially with the system size $L = \ln N$, where in this case N is the number of vertices in the RRG. Assuming $A \propto e^{-L/\xi_{\text{loc}}}$, one sees that $\beta = -1/\xi_{\text{loc}}$ and $\dot{\beta} = \dot{\xi}_{\text{loc}}/\xi_{\text{loc}}^2$. The effects encoded in this equation are *non-perturbative*, since the usual perturbation theory in the hopping term (locator expansion) only predicts exponential decay, without renormalization of the decay length.

The example considered so far admitted the presence of a localized phase. A second, natural class of forces to consider is the one in which all trajectories go to the ergodic fixed point $\alpha = 0$ (i.e. $A = 1$), corresponding to confining potentials. A paradigmatic form which has such a behavior is the logarithmic potential $V(\alpha) = \ln|\alpha|$, leading to Newton's equation

$$\ddot{\alpha} = -1/\alpha. \tag{2.29}$$

This equation can be solved by quadratures using the formula

$$\int_{\alpha_0}^{\alpha(t)} \frac{d\alpha}{\sqrt{2(E - \ln|\alpha|)}} = t - t_0, \tag{2.30}$$

since the energy reads

$$E = \frac{1}{2}\dot{\alpha}^2 + \ln|\alpha|. \tag{2.31}$$

All the trajectories have a turning point, located at $\alpha_A = -e^E$, and are therefore confined as claimed above. For such a potential, the localized phase—in the sense of observables exponentially decreasing with system size—does not exist. The only thing happening as the disorder is increased is a slower and slower approach to ergodicity. From the perspective of the renormalization of the localization length, the logarithmic

potential entails

$$\dot{\xi}_{\mathrm{loc}} \propto 1/\ln(1/A). \tag{2.32}$$

In the limit $A \to 0$ one sees that $\dot{\xi}_{\mathrm{loc}} = 0$, but such a slow convergence towards this value makes the entire localized phase *unstable* towards developing ergodicity.

2.2. Phenomenological RG analysis of MBL models.

Extending the RG analysis to interacting models has proven to be difficult. Some authors took inspiration from the Ma-Dasgupta-Hu-Fisher strong-disorder RG [153–157] and applied a similar procedure to models hosting MBL [158, 159]. More promising results were found, however, once the same real-space rules were applied not to the microscopic degrees of freedom but to a coarse-grained description of the chain, in which the system is represented as an alternating sequence of thermal and insulating regions [158, 160–162]. It is within this phenomenological framework that the first evidence for a Berezinskii–Kosterlitz–Thouless (BKT) character of the transition emerged [163–166].

The starting point of the phenomenological approach is to forget the individual spins and retain only the block structure of the chain: long "bubbles" that behave locally as thermal baths are interspersed with insulating regions. Each block is assigned a length, and each insulating block carries in addition a decay rate measuring how strongly it suppresses transport across itself [160, 161, 167]. The renormalization proceeds in the familiar strong-disorder spirit: one identifies the block with the smallest internal energy scale, eliminates it, and fuses it with its two neighbours according to a fixed set of merging rules. A short thermal block caught between two strong insulators is swallowed, enlarging the insulating region around it; a long thermal block, on the other hand, thermalizes its neighbours and grows at their expense. Iterating this decimation, one follows the joint distribution of block lengths and decay rates to ever larger scales, and the fate of the system is decided by whether the thermal fraction is dominant in the process. The earliest realizations of this idea [160, 167] could only be integrated numerically, but they already carried a suggestion that the fixed-point structure was unusual, i.e. that the two phases were not mirror images of one another across a symmetric critical point. The asymmetry between the two phases has a clear physical origin in the quantum avalanche instability [57, 58]: delocalization is not a bulk instability but a rare-region catastrophe, seeded by atypical thermal fluctuations that grow until the whole chain thermalizes. The two sides of the transition inherit this imbalance. The ergodic phase is governed by a single attractive fixed point, while

the localized phase enjoys only a marginal stability, protected until avalanche seeds begin to proliferate. This is precisely the anatomy of a Berezinskii–Kosterlitz–Thouless (BKT) transition [168, 169]: a whole line of fixed points –here the continuous family of stable MBL states– that survives until it terminates at a single critical point, beyond which the vortex-like thermal inclusions unbind and sweep the system into its ergodic phase.

Placing this analogy on a quantitative footing required identifying the right pair of variables, and here the analytically solvable formulations proved decisive [163, 164]. Their common conclusion is that the critical behavior is controlled not by a single relevant coupling but by *two* coupled scaling variables: the density of thermal regions, playing the role of the vortex fugacity, and the lengthscale governing the decay of typical matrix elements, playing the role of the stiffness. The resulting flow is of canonical BKT form, with a line of fixed points describing the MBL phase terminating at the transition, beyond which any bare density of thermal seeds grows without bound and the system runs away to the ergodic attractor.

This two-parameter structure yields predictions sharp enough to distinguish the BKT scenario from an ordinary continuous transition. Chief among them is that the localization length diverges not as a power law but with the essential singularity characteristic of BKT criticality, $\xi \sim \exp(c/\sqrt{W - W_c})$, so that the conventional exponent ν is effectively infinite. Several independent schemes [163–166] converge on this same Kosterlitz–Thouless flow, despite differing in their microscopic conventions. Yet all remain phenomenological in an essential way: the block rules and the identification of the two scaling variables are supplied by physical intuition rather than derived from a Hamiltonian. Whether the BKT universality class truly emerges from a microscopic model is a question these approaches cannot settle and that we investigate in the next chapters.

3. Renormalization group scaling in the random-field Heisenberg spin chain

In this chapter, the spectral properties of the Heisenberg spin-1/2 chain with random fields are analyzed in light of the renormalization group scaling theory that was discussed in the previous chapter. We reconstruct the beta function of the order parameter from the numerical data, and observe that it may not admit a one-parameter scaling form and a simple Wilson-Fisher fixed point. Rather, it appears to be more compatible with a two-parameter, Berezinskii–Kosterlitz-Thouless-like flow with a line of fixed points (the many-body localized phase) terminating at the localization transition critical point. We argue that this renormalization group framework provides a more coherent and intuitive explanation of numerical data, up to the system sizes available with the present technology.

3.1. Introduction

In this chapter we present a novel approach to the analysis of numerical data obtained by exact diagonalization of small systems, using the theory of finite-size scaling to infer the RG flow of the MBL transition in the light of the scaling theory discussed in the previous chapter, considering the case of the random-field XXZ spin 1/2 chain. Within the accuracy of our analysis, the numerical reconstruction of the model phase diagram appears consistent with the picture already discussed for the Anderson model in infinite dimensions [147]: the ergodic fixed point has the nature of a random matrix theory (RMT) fixed point [170], with volumic scaling (i.e. the natural scaling variable is the Hilbert space volume and not the physical volume of the system), while the critical point seems to lie at the end of a line of fixed points representing the localized phase.

The question is then reduced to understanding the flow near the line of fixed points, which is qualitatively reminiscent of a Berezinskii–Kosterlitz-Thouless (BKT) RG flow

(the appearance of BKT physics is a recurring theme in MBL [163–166]). We show that the flow can have two possible topologies. In one, like in the BKT analysis of the XY model or the Anderson model in infinite dimensions, the line of fixed points is attractive and corresponds to the MBL phase. Alternatively, the line can be repulsive, and the MBL phase does not exist for any value, no matter how large, of disorder. To discriminate between the two scenarios, we analyze the numerical data at moderately high disorder in terms of the RG trajectories. We further realize that the RG flow can be mapped onto the phase space orbit of a classical, Newtonian particle. We try to infer the potential in which the particle moves, and from this, the fate of the MBL phase.

3.2. Model

The random-field XXZ spin chain is defined by the Hamiltonian

$$\hat{H} = J \sum_{i=1}^{L} \hat{\mathbf{S}}_i \cdot \hat{\mathbf{S}}_{i+1} + \sum_{i=1}^{L} h_i \hat{S}_i^z \ , \tag{3.1}$$

where $\hat{\mathbf{S}}_i = (\hat{S}_i^x, \hat{S}_i^y, \hat{S}_i^z)$ are spin-1/2 operators and h_i are i.i.d. random variables distributed uniformly over the interval $[-W, W]$. Since the relevant parameter is the ratio between the disorder strength W and the hopping parameter J, in the following we will fix $J = 1$ and consider W as the only parameter. The model has a global symmetry given by the conservation of the total spin $\hat{S}^z = \sum_i \hat{S}_i^z$. For numerical efficiency, in this work we will always restrict to the $\hat{S}^z = 0$ sector, whose dimension is given by $\dim(\mathcal{H}) = \binom{L}{L/2} \lesssim 2^L$. It has been conjectured that the Hamiltonian (3.1) undergoes a many-body localization phase transition at a critical disorder strength W_c [42, 171]: while a small disorder W breaks the Bethe-ansatz integrability of the clean model and makes it ergodic, for $W > W_c$ the system becomes a non-ergodic insulator, failing to thermalize. Moreover, studies of transport properties in the disordered Heisenberg chain showed the presence of a transition from diffusive to subdiffusive transport within the ergodic phase [172, 173]. On one hand, the perturbative computation leading to MBL [40], extended in Refs. [45, 174, 175] to spin chains, predicts that the eigenstates at strong enough disorder assume the form of exponentially-localized integrals of motion (LIOMs) [43, 44]. Correspondingly, the spectral statistics is Poissonian. On the other hand, it has been argued that non-perturbative effects such as avalanches [57, 176] and many-body resonances [177, 178], can lead to delocalization. The conflict between these opposite views seems not to be solvable by numerical meth-

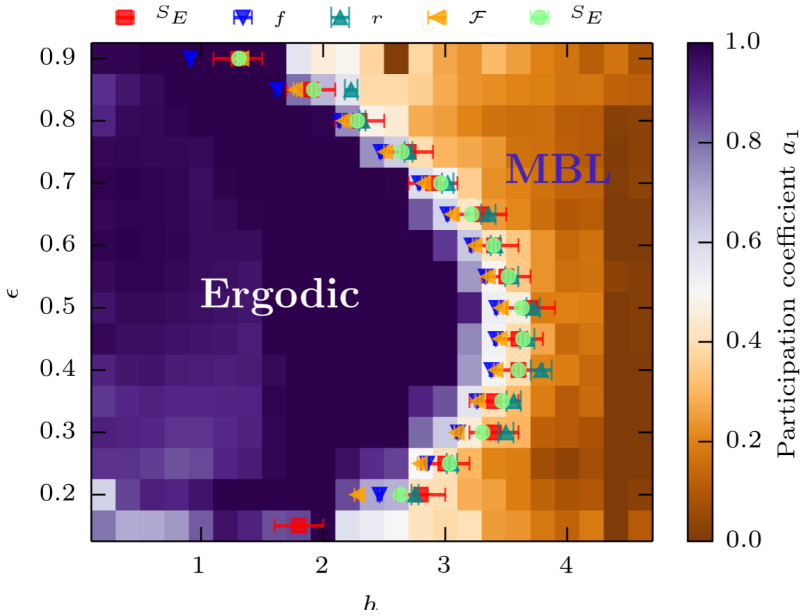

Figure 3.1.: Figure taken from Phys. Rev. B 91, 081103(R). Phase diagram of the random-field XXZ spin chain. ϵ and h are respectively the energy density and the variance of the random fields. The phase diagram was obtained by considering various figures of merit and resorting to exact diagonalization of systems of length $L \leq 22$

ods, as exact diagonalization is confined to too small systems [179–181], and tensor network methods to too short times [182]. The absence of clear-cut numerical results has led different authors to claim that MBL does not exist at all [183, 184] or that a wide, pre-thermal regime hinders the numerical observation of the actual MBL transition [178, 185].

3.3. Scaling of the average spectral gap ratio

In modern studies of disorder-induced localization in quantum systems, it is customary to analyze the spectral properties to probe the ergodic or localized nature of the model. A quantity typically considered for discriminating between chaotic or localized spectra is the spectral gap ratio, or r-parameter [186]:

$$r = \frac{1}{N_e - 2} \sum_{n=1}^{N_e-2} \frac{\min(\Delta E_n, \Delta E_{n+1})}{\max(\Delta E_n, \Delta E_{n+1})}, \tag{3.2}$$

where $\Delta E_n = E_{n+1} - E_n$ is the n-the energy gap in a narrow energy window containing N_e energy levels. Notice that the use of such a window in the ergodic case would define the microcanonical ensemble. The value $r_{\mathrm{P}} = 2\ln 2 - 1 \simeq 0.386$ is the Poisson value for integrable systems, while $r_{\mathrm{WD}} \simeq 0.5307$ is the Wigner-Dyson value for random matrices

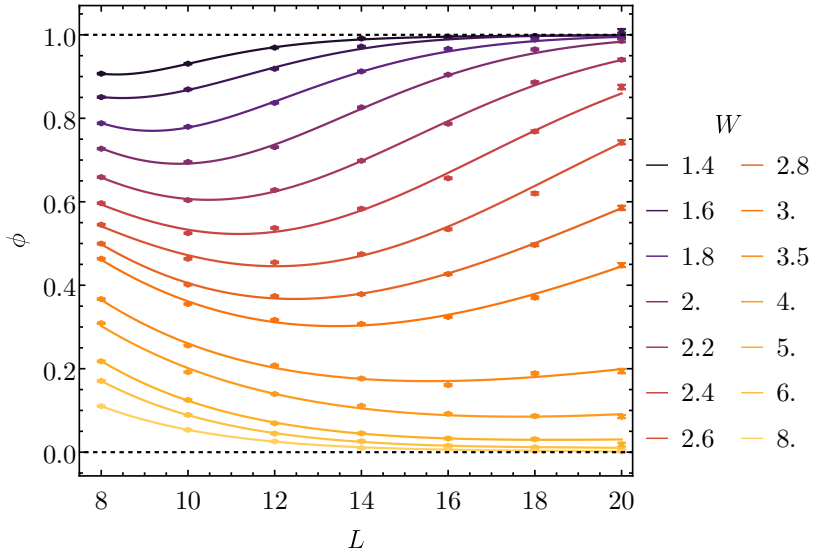

Figure 3.2.: System-size dependence of the rescaled r-parameter ϕ, Eq. (3.3), in the XXZ spin chain. Different colors correspond to different values of the disorder strength W. Dots represent numerical data, while solid lines are polynomial interpolating curves, later used for the β-function computations. Dashed lines represent the asymptotic values: $\phi = 0$ for the localized and $\phi = 1$ for the ergodic phase.

of the Gaussian Orthogonal Ensemble (GOE), corresponding to chaotic systems with time-reversal symmetry. For convenience, we rescale the average gap ratio, defining

$$\phi = \frac{r - r_{\mathrm{P}}}{r_{\mathrm{WD}} - r_{\mathrm{P}}}. \tag{3.3}$$

It follows that $\phi = 0$ corresponds to a non-ergodic behavior, while $\phi = 1$ to ergodicity.

The rescaled r-parameter of the random-field XXZ spin chain averaged over many disordered samples is shown as a function of the system size in Fig. 3.2. The data is obtained via exact diagonalization, see App. 3.6.1 for a short summary of the numerical methods (see also Ref. [187] for an extended discussion). The solid lines are polynomial interpolations of the data; we comment extensively on the numerical analysis in Sec. 3.4. First, however, we introduce in the next section the framework of the beta function, necessary to interpret coherently the numerical data.

Let us see what happens if we collapse our numerical data by working in the framework of the one-parameter scaling. As discussed in the previous chapter, the subleading corrections to Eq. (2.21) are taken into account as in Eq. (2.22). Near the critical point, the critical length $\xi(A_0)$ diverges, and therefore $x \ll 1$. In this limit, one can expand $f_1(x) = c + c_1 x + O(x^2)$, and we will consider the non-zero term $f_1(x) = c$, which is a customary choice in the literature (see, *e.g.*, Ref. [188]). In order to collapse

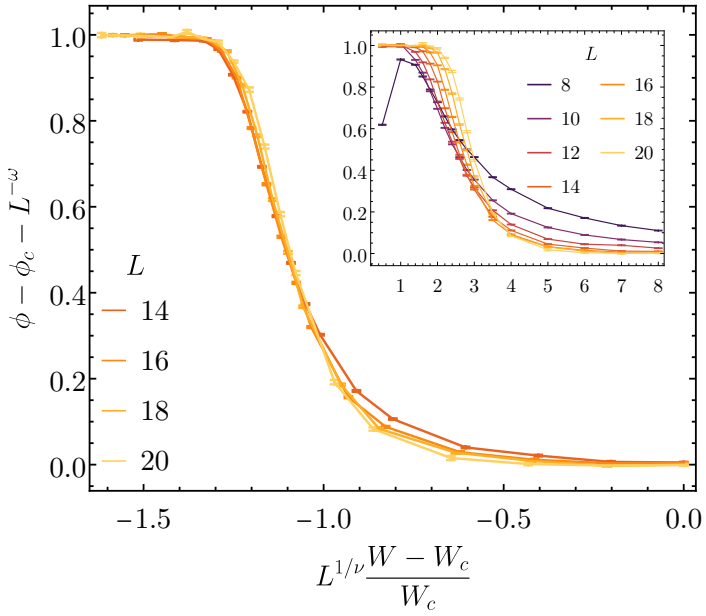

Figure 3.3.: Naive finite-size scaling for the average rescaled gap ratio ϕ. In the main plot, the collapse is shown for the larger sizes, $L > 12$, while the inset contains data before the collapse down to size $L = 8$. The collapse is obtained by fixing $\phi_c = 0$, and it yields a critical disorder $W_c \simeq 8.0$ and exponents $\nu \simeq 5.5$, $\omega \simeq 2.0$. We will present a different explanation for the critical exponent $\omega = 2$ in the next section. Notice also the similarity with the data for the Anderson model on the RRG in [188]. For a collapse in which we allow ϕ_c to vary, we refer to App. 3.6.2.

the rescaled r-parameter ϕ, we use the relation

$$\phi(L, W) = \phi_c + f\left(L^{1/\nu}\frac{W - W_c}{W_c}\right) + cL^{-\omega}, \tag{3.4}$$

where five constants—ϕ_c, W_c, ν, ω and c—and a function f are to be determined. In the argument of the scaling function, we have replaced $\xi \sim (W - W_c)^{-\nu}$ according to the usual scaling law, and we have chosen to use the chain length L instead of the Hilbert space dimension N, since it turned out to provide a better collapse of the data.

In Fig. 3.3 a fairly good data collapse is obtained for the rescaled r-parameter by fixing $\phi_c = 0$, which is what one expects observing the data in Fig. 3.2. The collapse yields a critical disorder $W_c \simeq 8.0$ and exponents $\nu \simeq 5.5$ and $\omega \simeq 2.0$. The collapse, however, cannot be taken too seriously. First, such a large ν exponent seems to signal an exponential scaling with system size near the critical point, rather than a power-law. Second, and more importantly, the function f in Eq. (3.4) appears not to be linear near $x = 0$ in Fig. 3.3, i.e. $df/dx = 0$ at the critical point, and this is a clear contradiction with the previous discussion.

As a workaround (see App. 3.6.2 for details), one could leave ϕ_c free and obtain a fairly good collapse by fixing the critical value of the disorder to $W_c \simeq 3.8$, which

can be linearly extrapolated from the finite-size zeros of the beta function (see e.g. the points ϕ_A in Fig. 3.6 up to $W = 3$), and which agrees with the literature [189]. However, this collapse yields a critical value $\phi_c \simeq 0.13$, which is larger than the upper bound one finds from the same numerical data: for $W = 4$ one already sees a turning point at $\phi_A = 0.085(4)$. Moreover, the best fit critical exponents are $\nu \simeq 1$ and $\omega \simeq 2$, with ν violating the Harris bound $\nu > 2/d$ [179, 190], where the spatial dimension is $d = 1$ in the present case.

3.3.1. Two possible scenarios for MBL

Let us here spend a few words to summarize the main results discussed in the previous sections. We have presented two possible scaling theories for localization transitions: the first one is compatible with the *one-parameter* scaling hypothesis, around both the ergodic and the localized fixed points and rules the critical behavior of the Anderson model in finite dimensions $d > 2$; the second one is instead characterized by one-parameter scaling only around the ergodic fixed point, while trajectories approach a line of localized fixed points according to a *two-parameter* scaling hypothesis. This is the case of the Anderson model in the limit $d \to \infty$, which is also the model defined on the RRG.

It is natural to ask what happens in many-body problems, e.g. the XXZ quantum spin chain. In this case, we can draw two possible scenarios, which will be addressed by our numerical analysis in the following section. The first is the *transition scenario*: if a localization transition occurs, the critical point has to be localized (as we will also discuss in the following) and, consequently, a two-parameter scaling theory describes the critical properties. This case corresponds to the beta function cartoon on the left in Fig. 2.2: the ergodic trajectories are separated from the localized ones by a critical line which terminates on the point $(\phi = 0, \beta = -1/\xi_{\text{loc}} = 0)$, which is the last of a line of localized critical points $(\phi = 0, \beta = -1/\xi_{\text{loc}} < 0)$. This scenario is well captured by a non-confining potential as the one sketched in the left panel of Fig. 2.3. The second scenario, on the other hand, is the *no-transition scenario*: in this case all the trajectories, despite displaying finite size localization, will flow eventually to the ergodic fixed point $A = 1$, governed by a one parameter curve in the large size limit (see right panel of Fig. 2.2). The no-transition scenario is well captured by a confining potential as the one sketched on the right in Fig. 2.3.

In the following Sec. 3.4 we present numerical data that will be analyzed in the light of the observations made above.

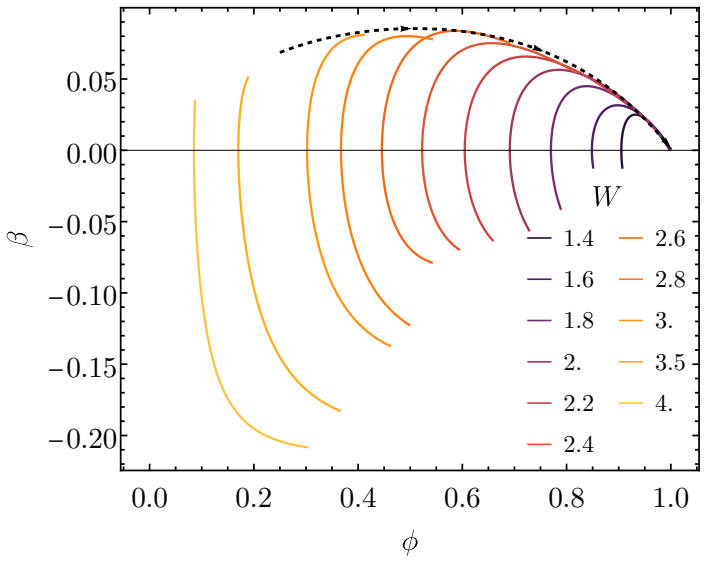

Figure 3.4.: Beta function of the rescaled r-parameter in the ergodic regime. Each line represents the flow of the observable towards the ergodic fixed point, and corresponds to a different value of the disorder strength W. The lines are parametrized by the system size (sizes increase from bottom to top). The figure is obtained by plotting the logarithmic derivatives in N of the fitting functions used in Fig. 3.2, according to the definition Eq. (2.5). The dashed black line is the envelope of the curves obtained numerically, and represents our best estimate of the one-parameter scaling curve $\beta_0(\phi)$.

3.4. Numerical results

We now analyze the beta function for ϕ, the rescaled r-parameter defined in Eqs. (3.2)–(3.3). Two regions can be identified in the RG flow, which will be discussed separately: in the (finite-size) ergodic region, the RG trajectories flow toward the fixed point at $\phi = 1$ reaching an asymptotic limit described by a one-parameter-scaling curve; in the (finite-size) localized region (where $\phi \ll 1$), the RG trajectories follow a two-parameter-scaling scenario, and flow to a line of fixed points terminating at the critical point $(\phi = 0, \beta = 0)$. The beta function is shown in Fig. 3.4 for the ergodic regime, where it is computed using the definition (2.5) [1]. We refer to Fig. 3.8 for the beta function in the localized region, to compute which we resorted to a more refined technique, discussed in Sec. 3.4.2.

3.4.1. The ergodic fixed point

From the numerical data in Fig. 3.4, one can observe that in the XXZ spin chain the RG curves flow towards the ergodic fixed point by eventually attaching to a one-

[1] The logarithmic derivatives in Eq. (2.5) are computed by using $N = 2^L$ in place of $N = \binom{L}{L/2}$, as they differ by a proportionality constant.

parameter-scaling curve $\beta_0(\phi)$. As the disorder W increases, the RG time needed to reach $\beta_0(\phi)$ also increases.

The one-parameter-scaling component $\beta_0(\phi)$ of the beta function can be obtained from the data by considering the envelope of the curves towards the ergodic fixed point, leading to the black dashed curve in Fig. 3.4. In practice, it is obtained by binning the values of ϕ and considering the maximum among the data corresponding to different W in each bin. The list of maxima is then interpolated with a polynomial function with simple zeros in $\phi = 0$ and $\phi = 1$:

$$\begin{aligned}\beta_0(\phi) = a_1\phi(1-\phi) + a_2\phi(1-\phi)^2 \\ + a_3\phi(1-\phi)^3 + a_4\phi^2(1-\phi) \\ + a_5\phi^2(1-\phi)^2 + a_6\phi^3(1-\phi).\end{aligned} \tag{3.5}$$

This is the best lower bound to the one-parameter scaling curve $\beta_0(\phi)$ that can be obtained with our data: the curves at $W = 3.5$ and 4, which reasonably also flow to $\phi = 1$ for system sizes larger than the ones numerically accessible, may produce an envelope which is greater than the dashed curve in Fig. 3.4, especially far from the region $\phi \simeq 1$.

Denoting with N_0 the smallest value of N allowing to approximate the flow with the one-parameter flow, i.e. $\beta(\phi, L > L_0) \simeq \beta_0(\phi)$, one has

$$\frac{d\ln\phi}{d\ln N} = \beta_0(\phi), \tag{3.6}$$

from which

$$\phi(W, L) = f(N/N_0 e^{G(\phi_0)}), \tag{3.7}$$

where $f(x) = G^{-1}(\ln(x))$, $G(x) = \int^x d\phi/\phi\beta_0(\phi)$ and G^{-1} is the inverse function. Notice that the scaling form is obtained by dividing the volume N by a critical volume N_0, which means

$$N/N_0 \simeq 2^{L-L_0}, \tag{3.8}$$

which needs to be contrasted with L/L_0.

The collapse near the ergodic fixed point is shown in Fig. 3.5. For each W, we determine $\ln N_0(W) = L_0(W)$ such that $\phi(W, L_0(W)) = 0.95$, so that all the curves are at the same point on the one-parameter arc $\beta_0(\phi)$. The specific value chosen for $\phi(W, L_0(W))$ is not important, provided that it is large enough to allow all curves to be in the one-parameter scaling regime.

Far from the ergodic fixed point $\phi = 1$, the functions $\phi(W, L)$ are regular and non-vanishing, and therefore the divergent lengthscale is given by N_0. The divergence of

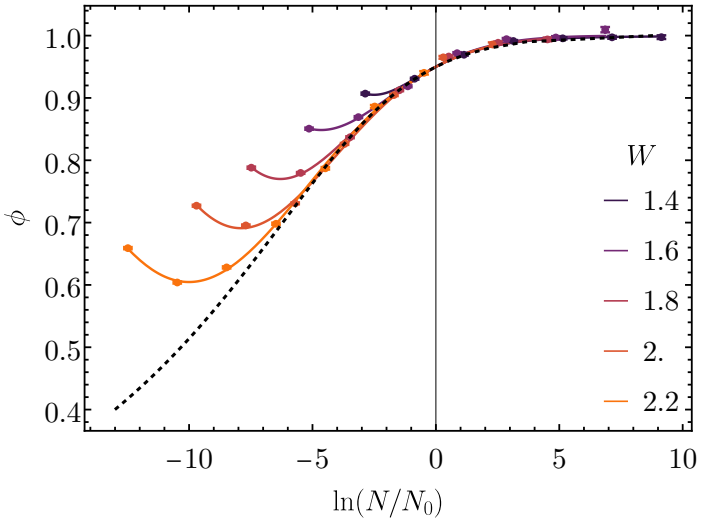

Figure 3.5.: Data collapse near the ergodic fixed point. The black dashed curve is the scaling function f obtained by integrating β_0 from Eq. (3.5). Data are collapsed according to Eq. (3.7) and as explained in the main text.

N_0 is entirely due to the two-parameter flow which goes close to $\phi = 0$ and therefore needs to be determined by this.

It is also instructive to plot, as a function of the disorder strength W, the values ϕ_A at which the beta function vanishes, i.e. $\beta(\phi_A) = 0$. If there was a transition, one should observe a zero of the function $\phi_A(W)$: extrapolating the data to the thermodynamic limit, one would then be able to pinpoint a localization transition. The points $\phi_A(W)$ displayed in Fig. 3.6 clearly display a curvature, not crossing the axis $\phi = 0$ at a finite value of W. It is thus not possible to use a simple linear fit to predict the critical disorder W_c, and different fitting functions lead to different values of W_c, possibly also infinite. The same analysis, when performed for the Anderson model on RRGs, shows instead no sign of curvature, and from a simple linear extrapolation, one is able to extract the value of W_c [147]. Such value agrees with the critical disorder strength predicted by the analytical computation on the Bethe lattice [191, 192] with an error of about 1%. Unfortunately, for the XXZ chain, there is no independent method of extracting the critical disorder value, and one is not able to assess the presence of a transition by looking only at the small disorder data. In the next section, we complement the analysis by looking at larger disorder strengths, and with the help of the two-parameter-scaling formalism, we analyze the possibility of a finite-W_c localization transition.

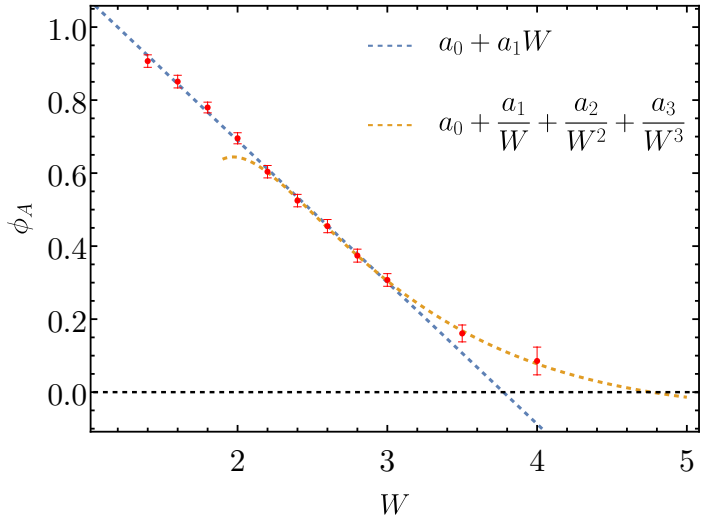

Figure 3.6.: Values of ϕ at which the beta function vanishes, i.e. $\beta(\phi_A) = 0$, as a function of the disorder W. The linear fit (blue) is obtained by considering points up to $W = 3$ and yields a critical value of the disorder $W_c \simeq 3.8$, which is consistent with the old estimate of Ref. [189]. The nonlinear fit (yellow) is obtained by fitting points with $W \geq 2.2$ and extrapolates to a larger value of the critical disorder $W_c \simeq 4.7$.

3.4.2. Large disorder: Localized and critical behavior

The numerical analysis of the β function in the critical localized region—i.e. the region defined by $\beta < 0$ and $\phi \ll 1$—presents an intrinsic difficulty, since the system sizes required are too large to be accessed numerically. In the following, we show what the expected behavior is for an observable near the critical region, given the dynamical system formulation developed in Sec. 2.1.3.

Upon defining $\alpha = \ln A = \ln \phi$, the two RG equations can be put in the form Eq. (2.25). The force $\gamma(\alpha) = -V'(\alpha)$ is to be determined from the numerical data. As discussed before, a confining potential corresponds to the absence of a transition, while a non-confining potential corresponds to the existence of a transition.

In order to explore the possible behaviors of α, we start by solving Hamilton's equations (2.25) with a force $\gamma(\alpha) = ce^{n\alpha}$. Later on, we will comment on the choice of this functional form. The exponent n and the coefficient c are left free for now, and will be fixed by confronting to the numerical data. This exponential force γ comes from a potential $V(\alpha) = -(c/n)e^{n\alpha}$, and therefore the conservation of energy can be written as

$$\frac{\beta^2}{2} - \frac{c}{n}\left(\phi^n + \frac{n}{c}E\right) = 0. \tag{3.9}$$

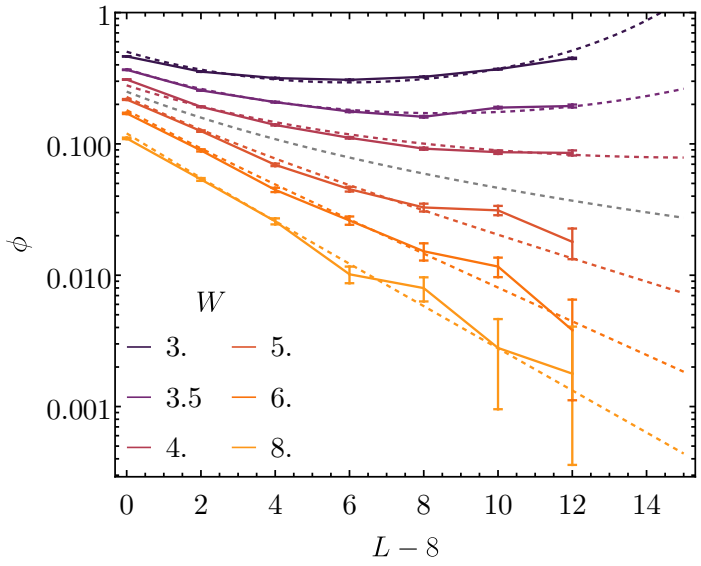

Figure 3.7.: Comparison between numerical results and trajectories obtained through the integration of the dynamical system, Eq. (2.25), with potential function $V(\alpha) = ce^{n\alpha}/n$, where $\alpha = \log\phi$. All the orbits are consistent with a scaling coefficient $c \simeq 0.1$ and an exponent $n \simeq 1$. The dashed gray line is the critical line according to Eq. (3.12), with $\phi_0 \simeq 0.25$.

From this, one finds that the beta function is given by

$$\beta(\phi) = \pm\sqrt{\frac{2c}{n}}\sqrt{\phi^n + \frac{n}{c}E}\,, \tag{3.10}$$

where negative E corresponds to the ergodic phase (which possesses both branches $\beta > 0$ and $\beta < 0$), while positive E corresponds to the localized phase (for which $\beta < 0$). The region $\phi \lesssim |\frac{n}{c}E|^{1/n}$ corresponds to the critical region.

Let us focus on the critical curve $E = 0$. If one integrates Eq. (3.10), using the definition $\beta = \dot{\phi}/\phi$, one finds an algebraic scaling with the system size

$$\beta = -\sqrt{\frac{2c}{n}}\phi^{n/2}, \tag{3.11}$$

and in turn

$$\phi(L) = \frac{\phi_0}{(1 + \sqrt{\frac{cn}{2}}\phi_0^{n/2}(L - L_0))^{2/n}}, \tag{3.12}$$

where (ϕ_0, L_0) are the initial conditions (ϕ_0 is a microscopic function of W, L_0 which can be obtained from the numerics). For large $L \gg L_0$, one finds a power-law decay

$$\phi(L) \sim L^{-2/n}. \tag{3.13}$$

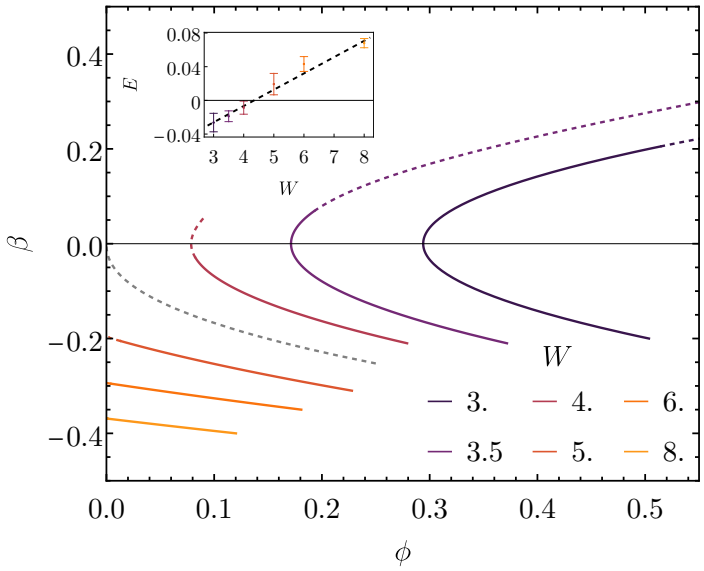

Figure 3.8.: Beta function of the rescaled r-parameter for the disorder strengths W in legend, obtained as a phase-space plot of the trajectories in Fig. 3.7. Lines are continuous up to the point where data are available. The dashed gray line is the critical line, separating the ergodic from the localized behavior. In the inset, the energies of each trajectory are shown as a function of the disorder, with the same color map. The linear fit yields a value $W_c = 4.4(4)$.

This is the same scenario found for the Anderson model on the RRG, where the data support $n = 1$ and a law $\phi \sim 1/L^2$ [147]. We will see in a moment that $n = 1$ is also compatible with the numerical data for the XXZ chain.

Inside the localized region, it holds $E > 0$. If the starting point has $\phi \gg (ncE/2)^{2/n}$, there is an initial decay which follows the critical law Eq. (3.13), after which an exponential scaling sets:

$$\beta \simeq -\sqrt{\frac{2c}{n}}|\phi_A|^{n/2} \equiv -1/\xi_{\rm loc} \ , \quad \phi(L) \sim e^{-L/\xi_{\rm loc}} \ . \tag{3.14}$$

In Fig. 3.7 we show a comparison between the trajectories obtained from the integration of the equations of motion and the numerical data. We have also included data corresponding to intermediate values of the disorder, to check whether it is possible to fit them with the same potential function. The free parameters n, c are obtained from a best fit of the data corresponding to small values of ϕ, or moderately large disorder values $W = 3.5, ..., 8$. The best fit values are $n = 1.0(1),\ c = 0.10(5)$.

Once n, c are fixed, the best fitting curves are obtained by choosing initial conditions (ϕ_0, β_0) for each W. In this way, a value of the energy can be associated with each trajectory by using Eq. (3.9) at the initial condition: we find $E < 0$ for disorder

values $W \leq 4$ and $E > 0$ for $W \geq 5$. This places the value of the critical disorder between $W = 4$ and $W = 5$. The critical line Eq. (3.12) is drawn by fixing ϕ_0 to a value such that that line does not cross the other trajectories: this results in a tiny interval of possible values around $\phi_0 \simeq 0.25$.

In Fig. 3.8 we show the phase space plot (ϕ, β) constructed from Fig. 3.7. Notice that the curves possessing a positive energy (corresponding to $W = 5, 6, 8$) attach to the negative β axis. On the other hand, the curves possessing a negative energy ($W = 3, 3.5, 4$) are confined by the potential and, though starting with a negative β, reach a turning point and flow away from the localized phase. The critical line Eq. (3.12) yields the separatrix between the ergodic and the localized behavior.

Let us stress that, although somewhat arbitrary, the choice of the potential function family $V(\alpha) = -(c/n)e^{n\alpha}$ to fit the data is the simplest option that is, *a priori*, compatible with both the transition and no-transition scenarios, depending on whether n is positive or negative. This choice is motivated by physical intuition, namely the approximate similarity between the topology of the Hilbert space of the Anderson model in infinite dimensions and that of the Fock space of the XXZ chain [193, 194]. The outcome of the fitting procedure corroborates this intuition. While more elaborate functional forms might yield slightly better numerical fits, such fits would be entirely phenomenological and would lack the suggestive physical interpretation provided by our approach.

3.4.3. Significance of the results at large disorder: a problem of statistics

Resolving the value of ϕ for large disorder necessitates a heavy numerical effort. In fact, since the critical point is the final point of a line of fixed points, one needs to distinguish between two different *decays* of $\phi(L)$, one in the critical region $W \simeq W_c$ and the other in the MBL phase $W \gg W_c$. If this is not done, one cannot *bona fide* claim that the transition is not just a crossover. This brings up the necessity to have very precise values of ϕ (or any other order parameter), whose value in the MBL region is zero.

After an initial power-law decay $\phi \sim L^{-\gamma}$ (with $\gamma = 2/n$, the critical power law obtained from (2.25)) the system either reverses the course and flows back to $\phi = 1$ at the ergodic fixed point, or settles on an exponential decay that will follow asymptotically for $L \to \infty$. At what values of ϕ, W, L this occurs is dictated by the value of W_c. If this is too large, ϕ will be very small already at small L (say $L \leq 14$), and a huge sample is needed to distinguish the signal from the noise. In this section, the

Kolmogorov-Smirnov hypothesis test is used to estimate how large a sample one needs to distinguish the data from a Poisson distribution, and therefore the significance of the value of ϕ itself.

The probability distribution function of the r-parameter for an integrable system is (see e.g. Ref. [195])

$$p(r) = \frac{2}{(1+r)^2} , \qquad r \in [0,1] . \tag{3.15}$$

This law is very broad in its domain; hence, the average value might not be an efficient numerical estimator. It is then convenient to quantify the difference between the numerical and the theoretical probability distribution function beyond the average value. This way, it is possible to provide an estimate of how much statistics is needed to have a significant dataset. To do so, we compute the difference between the theoretical and numerical cumulative distribution functions:

$$\kappa(r) \equiv \left| C^{\mathrm{P}}(r) - C^{\exp}(r) \right| , \tag{3.16}$$

where $C^{\mathrm{P}}(r) = 2r/(1+r)$ and $C^{\exp} = \{\sum_i n_i < r\}/N$. This choice is motivated by a physical argument: it is expected that, for small system sizes and in the large disorder limit, the system still exhibits some level repulsion, which is reflected in the small values of r. The error associated with $C^{\exp}$ is a simple Poissonian counting error: $\delta C^{\exp}(r) = \sqrt{C^{\exp}/N}$.

In Fig. 3.9 we compare the signal and noise from our data as a function of the system size, for the particular cases of $W = 6$ and 20. In the case of extremely large disorder $W = 20$, we considered a larger number of samples (from 10^5 to 6×10^5) to show that the difficulty of collecting meaningful statistics increases both with the disorder and with the system size.

The condition to have a significant dataset is that the signal is much greater than the noise, i.e. $\kappa(r) \gg \delta C^{\exp}(r)$. One can be more quantitative considering $\kappa_s = \sup_{r\in[0,1]} \kappa(r)$: κ_s is called the Kolmogorov-Smirnov parameter.

We compute $\kappa_s(L)$ and compare it with $\delta C^{\exp}(r_s)$, where r_s is the value at which $\delta C^{\exp}(r)$ is maximal. The data at $W = 6.0$ clearly shows exponential decay of the Kolmogorov-Smirnov value all the way from $L = 8$ to $L = 20$, therefore confirming the existence of a transition at $W < 6$. The data at $W = 20$ instead fall quickly into the region where the signal is comparable to the error.

We can provide a rough estimate of the size of a significant dataset N_{sig} extrapolating with an exponential fit $\kappa_s(L)$ for $W = 20$ (inset of the second panel of fig 3.9), and considering the point at which the signal is equal to the statistical error: $\sqrt{N_{\mathrm{sig}}} \sim \delta C^{-1} \sim k_s(L)$. We find $N_{\mathrm{sig}} \sim e^{0.6L}$; meaning that, with 50 eigenvalues per

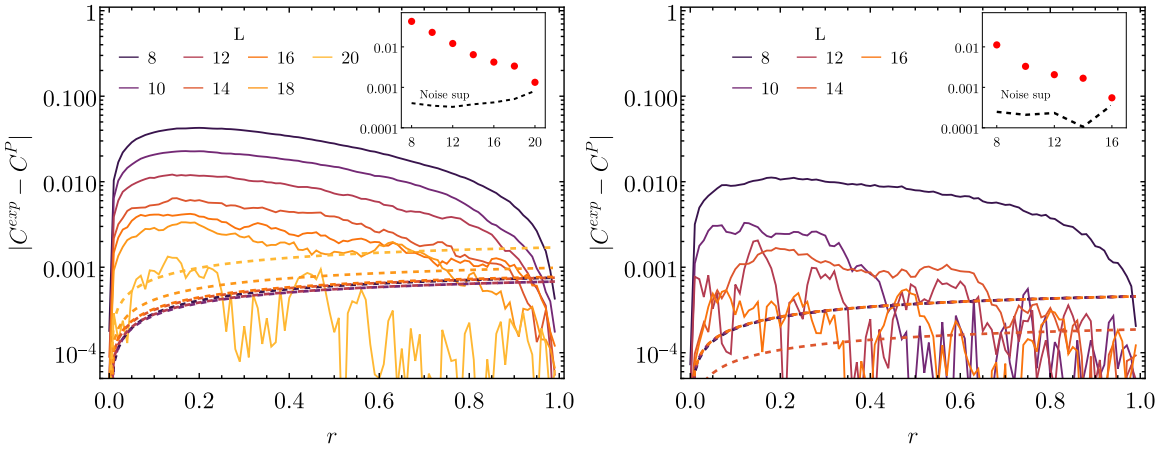

Figure 3.9.: Comparison of signal and noise for $W = 6$ (top) and $W = 20$ (bottom). The solid lines represent the numerical data, while dashed lines represent the Poissonian error associated with the signal (with matching color code). In the insets, the behavior of $\kappa_s(L)$ is compared to its associated error.

sample, the number of samples needed to have an accurate estimate of the average value of the r-parameter at $L = 20$ is $\gtrsim 10^6$. This *bona fide* computation shows that a meaningful statement is quite hard to make, even in the localized region.

3.5. Discussion and Conclusions

Motivated by the recent progress in the scaling theory of Anderson localization transitions [147, 151] and by the even more recent analytical work on the Imbrie model [196], we developed the renormalization group (RG) analysis of the many-body localization (MBL) transition in the random-field XXZ spin chain. The presence of a localization transition in this model, though initially assessed by analytical (approximate) and numerical studies, has been undermined by general arguments based on non-perturbative effects, such as many-body resonances and thermal avalanches, and still remains debated in the community. In this chapter, we provide a novel contribution to the debate by focusing on the scaling theory and giving particular attention to the methodological aspects of analyzing numerical data for MBL at the small system sizes that are currently available with the present technology.

By exploiting numerical data for the rescaled r-parameter ϕ, Eqs. (3.2)–(3.3), obtained via exact diagonalization, our approach allows for the reconstruction of the beta function of the model. This is an essential tool for the understanding of the scaling theory of phase transitions in general, and localization transitions in particular. In fact, as discussed in Sec. 2.1.2, the properties of the beta function determine the nature of the scaling functions with which one can obtain a good data collapse near the critical

point. If one assumes that the critical point is a simple zero of the beta function, and therefore the flow to the attractive fixed points is ruled by a one-parameter scaling curve (as it usually happens in critical phenomena), then one is led to inconsistent data collapses in the case of MBL, as the one shown in Fig. 3.3.

The main message of this chapter can be summarized as follows. There are two possible scenarios for the fate of MBL in the XXZ spin chain: either there is no transition in the thermodynamic limit and the observed localized regime is just a pre-asymptotic effect which is eventually destabilized non-perturbatively; or, if there is a stable localized phase, then the transition is characterized by a two-parameter scaling towards a line of fixed points, of which the critical point is the endpoint, in a way that resembles the Berezinskii–Kosterlitz–Thouless (BKT) transition. This critical theory, which has also been observed in the Anderson model on random regular graphs (RRG) [147], is more difficult to study with respect to usual critical phenomena. Since the critical point coincides with a localized fixed point, the system is both repulsed and attracted in the critical region: to understand whether the system is actually flowing towards the localized phase means being able to distinguish between a power-law or exponential decay. This is a very subtle task, which requires having access not only to larger system sizes, but also to huge statistics for the higher accessible sizes.

We therefore analyze the data in the light of the two-parameter scaling transition scenario. We divided our analysis by focusing first on the flow to the ergodic fixed point for small disorder values W in Sec. 3.4.1, and then on the localized behavior at larger disorder values in Sec. 3.4.2. The former is governed by a one-parameter scaling function β_0, to which each finite-size curve attaches for a certain value of the Hilbert space volume $N_0(L, W)$. A consistent data collapse of the values of the rescaled r-parameter ϕ near the ergodic fixed point can be obtained by exploiting the one-to-one correspondence between $\beta_0(\phi)$ and the scaling function f used for the collapse. The volume N_0 sets a scale (i.e. a correlation length) which is larger and larger upon increasing W. The divergence of N_0 reflects the fact that the observable displays a minimum which is more and more flat as W grows. The question is then: is there a finite value of the disorder for which the minimum shifts to the localized value at infinite N_0?

In order to answer this question, we fitted the numerical data for large disorder by adopting a more "physical" point of view, rather than just using some fitting functions depending on many parameters. In fact, our purpose has been to avoid nasty fluctuations in the data and to find their general trend, in a way that is grounded in the understanding of the scaling theory. For this purpose, we realized that the phenomenological equations of the two-parameter scaling of a generic observable A

can be cast into the equations of motion for a Newtonian one-dimensional particle with coordinate $\alpha = \ln \phi$. The Hamiltonian part of these equations involves a force term, which can be derived from a potential $f(\alpha) = -V'(\alpha)$, and rules the scaling of the observable near the critical point and in the localized region. Whether the potential is non-confining/confining corresponds to the presence/absence of the transition: in the first case, there is a critical energy (related to the critical disorder W_c) above which orbits can escape the potential and have access to the localized phase.

We focused on the Hamiltonian dynamics for intermediate and high values of the disorder strength, and found the free parameters n and c of the non-confining potential $V(\alpha) = -ce^{n\alpha}$ that allow for a better fit of the data. It turned out that $n \simeq 1$, leading to a scaling near the critical point of the kind $\phi \sim 1/L^2$, which is precisely the same scaling observed in the Anderson model on RRGs. This suggests that the two models may belong to the same universality class. From the sign of the energy labeling the orbits, we were able to assess that in this scenario the critical disorder should be between $W = 4$ and 5. This is confirmed by a fit of the minima of ϕ, i.e., the zeros of the beta function at finite size.

Given the fact that the observable is flowing to its localized value at the critical point, it is challenging to resolve an exponentially decaying observable from the statistical fluctuations in the data. For this reason, we performed a careful analysis of the signal and noise extracted from our data by means of the Kolmogorov-Smirnov test.

Summarizing, we believe that the study of the full RG beta function is the correct way to address ergodicity-breaking transitions in quantum systems, lacking strong analytical arguments in favour of a simple one-parameter scaling fixed point. In the case of the XXZ model, our study of the beta function points quite strongly against the possibility of having such a simple critical fixed point. This observation has important consequences, namely, if a localization transition occurs at finite W_c, it must be described by two-parameter scaling, and we provided a suitable candidate that fits the data. If a localization transition *does not* exist at any W_c then this is an even stronger reason to prefer a two-parameter scaling, and we have shown concretely how to describe this scenario. Further work is needed to resolve the correct two-parameter RG flow for the XXZ (our analysis suggests that this is within reach of existing computing power), and for the other many-body models showing breaking of ergodicity due to disorder (for example [145, 197–199]).

3.6. Appendix of Chapter 3

3.6.1. Details of the numerical procedure

We performed an exact diagonalization algorithm using the shift-invert method, implemented in the libraries SLEPc [200], PETSc [201]. The main numerical bottleneck is the amount of memory needed to solve the linear system to invert the resolvent operator [187], that scales as $\sim \dim(\mathcal{H})^3$. In the present case, we focused on the spin-0 sector, which is the largest symmetry sector for even sizes, for which we remind that $\dim(\mathcal{H}) = \binom{L}{L/2}$.

In the following table we present a summary of the data that we used to perform the analysis.

Size	No. of samples	RAM required
8	5×10^4	$\mathcal{O}(1)$ MB
10	5×10^4	$\mathcal{O}(10)$ MB
12	5×10^4	$\mathcal{O}(10)$ MB
14	5×10^4	$\mathcal{O}(100)$ MB
16	3×10^4	$\mathcal{O}(100)$ MB
18	2×10^4	2 GB
20	1.5×10^4	30 GB

Table 3.1.: Approximate number of samples for each size L and value of disorder W, and RAM required for the diagonalization of a single sample.

3.6.2. Data collapse in the one-parameter-scaling framework

In this appendix we show the other data collapse mentioned in the main text in Sec. 2.1.2, which wrongly assumes a one parameter scaling at the critical point. This collapse is shown in Fig. 3.10. Here, instead of fixing $\phi_c = 0$, we leave it as a free parameter, while fixing $W_c \simeq 3.8$ as results from the linear extrapolation in Fig. 3.6. This fit yields the same exponent $\nu \simeq 0.9$ already obtained in [189], which violates the Harris bound. Moreover, it gives a value of $\phi_c \simeq 0.13$, which is inconsistent with the lowest finite-size critical value for the turning point $\phi_A = 0.085(4)$ observed for $W = 4$.

In the inset of Fig. 3.10 we show the crossing point ϕ_c between data for the r-parameter at adjacent sizes as a function of the disorder strength W. One can observe as the crossing point is drifting towards $\phi_c = 0$, instead of saturating to a finite value.

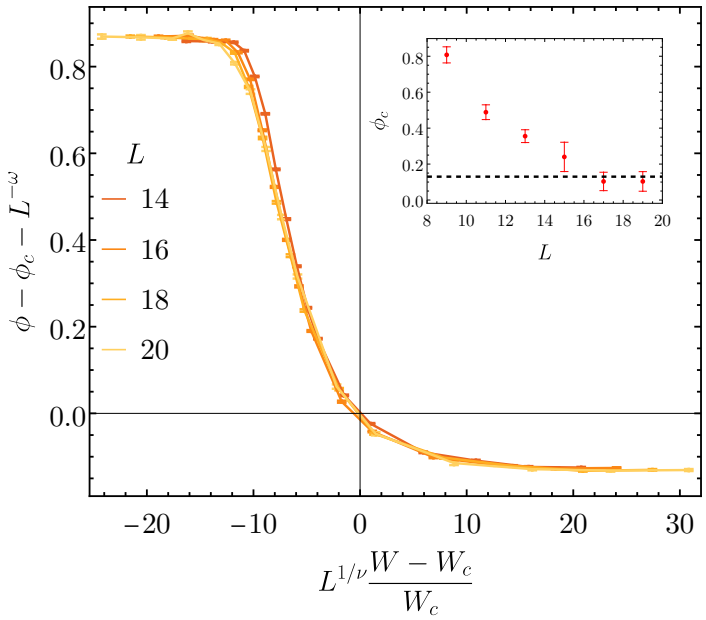

Figure 3.10.: Data collapse near the critical point according to the one-parameter scaling hypothesis of the first works on MBL [189, 202], estimating $W_c \simeq 3.8$, $\nu \simeq 0.9$, and $\omega \simeq 2$. The dashed line denotes the "fake" critical value $\phi_c \simeq 0.13$. The two-parameter scaling discussed in this paper starts from the assumption that $\phi_c = 0$. In the inset the drift of the crossing point between the rescaled r-parameter of adjacent sizes is shown. The dashed line in in $\phi_c \simeq 0.13$, which is compatible with the error bars of the the last two crossing points.

4. Renormalization group scaling in the quantum random energy model

In this Chapter we study the many-body localization transition of the quantum random energy model (QREM) within the scaling-theory framework introduced in the previous Chapters. We show that at finite energy the localization transition is described by a two parameter scaling. The same RG flow is found at zero energy, upon an appropriate rescaling of the couplings.

4.1. Model and observables

The quantum random energy model (QREM) is a prototypical toy model for many-body localization. It retains the essential ingredient of MBL, namely a particle hopping on the exponentially large Fock-space graph of a disordered spin system, while discarding the correlations of the disorder, which is replaced by i.i.d. on-site energies. This makes it a mean-field model, that still retains the two features which make MBL hard to study: an exponentially growing connectivity, and the short loops inherited from the hypercubic geometry.

The QREM is defined by the Hamiltonian

$$H = \Gamma \sum_{i=1}^{L} \sigma_i^x + \mathrm{diag}\{\epsilon_1, \ldots, \epsilon_{2^L}\}, \tag{4.1}$$

where ϵ_j, $j = 1, \ldots, 2^L$, are i.i.d. gaussian random variables with average zero and standard deviation $\sqrt{L/2}$, and Γ is the transverse field strength. In the following, we will interchangeably use also the effective disorder strength $W \equiv 1/\Gamma$. The scaling of the disorder with $\sqrt{L}$ is necessary for the Hamiltonian (4.1) to be extensive in L.

The QREM is the quantum version of the random energy model, introduced by Derrida as an exactly solvable model arising from the limit $p \to \infty$ of p-spin glasses [203]. Its classical version ($\Gamma = 0$) is typically considered as the simplest statistical mechanics model displaying a glassy phase below the critical temperature $T_{\mathrm{glass}} = 1/2\sqrt{\log 2}$ [204]. Reintroducing quantum fluctuations, the equilibrium phase diagram of the model dis-

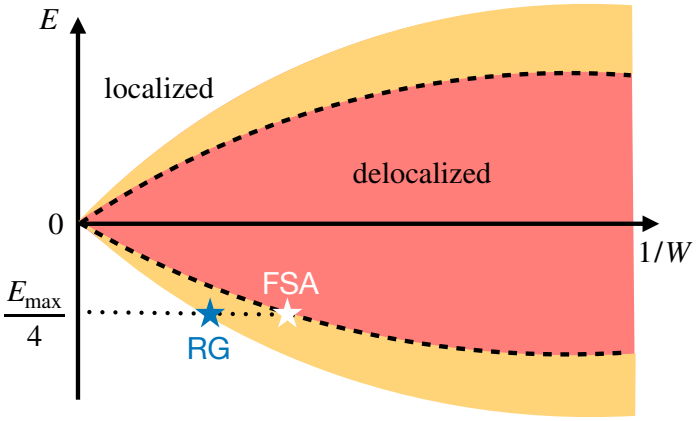

Figure 4.1.: Cartoon of the phase diagram of the quantum random energy model in the $E, 1/W$ plane. The red-shaded area indicates the delocalized region, the yellow-shaded area indicates the region that is localized in perturbation theory, but is destabilized by non-perturbative effects, and the white area is the localized phase. The dashed line corresponds to the mobility edge obtained via the forward scattering approximation (FSA). The white and blue marks are respectively the transition point predicted by FSA at $E = E_{\max}/4$ and the one that we extrapolate via renormalization group techniques. As expected, the position of the mobility edge found via exact diagonalization is at a greater value of disorder than the one given by the FSA.

plays also a quantum paramagnetic phase, on top of the classical paramagnetic and glassy phases [205–207].

From a dynamical viewpoint, the system can be thought of as a particle hopping on a hypercubic lattice, in the presence of a random on-site potential that is size-dependent: the model is thus strictly equivalent to the Anderson model on this geometry. Thanks to this mapping, the QREM can be also considered as a "mean-field" version of disordered spin chains, such as the XXZ chain in a random field: these systems can be represented as Anderson models on a Fock-space graph with correlated disorder. In the QREM, the only difference is that the disorder becomes artificially uncorrelated in the computational basis, while retaining the scaling $\sim L^{1/2}$ expected from the sum of L independent disordered fields in real space. The QREM is a toy model for many-body localization transitions, as it retains the Fock space structure of many-body hopping, while disregarding the correlations that build up in the disorder term. The QREM can also be regarded as an unconventional infinite-dimensional limit of the Anderson model, where the side of a hypercube is kept fixed while the number of dimensions is increased (on the contrary, expander graphs such as the RRG represent the infinite-dimensional limit taken *after* the infinite-volume limit). These particular features endow the QREM with a distinguished phase diagram: at the center of the spectrum ($E = 0$) the dynamics never localizes, while away from it ($E \neq 0$) a mobility edge is present.

More specifically, the QREM hosts a many-body localized phase for energy densities $|E/L| > \Gamma$, as demonstrated both via perturbation theory and numerically [145, 146, 208, 209], see Fig. 4.1 for a sketch. This means that the critical temperature of the MBL transition is $T_{\rm MBL} = (2\Gamma)^{-1}$, much larger than the equilibrium glass transition $T_{\rm glass}$ for sufficiently small Γ. At the center of the spectrum, i.e. at zero energy density, the QREM remains ergodic regardless of the value of Γ.

The best estimate for the mobility edge $E_c(\Gamma)$ was found using a perturbative expansion of the resolvent, to estimate the probability of having a resonance at a given distance [145, 146]. Within this approach, commonly called forward scattering approximation (FSA) [210], the error committed is to neglect repeating paths connecting two sites, thus the approximation becomes accurate in absence of loops (e.g. on the Bethe lattice [191]), and is well-controlled if there are no short-scale loops (e.g. on RRGs). In the case of the QREM, however, small loops are naturally present because of the hypercubic geometry, and therefore the FSA can only give a rough estimate of the critical point.

In order to probe the ergodic or localized behavior of the model, we use two different figures of merit, both calculated through exact diagonalization of the Hamiltonian in Eq. (4.1) [187].

The first is the rescaled spectral gap ratio, introduced in the previous Chapter. The second observable which will be used as an order parameter for the localization transition is the eigenstate fractal dimension D, defined as $D(L) = \mathrm{d}S(L)/\mathrm{d}\ln N$, where $N = 2^L$ is the Hilbert space volume. $S(L)$ is the average eigenfunction Shannon entropy at size L, i.e. $S(L) = -\mathbb{E}\Big[\sum_j |\langle j\rangle \psi_n|^2 \ln |\langle j\rangle \psi_n|^2\Big]$, where j labels the computational basis states and $|\psi_n\rangle$ are the eigenstates within a narrow energy window as above. In the thermodynamic limit, the fractal dimension is $D = 1$ for eigenfunctions extended over the whole Hilbert space, and $D = 0$ for localized eigenfunctions.

4.2. Numerical results

Numerical data qualitatively agree with the picture coming from perturbation theory [145, 146]. The fractal dimension at the center of the spectrum, $E = 0$, is reported as a function of system size in Fig. 4.2(a), and the corresponding beta function in Fig. 4.2(b): all curves flow to the ergodic fixed point for any value of W, as long as one keeps $W = O(1)$. The same conclusion can be reached from the r-parameter data, that we report in the appendix. We anticipate that one can observe a transition for $E = 0$, provided one rescales the disorder as already pointed out in Refs. [145, 146]. We will explore this transition in the next section.

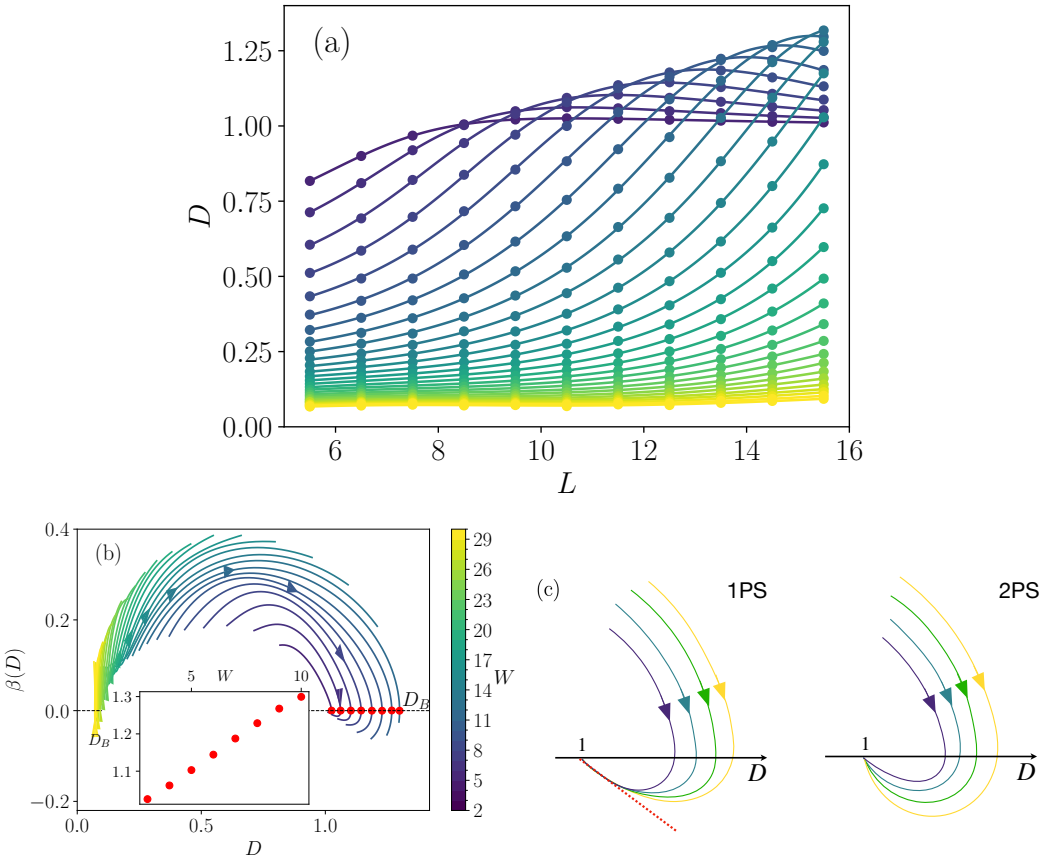

Figure 4.2.: (a) System-size dependence of the fractal dimension D at the center of the spectrum (i.e. at infinite temperature). Dots are the numerical data, obtained by taking the finite-difference derivative of the participation entropy, and solid lines are the interpolation of the data, used for computing the beta function. For any W, the curves reach $D = 1$ for sufficiently large system size. At intermediate L, the fractal dimension becomes $D > 1$, signaling that the eigenfunction support set grows faster than the system size. (b) Beta function at $E = 0$, with direction of the RG flow indicated by the arrows. The red dots in the main plot are the zeros of the beta function at $D > 1$, and we denote with D_B the corresponding value of D. In the inset, we report the dependence of D_B on W: a linear behavior is observed, suggesting the persistence of this effect for large sizes. (c) Pictorial representation of the two possible scenarios for the RG flow at the ergodic fixed point, one-parameter (1PS) or two-parameter (2PS) scaling. The red dashed line is a sketch for the 1PS asymptotic curve.

As one can notice, in the ergodic regime the fractal dimension reaches the ergodic fixed point $D = 1$ from *above*, signaling that the support set of the wave functions is growing faster than the Hilbert space dimension. While in the thermodynamic limit the fractal dimension must be smaller than (or at most equal to) one, the appearance of $D(L) > 1$ at finite size was observed also in the Anderson model in $d = 2$ [151], in Josephson junction arrays [211] and, more interestingly, in Gaussian and log-normal Rosenzweig-Porter models. This behavior can be deduced from the data reported in Ref. [170], even if the fact is not explicitly commented. We conjecture that this behavior is common to models whose connectivity grows with the system size and whose disorder is uncorrelated in Hilbert space.

Because of the overshooting described above, the beta function of the fractal dimension approaches the ergodic fixed point in a peculiar way. The zeros of β at $D > 1$, which correspond to the maxima of D as a function of L (see Fig. 4.2(a)), increase with W, as shown in the inset of Fig. 4.2(b): it is reasonable to assume that this behavior may persist even at very large disorder and system sizes. Although the fractal dimension eventually reaches $D = 1$ in the thermodynamic limit, the approach to the ergodic fixed point may follow either 1PS or 2PS, depending on whether there is a residual dependence of the slope on W, see Fig. 4.2(c) for a sketch of these two cases. The numerical data available do not allow us to conclude which scenario is correct. However, as will be discussed in the following, the 1PS to the ergodic fixed point is recovered both if the disorder rescaling is introduced, and away from the center of the spectrum. This suggests that the 1PS scenario is most likely the correct one for the RG flow at the ergodic fixed point.

4.3. Rescaling the disorder

While the QREM is always ergodic at the center of the spectrum, a localization transition can be induced by rescaling the disorder to $\overline{W} = W/\sqrt{L}\log L$. The additional logarithmic factor arises from the careful treatment of the perturbative expansion [145, 146], following the seminal example of the Bethe lattice [191]. With this rescaling, the diagonal term becomes $O(L)$ from the single-particle perspective, and compensates for the $O(L)$ connectivity of the Fock space graph: it is a form of Kac rescaling [212, 213]. However, from the perspective of spins, the extensivity of the energy is no longer maintained. This non-extensivity of energy is not a cause for concern, as localization is fundamentally a dynamical phase transition. On the other hand, the scaling required to ensure thermodynamic extensivity prevents the observation of the localization transition at the center of the spectrum.

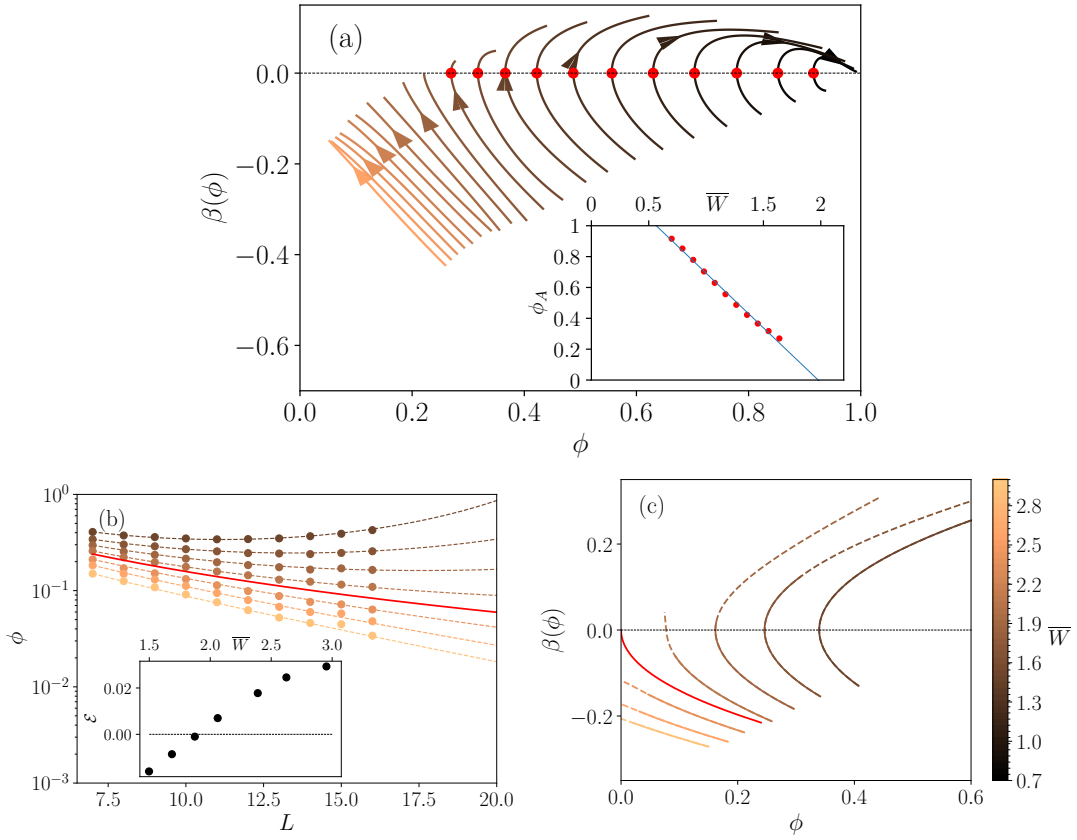

Figure 4.3.: (a) Beta function of the rescaled r-parameter ϕ, parametrized by the rescaled disorder strength $\overline{W} = W/\sqrt{L}\log L$. The flow is consistent with the presence of a line of fixed points on the negative β axis, see also panel (c). In the inset, the turning points of the RG dynamics are shown as a function of $\overline{W}$: a linear fit extrapolates to $\phi_c = 0$ at $\overline{W}_c \simeq 1.95$. (b) Fits of the numerical data obtained from the orbits of the dynamical system with potential $V(\alpha) = -(c/n)e^{n\alpha}$ and parameters $c \simeq 0.05$ and $n \simeq 1$. In the inset, the energies labeling the orbits are plotted as a function of $\overline{W}$. (c) Phase-space plot of the dynamical system orbits: lines are continuous up to the RG time at which data are available, and become dashed along the extrapolations to higher sizes.

We plot the beta function of the rescaled r-parameter, parametrized by the rescaled disorder $\overline{W}$, in Fig. 4.3. While bigger system sizes are needed to draw definitive conclusions on the nature of the transition, it appears plausible that it is described by a 2PS theory, with a line of fixed points on the negative β axis. The situation appears similar to the Anderson transition on expander graphs [147], and potentially to the random-field XXZ spin chain [3]. The approach to the ergodic fixed point follows instead a 1PS curve, as the beta function curves collapse on one another.

The turning points ϕ_A of the RG dynamics, i.e. the minima of ϕ, decrease linearly to $\phi_c = 0$ at the finite value $\overline{W}_c \simeq 1.95$, when plotted as a function of $\overline{W}$ (see inset of Fig. 4.3(a)). Note that, with our definitions of the disorder strength, the critical disorder on a Bethe lattice would be $\overline{W}_c^{\mathrm{BL}} = 2/\sqrt{\pi} \simeq 1.12$ [192]. It is possible that the value in the QREM turns out to be larger because of the presence of loops in the Fock-space graph, which favor resonances. Here loops are particularly important because the number of dimensions of the Fock space is increased while keeping the side of the hypercubic lattice fixed to 1. The Bethe lattice, instead, is reached by keeping the number of spins fixed and increasing the spin representation: this is equivalent to considering the Anderson model in finite d-dimensional space [151] and taking the limit $d \to \infty$. A possible way to interpolate the two situations would be to consider, instead of spins-1/2, an arbitrary spin S which generates an L-dimensional hypercube with $(2S+1)^L$ vertices of size $2S+1$ in each direction. We conjecture that the critical value $\overline{W}_c(S) \to \overline{W}_c^{\mathrm{BL}}$ as $S \to \infty$.

It is interesting to study the RG dynamics around the transition and in the localized phase via the effective dynamical system introduced above. In order to fit the data, we use the orbits of a Hamiltonian system with potential $V(\alpha) = -(c/n)e^{n\alpha}$, where $\alpha = \ln \phi$; see Fig. 4.3(b,c). Each curve is obtained with a different choice of the initial conditions of the dynamics, which can be used to compute the effective energies $\mathcal{E} = \beta^2/2 - (c/n)e^{n\alpha}$. The best fits yield $c \simeq 0.05$ and $n \simeq 1$; the exponent n, characterizing the scaling on the critical line $\phi(L) \sim L^{-2/n}$, has remarkably the same value as in the Anderson model on RRG [147], and it is also consistent with what observed in the XXZ spin chain [3]. The energies of each trajectory are in one-to-one correspondence with the disorder values $\overline{W}$. The value of $\overline{W}$ at which the energies cross the horizontal axis $\mathcal{E} = 0$ corresponds to the critical point: a linear fit yields a critical disorder $\overline{W}_c \simeq 1.9$, which is consistent with the value obtained from the turning points ϕ_A. The critical line can be obtained by integrating the equations of motion for $\mathcal{E} = 0$ and is marked with red in the figure. A line of fixed points becomes apparent for the larger values of $\overline{W}$, leading to a 2PS behavior with one relevant and one marginal direction

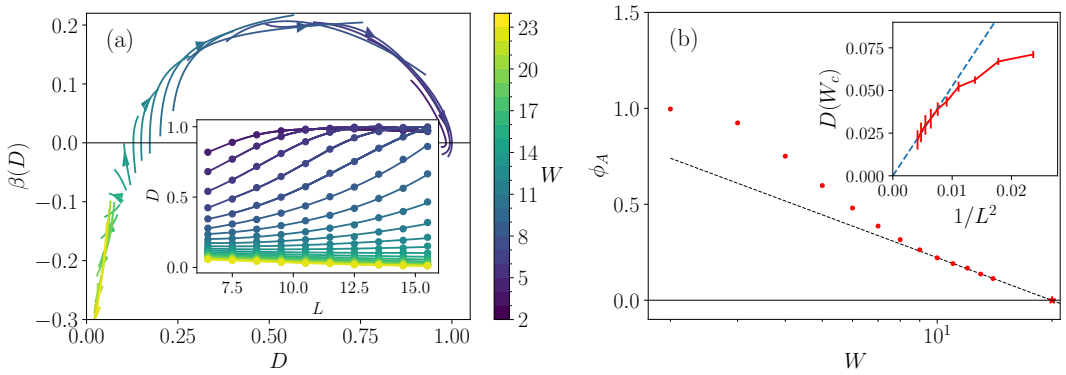

Figure 4.4.: (a) Beta function (main) and the corresponding fractal dimension (inset) away from the center of the spectrum, at $E = E_{\max}/4$ with $E_{\max}$ largest energy eigenvalue. The approach to $D = 1$ suffers from less severe finite-size effects, and D only slightly exceeds 1. Moreover, at large W the curves $D(L)$ approach $D = 0$, signaling the presence of the localized phase. (b) (Main) Determination of the critical value W_c at energy $E = E_{\max}/4$. In the plot, ϕ_A is such that $\beta(\phi_A) = 0$, and it extrapolates to $\phi_A = 0$ for $W_c \simeq 20$. At $W = W_c$, quantities as the fractal dimension D (inset) vanish as $1/L^2$, a behavior typical of expander graphs [147, 188].

4.4. On the mobility edge

Away from the center of the spectrum, numerical data confirm the presence of a mobility edge, see Fig. 4.4(a). We argue that the beta function behaves, in the large system size limit, similarly to the one of the Anderson model on RRGs, for the following reason. At finite energy density, the density of states is smaller than at infinite temperature, and the subset of resonant sites (for $\Gamma = 0$) is exponentially smaller than the complete Hilbert space. In general, the resonant sites will be distributed randomly on the hypercube, in a fashion similar to a random graph. Turning on the hopping, one expects therefore the localization transition universality class to be the same of the RRG [188]. Finite-size effects which are regulated by irrelevant operators, however, can in general be different, as one can notice from comparing the beta function in the localized region to the RRG result. More about this can be found in 4.6.

In the main panel of Fig. 4.4(b), we plot the turning points of the rescaled r-parameter as a function of the disorder. A linear extrapolation to the critical value $\phi = 0$ yields the critical disorder $W_c \simeq 20$. The FSA presented in Ref. [146] gives $\Gamma_c \simeq 0.283$ for energy densities $\epsilon = \sqrt{\log(2)}/4$ [1], corresponding to $W_c^{\mathrm{FSA}} \simeq 3.5$. In the inset, the scaling of the fractal dimension on the critical line is shown: data are compatible with $D(L, W_c) \sim L^{-2/n}$, $n \simeq 1$, which corresponds to what we find integrating the equation of motion with the potential $V(\delta) = -(c/n)e^{n\delta}$, with $\delta = \ln D$.

[1] Notice that $\epsilon_0 = \pm\sqrt{\log(2)}$ is the ground-state energy of the classical REM, that approximates well the edge of the spectrum $E_{\max}$. The value of Γ_c has been obtained using Eq. (35) of Ref. [146].

This is the same potential characterizing the scaling of the rescaled r-parameter on the critical line at the spectrum center, after the disorder rescaling. Therefore, the universality class of the localization transition at finite energy is identical to that at the center of the spectrum, exemplified paradigmatically by the Anderson model on RRGs.

Finally, we notice that the rescaling of disorder considered in Sec. 4.3, which makes the localization transition appear at the center of the spectrum, changes as well the scenario at finite energy density: the system becomes always localized, as a finite value of W in the thermodynamic limit corresponds to $\overline{W} = 0$.

4.5. Discussion

The scaling theory of the localization transition in the QREM has been studied in the present work by reconstructing numerically the beta function of spectral observables. In the "natural" scaling of the disorder variance, which makes the model a mean-field version of MBL models, our analysis confirms the absence of transition at the center of the spectrum and opens two possible scenarios for the approach to the ergodic fixed point: either a one- or a two-parameter scaling. On the other hand, at finite energy density a localization transition is described by a two-parameter scaling theory similarly to the Anderson model on expander graphs. A transition to a localized phase emerges also at the center of the spectrum if one suitably rescales the variance of the disorder: the transition appears to be described by a two-parameter scaling theory even in this case, with the same critical exponent of the Anderson model on the RRG and possibly of the XXZ spin chain. Our results show that the universality class of the localization transition in the QREM is the same of the Anderson model on any random graph and, remarkably, does not change by rescaling the disorder. This is a consequence of the fact that the RG is blind to the scaling of the microscopic variables.

4.6. Appendix of Chapter 4

In the main text we provided numerical evidence for the absence of a localization transition in the QREM at the center of the spectrum and its presence at finite energy density, through the analysis of the beta function of the fractal dimension at $E = 0$ and $E = E_{\max}/4$. Additional evidence in support of this scenario can be found from the rescaled r-parameter ϕ.

In the inset of Fig. 4.5 we plot ϕ as a function of system size. The minima of the curves $\phi(L)$, which we call ϕ_A, are instead plotted as a function of the disorder strength W in the main panel. These points correspond to turning points of the RG dynamics, i.e. the points at which the flow stops pointing towards the localized fixed point, and starts turning towards the ergodic one. Since ϕ_A decreases to 0 as the disorder W increases, if a transition is present, then the turning points ϕ_A should extrapolate to the value $\phi_c = 0$ at a finite value of the disorder in the thermodynamic limit. The data in Fig. 4.5 instead fit well to a polynomial that extrapolates to 0 only in the infinite disorder limit, thus signaling that the system will eventually flow to the ergodic phase for every finite value of W.

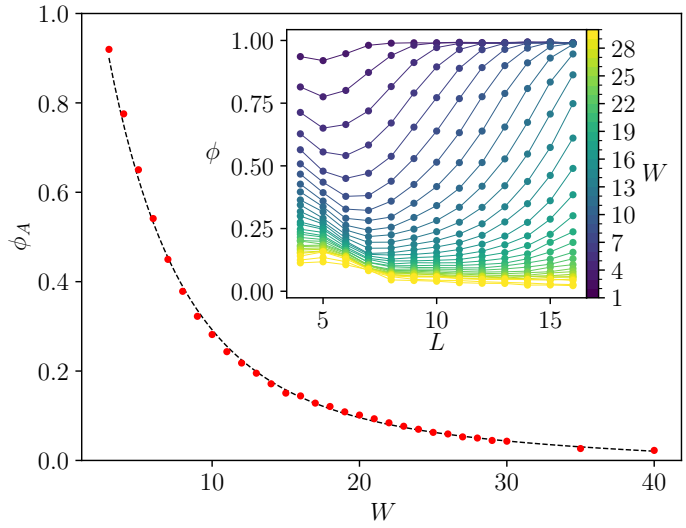

Figure 4.5.: In the inset we show the scaling of ϕ with the system size, for different values of the disorder W. In the main panel, the minima ϕ_A of the curves $\phi(L)$ are plotted as a function of the disorder parameter W. The points ϕ_A correspond to the turning points of the RG dynamics, as explained in the text. The points $\phi_A(W)$ are well fitted by a polynomial that extrapolates to 0 when $W \to \infty$.

4.6.1. Finite-size scaling of the rescaled gap ratio

Here we provide additional details regarding the finite-size scaling of our numerical data. By denoting with A any of the spectral observables considered in the main text, its beta function is defined as

$$\beta = \frac{\mathrm{d}\ln A}{\mathrm{d}\ln N}. \tag{4.2}$$

Under the one-parameter scaling (1PS) hypothesis, the beta function is a function of A alone, i.e. $\beta \equiv \beta(A)$. The dependence of A on the system size $\ln N$ can be obtained by integrating the equation defining the beta function, i.e. $\beta = \mathrm{d}\ln A/\mathrm{d}\ln N$, by separation of variables. Defining the primitive $G(A) = \int_{A_0}^{A} \mathrm{d}A'/(A'\beta(A'))$, one gets

$$A(N) = f(N/\tilde{N}_0), \tag{4.3}$$

where $\tilde{N}_0 \equiv N_0 e^{-G(A_0)}$ and the function $f(x) = G^{-1}(\ln x)$. This scaling form can be modified by taking into account finite-size corrections from the *irrelevant* part of the RG flow. Denoting by ω the scaling dimension of the least irrelevant operator, it can be shown that [3]

$$A(N) = f(N/\tilde{N}_0) + f_1(N/\tilde{N}_0)N^{-\omega}, \tag{4.4}$$

with a second scaling function f_1.

The scaling theory described above holds when the critical point is a well-isolated fixed point of the RG flow, as in the Anderson model in finite dimensions [151]. When, instead, the critical value of the observable A drifts to the localized value $A = 0$, one direction of the RG flow must necessarily become flat and the scaling theory must be supplemented with the addition of a second parameter [3, 147].

If one blindly applies the 1PS ansatz (2.14) to the QREM at infinite temperature, where there is no localization transition and the model is ergodic for all values of W, they will obtain an inconsistent result. Referring to Fig. 4.6(a), one can see that a fairly good scaling collapse of the rescaled r-parameter ϕ is obtained for large system sizes, identifying a *fake* critical point at $W_c \simeq 40$ with critical exponents $\nu \simeq 3/2$ and $\omega \simeq 2$.

On the other hand, at finite energy $E = E_{\max}/4$ the data are compatible with a localization transition at $W_c \simeq 20$. Moreover, from the beta function of the fractal dimension reported in the main text, it is expected that the transition be described by a 2PS theory. It is therefore wrong to use the 1PS form Eq. (2.14) to collapse the data. In Fig. 4.6(b), we show the collapse of the rescaled r-parameter at $E = E_{\max}/4$, obtained with critical exponents $\nu \simeq 2$ and $\omega = 2$: the collapse yields a critical value

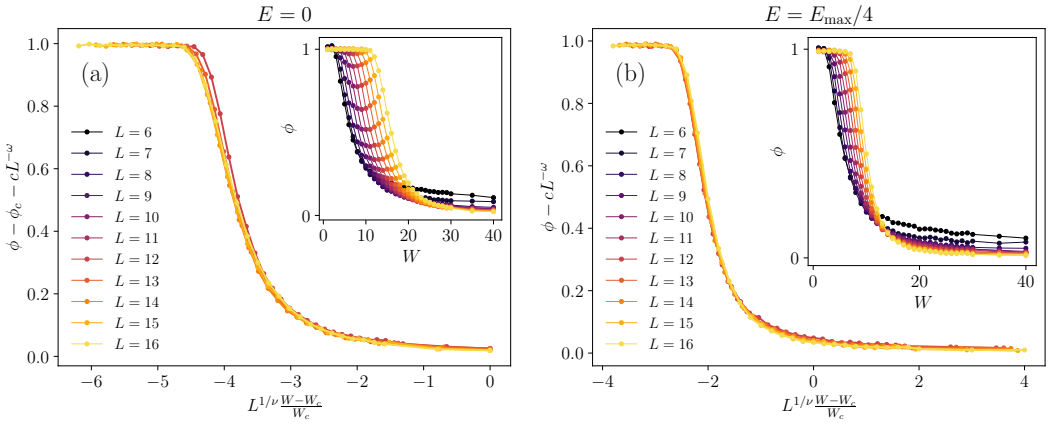

Figure 4.6.: (a) Naive finite-size scaling for the rescaled r-parameter ϕ at $E = 0$, where the model does not have a localization transition. Despite this known fact, by fixing $\phi_c = 0$, it is still possible to obtain a good data collapse with a *fake* critical point at $W_c = 40$, obtaining (fake) critical exponents $\nu = 1.5$ and $\omega = 2$. In the main plot we show the collapse for the larger sizes, $L > 11$, while the inset contains the same data down to $L = 6$, where finite-size effects are stronger. (b) Finite-size scaling for the average rescaled gap ratio ϕ at $E = E_{\max}/4$. The collapse is obtained for $W_c \simeq 20$ and $\phi_c = 0$. The critical exponent $\nu \simeq 2$ and $\omega = 2$. Despite the presence of a localization transition (as discussed in the main text), the one-parameter scaling ansatz does not apply, and therefore the critical properties extracted from the FSS should not be trusted.

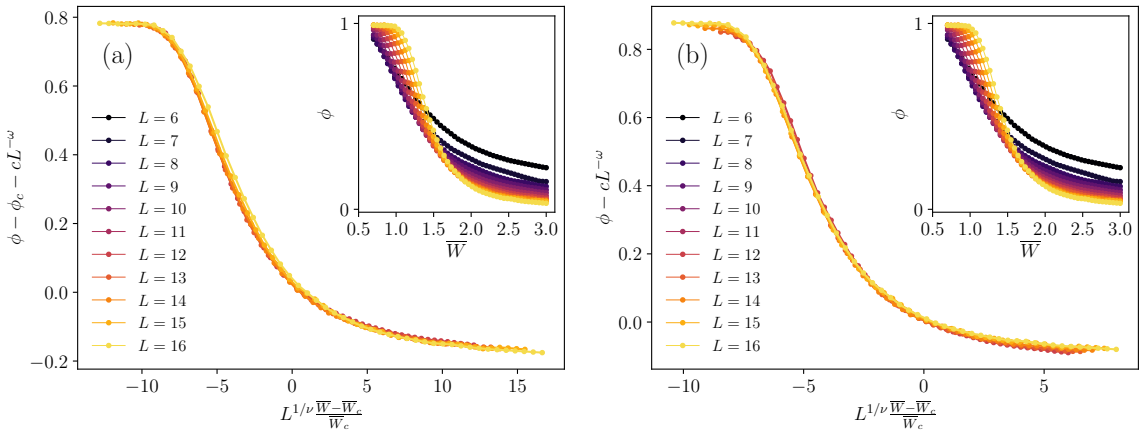

Figure 4.7.: Finite-size scaling for the rescaled r-parameter ϕ at $E = 0$ as a function of $\overline{W} = W/\sqrt{L}\log L$. (a) The collapse is obtained leaving both $\overline{W}_c$ and ϕ_c as free parameters, obtaining from the fit $\overline{W}_c \simeq 1.7$ and $\phi_c \simeq 0.2$. This is compatible with the result obtained from the zeros of the beta function (see inset of Fig. 4.5). The critical exponents are found to be $\nu \simeq 0.9$ and $\omega = 2$. (b) The collapse is obtained keeping $\phi_c = 0$ and $\overline{W}_c \simeq 2$, obtained in the main text from the zeros of beta function and the energies of the dynamical system. This is compatible with the result obtained from the zeros of the beta function (see inset of Fig. 4.5). The critical exponent are $\nu \simeq 1$ and $\omega = 1$.

$\phi_c \simeq 0.1$ at a disorder $W_c \simeq 20$, compatible with the value obtained by studying the turning points ϕ_A.

Finally, we report two scaling collapses of ϕ obtained with the rescaling of the disorder $\overline{W} = W/\sqrt{L}\ln L$, which makes a localization transition emerge at the center of the spectrum. However, one can observe that, while the collapses look convincing to the naked eye, they lead to a misleading interpretation of the data. The analysis of the beta function of ϕ performed in the main text shows that the transition is described by a 2PS theory, with a drift of the critical point to $\phi_c = 0$. If instead ϕ_c is left as a free parameter in the collapse, one obtains the incorrect value $\phi_c \simeq 0.2$ in Fig. 4.7(a). On the other hand, a collapse in which $\phi_c = 0$ is imposed is shown in Fig. 4.7(b): despite being a good collapse, with $W_c \simeq 2$ as predicted by the zeros of the beta function, it gives the non-physical result $\phi < 0$ for $\overline{W} > \overline{W}_c$, signaling that the 1PS ansatz is not valid for the QREM at $E = 0$.

Part II.

Semiclassical analysis of the two dimensional quantum Heisenberg spin glass

5. Semiclassical approach to quantum spin models in absence of translational symmetry

In this chapter we present a detailed approach to the study of semiclassical, low-energy excitations in quantum magnets and we show how this method may give a quantitatively good of the interacting quantum problem. We focus on the two dimensional case and we consider Heisenberg-like spin models with ferromagnetic, antiferromagnetic and random bonds, where translational invariance is lost, which is the case for disordered systems. We show how to construct the single particle Hamiltonian describing the spin-waves dynamics and we give a general construction to foresee the scaling of the lowest energy gap in the theory.

5.1. Introduction

Understanding the phase diagram of interacting quantum spin systems remains one of the central challenges of condensed matter physics. The difficulty originates from the strongly correlated nature of quantum magnets: even simple microscopic Hamiltonians generally cannot be solved exactly, and quantum fluctuations often compete with classical interactions. As a consequence, determining the nature of the ground state and its low-energy excitations requires the development of controlled approximation schemes.

One of the simplest and most successful approaches is the spin-wave approximation. The method is based on a semiclassical ($\hbar \to 0$) expansion around a zero temperature classical ordered ground state in which a continuous symmetry is spontaneously broken. Quantum fluctuations can then be treated as small deviations around this ordered configuration, leading to a systematic expansion in powers of the spin length S.

The resulting elementary excitations are known as magnons, collective oscillations of the local magnetic moments analogous to waves propagating through the ordered

spin background. At the lowest order, the spin-wave approximation reduces the original interacting many-body problem to a quadratic bosonic Hamiltonian describing non-interacting single-magnon excitations, providing a straightforward way to compute observables. We are interested in discussing the zero temperature case: typically, quantum fluctuations cause a decrease of the classical order parameter, that at the spin-wave level can be written as

$$\langle \mathcal{O} \rangle_{SC} = \mathcal{O}_{Cl} - \frac{1}{S}\,\delta\mathcal{O} + o\left(\frac{1}{S}\right) . \tag{5.1}$$

The success of the spin-wave theory relies deeply on how similar the quantum ground state is to the classical one, and the size of the correction $\delta\mathcal{O}$ is controlled first of all by dimensionality. In one dimension, fluctuations are typically strong enough to destroy classical long-range order altogether. In two and three dimensions ordered phases are far more robust, and spin-wave theory frequently provides an accurate quantitative description. The prototypical success is the $S = 1/2$ Heisenberg antiferromagnet on the square lattice, where the sublattice magnetization obtained from spin-wave theory including $1/S$ corrections agrees remarkably well with unbiased quantum Monte Carlo estimates [214, 215].

Whenever the ordered phase results from the spontaneous breaking of a continuous symmetry, the low-energy spectrum contains gapless collective modes. These are the realization of Goldstone modes in magnetic systems, and their dispersion relation is determined by the symmetry of both the Hamiltonian and the ordered state. In the following, we introduce the spin-wave formalism, derive the quadratic magnon Hamiltonian, and discuss how quantum fluctuations modify classical magnetic order and determine the low-energy excitation spectrum

5.2. The Holstein-Primakoff representation

The starting point of a spin-wave expansion is to find a representation of spin S operators in terms of bosonic variables. Before discussing the technical details, let us spend a few words on the physical meaning of this mapping. The Holstein-Primakoff (HP) representation is a highly anisotropic map from a set of 3 non-commuting spin variables to a set of 2 non-commuting bosonic variables: the classical spin direction, that for simplicity we choose to be the $\hat{z}$ axis, defines also the axis of quantization and

operators $\hat{S}^{x,y}$ create fluctuations in the orthogonal plane. In order to do so we define

$$\begin{aligned} \hat{S}^z &= S - \hat{n} \\ \hat{S}^+ &= f(\hat{n})\hat{a} \\ \hat{S}^- &= \hat{a}^\dagger f(\hat{n}) \end{aligned} \tag{5.2}$$

where $\hat{a}, \hat{a}^\dagger$ are bosonic operators satisfying $[\hat{a}, \hat{a}^\dagger] = 1$ and $\hat{n} = \hat{a}^\dagger\hat{a}$. For the representation to be meaningful, we need to find a function $f(\hat{n})$ such that the $SU(2)$ commutation rules are satisfied. We evaluate the commutator between ladder operators and we require

$$[\hat{S}^+, \hat{S}^-] \equiv f^2(\hat{n})(\hat{n}+1) - f^2(\hat{n})\hat{n} = 2(S - \hat{n}) \ . \tag{5.3}$$

In order to solve the previous equation, let us introduce the change of variable $h(\hat{n}) = f^2(\hat{n}-1)$, for which we can write the recursion

$$h(\hat{n}) = h(0) + 2nS - 2\sum_{k=0}^{n-1} 2(S-k) \ . \tag{5.4}$$

From here we find

$$f(\hat{n}) = \sqrt{2S}\sqrt{1 - \frac{n}{S}} \tag{5.5}$$

It is possible to check that this solution satisfies the other $SU(2)$ commutation rules $[S^+, S^z]$ and $[S^-, S^z]$.

It is particularly helpful to consider what happens to this map in the limit of large spin length $S \to \infty$. Let us notice that this limit corresponds to the semiclassical limit: indeed the spin operator acts on an eigenstate as $\hat{S}\,|S\rangle = \hbar S\,|S\rangle$. Keeping $\hbar S$ fixed we see that sending S to infinity corresponds to sending $\hbar \to 0$, hence considering a classical system.

The Holstein-Primakoff representation, expanding at leading order the function $f(\hat{n})$ and switching to $\hat{S}_x = \frac{1}{2}(\hat{S}^+ + \hat{S}^-)$ $\hat{S}_y = \frac{i}{2}(\hat{S}^+ - \hat{S}^-)$ reads

$$\begin{cases} \hat{S}_i^z \sim S - \hat{a}_i^\dagger\hat{a}_i \ , \\ \hat{S}_i^y \sim -i\sqrt{\frac{S}{2}}(\hat{a}_i - \hat{a}_i^\dagger) \ , \\ \hat{S}_i^x \sim \sqrt{\frac{S}{2}}(\hat{a}_i + \hat{a}_i^\dagger) \end{cases} \tag{5.6}$$

Let us briefly comment on the physical picture that emerges from the approximated description of spin operators in terms of bosons: the magnon number operator $\hat{n}_i = \hat{a}_i^\dagger\hat{a}_i$ measures the deviation from the fully polarized classical state, and the oper-

ators $\hat{S}_x, \hat{S}_y$ generate fluctuations in the orthogonal plane, with their amplitude being proportional to the spin length reduction due to quantum fluctuations.
In the next pages, we illustrate two simple examples in which the Holstein-Primakoff spin-wave theory can be applied, the two dimensional Heisenberg ferromagnet and antiferromagnet. We show how, in these cases, the predictions obtained truncating the HP expansion at order $\mathcal{O}(1/S)$ yield quantitatively accurate values of the order parameter for the $S = 1/2$ model.

5.2.1. The ferromagnet

As the simplest application of the Holstein-Primakoff representation, we consider a ferromagnet described by the Heisenberg Hamiltonian with nearest-neighbor interactions

$$\hat{H} = -J \sum_{\langle ij \rangle} \hat{\mathbf{S}}_i \cdot \hat{\mathbf{S}}_j \ , \tag{5.7}$$

where $J > 0$ favors parallel alignment of spins, and $\langle ij \rangle$ denotes nearest-neighbor pairs. We assume the ground state is ferromagnetically ordered with all spins pointing in the $\hat{z}$ direction.

Using the Holstein-Primakoff representation from the previous section, we express the spin operators in terms of bosonic creation and annihilation operators. where we have dropped higher-order terms in $1/S$. Now we substitute these expressions into the dot product $\hat{\mathbf{S}}_i \cdot \hat{\mathbf{S}}_j$:

$$\hat{\mathbf{S}}_i \cdot \hat{\mathbf{S}}_j = \hat{S}_i^z \hat{S}_j^z + \frac{1}{2}(\hat{S}_i^+ \hat{S}_j^- + \hat{S}_i^- \hat{S}_j^+) \ . \tag{5.8}$$

Computing each term:

$$\hat{S}_i^z \hat{S}_j^z = (S - \hat{n}_i)(S - \hat{n}_j) = S^2 - S(\hat{n}_i + \hat{n}_j) + \hat{n}_i \hat{n}_j \tag{5.9}$$

$$\frac{1}{2}(\hat{S}_i^+ \hat{S}_j^- + \hat{S}_i^- \hat{S}_j^+) \approx S(\hat{a}_i \hat{a}_j^\dagger + \hat{a}_i^\dagger \hat{a}_j) \tag{5.10}$$

At leading order in $1/S$, we drop the $\hat{n}_i \hat{n}_j$ term as it is $O(1/S^2)$. Thus:

$$\hat{\mathbf{S}}_i \cdot \hat{\mathbf{S}}_j \approx S^2 - S(\hat{n}_i + \hat{n}_j) + S(\hat{a}_i \hat{a}_j^\dagger + \hat{a}_i^\dagger \hat{a}_j) \ . \tag{5.11}$$

Substituting into the Heisenberg Hamiltonian and summing over nearest-neighbor

pairs:

$$\hat{H} = -J \sum_{\langle ij \rangle} \left[S^2 - S(\hat{n}_i + \hat{n}_j) + S(\hat{a}_i \hat{a}_j^\dagger + \hat{a}_i^\dagger \hat{a}_j) \right] \tag{5.12}$$

$$= -JS^2 N_b + JS \sum_{\langle ij \rangle} (\hat{n}_i + \hat{n}_j) - JS \sum_{\langle ij \rangle} (\hat{a}_i \hat{a}_j^\dagger + \hat{a}_i^\dagger \hat{a}_j) \ , \tag{5.13}$$

where N_b is the number of bonds. The first term is the classical ground state energy. The second term can be rewritten: each site i appears in z neighboring bonds (where z is the coordination number), so

$$\sum_{\langle ij \rangle} (\hat{n}_i + \hat{n}_j) = z \sum_i \hat{n}_i \ . \tag{5.14}$$

Collecting terms and dropping the constant energy, we obtain a quadratic Hamiltonian describing the spin-wave excitations of the Heisenberg ferromagnet:

$$\hat{H}_{sw} = JS \sum_i (z - \hat{n}_i) \hat{n}_i - JS \sum_{\langle ij \rangle} (\hat{a}_i^\dagger \hat{a}_j + \hat{a}_j^\dagger \hat{a}_i) \ . \tag{5.15}$$

To solve the problem, and find the magnon dispersion relation, we introduce Fourier-transformed operators in momentum space:

$$\hat{a}_i = \frac{1}{\sqrt{N}} \sum_{\mathbf{k}} e^{i \mathbf{k} \cdot \mathbf{R}_i} \hat{a}_{\mathbf{k}} \ , \tag{5.16}$$

where N is the number of sites and $\mathbf{R}_i$ is the position of site i. Plugging the Fourier expanded modes into the Hamiltonian we find, with a simple calculation

$$\hat{H}_{sw} = \sum_{\mathbf{k}} \varepsilon(\mathbf{k}) \hat{a}_{\mathbf{k}}^\dagger \hat{a}_{\mathbf{k}} \ , \tag{5.17}$$

where the magnon dispersion relation is

$$\varepsilon(\mathbf{k}) = 2JS[z - \gamma(\mathbf{k})] \ . \tag{5.18}$$

and $\gamma(\mathbf{k}) = \frac{1}{d} \sum_{\alpha=1}^{d} \cos(k_\alpha)$. A crucial observation is that the dispersion relation vanishes at $\mathbf{k} = 0$:

$$\varepsilon(\mathbf{0}) = 0 \ . \tag{5.19}$$

This is the manifestation of the Goldstone theorem: the spontaneous breaking of the continuous $SU(2)$ spin-rotation symmetry (broken down to $U(1)$ by the classical ferromagnetic order) guarantees the existence of a gapless mode. Physically, this

gapless excitation corresponds to a long-wavelength precession of all spins around the $\hat{z}$ axis. The dispersion relation of the magnon is quadratic, meaning that it is a Galilean, and not relativistic, particle. This is a consequence of the fact that the order parameter is a conserved quantity. In section 5.4 we will comment further about this. In principle, we could compute the correction to the classical magnetization due to quantum fluctuations in the spin-wave theory. However it is immediate to realize that these are exactly zero! Indeed for the ferromagnet, classical and quantum ground states exactly coincide, provided that the rotational symmetry is spontaneously broken.

5.2.2. The antiferromagnet

The ground state of the antiferromagnetic Heisenberg model on a bipartite lattice

$$\hat{H} = J \sum_{\langle ij \rangle} \hat{\mathbf{S}}_i \cdot \hat{\mathbf{S}}_j \ , \tag{5.20}$$

is the Néel state, where spins on different sublattices point in opposite directions. The key difference from the ferromagnet is that the two sublattices have opposite spin quantization axes.

On sublattice A we use the standard Holstein-Primakoff representation:

$$\begin{cases} \hat{S}_i^z = S - \hat{n}_i \\ \hat{S}_i^+ = \sqrt{2S}\hat{a}_i \\ \hat{S}_i^- = \sqrt{2S}\hat{a}_i^\dagger \end{cases} \tag{5.21}$$

On sublattice B (the "down" sites), the spin is rotated: $\hat{S}^z \to -\hat{S}^z$ and $\hat{S}^\pm \to -\hat{S}^\mp$. In terms of the same bosonic operators:

$$\begin{cases} \hat{S}_j^z = -S + \hat{n}_j \\ \hat{S}_j^+ = \sqrt{2S}\hat{a}_j^\dagger \\ \hat{S}_j^- = \sqrt{2S}\hat{a}_j \end{cases} \tag{5.22}$$

For nearest-neighbor pairs, computing $\hat{\mathbf{S}}_i \cdot \hat{\mathbf{S}}_j$ at leading order in $1/S$:

$$\hat{\mathbf{S}}_i \cdot \hat{\mathbf{S}}_j = -S^2 + S(\hat{n}_i + \hat{n}_j) + S(\hat{a}_i \hat{a}_j + \hat{a}_i^\dagger \hat{a}_j^\dagger) \ . \tag{5.23}$$

The spin-wave Hamiltonian is

$$\hat{H}_{sw} = JSz \sum_i \hat{n}_i - JS \sum_{\langle ij \rangle} (\hat{a}_i \hat{a}_j + \hat{a}_i^\dagger \hat{a}_j^\dagger) \,, \tag{5.24}$$

where the last term is the anomalous coupling that mixes magnons from the two sublattices.

Introducing momentum-space operators $\hat{a}_{\mathbf{k}}$, the Hamiltonian becomes

$$\hat{H}_{sw} = JSz \sum_{\mathbf{k}} \hat{n}_{\mathbf{k}} - JS \sum_{\mathbf{k}} \lambda(\mathbf{k}) (\hat{a}_{\mathbf{k}} \hat{a}_{-\mathbf{k}} + \hat{a}_{-\mathbf{k}}^\dagger \hat{a}_{\mathbf{k}}^\dagger) \,, \tag{5.25}$$

where $\lambda(\mathbf{k}) = \frac{1}{z} \sum_\delta e^{i\mathbf{k}\cdot\boldsymbol{\delta}}$ is the form factor.

The anomalous terms prevent direct diagonalization. We need to find a more general canonical transformation, that mixes a and $a^\dagger$ operator into $b, b^\dagger$quasiparticle, requiring the same bosonic commutation relations for the new set of operators. This transformation [216] is called a Bogoljubov transformation:

$$\begin{pmatrix} \hat{\alpha}_{\mathbf{k}} \\ \hat{\alpha}_{-\mathbf{k}}^\dagger \end{pmatrix} = \begin{pmatrix} u_{\mathbf{k}} & v_{\mathbf{k}} \\ v_{\mathbf{k}} & u_{\mathbf{k}} \end{pmatrix} \begin{pmatrix} \hat{a}_{\mathbf{k}} \\ \hat{a}_{-\mathbf{k}}^\dagger \end{pmatrix} \,, \tag{5.26}$$

The canonicity condition is obtained imposing $u_{\mathbf{k}}^2 - v_{\mathbf{k}}^2 = 1$. Writing the Hamiltonian in matrix form:

$$\hat{H}_{sw} = \sum_{\mathbf{k}} \begin{pmatrix} \hat{a}_{\mathbf{k}}^\dagger & \hat{a}_{-\mathbf{k}} \end{pmatrix} \begin{pmatrix} JSz & -JS\lambda(\mathbf{k}) \\ -JS\lambda(\mathbf{k}) & JSz \end{pmatrix} \begin{pmatrix} \hat{a}_{\mathbf{k}} \\ \hat{a}_{-\mathbf{k}}^\dagger \end{pmatrix} \,, \tag{5.27}$$

the eigenvalues give the magnon dispersion:

$$\varepsilon(\mathbf{k}) = JS\sqrt{z^2 - \lambda^2(\mathbf{k})} \,. \tag{5.28}$$

For the square lattice with $z = 4$ and $\lambda(\mathbf{k}) = 2(\cos k_x + \cos k_y)$:

$$\varepsilon(\mathbf{k}) = 2JS\sqrt{1 - \frac{(\cos k_x + \cos k_y)^2}{4}} \,. \tag{5.29}$$

The spectrum is gapless at both $\mathbf{k} = 0$ and $\mathbf{k} = (\pi, \pi)$. Near the zeros the dispersion relation is linear $\varepsilon(\mathbf{k}) \approx \sqrt{2}JS|\mathbf{k}|$. Also in this case the spectrum of the spin-wave Hamiltonian is gapless, as a consequence of the spontaneous symmetry breaking of the rotational symmetry, but, although the SSB pattern is the same as the ferromagnet, the dispersion relation is different.

The staggered magnetization in the Néel state is defined as

$$M_s = \frac{1}{N}\sum_i (-1)^i \langle \hat{S}_i^z \rangle \ , \tag{5.30}$$

where $(-1)^i$ picks up a sign depending on the sublattice. At the classical level the staggered magnetization takes its maximal value, $M_{s,\mathrm{Cl}} = S$. Quantum fluctuations reduce it, and the reduction is fixed by the density of Holstein–Primakoff bosons in the ground state,

$$\delta M_s = \frac{1}{N}\sum_{\mathbf{k}} \langle \hat{a}_{\mathbf{k}}^\dagger \hat{a}_{\mathbf{k}} \rangle \ , \tag{5.31}$$

where the average is taken in the magnon vacuum, i.e. the state annihilated by the Bogoljubov quasiparticle operators $\hat{\alpha}_{\mathbf{k}}$.

The point worth stressing is that this vacuum is *not* an eigenstate of the spin-deviation number operator $\hat{a}_{\mathbf{k}}^\dagger \hat{a}_{\mathbf{k}}$: the Bogoljubov rotation dresses it into a superposition containing a finite density of bosons on top of the Néel configuration. The classical ordered state is therefore not the ground state of the quantum Hamiltonian, in sharp contrast with the ferromagnetic case, where the fully polarized state is an exact eigenstate and receives no zero-point correction.

The recipe to evaluate δM_s is then straightforward: express the boson occupation through the Bogoljubov coefficients, so that each mode contributes an amount controlled by the ratio between the bare exchange scale and the magnon dispersion $\varepsilon(\mathbf{k})$, and average this contribution over the magnetic Brillouin zone. The vanishing of $\varepsilon(\mathbf{k})$ at the antiferromagnetic ordering wavevectors makes the integrand singular there, and whether the correction stays finite is decided by the competition between this singularity and the phase-space volume available around those points.

In two dimensions the Brillouin-zone integral converges and one finds, to leading order in $1/S$,

$$\delta M_s \simeq 0.197 \ , \tag{5.32}$$

independent of S at this order. The square-lattice antiferromagnet thus retains long-range order, with $M_s = S - 0.197$; the relative correction is substantial for $S = 1/2$, where the order parameter is reduced by roughly 40%, but becomes progressively less important as S grows, confirming the semiclassical expansion as controlled. In one dimension, by contrast, the same average diverges logarithmically, signalling the destruction of long-range order and the breakdown of the spin-wave treatment. Quantum fluctuations therefore reduce the staggered order parameter from its classical value $M_{s,\mathrm{Cl}} = S$ to

$$M_s = S - \delta M_s \simeq 0.303 \qquad (S = 1/2) \ , \tag{5.33}$$

a suppression of nearly 40%, yet crucially the order parameter stays finite: unlike the one-dimensional chain, the square lattice sustains genuine long-range Néel order at $T = 0$. The size of the correction is set by dimensionality and spin, growing for small S and low dimension. Remarkably, this leading-order spin-wave estimate is already close to the essentially exact quantum Monte Carlo value $M_s \simeq 0.307$ [215], the small residual mismatch being filled by higher-order $1/S$ corrections.

5.3. Non-translational invariant classical ground state

Let us know illustrate the most generic case, a spin system described by a Hamiltonian without any kind of lattice symmetry, being of course particularly interested in the disordered case. Notice that the classical configuration of minimal energy will be in general non collinear: this implies the presence of both standard ($\hat{a}_i^\dagger \hat{a}_j$) and anomalous ($\hat{a}_i \hat{a}_j$) terms. In this case we cannot simply introduce Fourier modes to solve the problem, but we need to numerically diagonalize the spin-wave Hamiltonian. From an operative point of view we approach the problem defining the local change of basis

$$R_i^{\alpha\beta} \boldsymbol{S}_i^\beta = \boldsymbol{\Sigma}_i^\alpha \ , \tag{5.34}$$

where $\boldsymbol{\Sigma}$ is a coordinated direction, around which we perform the rotation. Notice that in the case of the antiferromagnet this reduces to minus the identity on one sublattice. We write the classical Hamiltonian in the coordinated basis

$$E_{cl} = \sum_{ij} J_{ij} R_i^{\beta\alpha} R_j^{t,\alpha\gamma} \boldsymbol{\Sigma}_i^\beta \boldsymbol{\Sigma}_j^\gamma \ , \tag{5.35}$$

where $R_i^{\alpha\beta} \boldsymbol{S}_i^\beta = \boldsymbol{\Sigma}_i^\alpha$. In the previous equation, summation over repeated indices is assumed. In this notation, that may seem cumbersome, the rotations matrices specify the full spin configurations. By applying the HP map to the rotated spin operators $\hat{\boldsymbol{\Sigma}}_i$ and truncating the $1/S$ expansion at the leading order, one finds

$$\frac{\hat{H}}{S^2} = E_{cl} + \frac{1}{S} \hat{H}_{SW} + o(1/S) \ , \tag{5.36}$$

where

$$\hat{H}_{SW} = \frac{1}{2} \sum_{ij} \left(\hat{a}_i^\dagger A_{ij} \hat{a}_j + \hat{a}_i^\dagger B_{ij} \hat{a}_j^\dagger \right) + \text{h.c.} \ . \tag{5.37}$$

Since the Hamiltonian $\hat{H}$ is of order $O(S^2)$, we divided it by a factor S^2 in Eq. (5.36), in order for $\hat{H}_{SW}$ to appear at order $O(1/S)$. Let us define the tensor $\mathcal{R}_{ij}^{\alpha\beta} = R_i^{\alpha\gamma} R_j^{t,\gamma\beta}$,

with $\alpha = \{x, y, z\}$. Then, the matrix elements of the spin-wave Hamiltonian in Eq. (5.37), are given by the following expressions. For $i \neq j$:

$$A_{ij} = \frac{J_{ij}}{2}\left[\left(\mathcal{R}_{ij}^{xx} + \mathcal{R}_{ij}^{yy}\right) + i\left(\mathcal{R}_{ij}^{yx} - \mathcal{R}_{ij}^{xy}\right)\right] \tag{5.38a}$$

$$B_{ij} = \frac{J_{ij}}{2}\left[\left(\mathcal{R}_{ij}^{xx} - \mathcal{R}_{ij}^{yy}\right) + i\left(\mathcal{R}_{ij}^{yx} + \mathcal{R}_{ij}^{xy}\right)\right] , \tag{5.38b}$$

and for the diagonal elements:

$$A_{ii} = -\sum_{j\in\partial i} J_{ij}\mathcal{R}_{ij}^{zz} , \quad B_{ii} = 0 . \tag{5.39}$$

5.3.1. Geometrical interpretation of A_{ij} and B_{ij}

The matrix elements in Eqs. (5.38)-(5.39) admit a compact geometrical reading in terms of the local frames themselves. Denote by $\hat{\boldsymbol{e}}_i^x, \hat{\boldsymbol{e}}_i^y, \hat{\boldsymbol{e}}_i^z \equiv \hat{\boldsymbol{S}}_i$ the rows of R_i, i.e. the local triad obtained by rotating the fixed lab frame onto the classical direction of spin i. Since $\mathcal{R}_{ij}^{\alpha\beta} = R_i^{\alpha\gamma} R_j^{\beta\gamma} = \hat{\boldsymbol{e}}_i^{\alpha} \cdot \hat{\boldsymbol{e}}_j^{\beta}$, it is natural to introduce, at every site, the vectors

$$\hat{\boldsymbol{e}}_i^{+} \equiv \hat{\boldsymbol{e}}_i^{x} + i\,\hat{\boldsymbol{e}}_i^{y} , \quad \hat{\boldsymbol{e}}_i^{-} \equiv \hat{\boldsymbol{e}}_i^{x} - i\,\hat{\boldsymbol{e}}_i^{y} \tag{5.40}$$

satisfying $\hat{\boldsymbol{e}}_i^{\pm} \cdot \hat{\boldsymbol{e}}_i^{\pm} = 0$, $\hat{\boldsymbol{e}}_i^{\pm} \cdot \hat{\boldsymbol{e}}_i^{\mp} = 2$ and $\hat{\boldsymbol{e}^{+}}_i \times \hat{\boldsymbol{e}}_i^{-} = 2i\,\hat{\boldsymbol{S}}_i$. This is the standard circular-polarization vector associated with the precession plane of the local spin-wave fluctuation, its phase encoding the sense of rotation around $\hat{\boldsymbol{S}}_i$. A direct substitution shows that Eqs. (5.38) take the remarkably simple form

$$A_{ij} = \frac{J_{ij}}{2}\,\hat{\boldsymbol{e}}_i^{+} \cdot \hat{\boldsymbol{e}}_j^{-} , \qquad B_{ij} = \frac{J_{ij}}{2}\,\hat{\boldsymbol{e}}_i^{+} \cdot \hat{\boldsymbol{e}}_j^{+} , \tag{5.41}$$

while $A_{ii} = -\sum_{j\in\partial i} J_{ij}\,\hat{\boldsymbol{S}}_i \cdot \hat{\boldsymbol{S}}_j$, .

Equation (5.41) makes the physical content of the two couplings transparent. A_{ij} is proportional to the overlap of the two *co*-rotating polarization vectors and describes ordinary, magnon-number-conserving hopping between sites i and j; B_{ij}, involving $\hat{\boldsymbol{e}}_j$ rather than $\hat{\boldsymbol{e}}_j^{*}$, is instead the overlap with the *counter*-rotating component and generates the anomalous pair-creation/annihilation terms. This reproduces the familiar limits: for a ferromagnetic bond $\hat{\boldsymbol{e}}_i = \hat{\boldsymbol{e}}_j$ and $B_{ij} = 0$ identically, while for a collinear antiferromagnetic bond $\hat{\boldsymbol{e}}_j = \hat{\boldsymbol{e}}_i^{*}$, so that $A_{ij} = 0$ and $B_{ij} = J_{ij}$. More generally, B_{ij} vanishes whenever the local frames at i and j are related by a rotation about their common axis, which is precisely the condition violated in a non-collinear configuration: the impossibility of choosing a single global quantization axis is equivalent, bond by

bond, to $\hat{\boldsymbol{e}}_i$ and $\hat{\boldsymbol{e}}_j$ having nonzero overlap under complex conjugation. This is the geometric origin of the unavoidable anomalous terms. Finally, we note that the phases of A_{ij} are not pure gauge: around any closed loop $i \to j \to k \to i$ the combination $\arg(A_{ij}A_{jk}A_{ki})$ is gauge invariant and coincides with half the solid angle spanned by $\hat{\boldsymbol{S}}_i, \hat{\boldsymbol{S}}_j, \hat{\boldsymbol{S}}_k$ on the unit sphere, i.e. with the scalar spin chirality $\hat{\boldsymbol{S}}_i \cdot (\hat{\boldsymbol{S}}_j \times \hat{\boldsymbol{S}}_k)$. We can imagine to associate a fictitious magnetic field to the spin chirality, that, as it will be shown in 7.3 is responsible for the breaking of time reversal symmetry.

5.3.2. Solving the non-translationally invariant Bogoljubov Hamiltonian

In order to have more compact expressions, we introduce the following notation [217]. We define $2N \times 2N$ block matrices:

$$\gamma = \begin{pmatrix} 0 & 1_N \\ 1_N & 0 \end{pmatrix} \quad \eta = \begin{pmatrix} 1_N & 0 \\ 0 & -1_N \end{pmatrix} , \tag{5.42}$$

acting on $\hat{\boldsymbol{\alpha}} = (\hat{a}_1, \cdots, \hat{a}_N, \hat{a}_1^\dagger, \cdots, \hat{a}_N^\dagger)^t$. The matrix γ implements charge conjugation: $\hat{\boldsymbol{\alpha}}^\dagger = \gamma\hat{\boldsymbol{\alpha}}$, while η is a $2N$-dimensional metric, in terms of which the bosonic commutation relations can be written as $[\hat{\boldsymbol{\alpha}}, \hat{\boldsymbol{\alpha}}^\dagger] = \eta$. It holds: $\gamma^2 = \eta^2 = 1_{2N}$. With this notation:

$$\hat{H}_{SW} = \frac{1}{2}\hat{\boldsymbol{\alpha}}^\dagger M \hat{\boldsymbol{\alpha}} - \frac{1}{2}\mathrm{tr}A , \tag{5.43}$$

where M is a block matrix defined as:

$$M = \begin{pmatrix} A & B \\ B^* & A^* \end{pmatrix} . \tag{5.44}$$

The spin-wave Hamiltonian $\hat{H}_{SW}$ describes a system of coupled harmonic oscillators in terms of the bosonic creation and annihilation operators $\hat{a}_i^\dagger, \hat{a}_i$. The number operators $\hat{n}_i = \hat{a}_i^\dagger \hat{a}_i$ measure the local deviations from the classical background and the corresponding amplitude of the fluctuations in the planes orthogonal to the classical spin orientations. One could also express the Hamiltonian in terms of position and momentum operators: $\hat{x}_i \equiv \hat{S}_i^x/\sqrt{S}$ and $\hat{p}_i \equiv \hat{S}_i^y/\sqrt{S}$, which at order $1/S$ satisfy the commutation relations $[\hat{x}_i, \hat{p}_j] = i\delta_{ij}$. In these variables the Hamiltonian has a coupling term between position and momentum [218]. We will return to this representation in the following sections, whenever it provides a more insightful physical description. The quadratic problem defined in Eq. (5.43) can be solved with a Bogoljubov transformation [216, 217, 219]. We define *quasiparticle* operators $\hat{\boldsymbol{\beta}} = (\hat{b}_1, \cdots, \hat{b}_N, \hat{b}_1^\dagger, \cdots, \hat{b}_N^\dagger)^t$,

which are connected to the original bosonic operators by a linear transformation: $\hat{\boldsymbol{\beta}} = T\hat{\boldsymbol{\alpha}}$. As usual, we require T to be symplectic, *i.e.* $T\eta\gamma T^t = \eta\gamma$, so that $[\hat{\boldsymbol{\beta}}, \hat{\boldsymbol{\beta}}^\dagger] = \eta$, and unitary, *i.e.* $T = \gamma T^* \gamma$, leading to the following condition

$$T\eta T^\dagger \eta = 1_{2N} \ . \tag{5.45}$$

This equation can be used to write an explicit expression of the matrix T and of its inverse:

$$T = \begin{pmatrix} X^* & -Y^* \\ -Y & X \end{pmatrix} \qquad T^{-1} = \begin{pmatrix} X^t & Y^\dagger \\ Y^t & X^\dagger \end{pmatrix} \ , \tag{5.46}$$

from which we can derive a form of the canonicity condition that is the straightforward generalization of the TI case, in the original theory of superconductors [216]:

$$\begin{aligned} XX^\dagger - YY^\dagger &= 1_N \qquad X^\dagger X - Y^t Y^* = 1_N \\ XY^t - YX^t &= 0_N \qquad X^t Y^* - Y^\dagger X = 0_N \ . \end{aligned} \tag{5.47}$$

Then, by expressing $\hat{H}_{SW}$ in terms of the quasiparticle operators, we realize that T is not exactly the matrix diagonalizing M, but rather ηM:

$$\hat{H}_{SW} = \frac{1}{2}\hat{\boldsymbol{\beta}}^\dagger \eta\Omega\hat{\boldsymbol{\beta}} - \frac{1}{2}\mathrm{tr}A \ , \tag{5.48}$$

with

$$\Omega = TDT^{-1}, \qquad D = \eta M \ . \tag{5.49}$$

The matrix D is called *dynamical matrix* [219], it is non-Hermitian in general and its presence represents the main difference with respect to *fermionic* Bogoljubov-de Gennes systems. The diagonalization procedure is affected by mathematical subtleties regarding the kernel of D, which are discussed in Appendix 5.6.1.

5.4. Symmetry breaking and zero modes

In this section we review the physics of low energy excitations in the presence of spontaneous symmetry breaking. It is well known that, in the presence of Lorentz symmetry, to each of the broken generators corresponds a massless particle, the Goldstone boson. In condensed matter systems however the situation is less clear, because the absence of relativistic invariance loosens some constraints of the Goldstone theorem, making it possible to have fewer particles than broken generators and in general non-linear dispersion relations. A crucial role is played by the commutation relation

of the charges. In the next subsection we will provide a demonstration based on the Bogoljubov inequalities and we will show how the scaling of the lowest energy gap in the system depends on the algebra of the conserved currents.

5.4.1. Gapless spin-wave spectrum

We want to prove the Bogoljubov inequality: given two local operators X and Q and a Hamiltonian, it is possible to show that

$$\Delta^2 \leq \frac{\langle [X^\dagger, [H, X]] \rangle \langle [Q^\dagger, [H, Q]] \rangle}{| \langle [X, Q] \rangle |^2} , \tag{5.50}$$

where Δ is the smallest energy gap in the system, simply called the gap.
Let us start introducing the spectral weight on mode n for a local operator X

$$w_n = | \langle n|X|0 \rangle |^2 \tag{5.51}$$

where $|0\rangle$ is the ground state of the system and we introduce the gap $\omega_n = E_n - E_0$. Now we define the susceptibility

$$\chi_X = \sum_{n>0} \frac{w_n}{\omega_n} , \tag{5.52a}$$

the structure factor

$$S_X = \sum_{n>0} w_n = \frac{1}{2} \langle \{X, X^\dagger\} \rangle \tag{5.52b}$$

and the energy weighted structure factor

$$f_X = \sum_{n>0} w_n \omega_n = \frac{1}{2} \langle [X^\dagger, [H, X]] \rangle . \tag{5.52c}$$

It is easy to show that

$$\Delta^2 \leq \frac{f_X}{\chi_X} . \tag{5.53}$$

The proof is based on considering

$$f_X \geq \Delta \sum_{n>0} w_n \implies \Delta \leq \frac{f_X}{S_X} \tag{5.54}$$

and

$$\chi_X \leq \frac{1}{\Delta} \sum_{n>0} w_n \implies \Delta \leq \frac{S_X}{\chi_X} . \tag{5.55}$$

Plugging the two inequalities together we find the result in 5.53.
Now we introduce a third local operator P, with spectral weights $w_n^Q = |\langle n|Q|0\rangle|^2$, and derive the central inequality relating the two. Writing the equal-time commutator on the eigenbasis,

$$\langle [X,Q]\rangle = \sum_{n>0} \left(\langle 0|X|n\rangle \langle n|Q|0\rangle - \langle 0|Q|n\rangle \langle n|X|0\rangle\right) , \tag{5.56}$$

we bound it term by term,

$$|\langle [X,Q]\rangle| \leq 2 \sum_{n>0} |\langle n|X|0\rangle|\,|\langle n|Q|0\rangle| . \tag{5.57}$$

Then we split each term as

$$|\langle n|X|0\rangle|\,|\langle n|Q|0\rangle| = \left(\frac{|\langle n|X|0\rangle|}{\sqrt{\omega_n}}\right)\left(\sqrt{\omega_n}\,|\langle n|Q|0\rangle|\right) \tag{5.58}$$

and apply the Cauchy-Schwartz inequality

$$|\langle [X,Q]\rangle| \leq 2\sqrt{\sum_{n>0} \frac{w_n^X}{\omega_n}}\sqrt{\sum_{n>0} \omega_n w_n^Q} = 2\sqrt{\chi_X\, f_Q} , \tag{5.59}$$

obtaining

$$|\langle [X,Q]\rangle|^2 \leq 4\, f_Q\, \chi_X . \tag{5.60}$$

Substituting the previous inequality in Eq. 5.53 we finally find Eq. 5.50. The physical relevance enters through the choice of the pair (X,Q). We choose Q to be a Fourier component of a conserved density,

$$q_k = \sum_x e^{-ik\cdot x}\, q_x , \tag{5.61}$$

where $Q = \sum_x q_x = q_{k=0}$ satisfies $[H,Q] = 0$ and H is local. X is a local order parameter satisfying

$$\psi \equiv \lim_{V\to\infty} \frac{1}{V} \langle [X,Q]\rangle \neq 0 , \tag{5.62}$$

which is the definition of spontaneous breaking of the continuous symmetry generated by Q.
Conservation controls the behavior of f_{q_k}: At $k=0$ one has $q_0 = Q$ and $[H,Q]=0$, so $f_Q = 0$; moreover f_{q_k} is real and non-negative and even in k (from $q_{-k} = q_k^\dagger$ and

Hermiticity of H). Its Taylor expansion around $k = 0$ therefore starts at second order,

$$f_{q_k} \sim c_1\, k^2\, V + \mathcal{O}(k^4)\ . \tag{5.63}$$

Physically 5.63 is the continuity equation: a conserved density possesses a current, $[H, q_k] \sim k\, j_k$, and the double commutator collects one power of k from each side.
For a generic local operator that is *not* conserved the double commutator has no reason to vanish and $f_X = f_0 V + \mathcal{O}(k^2)$ with $f_0 > 0$. Collecting everything, with $|\langle [X, Q] \rangle| = \psi V$ extensive by 5.62, the factors of V cancel in 5.50 and the bound becomes a pure power counting in k: if both members of (X, Q) are conserved, $\Delta \lesssim \sqrt{k^2 \cdot k^2} = k^2$, which requires two conserved charges whose commutator has nonzero ground-state expectation, $\langle [Q^a, Q^b] \rangle \neq 0$, i.e. the order parameter is itself a charge density.
If only one member is conserved, the power counting gives $\Delta \lesssim \sqrt{k^2 \cdot 1} = |k|$. In every case with at least one conserved member, taking $k \to k_{\min} \sim 1/L$ closes the gap in the thermodynamic limit: this is the Goldstone theorem in its non-relativistic form. The rate of closure, $1/L^2$ versus $1/L$, is decided by the commutator algebra of the broken charges.
In the following we discuss some relevant cases for this work:

Ferromagnet. The ground state is fully polarized along the z direction. Choosing $X = S^x_k$ and $P = S^y_{-k}$, the $SU(2)$ commutation relations imply $[S^x_k, S^y_{-k}] = iS^z_0$, so that $\langle [X, P] \rangle = i\langle S^z_{\text{tot}} \rangle \propto V$. Since both X and P are components of the conserved total spin, their oscillator strengths satisfy $f_X, f_P \leq \rho\, k^2 V$. Equation (5.60) therefore yields the quadratic bound $\Delta \leq (2\sqrt{2}\rho/m)\, k^2$, which is saturated by the exact magnon dispersion $\omega_k = 2JS(1 - \cos k)$. The quadratic Goldstone mode thus follows directly from the fact that the two non-commuting operators are themselves conserved charges.

Antiferromagnet. On a bipartite lattice, the ordered phase is characterized by a finite staggered magnetization $n_s = \langle N^z \rangle / V \neq 0$, where $N^z = \sum_i (-1)^i S^z_i$. In this case, the uniform spin operators satisfy $\langle [S^x_k, S^y_{-k}] \rangle = 0$, so the relevant non-vanishing commutator must involve the staggered spin. Choosing $X = S^x_{\pi+k}$ and $P = S^y_{-k}$, one finds $\langle [X, P] \rangle = i\langle S^z_\pi \rangle = i n_s V$. Unlike the uniform spin, the staggered spin is not conserved, as the bond contributions to its continuity equation add rather than cancel. Consequently, $f_X = f_0 V$ remains finite as $k \to 0$, whereas the conserved uniform spin obeys $f_P \leq \rho_s k^2 V$. Equation (5.60) then gives $\Delta \leq (2\sqrt{2 f_0 \rho_s}/n_s)\, |k|$, in agreement with the linear magnon dispersion of the antiferromagnet. More generally, this reflects the fact that the two broken generators give rise to two independent type-A Goldstone

modes.

Spin glass. We turn to the case that motivated this whole discussion. Consider

$$H = -\sum_{ij} J_{ij}\, \mathbf{S}_i \cdot \mathbf{S}_j, \tag{5.64}$$

with random, bounded, short-ranged couplings J_{ij}. The Hamiltonian remains $SU(2)$-invariant, since the disorder enters as a scalar coefficient on each bond and does not couple to spin direction, so the three total spin components $Q^a = \sum_i S_i^a$ are all conserved and can play the role of P.

The state, on the other hand, looks nothing like a ferromagnet or a Néel antiferromagnet. Below the freezing temperature the spins acquire local expectation values,

$$\mathbf{m}_i \equiv \langle \mathbf{S}_i \rangle\,, \tag{5.65}$$

that point in random directions, determined by the disorder-dependent ground state selected . The disorder average of $\mathbf{m}_i$ vanishes, $\overline{\mathbf{m}_i} = 0$, which is why no linear operator (uniform or staggered) has an expectation value: there is no coherent pattern. What survives is the Edwards–Anderson parameter

$$q_{\mathrm{EA}} \equiv \overline{|\mathbf{m}_i|^2}, \tag{5.66}$$

which is nonzero in the glass and vanishes in the paramagnet. Physically, q_{EA} measures whether spins freeze at all, regardless of the direction they choose.

Since a generic frozen texture is non-coplanar, all three rotations move the state, and all three generators Q^a are spontaneously broken. This is the key difference from ferro and antiferro, where only two of the three generators break. In this case the symmetry group is fully broken, without residual symmetry generator:

$$O(3) \to O(1)\,. \tag{5.67}$$

To capture the breaking we need three independent SSB conditions, one per rotation axis, which requires an order parameter with enough index structure. Because $\mathbf{m}_i$ is a c-number vector and $\mathbf{S}_i$ is a quantum-mechanical operator vector, the natural object is the tensor

$$M_{\mathrm{sg}}^{ab} = \sum_i m_i^a\, S_i^b, \tag{5.68}$$

in direct analogy with $S^z_{\mathrm{tot}} = \sum_i 1 \cdot S_i^z$ for the ferromagnet and $N^z = \sum_i (-1)^i S_i^z$ for

the antiferromagnet. Its expectation value is manifestly nonzero,

$$\langle M^{ab}_{\rm sg}\rangle = \sum_i m_i^a \langle S_i^b\rangle = \sum_i m_i^a m_i^b = \tfrac{V}{3}\, q_{\rm EA}\, \delta^{ab}, \tag{5.69}$$

where the last step assumed an isotropic frozen texture, which is the generic case in a Heisenberg glass with rotationally invariant disorder. To get the SSB conditions, we compute the commutator with the three conserved charges using $[Q^a, S_i^c] = i\epsilon^{acd} S_i^d$:

$$\langle [Q^a, M^{bc}_{\rm sg}]\rangle = i\epsilon^{acd}\langle M^{bd}_{\rm sg}\rangle = \frac{iV}{3}\, q_{\rm EA}\, \epsilon^{acb}. \tag{5.70}$$

For each of the three broken generators Q^a, one can find a pair of tensor indices (b, c) such that $\epsilon^{acb} \neq 0$, giving a nonzero SSB commutator of order $Vq_{\rm EA}$. Explicitly, $\langle [Q^x, M^{yz}_{\rm sg}]\rangle$, $\langle [Q^y, M^{zx}_{\rm sg}]\rangle$ and $\langle [Q^z, M^{xy}_{\rm sg}]\rangle$ are all $iVq_{\rm EA}/3$. Three independent SSB conditions, corresponding to the three broken rotations. Also in this case then Eq. 5.60 predicts a linearly vanishing gap.

Counting zero modes

So far, we have only established the scaling of the gap associated with spontaneous symmetry breaking. A complementary question concerns the *number* of gapless excitations. In relativistic quantum field theory, this is answered by the Goldstone theorem [220], which states that every spontaneously broken continuous symmetry gives rise to one massless bosonic excitation.

The situation is richer in non-relativistic systems, where Lorentz invariance is absent and the number of Goldstone modes need not coincide with the number of broken generators. The first general classification was proposed by Nielsen and Chadha [221], while the complete counting rule was established later by Watanabe and Brauner [222] and rigorously proved by Watanabe and Murayama [223]. The magnetic systems discussed in this thesis provide textbook examples of this physics: ferromagnets, antiferromagnets, and spin glasses realize three distinct symmetry-breaking scenarios.

In non-relativistic systems, Goldstone modes are classified according to their low-momentum dispersion [221]:

- **Type-A** Goldstone modes have a dispersion $\omega \propto |\mathbf{k}|^n$ with n odd, generically linear ($n = 1$). Each mode is associated with a single broken generator, as in relativistic systems.

- **Type-B** Goldstone modes have a dispersion $\omega \propto |\mathbf{k}|^n$ with n even, generically quadratic ($n = 2$). Each such mode is associated with a pair of broken generators.

Nielsen and Chadha showed that these numbers satisfy the inequality

$$N_{\mathrm{BG}} \geq N_A + 2N_B, \tag{5.71}$$

where N_{BG} denotes the number of broken generators and N_A and N_B are the numbers of type-A and type-B Goldstone modes, respectively. Watanabe and Brauner subsequently showed that the difference between N_{BG} and the number of Goldstone modes is entirely determined by the expectation values of the commutators of the broken charges, while Watanabe and Murayama proved that the above inequality is always saturated. The resulting counting rule reads

$$N_{\mathrm{GB}} = N_{\mathrm{BG}} - \frac{1}{2}\operatorname{rank}\rho, \tag{5.72}$$

where

$$\rho_{ab} = -\frac{i}{V}\langle [Q_a, Q_b]\rangle \tag{5.73}$$

is the antisymmetric matrix constructed from the broken symmetry generators Q_a.

Physically, whenever two broken generators satisfy $\langle [Q_a, Q_b]\rangle \neq 0$, they cease to generate independent low-energy fluctuations. Instead, they form a canonically conjugate pair, analogous to position and momentum, and together produce a single type-B Goldstone mode with quadratic dispersion. When all commutators vanish, every broken generator gives rise to an independent type-A mode with linear dispersion.

5.5. Continuum limit

Everything obtained so far is tied to the lattice. At wavelengths much longer than the lattice spacing this detail is irrelevant, and the low-energy physics is governed by smooth fields describing how the ordered state varies from region to region. For the clean ferromagnetic and antiferromagnetic cases constructing this continuum theory is straightforward and isolates the universal low-energy content of the spin-wave Hamiltonian.

We begin with the ferromagnet. The Holstein-Primakoff bosons fluctuate about a uniform background, and it is possible to rewrite the Hamiltonian like

$$H_{\mathrm{FM}} = JS\sum_{\langle ij\rangle}\left(a_i^\dagger - a_j^\dagger\right)\left(a_i - a_j\right). \tag{5.74}$$

At low energy only slowly varying configurations contribute, so we replace $a_i \to a(\mathbf{x})$

and the finite difference by a gradient, obtaining

$$H_{\mathrm{FM}} \simeq D \int d^d x \, \nabla a^\dagger \cdot \nabla a, \qquad D = J S a_l^2, \tag{5.75}$$

where a_l is the lattice spacing. The corresponding action is the standard one for a bosonic field,

$$S_{\mathrm{FM}} = \int dt \, d^d x \left[i \, a^\dagger \partial_t a - D \, \nabla a^\dagger \cdot \nabla a \right], \tag{5.76}$$

and its defining feature is the kinetic term $i \, a^\dagger \partial_t a$, which is first order in time.

As we showed in the previous sections, the origin of this single time derivative lies in the algebra of the spin components. Writing $a \sim S^x + i S^y$, the real and imaginary parts of the field are the two transverse spin components, and these are canonically conjugate: from $[S^x, S^y] = i S^z$ and the nonzero magnetization of the ground state, $\langle S^z \rangle = S$, one has $\langle [S^x, S^y] \rangle = i S \neq 0$. A finite uniform magnetization therefore ties the two transverse fluctuations together as a coordinate and its conjugate momentum, rather than leaving them as independent degrees of freedom. The kinetic term in (5.76) is precisely the canonical form $p \, \dot{q}$, with the single complex field already containing both members of the pair. Two consequences follow. There is one oscillator, hence one magnon, per site; and the equation of motion,

$$i \, \partial_t a = [a, H_{\mathrm{FM}}] = -D \, \nabla^2 a, \tag{5.77}$$

is first order in time, describing precession rather than oscillation, with $\omega \sim k^2$. The uniform magnetization is conserved because it commutes with the Hamiltonian, which is what makes the transverse components conjugate in the first place.

For the antiferromagnet the background is staggered, and the order parameter is the Néel vector $\mathbf{n}(\mathbf{x})$ giving the local direction of the staggered magnetization. The essential difference from the ferromagnet is that the ground state carries no net moment, $\langle S^z_{\mathrm{tot}} \rangle = 0$, so the mechanism that paired the transverse components there is absent: the two transverse tilts of $\mathbf{n}$ have vanishing commutator expectation and are genuinely independent coordinates, not a conjugate pair. Their conjugate momentum must then be supplied by a separate field and the Lagrangian takes the form

$$\mathcal{L}_{\mathrm{AFM}} = \frac{\chi_\perp}{2} (\partial_t \mathbf{n})^2 - \frac{\rho_s}{2} (\nabla \mathbf{n})^2, \qquad \mathbf{n}^2 = 1. \tag{5.78}$$

The two time derivatives are generated by integrating out the momentum, exactly because that momentum is a field distinct from the order parameter itself. This is the relativistic $O(3)$ action, with velocity $c = \sqrt{\rho_s / \chi_\perp}$; the two independent transverse

directions of $\mathbf{n}$ give two degenerate Goldstone branches with linear dispersion $\omega = ck$, in place of the single quadratic mode of the ferromagnet.

5.6. Appendix of Chapter 5

5.6.1. Dealing with zero modes

The numerical implementation of the Bogoljubov transformation has to be taken with care, since it involves the diagonalization of the non-Hermitian matrix $D = \eta M$. It is possible to show that, despite being non-Hermitian, D has a real spectrum, provided that the matrix M is semi-positive definite [217], which comes as a consequence of expanding around a minimum. Moreover, in the presence of disorder the only degenerate eigenspace is the kernel of the matrix, where the zero modes related to the broken symmetries live. Then, the only difficulty that one faces numerically lies in counting the number of exactly zero eigenvalues of D. It is worth stressing this point because, for non-normal matrices (*i.e.* $MM^\dagger \neq M^\dagger M$), the *algebraic* and the *geometric* multiplicity of an eigenvalue do not coincide in general. This is to be interpreted as a pathology of the eigenvector decomposition, when applied beyond the scope of its hypothesis. Indeed, by naively performing the numerical diagonalization of the dynamical matrix D, one finds four very small eigenvalues and would be tempted to conclude that this is the number of zero modes in the theory.

We checked numerically that the matrix M has exactly three 0 (machine precision) eigenvalues, as expected from the Goldstone mechanism. A robust check of the number of the dynamical matrix D true zero modes can be done considering the singular value decomposition (SVD), whose zero singular values reveal the kernel of the matrix. We confirmed that the number of zero singular values of the dynamical matrix is exactly three, as expected. The extra 0 eigenvalue of D is called *defective*, because its algebraic multiplicity is greater than its geometric multiplicity. It can be checked that the spurious zero eigenvector belongs to the kernel of D^2, that is normal and can be safely diagonalized.

Since the zero modes are associated to global rotations of the system, in principle, the Bogoljubov Hamiltonian in Eq. (5.48) could be written as

$$H = \sum_{\alpha\in\Omega_0} \frac{\hat{\mathcal{B}}_\alpha \hat{\mathcal{B}}_\alpha}{\mathcal{I}} + \sum_{\alpha\in\Omega_+} \omega_\alpha (\hat{b}_\alpha^\dagger \hat{b}_\alpha + \text{h.c.}) \,, \tag{5.79}$$

where Ω_0, Ω_+ are respectively the set of zero and positive modes, $\hat{\mathcal{B}}_\alpha$ is a zero mode operator and $\hat{b}_\alpha$ is a true quasiparticle mode. The quantity $\mathcal{I}$ is the macroscopic moment of inertia, making the contribution of the zero modes vanishingly small in the thermodynamic limit, unless they are macroscopically populated. Therefore, in the thermodynamic limit, we can treat these modes semiclassically, assigning to them a

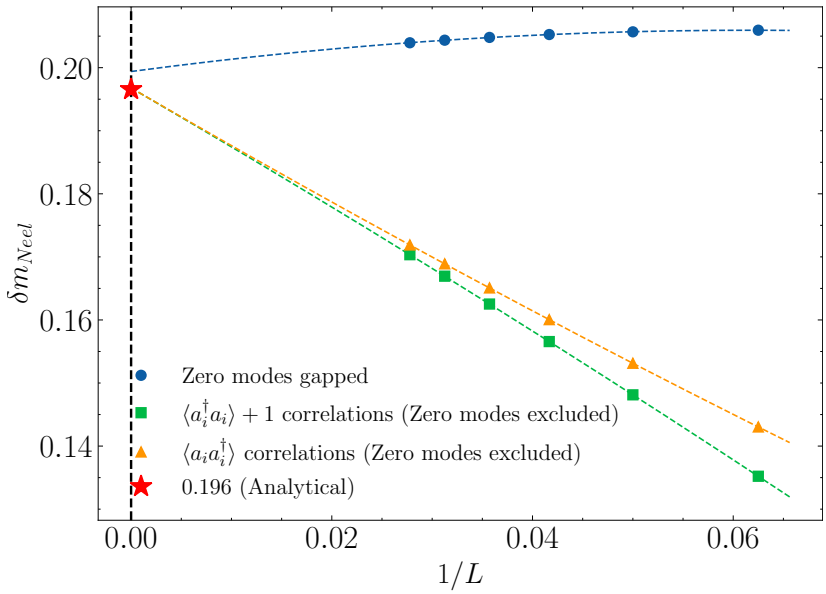

Figure 5.1.: Leading order spin-wave theory correction to the Nèel order parameter. The Nèel order parameter is $m_{\text{Nèel}} = \frac{1}{L^2}$ and the leading order correction in the HP theory is given by $\delta m_{\text{Nèel}} = \frac{1}{SL^2} \sum_i \langle \hat{a}_i^\dagger \hat{a}_i \rangle$. The blue curve is obtained by only adding a symmetry breaking field on the first two sites of magnitude $\varepsilon = 0.5$, the yellow and green curves are obtained by manually excluding the zero modes from the sum over the quasiparticles.

well-defined value, irrespective of their commutation relations. While this decomposition can be easily obtained in translational invariant cases, in the present case we are not able to write the Hamiltonian as in Eq. (5.79) for every realization of disorder, since, as explained above, the presence of a defective eigenvalue prevents one to find all the operators $\hat{\mathcal{B}}_\alpha$. It might then seem that this must be a halting point in our analysis: these modes can not be completely excluded from the theory for a given system size N, since their presence is essential in order to preserve the algebra of the bosonic operator. However, we can choose the Bogoljubov vacuum in the thermodynamic limit, to have simultaneously a precise value of all 3 expectation values of $\hat{\mathcal{B}}_\alpha$, irrespective of the fact that they do not commute which allows one to exclude the contribution of these modes from the expectation values. This is equivalent to considering the zero modes as c-numbers that can be set, for simplicity, to 0. By adopting this procedure, one is making an error on the expectation values of the observables, which vanishes in thermodynamic limit. The procedure can be benchmarked in the case of the antiferromagnet, where the analytical correction to the Nèel order parameter $\delta m_{\text{Nèel}} = \frac{1}{SL^2} \sum_i \langle \hat{a}_i^\dagger \hat{a}_i \rangle$ is known. Though at finite size $\langle \hat{a}_i^\dagger \hat{a}_i \rangle \neq 1 + \langle \hat{a}_i \hat{a}_i^\dagger \rangle$, the correct result for $\delta m_{\text{Nèel}}$ is recovered by both computing $\langle \hat{a}_i^\dagger \hat{a}_i \rangle$ and $1 + \langle \hat{a}_i \hat{a}_i^\dagger \rangle$ in the thermodynamic limit. The results of this test are shown in Fig. 5.1, where we compare this procedure to the addition of a small symmetry breaking field, which gaps the zero

modes. As one can see, the two different procedures to compute the correction to the Néel order parameter tend to the same value in the thermodynamic limit, which is also reached in the case of the small external field. Since the finite size error is smaller in the previous cases than in the latter, we choose to simply exclude the zero modes from the computation of every observable.

6. The two dimensional Heisenberg quantum spin glass

In this chapter we investigate the ground-state properties of the two-dimensional quantum Heisenberg model on a square lattice with binary bond disorder in nearest-neighbor couplings. First, we present large scale numerical simulations based on a state of the art neural quantum states technique, that show the presence of an extended, zero temperature quantum spin glass phase. Second, we benchmark this result against a semiclassical calculation, starting from the minimum of the classical analogous problem.

6.1. Introduction

Besides its intrinsic relevance to the theory of quantum spin glasses (QSG), the study of the bond-disordered Heisenberg model is experimentally motivated by the physics of the copper-oxygen planes in lightly doped insulating high-T_c superconductors. According to Refs. [224–226], localized vacancies on oxygen sites induce effective ferromagnetic couplings between neighboring copper spins, generating magnetic frustration and potentially leading to spin-glass behavior. In general, studying frustrated disordered quantum magnets in two dimensions is notoriously challenging. Quantum Monte Carlo (QMC) algorithms are often hindered by the sign problem, while exact diagonalization is restricted to small system sizes [227–231]. Density Matrix Renormalization Group (DMRG) and related tensor-network techniques have proven highly accurate even in two-dimensional disordered systems [232], but they face significant limitations compared to their one-dimensional counterparts. These include the need for high-rank tensor structures or, alternatively, restrictions to quasi-one-dimensional geometries using low-rank tensors arranged along a snaked path [233]. Moreover, such approaches often struggle to efficiently implement fully periodic boundary conditions, which are important for mitigating finite-size effects. Regardless of the computational method employed, one of the main challenges in studying disordered systems lies in the large number of realizations required to precisely compute disorder-averaged observ-

ables. To tackle this problem, we employ the Foundation Neural-Network Quantum States (FNQS) variational framework introduced in Ref. [234]. This approach allows us to circumvent the sign problem, retain fully periodic boundary conditions, and efficiently perform disorder averaging on lattice sizes that are inaccessible to exact diagonalization. The central result of this study is the identification of an intermediate phase, characterized as a QSG state, between a ferromagnetic and an antiferromagnetic phase by tuning the disorder strength. A schematic phase diagram of the model summarizing these findings is presented in Fig. 6.1. To further support our conclusions, we perform a semiclassical analysis based on a large-spin expansion at the leading order in $1/S$. This analysis shows that the classical spin-glass order found at $T = 0$, which is known to be unstable for any $T > 0$ [235, 236], is instead stable against quantum fluctuations. In particular, we find that the leading $1/S$ correction to the spin-glass order parameter yields a value compatible with the quantum value obtained through the FNQS approach in the thermodynamic limit, supporting the existence of a stable QSG phase at $S = \frac{1}{2}$, as indicated by our fully quantum numerical simulations.

6.2. The model

The two-dimensional Heisenberg model with binary random couplings on an $L \times L$ square lattice is defined by:

$$\hat{H} = \sum_{\langle i,j \rangle} J_{ij} \hat{\mathbf{S}}_i \cdot \hat{\mathbf{S}}_j \ , \tag{6.1}$$

where $\hat{\mathbf{S}}_i = (\hat{S}_i^x, \hat{S}_i^y, \hat{S}_i^z)$ is the $S = \frac{1}{2}$ spin operator at site i, and the sum runs only over nearest-neighbor sites, assuming periodic boundary conditions. The exchange couplings J_{ij} are randomly distributed according to the probability distribution:

$$P(J_{ij}) = (1-p)\delta(J_{ij}+1) + p\delta(J_{ij}-1) \ , \tag{6.2}$$

being $p \in [0,1]$ the probability of having an antiferromagnetic bond between site i and j. The ground state is well understood in two limiting cases: at $p = 1$, where the model reduces to the antiferromagnetic Heisenberg model, exhibiting long-range Néel order [215, 237], and at $p = 0$, where ferromagnetic order dominates. However, for a generic value of $0 < p < 1$, this model is notably challenging to simulate with standard techniques, and in the highly frustrated regime $p \approx 1/2$, the nature of the ground state remains elusive.

As a consequence, the numerical study of this and related disordered quantum magnets has been restricted to a few special cases. Previous studies [227–229] have

suggested the possibility of a QSG phase in the two-dimensional disordered Heisenberg model; however, these findings were limited by exact diagonalization results obtained on small 4×4 clusters and are far from compelling. In Ref. [238], square-lattice antiferromagnets were studied at low temperatures on clusters of up to 10×10 sites. However, only up to 10% ferromagnetic bonds were considered, limiting access to the spin-glass regime of primary interest in the present work (which we show appears when the fraction of ferromagnetic bonds exceeds 20%). Related studies have also considered limited random site or bond dilution [239]. More recently, a QSG phase has also been proposed in the corresponding one-dimensional model [240], although its nature is still under debate: while spin-wave and DMRG studies have provided evidence in favor of spin-glass order [240], recent ultra-low-temperature sign-free QMC simulations have instead suggested an unconventional critical state with power-law correlations [241].

At the mean-field level, complementary evidence indicates that quantum fluctuations do not necessarily destroy spin-glass order in this model. A quantum spin-glass phase in the fully connected Heisenberg model was already found by Bray and Moore [71] for every value S of the spin magnitude, under the assumption of unbroken replica symmetry (RS). The full RSB solution for $S = \frac{1}{2}$ has instead only recently been found, through a sophisticated dynamical mean-field approach combining replica symmetry breaking with continuous-time Quantum Monte Carlo, in Ref. [242]. As usual, however, the applicability of mean-field theory to low dimensions can be questioned. Establishing the stability of spin-glass order for this disordered Heisenberg model – which, unlike the transverse-field Ising case, is generally affected by the sign problem – would therefore provide nontrivial evidence that the spin-glass phase survives fully $SU(2)$-symmetric quantum fluctuations even in finite dimension. Whether spin-glass order survives in this model in two dimensions remains an open question, which we aim to address in this chapter.

6.3. Results

We adopt the methodology introduced in Ref. [234], in which a variational quantum state $|\psi_\theta(\mathbf{J})\rangle$, parametrized by neural networks and referred to as a Foundation Neural-Network Quantum State (FNQS), is optimized to minimize the disorder-averaged energy:

$$\mathcal{L}(\theta) = \mathbb{E}_{\mathbf{J}} \left[\frac{\langle \psi_\theta(\mathbf{J}) | \hat{H}_{\mathbf{J}} | \psi_\theta(\mathbf{J}) \rangle}{\langle \psi_\theta(\mathbf{J}) | \psi_\theta(\mathbf{J}) \rangle} \right] , \tag{6.3}$$

where θ are the variational parameters and $\mathbf{J}$ denotes the full set of binary couplings J_{ij} defining the disordered Hamiltonian in Eq. (6.1). The expectation value $\mathbb{E}_{\mathbf{J}}[\cdots]$ in

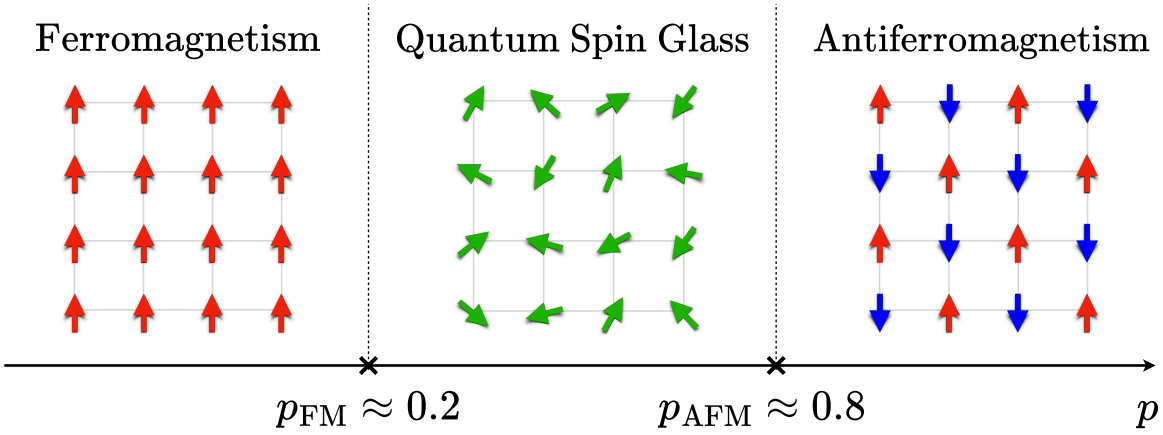

Figure 6.1.: Ground-state phase diagram of the disordered Heisenberg model [see Eq. (6.1)] in the thermodynamic limit, as a function of the probability $p \in [0, 1]$ [see Eq. (6.2)]. Three distinct phases are identified: a ferromagnetic phase for $p \leq p_{\mathrm{FM}} \approx 0.2$, an antiferromagnetic phase for $p \geq p_{\mathrm{AFM}} \approx 0.8$, and an intermediate quantum spin glass phase characterized by the absence of magnetic order and a finite Edwards-Anderson order parameter Q (see *Order parameters* for details). The phase diagram is obtained using the variational approach based on Foundation Neural-Network Quantum States (refer to App. 6.6).

Eq. (6.3) is approximated by averaging over $\mathcal{R}$ disorder realizations, with $\mathcal{R}$ typically on the order of hundreds, sampled from $\mathcal{P}(\mathbf{J}) = \prod_{ij} P(J_{ij})$. For each realization, the variational energy is computed using the Variational Monte Carlo framework [243]. In the following, for simplicity in the notation, we indicate with $\langle \cdots \rangle_{\mathbf{J}}$ the expectation value on $|\psi_\theta(\mathbf{J})\rangle$.

The key feature of the FNQS approach is that, at no additional computational cost compared to the single-instance case, a variational state parametrized through a Vision Transformer (ViT) architecture [244–248] can be optimized simultaneously across multiple disorder realizations (refer to App.6.6 for additional details about the variational Ansatz) [234]. This approach enables the efficient evaluation of disorder-averaged observables within a single simulation, substantially improving the scalability of variational methods for disordered systems. Remarkably, the accuracy of the model exhibits minimal degradation with increasing numbers of disorder realizations. Even when trained across hundreds of distinct disorder instances, the FNQS yields observable estimates that closely match those obtained from training on individual realizations with the same architecture (see 6.6.1).

6.3.1. Order parameters

To investigate the possible emergence of a non-magnetic ordered phase at intermediate disorder strengths $0 < p < 1$, we compute the magnetic order parameters char-

acterizing the two limiting cases: ferromagnetic order at $p = 0$ and antiferromagnetic (Néel) order at $p = 1$. The magnetic order parameters are defined as averages over the disorder distribution: $\mathcal{M}^2_{\text{Ferro}} = \mathbb{E}_{\mathbf{J}}\left[m^2_{\text{Ferro}}(\mathbf{J})\right]$ and $\mathcal{M}^2_{\text{Néel}} = \mathbb{E}_{\mathbf{J}}\left[m^2_{\text{Néel}}(\mathbf{J})\right]$, where, for a fixed realization $\mathbf{J}$, the ferromagnetic order parameter is given by

$$m^2_{\text{Ferro}}(\mathbf{J}) = C(0,0;\mathbf{J})/L^2 \tag{6.4}$$

while the Néel order parameter is

$$m^2_{\text{Néel}}(\mathbf{J}) = C(\pi,\pi;\mathbf{J})/L^2\ . \tag{6.5}$$

Both quantities are computed from the spin structure factor, defined as $C(\mathbf{k};\mathbf{J}) = \sum_{\mathbf{r}} e^{i\mathbf{k}\cdot\mathbf{r}} \langle \hat{\mathbf{S}}_{\mathbf{0}} \cdot \hat{\mathbf{S}}_{\mathbf{r}} \rangle_{\mathbf{J}}$. At the two limiting values of the disorder parameter $p = 0$ and $p = 1$, the distribution $\mathcal{P}(\mathbf{J})$ becomes a delta function. Specifically, in the pure ferromagnetic case ($p = 0$), the ground state is fully polarized, and the order parameter can be computed exactly as $\mathcal{M}^2_{\text{Ferro}} = \frac{1}{4} + \frac{1}{2L^2}$ [1]. In the antiferromagnetic limit ($p = 1$), the model reduces to the standard square-lattice Heisenberg antiferromagnet, for which the Néel order parameter remains finite in the thermodynamic limit, with a known value of $\mathcal{M}_{\text{Néel}} = 0.3070(3)$ [215, 237].

In the interesting intermediate regime $0 < p < 1$, no results are available from other numerical methods aside from exact diagonalization, which we perform up to 6×6 clusters (see 6.6.1) . In the left panel of Fig. 6.2, we show the behavior of the magnetic order parameters as a function of p, for system sizes ranging from $L = 4$ to $L = 14$. Each data point corresponds to a single simulation that averages over $\mathcal{R} = 600$ disorder realizations. Then, for each value of p, we perform a finite-size extrapolation in $1/L$ to estimate the magnetic order parameters in the thermodynamic limit (see 6.6.2 for additional details). Our extensive numerical calculations identify a region in the phase diagram $0.2 \lesssim p \lesssim 0.8$ where both magnetic order parameters vanish in the thermodynamic limit.

When both magnetic order parameters vanish, it is still possible for the system to exhibit glassy order. In a spin glass phase, each spin is aligned along some preferred random direction, which is strongly realization-dependent. To capture the SG order, we examine the long-distance behavior of the correlation function squared, or the *self-overlap*; see, for example, Ref. [249]. We refer to this quantity as the overlap order

[1] By definition, $C(0,0) = \langle \hat{\mathbf{S}}^2 \rangle$, where $\hat{\mathbf{S}}$ is the total spin operator. For a fully polarized state $\langle \hat{\mathbf{S}}^2 \rangle = S(S+1) = \frac{L^2}{2}(\frac{L^2}{2}+1)$, from which the order parameter follows.

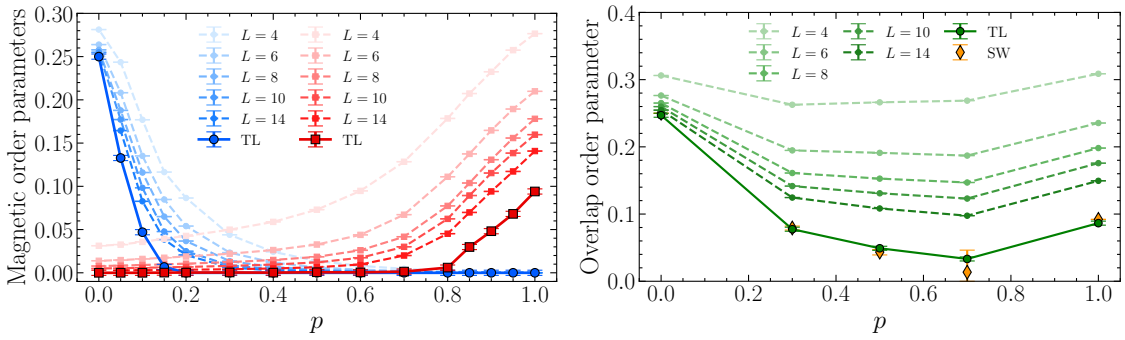

Figure 6.2.: Left panel: Ferromagnetic order parameter $\mathcal{M}^2_{\text{Ferro}}$ (blue circles, dashed lines) and Néel antiferromagnetic order parameter $\mathcal{M}^2_{\text{Néel}}$ (red squares, dashed lines) are shown as a function of the probability p for system sizes ranging from $L = 4$ to $L = 14$. Extrapolated values in the thermodynamic limit (TL), obtained via finite-size scaling in $1/L$ (see Sec. 6.6.2 of the appendix for details), are indicated by solid lines connecting the corresponding symbols. **Right panel:** Overlap order parameter Q (green circles, dashed lines) as a function of p for the same system sizes and averaging procedure. Extrapolated TL values are shown as green circles connected by a solid line. Results in both panels are averaged over $\mathcal{R} = 600$ disorder realizations. The error on the extrapolated values in the thermodynamic limit is estimated via a resampling technique with Gaussian noise. The semiclassical value of the overlap obtained in the TL of the non-interacting spin-wave theory is shown for comparison (orange diamonds), in great agreement with the FNQS values

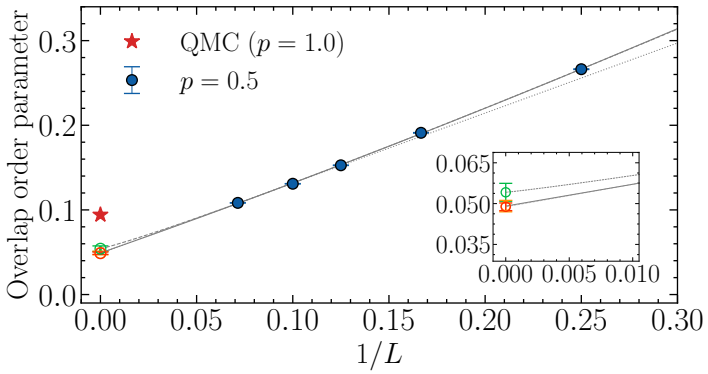

Figure 6.3.: Finite-size scaling of the overlap order parameter Q [see Eq. (6.6)] as a function of the inverse system size $1/L$ for $L = 4$ to $L = 14$ at $p = 0.5$. Quadratic (solid line and yellow circle) and power-law (dashed line and green circle) fits are performed over all data points, while a linear fit (dotted line and red circle) is applied to the last three points. **Inset:** Zoom of the extrapolations close to $1/L \to 0$. The error bars of the extrapolated values in the thermodynamic limit are estimated via a resampling technique with Gaussian noise. The red star indicating the extrapolated value at $p = 1.0$ is showed for comparison.

parameter, denoted here as Q, and defined as:

$$Q^2 = \mathbb{E}_{\mathbf{J}} \left[\frac{1}{L^4} \sum_{\mathbf{r},\mathbf{r}'} \langle \hat{\mathbf{S}}_{\mathbf{r}} \cdot \hat{\mathbf{S}}_{\mathbf{r}'} \rangle_{\mathbf{J}}^2 \right] . \tag{6.6}$$

Here, $\mathbf{r}$ and $\mathbf{r}'$ run over all lattice sites, and the value of the overlap is $Q_0^2 = S^4/3$ for a product state of classical, randomly oriented spins of the form $\prod_i |\mathbf{S}_i\rangle$, with $\mathbf{S}_i$ uniformly distributed on the Bloch sphere [2]

Any reduction from the classical value, i.e. $Q^2 < Q_0^2$, means that the fluctuations (quantum or thermal) reduce the persistence of the spins in the chosen random directions. In Fig. 6.3 we show the finite-size behavior of the overlap order parameter Q as a function of the inverse system size $1/L$ for the challenging case $p = 0.5$. For this probability value, both magnetic order parameters vanish in the thermodynamic limit (see the left panel of Fig. 6.2), making it crucial to assess the presence of spin-glass order. By performing different finite-size extrapolations, we find strong numerical evidence that Q remains finite at $p = 0.5$, with an extrapolated value estimated as $Q = 0.049(3)$. We repeat the analysis for different values of p, reporting the results in the right panel of Fig. 6.2. Extrapolating to the thermodynamic limit, we find that Q remains finite throughout the intermediate region $0.2 \lesssim p \lesssim 0.8$, where both magnetic order parameters vanish (see 6.6.2 for additional details about the extrapolations). These results rule out disordered phases such as quantum spin liquids or valence-bond solids, both characterized by a vanishing overlap order parameter, and provide compelling numerical evidence for the existence of a quantum spin-glass phase extending over a broad portion of the phase diagram. Although we cannot entirely exclude the presence of narrow intermediate regions near the magnetic transitions where Q might vanish (in particular close to the antiferromagnetic phase transition), our findings strongly support that at least a quantum spin-glass phase is realized. Moreover, in the App.6.6 we explicitly show, through calculations for a quantum spin-liquid state, that the overlap order parameter vanishes in the thermodynamic limit.

6.4. The semiclassical expansion

In this section we apply the method developed in the previous Chapter to study this particular problem. After numerically finding the ground state of the classical system

[2] In fact,

$$\frac{1}{L^4} \sum_{i,j} \sum_{\alpha,\beta} S_i^\alpha S_j^\alpha S_i^\beta S_j^\beta = S^4 \sum_{\alpha,\beta} \frac{1}{3}\delta_{\alpha\beta} \frac{1}{3}\delta_{\alpha\beta} = \frac{S^4}{3} \tag{6.7}$$

(in section 7.2 we will discuss more about this problem) we exploit the Holstein-Primakoff machinery to carry out the disordered spin wave expansion. In this way, the variational results obtained with the FNQS framework can be compared against a large-spin analysis by computing the leading order corrections in the inverse spin representation $1/S$ to the correlation functions and EA order parameter and then evaluating them in the fully quantum regime $S = \frac{1}{2}$. This approach also provides physical insight into the QSG phase. Spin waves in disordered systems have been extensively studied in the past [250–254]; more recently, they have found application in the study of disordered superconductors [255, 256] and of the one-dimensional version of the model under study [240]. Building upon these results, we carry out the full computation of the correction to the spin glass order parameter in the spin wave approximation. Before discussing the details of the overlap order parameter in spin wave theory let us summarize the finding of this technique: First we compute the $\mathcal{O}(1/S)$ order parameter correction for various values of p, as in Eq. (5.1) (the result of this for $p = 1/2$ are shown in Fig.6.4) and then we extrapolate the result at $S = 1/2$, see Figs. 6.5 and 6.2. For every value of p we find a very good agreement with the results of the FNQS simulation. In the general spirit of the spin wave theory discussed in the previous Chapter, this suggests that the quantum ground state is not tremendously different from the classical one.

Two point correlation function and the order parameter quantum correction.

In order to compute the effect of quantum fluctuations on the overlap order parameter in the semiclassical theory, one is interested in computing the leading order correction in the $1/S$ expansion to the 2-point correlation function, which enters the definition of Q^2:

$$Q^2 = \frac{1}{L^4} \sum_{ij}^{n} C_{ij}^2 \,, \tag{6.8}$$

where $C_{ij} \equiv \langle \hat{\mathbf{S}}_i \cdot \hat{\mathbf{S}}_j \rangle$. It is convenient to use the following expression of the spin operator: $\hat{\mathbf{S}} = \mathbf{S}_{cl} + \delta\hat{\mathbf{S}}/S$, with $|\mathbf{S}_{cl}|^2 = 1$, and an equivalent one for the rotated spin operator $\hat{\mathbf{\Sigma}}$, for which $\mathbf{\Sigma}_{cl} = \hat{z}$. In the bosonic HP representation, the leading order quantum fluctuation is given by

$$\delta\hat{\mathbf{\Sigma}}/S = \begin{pmatrix} \frac{a^\dagger + a}{\sqrt{2S}} \\ -i\frac{a - a^\dagger}{\sqrt{2S}} \\ -\frac{a^\dagger a}{S} \end{pmatrix} = \frac{1}{\sqrt{S}} \delta\hat{\mathbf{\Sigma}}_{1/2} + \frac{1}{S} \delta\hat{\mathbf{\Sigma}}_1 \,, \tag{6.9}$$

with $\delta\hat{\mathbf{\Sigma}}_{1/2}$ and $\delta\hat{\mathbf{\Sigma}}_1$ of order $O(1)$. In the previous expression, we have extracted the dependence on S and separated the x and y components, which are of order $1/\sqrt{S}$, from the z component, which is of order $1/S$. The quantum correlation function has the following expression:

$$C_{ij} = \mathbf{S}_{cl,i} \cdot \mathbf{S}_{cl,j} + \mathbf{S}_{cl,i} \cdot \langle \delta\hat{\mathbf{S}}_j/S \rangle + \mathbf{S}_{cl,j} \cdot \langle \delta\hat{\mathbf{S}}_i/S \rangle + \langle \delta\hat{\mathbf{S}}_i/S \cdot \delta\hat{\mathbf{S}}_j/S \rangle \ . \tag{6.10}$$

At order $1/S$ one finds that:

$$\langle \delta\hat{\mathbf{S}}_i/S \cdot \delta\hat{\mathbf{S}}_j/S \rangle = \frac{1}{S}\mathcal{R}_{ij}^{\alpha\beta} \langle \delta\hat{\Sigma}_{1/2,i}^{\alpha} \delta\hat{\Sigma}_{1/2,i}^{\beta} \rangle \tag{6.11a}$$

$$\mathbf{S}_{cl,i} \cdot \langle \delta\hat{\mathbf{S}}_j/S \rangle = -\frac{1}{S}\mathcal{R}_{ij}^{zz} \langle \delta\hat{\Sigma}_{1,j}^{z} \rangle \ , \tag{6.11b}$$

where $\alpha, \beta = \{x, y\}$ and $\langle \cdot \rangle = \langle 0| \cdot |0\rangle$ stands for the Bogoljubov vacuum state average. Therefore, the 2-point correlation function can be written as

$$C_{ij} = \mathbf{S}_{cl,i} \cdot \mathbf{S}_{cl,j} + \frac{1}{S} c_{ij}^{(1)} \tag{6.12}$$

with

$$c_{ij}^{(1)} = \mathcal{R}_{ij}^{\alpha\beta} \langle \delta\hat{\Sigma}_i^{\alpha} \delta\hat{\Sigma}_i^{\beta} \rangle - \mathcal{R}_{ij}^{zz} \left(\langle \delta\hat{\Sigma}_i^{z} \rangle + \langle \delta\hat{\Sigma}_j^{z} \rangle \right) \ . \tag{6.13}$$

By squaring the correlation, one finds:

$$C_{ij}^2 = (\mathbf{S}_{cl,i} \cdot \mathbf{S}_{cl,j})^2 + \frac{2}{S} \mathbf{S}_{cl,i} \cdot \mathbf{S}_{cl,j} \ c_{ij}^{(1)} + \frac{1}{S^2} \left(c_{ij}^{(1)} \right)^2 \ , \tag{6.14}$$

where we also retain the $1/S^2$ term. It is important to stress that Eq. (6.14) does not represent the complete result at order $1/S^2$, since magnon interactions also contribute at that order and are not captured by linear spin-wave theory. Rather, it is obtained by computing the correlations within linear spin-wave theory, setting $S = 1/2$, and then constructing Q^2. The consistency of this procedure is confirmed in the antiferromagnetic limit, where linear spin-wave theory correctly reproduces $Q^2 = \mathcal{M}^4_{\text{Néel}}$. We can therefore write:

$$Q^2(S, L) = \bar{Q}_0^2 - \frac{2}{S} c_1(L) + \frac{1}{S^2} c_2(L), \tag{6.15}$$

where $\bar{Q}_0^2 = 1/3$ is the classical value,

$$c_1(L) = -\frac{1}{L^4} \sum_{ij}^{n} \mathbf{S}_{cl,i} \cdot \mathbf{S}_{cl,j} \ c_{ij}^{(1)} \tag{6.16a}$$

$$c_2(L) = \frac{1}{L^4} \sum_{ij}^{n} \left(c_{ij}^{(1)} \right)^2 \ . \tag{6.16b}$$

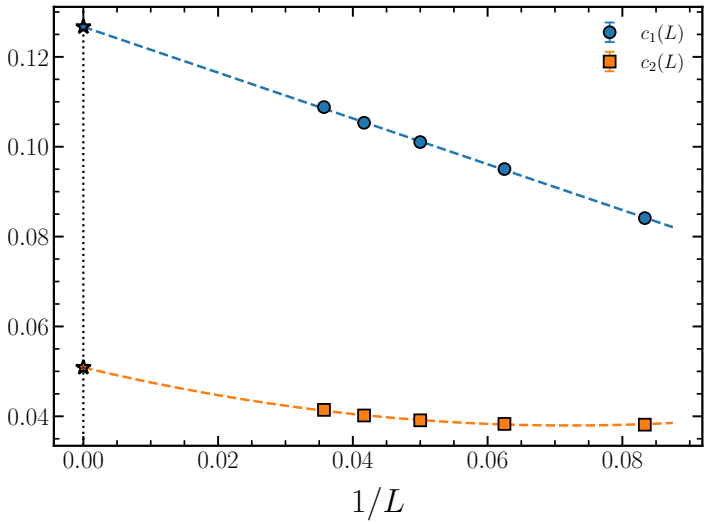

Figure 6.4.: Finite size extrapolations of the corrections to the overlap, for $p = 0.5$. Each point is obtained considering an average over approximately 1000 disorder realizations. The infinite size values are extracted with a quadratic fit in $1/L$ and are respectively $c_1^\infty = 0.127(3)$ and $c_2^\infty = 0.051(1)$.

Notice that, in order to compare the semiclassical prediction for the overlap with the fully quantum one, the right-hand side of Eq. (6.15) has to be multiplied by a factor S^4, due to the spin normalization mismatch between the classical case ($|\mathbf{S}_{cl}|^2 = 1$) and the quantum ($S = 1/2$) case. This way, we obtain: $Q^2 = Q_0^2 + \Delta Q^2$, with $Q_0^2 = S^4/3$ and

$$\Delta Q^2 = -2S^3 c_1^\infty + S^2 c_2^\infty \ , \tag{6.17}$$

where $c_{1,2}^\infty$ denote the extrapolated values of $c_{1,2}(L)$ in the thermodynamic limit (Fig. 6.4). By taking the square root of Q^2, one has

$$Q_{\mathrm{SW}} = \frac{S^2}{\sqrt{3}} \sqrt{1 - \frac{6c_1^\infty}{S} + \frac{3c_2^\infty}{S^2}} \ . \tag{6.18}$$

For completeness, let us also write the explicit expression of $c_{ij}^{(1)}$ in terms of the HP bosonic operators

$$c_{ij}^{(1)} = \langle \hat{a}_i^\dagger \hat{a}_j \rangle \mathcal{A}_{ij} + \langle \hat{a}_i \hat{a}_j^\dagger \rangle \mathcal{A}_{ij}^* + \langle \hat{a}_i^\dagger \hat{a}_j^\dagger \rangle \mathcal{B}_{ij} + \langle \hat{a}_i \hat{a}_j \rangle \mathcal{B}_{ij}^* - \mathbf{S}_{cl,i} \cdot \mathbf{S}_{cl,j} (\langle a_i^\dagger a_i \rangle + \langle a_j^\dagger a_j \rangle) \ , \tag{6.19}$$

where $\mathcal{R}_{ij}^{zz} = \mathbf{S}_{cl,i} \cdot \mathbf{S}_{cl,j}$. Expectation values of the creation/annihilation operators need to be evaluated on the ground state of the quantum theory. By exploiting the

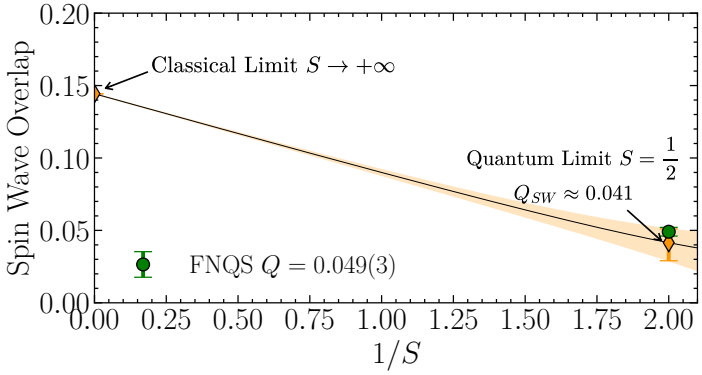

Figure 6.5.: Semiclassical prediction for the overlap order parameter in the thermodynamic limit as a function of the inverse spin representation $1/S$ at $p = 0.5$. On the vertical axis we plot Q_{SW} [see Eq. (6.15)] divided by $4S^2$ to have a comparison with the FNQS result at $S = \frac{1}{2}$ and at the same time with the classical value $Q_0/(4S^2) = 0.1443$. The semiclassical correction is obtained through a non-interacting spin wave-theory computation. For $S = \frac{1}{2}$ the value of the overlap is compatible with the value obtained for the fully quantum model with the FNQS, within the error bars.

definition of the inverse Bogolyubov transformation one finds

$$\begin{aligned} \langle \hat{a}_i^\dagger \hat{a}_j \rangle &= (Y^t Y^*)_{ij} \qquad \langle \hat{a}_i \hat{a}_j^\dagger \rangle = (X^t X^*)_{ij} \\ \langle \hat{a}_i \hat{a}_j \rangle &= (X^t Y^*)_{ij} \qquad \langle \hat{a}_i^\dagger \hat{a}_j^\dagger \rangle = (Y^t X^*)_{ij} \, . \end{aligned} \tag{6.20}$$

These are the only surviving terms, since the only nonzero contributions in the inverse Bogoljubov transformation come from $\langle \hat{b}\hat{b}^\dagger \rangle$. The components of X and Y corresponding to the kernel eigenvectors have been excluded from the computation, in line with the discussion at the end of the previous Section.

6.5. Discussion

In this Chapter, we explored the phase diagram of the two-dimensional Heisenberg model with binary disorder in the nearest-neighbor couplings, presenting compelling evidence for a quantum spin glass phase in the thermodynamic limit. Methodologically, we employed a novel variational framework based on FNQS [234], which proves particularly effective for disordered quantum systems. Unlike conventional approaches, FNQS mitigate the high computational cost associated with averaging over many disorder realizations. We support the numerical result by performing a semiclassical expansion around the classical minimum energy configuration.

This work marks an important advance in the study of disordered two-dimensional quantum magnets, both conceptually and methodologically. On the conceptual side, it provides the first evidence, based on large-scale simulations, that the disordered Heisenberg model can host a quantum spin-glass phase. On the methodological side, it shows the application of an efficient and broadly applicable computational framework for investigating this class of frustrated, disordered spin systems.

This work could be naturally extended along some of the following directions. First, a more detailed characterization of the antiferromagnetic transition near $p \approx 0.8$ seems compelling. In related frustrated models, this transition has been argued to support the emergence of a quantum spin-liquid state [245, 257, 258]; a spin-liquid phase could account for a small intermediate region between the antiferromagnetic and spin-glass phase where the overlap order parameter can vanish. Second, key properties of the QSG state must be characterized by studying its low-energy excitations, for instance using the real-time response to weak local perturbations and the resulting propagation of dynamical correlations.

6.6. Appendix of Chapter 6

6.6.1. Comparison with Exact Diagonalization

In Fig. 6.6, we show the spin-spin correlations for a representative disorder realization with $p = 0.7$ on a 6×6 cluster, which is the largest system size for which exact results from the Lanczos algorithm are available [259]. We compare the exact data (blue empty circles) with different variational approaches. First, we train a standard Neural-Network Quantum State (NQS) [260, 261] based on a ViT architecture [245] directly on this realization (green circles), reaching a relative energy error of $\Delta\varepsilon \approx 3 \times 10^{-3}$. Then, we test a foundation model trained on $\mathcal{R} = 600$ independent disorder realizations on the same sample. We consider two network sizes: a smaller FNQS with $P \approx 8 \times 10^5$ parameters (orange triangles) and a larger FNQS-L with $P \approx 1.2 \times 10^6$ parameters (red triangles). The larger network gives a better energy ($\Delta\varepsilon \approx 5 \times 10^{-3}$) compared to the smaller one ($\Delta\varepsilon \approx 7 \times 10^{-3}$) and shows systematically improved spin-spin correlations at all positions. Crucially, the spin structure factor (inset of Fig. 6.6) remains nearly identical for all variational methods, showing that the magnetic order parameters, related to the structure factor at $\mathbf{k} = (0, 0)$ and $\mathbf{k} = (\pi, \pi)$, are well reproduced (see *Numerical Results*). The overall agreement with the exact data confirms that the FNQS can accurately describe individual disorder realizations, with only about a factor-of-two increase in relative energy error compared to a network trained specifically on that sample. We remark that both approaches have similar computational costs, but the FNQS represent more general variational states since it is optimized over many realizations.

6.6.2. Finite-Size Extrapolations to the Thermodynamic Limit

In this section, we present the finite-size extrapolations of the three relevant order parameters: the antiferromagnetic order parameter $\mathcal{M}^2_{\text{Néel}}$, the ferromagnetic order parameter $\mathcal{M}^2_{\text{Ferro}}$, and the overlap order parameter Q (see *Numerical Results* for their definitions). The extrapolations are shown as a function of inverse system size $1/L$ for system sizes ranging from $L = 4$ to $L = 14$. Each value of the order parameters is obtained by averaging over $\mathcal{R} = 600$ disorder realizations. In the left panel of Fig. 6.7, we display the behavior of $\mathcal{M}^2_{\text{Néel}}$ for $p \in [0.4, 1.0]$. Notably, for $p_{\text{AFM}} \approx 0.8$, the extrapolated value vanishes in the thermodynamic limit, indicating the disappearance of antiferromagnetic long-range order. Additionally, we benchmark the variational results against Quantum Monte Carlo data [238] for the unfrustrated case $p = 1.0$, finding excellent agreement both at finite sizes and in the thermodynamic limit. The

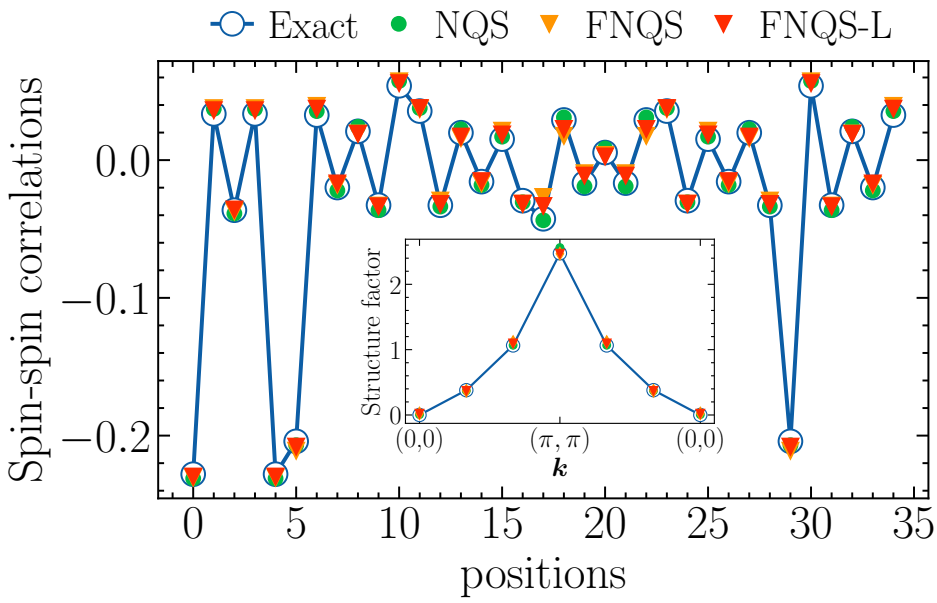

Figure 6.6.: Spin-spin correlations for a disorder realization with $p = 0.7$ on a 6×6 cluster. The two-dimensional lattice is unrolled using the row-major convention for visualization. Exact diagonalization results (blue empty circles) are compared with variational calculations: an NQS optimized on the specific realization (green circles), and two FNQS models optimized over $\mathcal{R} = 600$ independent disorder realizations. A smaller FNQS (orange triangles) with $P \approx 8 \times 10^5$ parameters and a larger FNQS-L (red triangles) with $P \approx 1.2 \times 10^6$ parameters. The inset shows the corresponding spin structure factor along the path connecting $\mathbf{k} = (0, 0)$ and $\mathbf{k} = (\pi, \pi)$.

central panel of Fig. 6.7 shows the extrapolation of the ferromagnetic order parameter $\mathcal{M}^2_{\text{Ferro}}$ for $p \in [0.0, 0.3]$. Here, for $p_{\text{FM}} \approx 0.2$, the extrapolated value also vanishes, signaling the suppression of ferromagnetic order. For $p = 0$, we compare the variational results with the exact analytical prediction available for this limit (see Section *Numerical Results*), again observing very good agreement. Finally, the right panel of Fig. 6.7 reports the behavior of the overlap parameter Q. For the limiting cases $p = 0$ and $p = 1$, we compare the extrapolated values of Q with the corresponding magnetic order parameters, confirming consistency between the different observables. We also show the extrapolation of Q for intermediate values $p = 0.3$, 0.5, and 0.7, where both magnetic orders vanish in the thermodynamic limit. In contrast to the magnetic order parameters, Q remains finite, suggesting the presence of a QSG phase in this parameter regime (refer to the Appendix for additional analysis on the overlap order parameter in a quantum spin liquid state).

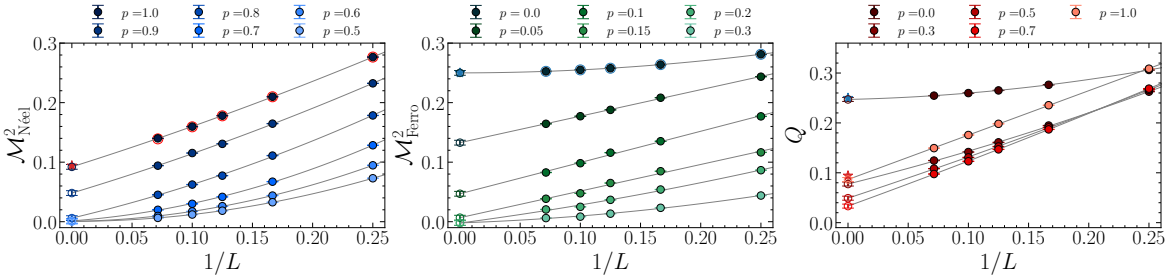

Figure 6.7.: Finite-size extrapolations of the order parameters as a function of $1/L$: the antiferromagnetic $\mathcal{M}^2_{\text{Néel}}$ (left panel), ferromagnetic $\mathcal{M}^2_{\text{Ferro}}$ (central panel), and overlap Q (right panel) order parameters, averaged over $\mathcal{R} = 600$ disorder realizations for system sizes ranging from $L = 4$ to 14. The data for $L = 4$ are obtained with exact diagonalization techniques. In the left panel, numerically exact Quantum Monte Carlo [215] results for $p = 1.0$ are shown for finite sizes (red empty circles) and thermodynamic limit (red star). In the central panel, analytic results for $p = 0.0$ are shown for finite sizes (blue empty circles) and thermodynamic limit (blue star). In the right panel, thermodynamic-limit values of the Néel (red star) and ferromagnetic (blue star) order parameters are shown for comparison with the overlap Q at $p = 1.0$ and $p = 0.0$, respectively. The error bars of the extrapolated values in the thermodynamic limit are estimated via a resampling technique with Gaussian noise.

6.6.3. Self-Averaging and Distribution of Order Parameters

In disordered systems, a central requirement for the validity of statistical predictions is the *self-averaging* property of physical observables. An observable is said to be self-averaging if its fluctuations across different disorder realizations vanish in the thermodynamic limit. This implies that ensemble-averaged quantities become representative of individual realizations as the system size increases. In Fig. 6.8 we analyze the distributions of the relevant order parameters for $p = 0.5$, namely, the antiferromagnetic order parameter $\mathcal{M}^2_{\text{Néel}}$ (left panel), the ferromagnetic order parameter $\mathcal{M}^2_{\text{ferro}}$ (central panel), and the square of overlap Q^2 (right panel), computed over $\mathcal{R} = 600$ independent disorder realizations. The width of these distributions systematically decreases with increasing system size L, providing strong evidence of self-averaging.

We emphasize that this property is not only fundamental from a theoretical standpoint, but it also has important computational implications in our variational approach. In the FNQS framework, a single variational wave function is optimized simultaneously across many disorder realizations. The efficiency and accuracy of this global optimization strategy improve with system size in a self-averaging model: as the fluctuations between different realizations diminish, the structure of the ground states becomes more similar across the various disorder realizations. Consequently, the variational state is able to effectively capture the common features of the ground

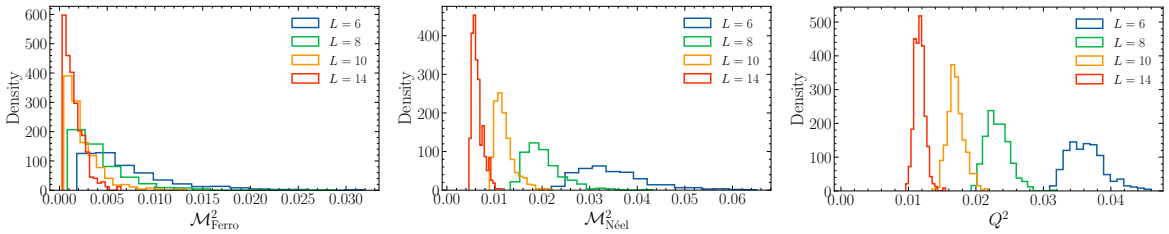

Figure 6.8.: Distributions of the order parameters $\mathcal{M}^2_{\text{Ferro}}$ (left panel), $\mathcal{M}^2_{\text{Néel}}$ (central panel), and Q^2 (right panel) for $p = 0.5$, considering system sizes ranging from $L = 6$ to $L = 14$. Each distribution is computed using $\mathcal{R} = 600$ independent disorder realizations.

states in the disordered ensemble.

6.7. Foundation Neural-Network Architecture

The computational advantage of Foundation Neural-Network Quantum States (FNQS) is achieved by making the variational many-body wave function amplitudes $\psi_\theta(\sigma|\mathbf{J}) = \langle\sigma|\psi_\theta(\mathbf{J})\rangle$ explicitly dependent on the Hamiltonian couplings $\mathbf{J}$. Here, σ denotes a spin configuration on a two-dimensional square lattice of linear size L, with local spin variables $\sigma_i = \pm 1$ at each site i, where $i = 1, \ldots, L^2$. The variational state $\psi_\theta(\sigma|\mathbf{J})$ is parametrized with a Vision Transformer (ViT) architecture [244–248], which processes a sequence of n input vectors $\mathbf{x}_1, \ldots, \mathbf{x}_n$, each in $\mathbb{R}^d$, where d is a tunable embedding dimension. In the FNQS framework, the input to the neural network is built to incorporate the Hamiltonian couplings $\mathbf{J}$ as input features of the neural network at the same level as the physical spin configurations σ [234]. Specifically, the spin configuration σ is divided into n non-overlapping patches of size b^2 [245], each embedded into $\mathbb{R}^{d/2}$ through a learnable linear transformation, producing the sequence $\mathbf{x}^\sigma_k$ with $k = 1, \ldots, n$. At the same time, each spin σ_i is associated with its two local couplings: the horizontal coupling $J_{i,i+1}$ and the vertical coupling $J_{i,i+L}$, assuming periodic boundary conditions. Using the same patching scheme, the sets of horizontal and vertical couplings are partitioned into patches and independently embedded into two sequences of vectors, $\mathbf{x}^h_k$ and $\mathbf{x}^v_k$ with $k = 1, \ldots, n$, each lying in $\mathbb{R}^{d/4}$. Finally, the input sequence of the model is obtained by concatenating the three embedding vectors at each patch location: $\mathbf{x}_k \equiv \text{Concat}(\mathbf{x}^\sigma_k, \mathbf{x}^h_k, \mathbf{x}^v_k) \in \mathbb{R}^d$. This set of n vectors is processed by the ViT wave function, yielding as output a set of another n vectors $\mathbf{y}_k \in \mathbb{R}^d$. The scalar amplitude $\text{Log}[\psi_\theta(\sigma|\mathbf{J})]$ is obtained by summing over the output tokens, $\mathbf{z} = \sum_{k=1}^n \mathbf{y}_k$, and applying a complex-valued two-layer feedforward network with a single output neuron, as detailed in Refs. [234, 245]. The hyperparameters of the ViT architecture

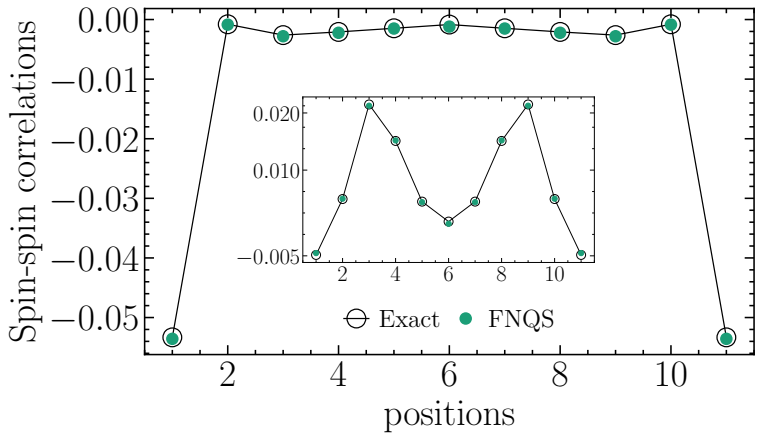

Figure 6.9.: Spin-spin correlations for the one-dimensional random-sign Heisenberg model [see Eq. (6.21)] on a chain of length $L = 12$. The FNQS is optimized simultaneously over $\mathcal{R} = 512$ disorder realizations and compared with exact diagonalization. The main panel shows the disorder-averaged spin-spin correlations, while the inset shows the correlations for a single disorder realization not included in the FNQS training set.

employed in the work are: $n_l = 6$ layers, $h = 14$ attention heads, and embedding dimension $d = 112$ (see Ref. [245] for more details about their role). The total number of variational parameters is $P = 793240$ for $L = 6$ and $P = 988120$ for $L = 14$. The FNQS state is optimized via Stochastic Reconfiguration (SR) [248, 262–264] for 10^4 steps, using a number of samples of $M = 6000$ configurations evenly distributed among $\mathcal{R} = 600$ disorder realizations used for training. The learning rate follows a cosine decay schedule with an initial value $\eta = 0.09$, and a diagonal shift parameter of $\lambda = 10^{-6}$ is used to regularize the inversion of the SR matrix (see Ref. [248]). To accelerate convergence in highly frustrated regimes, we employ a transfer learning protocol: the optimized parameters at a given p (e.g., $p = 0.9$) are used as initialization for nearby values (e.g., $p = 0.8$). We have verified that the final estimates of the order parameters are consistent with those obtained from longer simulations initialized from scratch.

6.8. One-dimensional Random-sign Heisenberg model

In this Section, we benchmark our method on the one-dimensional random-sign Heisenberg model

$$\hat{H} = \sum_{i=1}^{N} J_i \hat{\boldsymbol{S}}_i \cdot \hat{\boldsymbol{S}}_{i+1} \ , \tag{6.21}$$

where the couplings J_i take the values ± 1 with equal probability. This model has recently attracted renewed interest and has been investigated using different numerical approaches, including DMRG [240] and Quantum Monte Carlo [241]. As discussed in the main text, these studies reached different conclusions regarding the nature of the ground state. Here, we do not aim to settle this issue. Rather, we use small system sizes, for which exact diagonalization is available, to benchmark the FNQS approach and to test its generalization properties.

In Fig. 6.9, we compare spin-spin correlation functions (see definition in the main text) obtained with FNQS against exact diagonalization. The FNQS is optimized simultaneously over $\mathcal{R} = 512$ disorder realizations. In the main panel, we compare the disorder-averaged correlations with the exact average obtained by diagonalizing the Hamiltonian over all disorder realizations. In the inset, we instead consider a single disorder realization that was not included in the training set and compare the FNQS prediction with the corresponding exact result. In both cases, we find very good agreement between the variational and exact results.

This benchmark shows that FNQS can accurately describe the one-dimensional random-sign Heisenberg model and can generalize to unseen disorder realizations. Based on these small-cluster benchmarks alone, we do not aim to make a quantitative comparison with Quantum Monte Carlo in one dimension, where the absence of a sign problem allows simulations of very large system sizes [241]. Nevertheless, neural-network states are known to be very accurate for sign-problem-free systems [260], and the FNQS approach remains particularly promising because it provides an efficient way to treat disorder averages by optimizing simultaneously over many realizations. These results therefore indicate that FNQS may provide a useful complementary tool for future studies of this model, in particular for clarifying the nature of the ground state in regimes where different numerical approaches have led to apparently conflicting conclusions.

6.9. Edwards-Anderson Order Parameter in the J_1-J_2 Heisenberg model

In this Section, we use the J_1-J_2 Heisenberg model as a benchmark to test the behavior of the Edwards-Anderson order parameter Q (see definition in the main text) in a system where numerical evidence indicates the absence of magnetic order in the thermodynamic limit. The model is defined on an $L \times L$ square lattice with

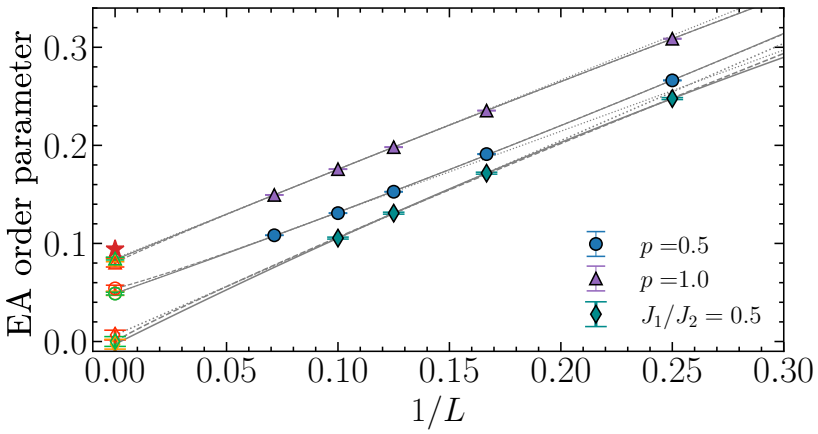

Figure 6.10.: Finite-size scaling of the Edwards-Anderson order parameter Q as a function of the inverse system size $1/L$. Quadratic (solid line and yellow markers) and power-law (dashed line and green markers) fits are performed over all data points, while a linear fit (dotted line and red markers) is applied to the last three points. Results are shown for the disordered Heisenberg model at $p = 0.5$ (blue circles) and $p = 1.0$ (purple triangles), and for the J_1-J_2 Heisenberg model at $J_2/J_1 = 0.5$ (green diamonds), with system sizes ranging from $L = 4$ to $L = 14$ (and up to $L = 10$ for the J_1-J_2 Heisenberg model). Error bars of the extrapolated thermodynamic values are obtained via a resampling procedure with Gaussian noise. The red star marks the extrapolated value at $p = 1.0$, corresponding to the square of the Néel magnetization of the Heisenberg model ($J_2/J_1 = 0$) in the thermodynamic limit, shown here for comparison.

periodic boundary conditions by the Hamiltonian

$$\hat{H} = J_1 \sum_{\langle i,j \rangle} \hat{\mathbf{S}}_i \cdot \hat{\mathbf{S}}_j + J_2 \sum_{\langle\langle i,j \rangle\rangle} \hat{\mathbf{S}}_i \cdot \hat{\mathbf{S}}_j \,. \tag{6.22}$$

We focus on the highly frustrated point $J_2/J_1 = 0.5$, where several numerical studies have reported the disappearance of Néel order and proposed a nonmagnetic ground state, possibly compatible with a gapless spin-liquid behavior [257, 258]. We stress, however, that the nature of the nonmagnetic phase of the J_1-J_2 Heisenberg model remains debated [257, 258, 264–266], and that we do not use this model as a definitive or archetypal realization of an algebraic spin liquid.

Rather, the purpose of this comparison is methodological. We want to verify that the neural-network variational approach can also describe a case in which the magnetic order parameter vanishes and the Edwards-Anderson order parameter does not extrapolate to a finite value. This provides a useful complementary benchmark to the disordered Heisenberg model studied in the main text, where the magnetic order parameter vanishes while Q remains finite in the thermodynamic limit.

For a translationally invariant periodic system, Q can be written as $Q^2 = \frac{1}{L^2} \sum_{\boldsymbol{r}} \langle \hat{\boldsymbol{S}}_{\mathbf{0}} \cdot \hat{\boldsymbol{S}}_{\boldsymbol{r}} \rangle^2$. If the spin-spin correlations decay algebraically at long distances, $\langle \hat{\boldsymbol{S}}_{\mathbf{0}} \cdot \hat{\boldsymbol{S}}_{\boldsymbol{r}} \rangle \sim \frac{1}{|\boldsymbol{r}|^{\eta+z}}$, with $\eta + z > 0$, then Q vanishes in the thermodynamic limit. For the J_1-J_2 model at $J_2/J_1 = 0.5$, previous numerical studies reported algebraic correlations with $\eta + z \approx 1.5$ [257], which are therefore consistent with $Q(L \to \infty) = 0$.

In Fig. 6.10, we compare the finite-size behavior of Q in three representative cases. For the unfrustrated Heisenberg antiferromagnet, $J_2/J_1 = 0$, Q extrapolates to a finite value related to the square of the Néel order parameter. For the frustrated J_1–J_2 model at $J_2/J_1 = 0.5$, Q decreases with system size and is consistent with a vanishing thermodynamic-limit value. By contrast, for the disordered Heisenberg model at $p = 0.5$, Q remains finite while the magnetic order parameter vanishes. This comparison shows that the finite value of Q found in the disordered case is not a generic artifact of the variational Ansatz, since the same numerical framework is able to reproduce a vanishing Q in a nonmagnetic benchmark system.

7. Localized spin waves and ergodicity restoring.

In this chapter, we further investigate the two-dimensional Heisenberg spin-glass model by means of the semiclassical expansion around classical states. We find that the nature of the spin-wave excitations, whether they are hydrodynamic or localized modes, depends crucially on the relevance/irrelevance – in the renormalization group sense – of the correlations induced by the underlying classical order in the spin-wave Hamiltonian matrix elements: low-energy excitations around magnetically ordered states are delocalized, whereas those around spin-glass ordered states are localized, albeit weakly. We interpret this phenomenology by relating the spontaneous breaking of spin-rotation symmetry in the original Heisenberg model to the symmetry and universality class of the resulting quadratic spin-wave Hamiltonian. We conjecture that the hydrodynamic picture can be recovered through the inclusion of interactions among the spin-wave excitations at higher order in the semiclassical expansion, favoring the onset of ergodic behavior.

7.1. Introduction

Understanding how ergodicity emerges in the presence of disorder in quantum systems represents a central and longstanding problem in modern condensed matter physics and it is at the heart of this thesis. Considering Heisenberg spin glasses (SG), since the seminal work of Halperin and Saslow [267], it is believed that hydrodynamics describes the low energy excitations, with Goldstone spin waves arising from the spontaneous breaking of the full $SO(3)$ symmetry group, in close analogy with the Heisenberg ferromagnet (FM) and antiferromagnet (AFM) [268]. In particular, the hydrodynamic theory predicts three polarizations for the spin waves, related to the fact all three generators of the rotational symmetry group are broken in a disordered spin-glass state. But hydrodynamics is rooted in the validity of ergodic dynamics close to an equilibrium state and, in particular in low dimensions, disorder is known to disrupt ergodicity in quantum systems through the mechanisms of Anderson Localization

(AL) and Many-Body Localization (MBL) [22, 269–271].

Localization phenomena are particularly striking in one and two dimensions, so the question arises: how can one assume the validity of hydrodynamics in presence of disorder in such systems? If, in some approximation, AL or MBL is at work, what is the way out? What are the timescales, if ever, on which hydrodynamics is valid?

To answer these questions, we further develop the semiclassical theory of the two-dimensional Heisenberg spin-glass model, that we discussed in the previous chapters. Remarkably, and similarly to what occurs in the case of the antiferromagnet [272–274], the leading order term in the $1/S$ expansion predicts the values of the order parameter within a few percent accuracy for $S = 1/2$. Besides validating the numerical evidence of a spin-glass phase in the ground state, this suggests that non-interacting spin-wave theory contains most of the information about the ground state of the model. The implications of this picture for dynamics and transport were not addressed in the previous chapter and we discuss them now.

Although the symmetry class of the quadratic spin-wave problem is easy to identify, the correlations in the Hamiltonian matrix elements prevent one from concluding anything *a priori* on its universality class, in the sense of the Altland-Zirnbauer (AZ) classification scheme [275]. These correlations arise from the minimum energy condition on the classical state around which the semiclassical expansion is performed and from the *bosonic* Bogoljubov-de Gennes structure of the Hamiltonian [218]. The main outcome of our analysis is that in the SG phase the whole spin-wave spectrum is weakly localized, as would happen for an uncorrelated random matrix theory with the same symmetries in $d = 2$, thereby hindering the definition of a wavenumber. We interpret this result in terms of renormalization group *irrelevance* of the correlations in the spin-wave Hamiltonian in the SG phase, and we contrast it to the case in which the underlying classical state is FM or AFM ordered. In the latter cases, we find a mobility edge in the spin-wave spectrum separating delocalized low-energy excitations from localized ones at higher energy, and therefore one cannot neglect the correlations induced by the underlying, polarized, classical state. The spin-wave localization in the SG phase has some important conceptual consequences. First, it means that the large part of the correction to the Edwards-Anderson order parameter found in [4] is not due to long-range correlations among linear spin-wave modes, which vanish in the thermodynamic limit, but rather to local rearrangements of the spin configuration from the classical state, due to quantum fluctuations. Second it means that, low energy modes at leading order in $1/S$, in two dimensions, where AL prevails, cannot be the basis of the delocalized hydrodynamic modes of Halperin and Saslow. One is led to conjecture then that to recover the Halperin and Saslow hydrodynamic prediction

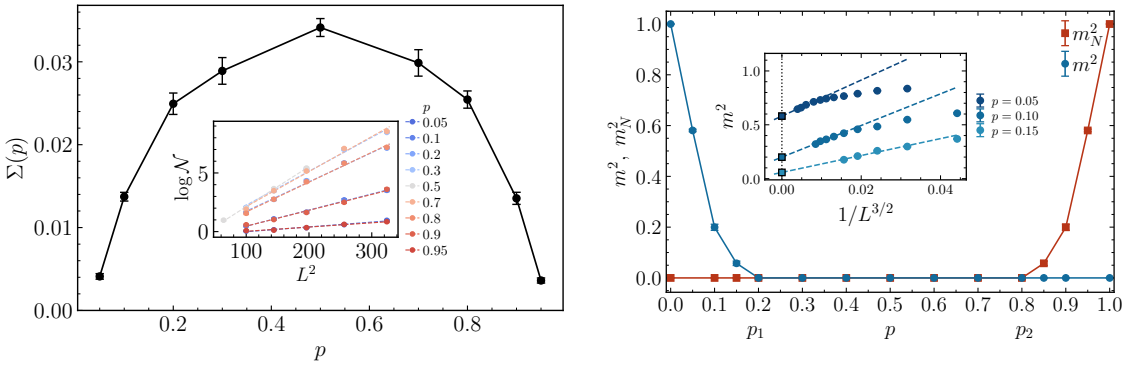

Figure 7.1.: Left panel: Quenched energy complexity $\Sigma(p)$ as a function of the antiferromagnetic bond concentration p. $\Sigma(p)$ is computed as the linear fit slope of the disorder-averaged logarithm of the total number of minima of the Hamiltonian $\mathcal{N}$ as a function of $N = L^2$, shown in the inset. **Right panel**: Magnetization magnitude m as function of p for different system sizes (colored points and dashed lines) and large L extrapolations (black points and continuous line). For each value of p, the extrapolated value of m is obtained with a second order fit in $1/L$, as shown in the inset.

in the thermodynamic limit, it is necessary to include interactions among the spin waves (naturally occurring at higher orders in the semiclassical expansion). The only mechanism which could prevent the onset of ergodicity in presence of interactions is MBL (even though this is thought not to exist in $d = 2$ [57, 160, 176, 178]) but we will see that the "upside-down" structure of the spectrum, with the localization length decreasing as the energy of the excitation increases prevents even from this possibility to take place. This chapter is organized as follows. We refer to the model discussed in the previous chapter. In Sec. 7.2, we describe the magnetic properties of the classical minima. In Sec. 7.3 we discuss the symmetries of the spin wave hamiltonian. The main results on the localization properties of the spin-waves are presented in Sec. 7.4 and discussed in the renormalization group and finite size scaling language. The role played by spin-wave interactions in recovering the hydrodynamics picture is discussed qualitatively in Sec. 7.5.

7.2. Classical minima

The classical energy function is given by Eq. (6.1), where the spin operators are replaced by three-dimensional vectors $\mathbf{S}_i$ of unit norm, $|\mathbf{S}_i|^2 = 1$. In order to find the classical minima, we adopt a mixed microcanonical-canonical Monte Carlo algorithm – known as *over-relaxation* – borrowed from [276], which combines gradient descent moves with energy conserving reflections, thereby enhancing a faster exploration of the energy landscape. The stationarity condition is given by $\mathbf{S}_i \propto \mathbf{h}_i$, where $\mathbf{h}_i =$

$-\sum_{j\in\partial i} J_{ij}\mathbf{S}_j$ are the local fields. The algorithm stops when the total misalignment between the spin and the local field configurations reaches a fixed threshold. As a final check, we verify that the Hessian matrix computed around the final configuration is positive semidefinite, as expected for a local minimum.

Since the algorithm tends to become trapped in local minima, it is restarted several times from random initial configurations, to which we will refer as *replicas*. Different replicas may end up in the same minimum depending on the size of its basin of attraction. We observe that the probability of finding a minimum is typically larger for low-energy minima. The global minimum is then found more frequently than any other state, so finding it is difficult only because of *entropic* reasons, since there is an exponential number of equilibrium states.

In the left panel of Fig. 7.1, the quenched energy complexity $\Sigma(p)$ is shown as a function of the antiferromagnetic bond concentration. $\Sigma(p)$ is defined as the logarithm of the *total* – *i.e.*, summed over all energy values – number of minima $\mathcal{N}(p)$ averaged over disorder realizations. To measure it, we limited this analysis to small system sizes ($L \leq 18$), where a sufficiently large number of replicas allows us to reliably sample all minima. We find that $\Sigma(p)$ is nonzero for all studied value of $p \in (0, 1)$. A more detailed analysis of the classical energy landscape is beyond the scope of this work and will be presented elsewhere [277]. Let us emphasize that even at small p, where the complexity is comparatively low, finding the global minimum remains challenging: for example, at $p = 0.05$, we find $\Sigma(p = 0.05) \simeq 0.004$, corresponding to order 10^6 minima already at $L = 60$. The situation becomes substantially worse at intermediate values of p, where the number of minima increases rapidly. Therefore, at the largest system sizes, no certificate of global optimality is available.

The most relevant property of the classical minima for the present analysis is whether they carry a magnetic signal. To characterize it, we measure the magnetization $\mathbf{m} = \frac{1}{N}\sum_i \mathbf{S}_i$ and the Néel order parameter $\mathbf{m}_N = \frac{1}{N}\sum_i (-1)^i \mathbf{S}_i$, averaged over disorder realizations. At the classical level, the value of the magnetization at p is expected to coincide with that of the Néel order parameter at $1 - p$ [1]. Having checked that this symmetry is satisfied by our minimum configurations, we only show the magnetization magnitude in the right panel of Fig. 7.1. The magnetization was already studied in Ref. [278], for system sizes up to $L = 20$ and a few disorder realizations. We find that the magnetization extrapolates to zero at $p = 0.2$. We also observe that the magnetization is approximately correlated with the energy of the minimum.

[1] One can obtain an AFM minimum of the classical energy from a FM one, by performing a staggered rotation, *i.e.* flipping all the spins on a sublattice, and changing sign to all the couplings, meaning that a minimum configuration at p corresponds to another one at $1 - p$. This symmetry is broken as soon as one takes $\hbar \neq 0$.

Consequently, if the optimization selects higher-energy minima at large system sizes, the true ground-state magnetization may be systematically underestimated.

At this point it is worth stressing that the robustness of the *classical* FM or AFM order against the addition of bond disorder in $d = 2$ is in fact a subtle issue, whose solution is not among the scopes of the present work. In fact, while it would be natural to assume that a $p_c > 0$ exists such that for $p < p_c$ the FM order is present, according to a comment by Villain in Ref. [279] (not brought up to a full argument in that paper and never mentioned again in the literature), a small density of defects can destabilize FM long-range order in two dimensions through the formation of dipolar distortions of the local spin orientation. However, even if this were the case, the associated magnetic domain size would diverge as $\ell \sim e^{c/p^2}$ and for $c = O(1)$ they would quickly become larger than the largest samples we considered between $p = 0.1$ and $p = 0.2$. Since we observe that for small enough values of p, the magnetization has an extremely slow dependence even when changing the system size by one order of magnitude (see the inset in the right panel of the Fig. 7.1), we believe that for all practical purposes the FM and AFM phases we observe can be considered as proper thermodynamic phases.

SG order, instead, is a proper classical, thermodynamic state, confined at $T = 0$. The Edwards-Anderson (EA) order parameter, defined as $Q^2 = \frac{1}{N^2}\sum_{ij}\left(\mathbf{S}_i \cdot \mathbf{S}_j\right)^2$, see *e.g.* [276, 280], extrapolates to 1/3 in the thermodynamic limit for any value of p for which the magnetic signal is absent [2]. We denote by p_1 and p_2 the two values of the antiferromagnetic bond concentration at which for the explored sizes the magnetic and, respectively, the Neél order parameter extrapolate to zero, while the EA parameter remains finite. From the inset of the right panel of Fig. 7.1, we have $p_1 \simeq 0.2$ and consequently $p_2 \simeq 0.8$. On the methodological side, deep in the SG phase, where the complexity is comparatively larger, which local minimum is selected to be the basis of the semiclassical expansion becomes less relevant, because the magnetization signal vanishes in all of them.

7.3. Symmetry class

Before discussing the symmetries of the spin-wave problem, let us first spend a few words on those of the classical states and discuss what one may expect from them regarding the low-energy excitations. In generic spatial dimensions, the symmetry breaking pattern of the Heisenberg model is $SO(3) \to SO(2)$ in the FM and AFM

[2] In fact,

$$\frac{1}{N^2}\sum_{i,j}\sum_{\alpha,\beta} S_i^\alpha S_j^\alpha S_i^\beta S_j^\beta = S^4 \sum_{\alpha,\beta}\frac{1}{3}\delta_{\alpha\beta}\frac{1}{3}\delta_{\alpha\beta} = \frac{S^4}{3}$$

	Classical state		SW Hamiltonian		
State	TRS	RRS	p	TRS	Charge
FM	No	$SO(2)$	0	Yes	$U(1)$
AFM	No	$SO(2)$	1	Yes	None
SG	No	None	$(0,1)$	No	None

Table 7.1.: Symmetry properties of the classical state for ferromagnetic (FM), antiferromagnetic (AFM), or spin-glass (SG) order and of the spin wave (SW) Hamiltonian for the clean FM/AFM case ($p = 0, 1$) and in presence of disorder ($p \neq 0, 1$). TRS denotes time-reversal symmetry; RRS stands for residual rotational symmetry in the classical state; charge refers to the possible global $U(1)$ particle number conservation in the spin-wave theory.

phases and $SO(3) \to O(1)$ in the SG phase. The Goldstone mechanism generates a number of gapless excitations that is related to the number of broken generators of the group. As is known, the AFM has two Goldstone modes with linear dispersion relation, while the FM has only one Goldstone mode with quadratic dispersion relation, in line with the correct Goldstone mode counting in non-relativistic theories [221–223]. From this argument, one would expect three linearly dispersing Goldstone bosons in the SG phase, coinciding with the hydrodynamic modes discussed by Halperin and Saslow [267]; however, it has to be noticed that a disordered state violates one assumption of the Goldstone theorem, by *completely* breaking translational invariance (TI), thereby impairing the very definition of a wavenumber.

Besides spin rotational symmetry, the classical state also breaks time reversal symmetry (TRS) in all three cases, since TRS acts on a spin by changing its sign [281]. We notice that the *clean* antiferromagnet ($p = 1$) is peculiar for this symmetry, since TRS is microscopically broken for the Néel state, but can be recovered in combination with lattice translations.

Let us now discuss the symmetries of a generic non-collinear and non-interacting bosonic Hamiltonian. The matrix elements defined in Eqs. (5.38) satisfy $A_{ij} = A^*_{ji}$ and $B_{ij} = B_{ji}$, implying $\hat{H}_{SW} = \hat{H}^\dagger_{SW}$. Besides being hermitian, the Hamiltonian is invariant under charge conjugation

$$\gamma K \hat{H}_{SW} K^{-1} \gamma^{-1} = \hat{H}_{SW} \,, \tag{7.1}$$

where K is the operator implementing complex conjugation. This symmetry is characteristic of Bogoljubov–de Gennes Hamiltonians, a notable example of which arise in the study of (disordered) superconductors with the pairing treated in the mean-field approximation [216, 218, 282, 283], the key difference here being the *bosonic* nature of the degrees of freedom.

We notice that the structure of the matrix elements of $\hat{H}_{SW}$ is directly tied to

the underlying classical spin configuration. In particular, when two neighboring spins are non-collinear in the classical state – which happens for all values of $p \neq 0, 1$ – the corresponding matrix element acquires a complex phase. As a consequence, the Hamiltonian is not invariant under complex conjugation alone, *i.e.* $K\hat{H}_{SW}K^{-1} \neq \hat{H}_{SW}$, and TRS is explicitly broken. By contrast, in the *clean* limits where the classical configuration is fully polarized (*i.e.* all spins are collinear), all matrix elements are real and TRS is preserved. From these considerations, we conclude that the model we are studying has the symmetries of class D in the Altland-Zirnbauer (AZ) classification scheme [275, 284].

However, it has to be noticed that this does not mean that the spin-wave problem is in the same universality class, since AZ classes comprise *random matrices with uncorrelated entries*, as the more traditional Wigner-Dyson ones [285]. The Hamiltonian in Eq. (5.37) has instead correlated random elements, due to the fact that it has been obtained by expanding around a minimum. A first source of correlations is the positive-definiteness of $\hat{H}_{SW}$, as always is for generic bosonic systems [218]. Most importantly, the matrix elements of A and B carry within their correlations the local structure of the classical minimum, which is encoded in the local rotation matrices R_i appearing in Eq. (5.35).

We conclude this section by reminding the reader that $B = 0$ for the clean ferromagnet ($p = 0$), leading to a $U(1)$ invariant $\hat{H}_{SW}$. The particle number conservation in the pure ferromagnet is what makes this case exceptional and is related to the fact that the order parameter is itself a constant of motion, *i.e.* $[\hat{H}, \hat{\mathbf{S}}^z] = 0$, where $\hat{\mathbf{S}}^z$ is the z-component of the total spin. As a consequence, the classical order is protected by this symmetry and receives no corrections from quantum fluctuations. In terms of the position and momentum variables $\hat{x}_i$ and $\hat{p}_i$ introduced before, $B = 0$ means that there is no direct coupling between $\hat{x}_i$ and $\hat{p}_i$, and the Hamiltonian can be diagonalized by a simple Fourier transformation.

The discussion about the symmetries of the classical state and of the spin-wave Hamiltonian is summarized in Table 7.1.

7.4. Localization of the spin waves

In this section we study the localization properties of the spin waves. This is the central result of this Chapter, which can summarized as follows: despite the symmetry class being the same (D in the AZ classification scheme), the correlations of the underlying classical state make the localization properties completely different for the three different phases: FM, SG, and AFM.

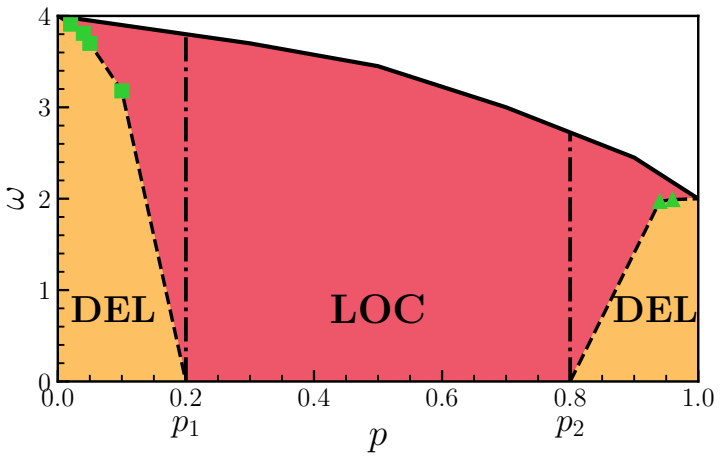

Figure 7.2.: Phase diagram of the spin-wave Hamiltonian. The continuous lines mark ground state transitions between the FM/AFM phases to the SG phase in the classical solution. The dashed lines mark a mobility edge between localized and extended regions inside the ordered phases. The points correspond to the mobility edge $\omega_c(p)$, as computed in Appendix 7.8.2.

For a classical SG state the whole excitation spectrum is localized, albeit *weakly*, according to the naive expectation in $d = 2$. For classical FM and AFM states, for $p < p_1$ or $p > p_2$, the signal of the magnetization and of the Néel order parameter respectively create a delocalized region at low energy. There is a *mobility edge* $\omega_c(p)$, such that modes with energy $\omega < \omega_c(p)$ are delocalized, while modes with energy $\omega > \omega_c(p)$ are localized. The dynamical phase diagram of the model is sketched in Fig. 7.2. It is important to stress that this is the opposite of what happens in the Anderson model, where the localized states are at *lower* energies. This is a manifestation of Goldstone's theorem and is important when one introduces interactions among the spin waves. We will give a qualitative description of the effect of the interactions in Sec. 7.5. The presence of a mobility edge in the low-energy excitation spectrum of a disordered model was already discussed in Ref. [286].

There is a simple, heuristic argument in support of this observation regarding why higher energy modes "feel" a stronger disorder. At any fixed p, for any wavelength λ of the spin wave, we can think of coarse-graining the system to lengths of $O(\lambda)$, below which the wave cannot resolve details (see Fig. 7.3). In this way, the effective fields acting on the effective spins in a box $B(\mathbf{r}, \lambda)$ of size λ, around the point $\mathbf{r}$ are random vectors $\mathbf{h}(\mathbf{r}, \lambda) \simeq \sum_{i \in B(\mathbf{r},\lambda)} \mathbf{h}_i$. Remembering that $\mathbf{h}_i \propto \mathbf{S}_i$ of the classical solution, in the SG phase these contributions are random, with average zero and amplitudes $h(\lambda) \sim \Delta h \sqrt{\lambda^2}$, where Δh^2 is the variance of the microscopic disorder strength, and

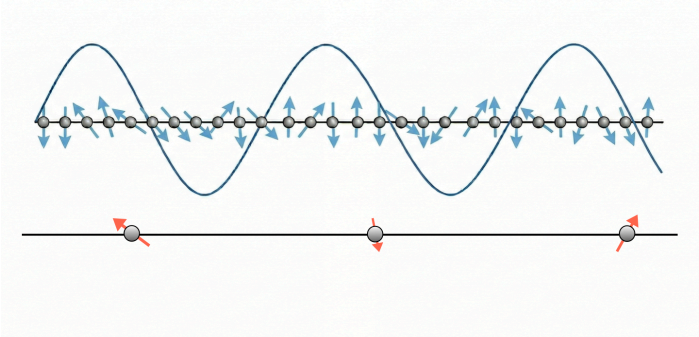

Figure 7.3.: Coarse graining the underlying classical spin system to long wavelengths λ reduces the local random fields by a factor of $1/\sqrt{\lambda}$ for every spatial dimension. In $d = 2$ the reduction is $1/\lambda$.

$\Delta h^2 \propto J^2$, *i.e.* the variance of the random coupling distribution. However, the effective spin grows like λ^2, which is the number of spins in the block [3]. We see then that the effective disorder is $W \sim J\lambda^{-1}$. Since the dispersion relation of the spin waves in the SG phase is $\omega \propto J\lambda^{-1}$ (again following [267]), the disorder "felt" by a wave is exactly proportional to the frequency of the wave, $W \propto \omega$. Similar considerations made for FM and AFM states need to take into account the fact that the underlying classical spin configuration is correlated to give a signal $\sum_i \mathbf{h}_i \propto \mathbf{m}$ and $\sum_i (-1)^i \mathbf{h}_i \propto \mathbf{m}_N$, which are both proportional to λ^2 and not $\sqrt{\lambda^2}$.

Summarizing, we expect the low-energy excitations of FM and AFM states to be as delocalized as their clean counterparts ($p = 0, 1$), while those of SG states to suffer from the presence of a disorder proportional to their frequency.

7.4.1. Observables

To characterize localization properties, we consider two standard observables, one based on spectral statistics and the other one on eigenstate properties, both normalized to take values in the interval $[0, 1]$.

As a spectral probe, we employ the rescaled r-parameter, that was defined in 7.2 . Averaging over small energy windows $[\omega, \omega + \Delta\omega]$ and disorder realizations at a given size L yields the mean value $r(\omega, L)$. This quantity takes universal values in the thermodynamic limit depending on the nature of the spectrum. For uncorrelated (Poisson) statistics, characteristic of localized systems, one finds $r_{\mathrm{P}} = 2\ln 2 - 1 \simeq 0.386$. By contrast, for chaotic systems described by random matrix theory in the Gaussian Unitary Ensemble (GUE), one obtains $r_{\mathrm{GUE}} \simeq 0.5996$ [287], which also corresponds to the

[3] The effective spin does not correspond to the coarse graining of a (disordered) spin configuration, but of the spins as *dynamical* variables, canonically conjugated to the rotation field. As such, each spin in a box of size λ gives to the effective field an $O(1)$ contribution.

ergodic fixed point value for systems in the AZ class D. For convenience, we introduce the rescaled quantity

$$\phi = \frac{r - r_{\mathrm{P}}}{r_{\mathrm{GUE}} - r_{\mathrm{P}}} \,, \tag{7.2}$$

which interpolates between $\phi = 0$ in the localized (Poisson) limit and $\phi = 1$ in the fully ergodic (GUE) regime.

As an eigenstate-based diagnostic, we consider the fractal dimension D [270], defined as

$$D = \frac{\partial S}{\partial \ln L^2} \,, \tag{7.3}$$

where S denotes the participation entropy, which will be defined shortly. For non-interacting systems, this quantity captures how broadly a given eigenmode is distributed in space (*i.e.* over the lattice), and is therefore sensitive to localization properties. In the present setting, however, its definition requires additional care due to the Bogoljubov structure of the eigenmodes. In fact, one must keep in mind that Bogoljubov modes are described by two-component vectors living in a space with double the sites of the lattice, corresponding to non-commuting degrees of freedom (*e.g.*, $\hat{x}_i$ and $\hat{p}_i$). Therefore, they cannot be naively interpreted as standard single-particle wavefunctions, whose square yields a well-defined probability according to the Born rule [4]. As a consequence, defining a properly normalized spatial distribution – commonly employed to characterize eigenstate localization in non-interacting systems becomes nontrivial. To circumvent this issue, we adopt a physically motivated definition based on the local increase of the oscillator *action*. Specifically, we define the quantity

$$R_\alpha(i)^2 = \mathcal{R}_\alpha^{-1} \left(\langle \alpha | \hat{a}_i^\dagger \hat{a}_i | \alpha \rangle - \langle 0 | \hat{a}_i^\dagger \hat{a}_i | 0 \rangle \right) , \tag{7.4}$$

which measures the increase in the action of the oscillator $\hat{a}_i$ (in units of $2\pi\hbar$), due to the creation of a quasiparticle mode $|\alpha\rangle = \hat{b}_\alpha^\dagger |0\rangle$ of energy ω_α. The normalization factor $\mathcal{R}_\alpha$ is chosen such that $\sum_i R_\alpha(i)^2 = 1$, ensuring that $R_\alpha(i)^2$ can be consistently interpreted as a spatial weight associated with the mode α. In Appendix 7.8.1 we derive two complementary expressions for this quantity: one in terms of the position and momentum variables, $\hat{x}_i$ and $\hat{p}_i$, which provides a natural interpretation of $R_\alpha(i)^2$ as an increase in the action; the other in terms of the eigenstate components X and Y, defined in Eqs. (5.46), which is used for the numerical evaluation of $R_\alpha(i)^2$. We

[4] From this point of view, Bogoljubov modes resemble many-body wavefunctions living in the Fock space, and this reflects the absence of particle number conservation. In fact, the same difficulties in studying eigenstate localization in real space also are found in the many-body case, even if in that case they are more severe.

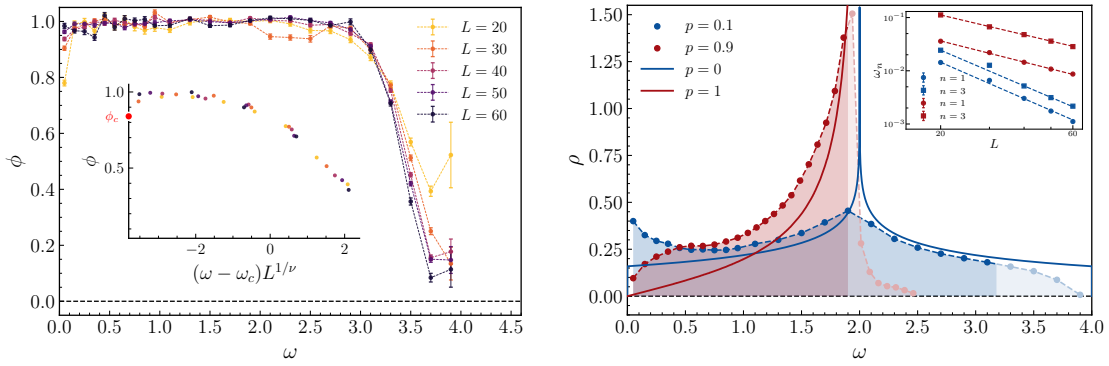

Figure 7.4.: Left panel: Rescaled r-parameter ϕ, Eq. (7.2), averaged over ~ 1000 disorder realizations at $p = 0.1$, with FM signal. There is a critical energy ω_c separating low-energy delocalized from high-energy localized modes. The inset contains a data collapse obtained with $\nu = 2.1$ and $\omega_c = 3.18$, yielding a $\phi_c = 0.84$. **Right panel**: Density of states for two different values of antiferromagnetic bond concentration, $p = 0.1$ and $p = 0.9$ (points and dashed lines), compared to their clean counterparts, $p = 0$ and $p = 1$ (continuous lines, computed analytically). Data pertains to the largest simulated size, $L = 60$, and is averaged over ~ 1000 disorder realizations. Different filling colors distinguish delocalized modes (darker) from localized ones (lighter). The scaling of the averaged n-th lowest eigenvalue with system size is shown in the inset. The values of the dynamical critical exponent z extracted respectively for $n = 1$ and $n = 3$ are: $z = 2.27(5), 2.25(3)$ at $p = 0.1$, and $z = 1.21(2), 1.23(1)$ at $p = 0.9$.

can now define the participation entropy of an excitation α as

$$S_\alpha = -\sum_i^N R_\alpha(i)^2 \ln R_\alpha(i)^2, \tag{7.5}$$

and, after averaging over states in small energy windows $[\omega, \omega + \Delta\omega]$ and disorder realizations, we get the entropy $S(\omega, L)$ and the fractal dimension $D(\omega, L)$ accordingly. In the case of magnon excitations for clean FM and AFM states, this definition gives $D(\omega, L) = 1$, therefore characterizing a fully ergodic excitation.

7.4.2. Ferromagnetic and antiferromagnetic phases: delocalization at low energies

As discussed before, the spin excitations in the FM and AFM phases show a mobility edge. This is characterized by a critical energy $\omega_c(p)$ which vanishes as $p \to p_1$ or p_2. At first sight, this appears to be in contradiction with the AZ classification, which assigns the system to class D. Indeed, bosonic class D systems are always localized in $d = 2$. This apparent discrepancy is resolved by noting that the coefficients of the quadratic expansion in Eq. (5.37) are not *iid* random variables. Indeed, these

coefficients, among other things, encode the presence of a finite magnetization (or Néel magnetization) in the underlying classical state. The existence of a preferred direction of spontaneous magnetization implies that an effective $SO(2)$ rotational symmetry is preserved at long wavelengths, thereby qualitatively modifying the localization properties of the low-energy excitations.

In a localization transition the system becomes scale invariant at the critical energy ω_c. The critical exponent ν controls the scaling, the localization length diverges as $\xi \sim (\omega - \omega_c)^{-\nu}$ and its value is universal and fixed only by symmetry and effective dimensionality, related to the value of p. For $p = 0.1$, we numerically extract both the critical value ω_c and the exponent ν. This analysis performed on the rescaled r-parameter ϕ is shown in the left panel of Fig. 7.4. We perform a data collapse to find the best values of (ω_c, ν): computing the reduced χ^2 for several fitting functions and defining the confidence interval as the fits whose χ^2 is lower than $1.05\chi^2_{min}$, we find $\omega_c \in [3.14, 3.24]$ and $\nu \in [1.8, 2.5]$. Other values of p are discussed in Appendix 7.8.2.

In recent studies [147, 288] a *super-universal* scaling relation between the critical values of the r-parameter and the fractal dimension in Anderson models has been conjectured, for both GUE and GOE (Gaussian Orthogonal Ensemble) symmetry classes. We check if this relation also holds in the present case for $p = 0.1$, where we find $r_c \simeq 0.57$ (corresponding to $\phi_c \simeq 0.84$ in Fig. 7.4) and $D_c \simeq 0.75$, matching the prediction in figure 5 of [288]. The value of the critical point D_c is estimated with the same procedure as for ϕ_c. The details are given in Appendix 7.8.2. This result is remarkable, considering that our system belongs to a different symmetry class with respect to GOE and GUE, *i.e.* bosonic AZ class D, in which the definition of the fractal dimension is affected by the issues discussed above.

In the right panel of Fig. 7.4, the densities of states in the FM state at $p = 0.1$ and in the AFM state at $p = 0.9$ are compared with their clean counterparts. Despite belonging to the same symmetry broken phase, data suggest that low-energy properties of the weakly disordered systems are different from those of the clean ones. In particular, the presence of disorder induces a decrease of the dispersion relation, leading to an abundance of low-energy modes, according to the relation $\rho(\omega) \propto \int d^2k\ \delta(\omega - k^z)$, where z is the dynamical exponent [5]. Although the system is not TI, one can define a dispersion relation $\omega \sim k^z$, in terms of a quasi-momentum k, and relate this to the scaling of system size $\omega \sim L^{-z}$. In the inset of Fig. 7.4, we show the scaling of the low-energy modes and extract the dynamical critical exponent. While only two eigenvalues are displayed, we have verified that the entire low-energy sector scales with the

[5] Notice: this is just a proxy of z, whose correct value can be extracted from the correlation functions as a function of time. This is beyond the scope of this work and is left for following research.

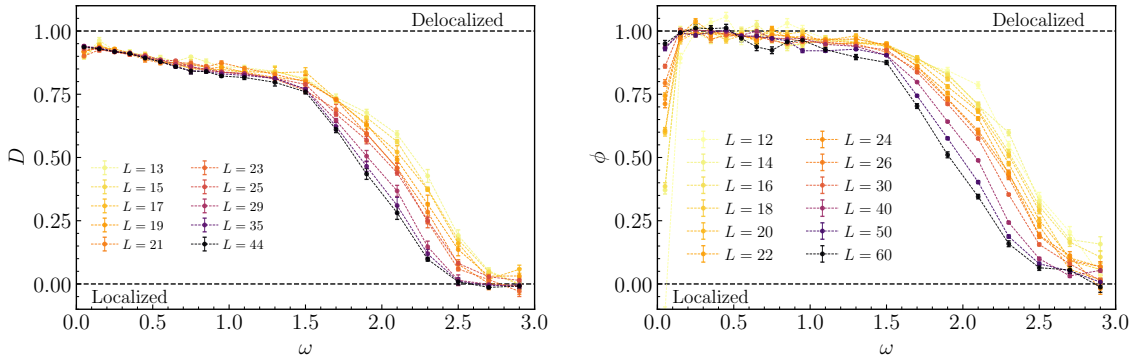

Figure 7.5.: Left panel: Fractal dimension, defined in Eqs. (7.3-7.5), in the SG phase for $p = 0.5$ averaged over ~ 1000 disorder realizations. The values of L in the legend correspond to the geometric mean of the sizes in each block, where D is computed through a linear fit of the participation entropy (see Appendix 7.8.3 for more details). **Right panel**: Rescaled r-parameter ϕ, Eq. (7.2), in the SG phase for $p = 0.5$, averaged over ~ 1000 disorder realizations. In both panels data are shown as a function of the energy ω for various system sizes.

same exponent: $z \simeq 2.26$ for $p = 0.1$ and $z \simeq 1.23$ for $p = 0.9$. Notably, these values exceed those of the clean systems, indicating sub-diffusive transport in the FM phase (clean FM, $z = 2$) and sub-ballistic transport for the AFM (clean AFM, $z = 1$). As we discuss in Sec. 7.5, interactions are expected to restore the standard hydrodynamic behavior.

7.4.3. Spin glass phase: Renormalization group scaling

In the spin-glass phase, for $p \in (p_1, p_2)$, the spin-wave excitations are fully localized. However, this localization is *weak*, in the sense that strong finite-size effects (logarithmic in system size) persist and simple diagnostics are not sufficient to capture the scaling behavior. For this reason, it is useful to adopt a more systematic framework based on scaling theory.

A powerful approach to Anderson localization (AL) is provided by the *one-parameter scaling* hypothesis [24], which organizes the dependence of physical observables on the system size. This framework has been successfully applied in all finite spatial dimensions d [148], and only breaks down in the limit $d \to \infty$, which is the case of expander graphs [147]. More recently, the same ideas have been extended to many-body systems [3, 5], where they helped systemize the finite-size effects which have puzzled researchers to the point of leading some of them to suggest MBL might actually not exist even in one dimensional models [6], but see also [45, 46] for the connections with

[6] To cut a long story short, we consider the situation settled by the theorems of [289] based on the work [175]

the perturbation theory of [269].

The central assumption of one-parameter scaling is that, *in the scaling limit* (*i.e.* for sufficiently large system sizes), the behavior of the system is controlled by a single parameter. In the renormalization group language, this corresponds to the existence of a single relevant operator. One can take as such the dimensionless conductance g [24] (with $g \to \infty$ in the ergodic phase and $g \to 0$ in the localized phase) or its inverse $t = 1/g$ [270] and write the beta function as

$$\beta_t = -\frac{dt}{d\ln L^2} \,, \tag{7.6}$$

where L is the largest scale in the problem (*i.e.* the system size). In the present case, which falls in the AZ symmetry class D, the conductance is the thermal one, since the particle number is not conserved, *i.e.* there is no electric charge. A key consequence of the one-parameter scaling hypothesis is that any observable in the scaling regime must be a smooth function of t, and, similarly, different observables must be analytically related to each other. We can then study the β function of any of such quantities, and obtain any other by a change of variables (with the appropriate Jacobian).

In absence of – or on the irrelevance of – the correlations in the matrix elements of the Bogoljubov-de Gennes Hamiltonian, we can expect that the phenomenology is that of symmetry class D. In $d = 2$, the β function for class D systems is always negative, reflecting the fact that these systems are localized even at infinitesimal disorder, and it approaches zero in the limit of vanishing inverse conductance, $t \to 0$. In particular, the prediction of the $2 + \epsilon$ expansion in the non-linear sigma model describing class D systems is: $\beta_t \sim -t^{\alpha_t}$, with $\alpha_t = 2$, for $\epsilon = 0$ [270], similar to the Anderson model in $d = 2$ with GOE symmetry class.

While t is the natural scaling variable to compare with field theoretical predictions, it is not directly accessible in our numerics. Instead, we measure the scaling variables D and ϕ, which are shown in Fig. 7.5, and whose beta functions are defined as

$$\beta_D = \frac{d\ln D}{d\ln L^2} \,, \qquad \beta_\phi = \frac{d\ln \phi}{d\ln L^2} \,. \tag{7.7}$$

However, we do not know what the relationship between the scaling variables D, ϕ and the inverse conductance t is. For the Anderson model in $d = 2$ it was argued in [148] (and amply supported numerically) that, close to the ergodic fixed point, as $t \to 0$ and $D \to 1$, then $1 - D \sim t$, thereby implying $\alpha_D = 2$. We will check whether the present case is compatible with this scenario in a moment.

Let us first introduce a set of reasonable assumptions that will serve as an inter-

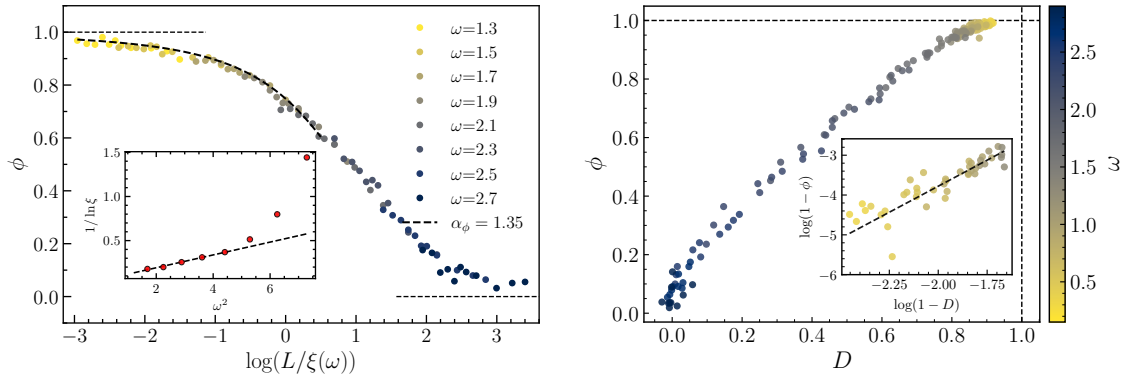

Figure 7.6.: Left panel: Data collapse of the rescaled r-parameter ϕ, Eq. (7.2). Each color corresponds to a different value of the energy ω. The black dashed curve is obtained by inverting Eq. (7.11) at leading order: $(1-\phi)^{1-\alpha_\phi} \sim \ln(L/\xi)$ with $\alpha_\phi = 1.35$, in order to find $\phi(\ln L/\xi)$. The inset shows the scaling of the localization length with energy, which follows the relation $\xi \sim e^{\omega_0^2/\omega^2}$, with $\omega_0 = 3.7(1)$. **Right panel**: Rescaled r-parameter ϕ as a function of the fractal dimension D. The points aligning on a single curve is a validation of the one-parameter scaling hypothesis. Inset: log-log fit of $1-\phi$ vs $1-D$ near the ergodic fixed point. The slope of the fit yields a value of the exponent γ defined in the text: $\gamma = 2.6(3)$, with an intercept 4.3(5).

pretative framework for our numerical results. A minimal hypothesis is that also β_D and β_ϕ have power law behaviors near the ergodic fixed point:

$$\beta_D \sim -(1-D)^{\alpha_D} , \qquad D \sim 1 , \tag{7.8a}$$

$$\beta_\phi \sim -(1-\phi)^{\alpha_\phi} , \qquad \phi \sim 1 , \tag{7.8b}$$

with some universal exponents α_D and α_ϕ. Moreover, we assume that in the same scaling regime the two observables D, ϕ are related as

$$1-\phi \sim (1-D)^{\gamma} , \tag{7.9}$$

for some exponent $\gamma > 1$, possibly non-integer. In that case, the relationship between the β functions of D and ϕ is simple and one can easily derive an equation connecting the three exponents α_D, α_ϕ and γ:

$$\frac{\alpha_D}{\gamma} = \frac{1}{\gamma} - 1 + \alpha_\phi . \tag{7.10}$$

We plan to test this relations with the values of the exponent extracted from our numerics.

Let us now turn to the numerical analysis. First, we directly extract β_D (see Appendix 7.8.3) and find that α_D is compatible with the value $\alpha_D = 2$. Next, we

estimate α_ϕ by integrating the flow equation for ϕ near the ergodic regime, *i.e.* for $\phi \sim 1$, see Eq. (7.8b):

$$2\ln(L/L_0) = \int_{\phi(L_0)}^{\phi(L)} \frac{d\phi}{\phi\beta_\phi} \sim \frac{(1-\phi)^{1-\alpha_\phi}}{1-\alpha_\phi} F(1,\, 1-\alpha_\phi;\, 2-\alpha_\phi;\, 1-\phi)\Big|_{\phi(L_0)}^{\phi(L)} , \tag{7.11}$$

and fitting the data as a function of $\ln(L/\xi)$ with the functional form above, where F is the Gauss hypergeometric function and ξ is defined in such a way as to absorb all the dependence on L_0 and $\phi(L_0)$. We obtain a good data fit for values of α_ϕ in the interval $[1.2, 1.5]$. In Fig. 7.6 we plot the scaling of the variable ϕ and the theoretical curve obtained by inverting Eq. (7.11) at leading order for $\alpha_\phi = 1.35$. For bosonic random systems in two dimensions it is expected that the localization length diverges as $\xi \sim e^{\omega_0^2/\omega^2}$, for $\omega \to 0$ [218, 290]. In the inset of Fig. 7.6 (left panel), we verify this scaling and extract the value of ω_0, which turns out to be $\omega_0 = 3.7(1)$. Finally, we study the relation between ϕ and D, shown in the right panel of Fig. 7.6, and extract the exponent γ as the slope of the logarithmic fit of $1-\phi$ vs $1-D$ (shown in the inset), finding $\gamma = 2.6(3)$. By using this value of γ and $\alpha_D = 2$ to compute α_ϕ through Eq. (7.10), we obtain $\alpha_\phi \in [1.3, 1.4]$, which is compatible with the interval estimated directly from the data for ϕ. This provides a validation of the one-parameter scaling relation in Eq. (7.10) and confirms the belonging of the model in the SG phase to the AZ class D.

7.4.4. Renormalization group scaling around the critical points

The RG analysis performed in the previous section can be extended to FM/AFM states, where, as discussed above, the correlations induced in the Hamiltonian matrix elements by the residual $SO(2)$ symmetry of the classical state lead to a delocalization transition in the lower part of the spectrum. In this case the beta function must have a zero in a finite value D_c and an attractive ergodic fixed point. To capture this phenomenology, we make the simplest assumption on the beta function form for FM/AFM states, close to the critical points:

$$\beta_D \simeq -c_1(1-D)^2 + c_2\frac{p_c - p}{p_c}(1-D) , \tag{7.12}$$

where $p_c = p_1$ or p_2 and c_1 is the coefficient of the beta function in the SG phase, which we assume to be independent of $p \in (p_1, p_2)$. By using the values: $c_1 = 1.3(1)$

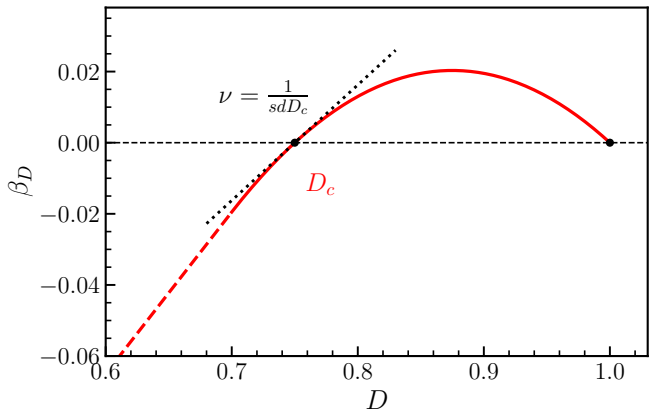

Figure 7.7.: Plot of the one-parameter scaling β function for the FM at $p = 0.1$, see Eq. (7.12). The critical exponent ν is inversely proportional to the slope s of the β function at the critical point.

at $p = 0.5$ (see Appendix 7.8.3) and $p_c = p_1 \simeq 0.2$, we solve the equation $\beta_D = 0$ for $p = 0.1$ and $D_c \simeq 0.7$ and extract the coefficient $c_2 = 0.60(5)$. From this, we can compute the critical exponent ν as [148]: $\nu = 1/(sdD_c)$, where $d = 2$ and $s = c_2 \frac{p_c - p}{p_c}$ is the slope of the beta function in $D = D_c$ (which coincides with the slope in $D = 1$, by symmetry). We find a value of $\nu = 2.0(2)$, compatible with the one extracted from the data of ϕ, see Fig. 7.4. This is an important consistency check of our numerical analysis. With these values of the coefficients c_1 and c_2, we plot the beta function for $p = 0.1$ in Fig. 7.7.

7.5. $1/S^{3/2}$ corrections and restoration of ergodicity

We have seen in the previous sections that the $1/S$ expansion to lowest order gives a mobility edge separating delocalized and localized excitations in the FM and AFM states, and a fully localized excitation spectrum in the SG phase. Upon the introduction of J/S corrections, which act as interactions between the spin waves, the three kinds of order behave in different ways.

While we do expect that the FM and AFM states will go quickly to ergodicity on local timescales $\tau \sim S/J$, with possibly some patches of relatively slow dynamics coming from the high-energy localized modes, the situation is completely different in the SG phase. The whole spectrum is localized, albeit weakly, and the interaction should first overcome the localization of the noninteracting modes to restore ergodicity. This situation is parallel to that encountered in Basko, Aleiner, and Altshuler (BAA) [269] and in [45] except for one fundamental difference: there can be no upper

bound to the localization length $\xi(\omega)$ as function of the mode energy ω. This is a fundamental property of the Goldstone modes, which changes the picture completely. In this section, which is the only speculative part of this paper, we shall picture the consequences of the interactions between the modes, which will be present in the full $S = 1/2$ Heisenberg model and, consequently, in experiments.

The interaction terms, in units in which the quadratic Hamiltonian is $O(S^0)$, are of the form

$$\hat{H}_3 \sim \sum_{i,j} \frac{J}{\sqrt{S}} \hat{a}_i^\dagger \hat{a}_i \hat{a}_j^\dagger + \text{h.c.} \,, \tag{7.13}$$

where i, j are nearest neighbors on the lattice. After passing to the Bogoljubov modes $\hat{b}_\alpha$ this becomes

$$\hat{H}_3 \sim \frac{J}{\sqrt{S}} \sum_{\alpha,\beta,\gamma} M_{\alpha,\beta,\gamma} \hat{b}_\alpha^\dagger \hat{b}_\beta^\dagger \hat{b}_\gamma + \text{h.c.} \,, \tag{7.14}$$

where the tensor element $M_{\alpha,\beta,\gamma}$ contains the information on the mode structure and can be written in terms of the Bogoljubov matrices X, Y.

If all the modes were localized by a localization length $\xi = O(1)$ (*i.e.* if there is an upper bound to the localization length $\xi(\omega)$) then this processes could be treated perturbatively and, in the approximations of [45, 269], one could argue for an MBL phase (however all the caveats of dealing with $d = 2$ apply [57, 160, 176, 178]). If this were the case, only a subtle, non perturbative effect $O(e^{-S})$ would restore ergodicity and hydrodynamics. However, if there is no upper bound and $\xi \sim e^{\omega_0^2/\omega^2}$ for small ω, this argument cannot be used.

In the present case, the situation is much more similar to the following scenario. The single-particle spectrum is split in two by an energy ω_c: the states with $\omega > \omega_c$ are localized with localization length ξ, and the states with $\omega < \omega_c$ are *effectively* delocalized spin waves. For example one can take ω_c such that $\xi(\omega_c) = L$, the system size. This would give $\omega_c = \omega_0/\sqrt{\ln L}$, with $\omega_0 \simeq 3.7$ from the numerics. We make a little error, if any, to consider this a simple quantity of $O(1)$, independent of L. For example for $L = 100$, $\omega_c \simeq 1.7$ and for $L = 10^6$, $\omega_c \simeq 1.0$. Using the data in Fig. 7.8, this corresponds to a fraction of localized excitations $P \simeq 2/3$ and delocalized excitations $1 - P \simeq 1/3$. In the following, we will refer to the delocalized excitations as spin waves, and to the localized ones as localized states. Moreover, for simplicity, we will assume that the delocalized modes are simple plane waves with some momentum $\mathbf{q}$ and energy $\omega(q)$.

By classifying the modes $\alpha \in \mathcal{L}$ or $\alpha \in \mathcal{D}$ (whether their localization length is smaller or larger than the system size L) we have now different possible cases which need to be treated (see Fig. 7.9).

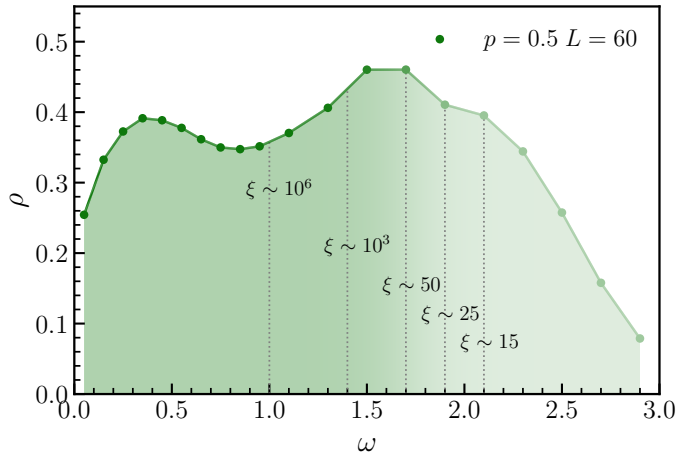

Figure 7.8.: Density of states at $p = 0.5$, $L = 60$. The shading represents the finite size crossover between localized and delocalized states. A darker color marks a finite size extended state, where $\xi_{loc} \geq 60$ which is the largest system size explored in this paper. The dashed vertical lines are the finite size crossover points, identified by $\xi_{loc} = L$.

If the α, β, γ modes are $\mathcal{L}$, as we said above, we are back in a BAA/MBL scenario where ergodicity cannot be restored, or if it does, the reason is the dimensionality of space [291, 292]. If the α, β, γ modes $\in \mathcal{D}$ then this is a typical matrix element of spin-wave interactions and it will restore ergodicity among the spin waves quickly, on timescales $O(S)$. This process is similar to what happens in phonon down-conversion processes due to interaction and it has been studied at length in the past (see [293], in particular Chapter 3 by Y. B. Levinson).

If $\alpha \in \mathcal{L}$ and $\beta, \gamma \in \mathcal{D}$ then we have the decay of a single localized mode into two spin waves. This can happen for all α such that $\omega_c < \omega_\alpha < 2\omega_c$, and the spin autocorrelation function decays exponentially on timescales $O(S)$. The effective matrix element contains also some $\mathbf{Q} = \mathbf{q}_\beta + \mathbf{q}_\gamma$ dependence, and it decays as $Q\xi \gg 1$.

The last channel is when $\alpha, \beta \in \mathcal{L}$ and $\gamma \in \mathcal{D}$. In this case the matrix element is

$$M_{\alpha,\beta,\gamma} \sim e^{-|\mathbf{r}_\alpha - \mathbf{r}_\beta|/\xi}/\sqrt{V}, \tag{7.15}$$

where the $\mathbf{r}$'s are the centers of localization (again dropping terms containing $q_\gamma \xi$). This channel is the only one open if the energy of the initial localized state is higher than $2\omega_c$. In this way, a localized state α can "decay" into a neighboring localized state β, by emitting a spin wave of energy $\omega_\gamma = \omega_\alpha - \omega_\beta$. As long as $\omega_\gamma < \omega_c$, this process is possible and its rate can be computed using Fermi's golden rule:

$$\Gamma_{\alpha\to\beta} = \pi e^{-|\mathbf{r}_\alpha - \mathbf{r}_\beta|/\xi} \frac{J^2}{S} \rho(\omega_\alpha - \omega_\beta). \tag{7.16}$$

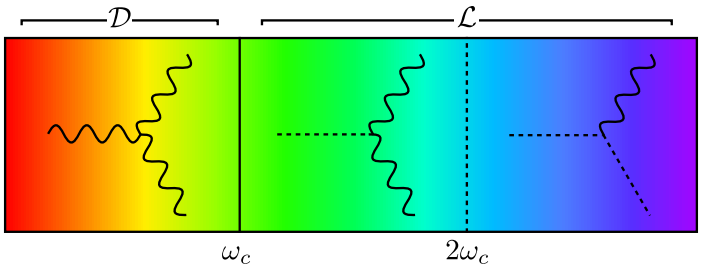

Figure 7.9.: The open decay channels of excitations, depending on the energy of the initial state. From left to right (low energy to high energy), delocalized to two delocalized, localized to two delocalized, and localized to localized and delocalized modes. Dashed/wiggly lines represent localized/delocalized excitations.

We can replace $\rho(\omega_\alpha - \omega_\beta) \sim \rho_0 = c/(\pi J)$ with some $c = O(1)$ and obtain a rate of decay of an excitation to a neighboring excitation (therefore $e^{-|\mathbf{r}_\alpha - \mathbf{r}_\beta|/\xi} \sim 1$) with the emission of a spin wave:

$$\Gamma = c\frac{J}{S}. \tag{7.17}$$

We conclude then that *a single excitation* can decay to neighboring, lower energy localized states by emission of low-energy spin waves. This process can lead to two possible outcomes: either the localized state decays to another localized state with energy $\omega < 2\omega_c$ and then it can decay further to localized states with energy $\omega < \omega_c$ and then eventually into spin waves; or it gets trapped because no neighbor in a radius of ξ has energy $\omega < 2\omega_c$. The decay out of this "high disorder trap" can only occur through higher order processes, therefore on timescales which are $O(S^2)$ and higher.

Summarizing, the picture we obtain is the following: flipping a single spin on top of a SG ground state will create a localized excitation with a certain probability P and a properly delocalized spin wave, with probability $1 - P$. Some of the former localized excitations can directly decay into spin waves, while others move in the neighborhood until they either decay or get trapped between similarly high-energy localized modes and eventually will decay through higher-order processes in $1/S$ (a larger typical timescale). Since these excitations are the ones which have higher energy, this will lead to violation of the equipartition and therefore the system will be out of equilibrium.

7.6. Truncated Hilbert space approach

In the previous section we conjectured what the mechanism leading to ergodicity restoring is, and reconciling the spin-wave approximation with the Halperin-Saslow picture. In order to make this argument quantitative, we resort to the truncated

Hilbert space exact diagonalization (THED). The central idea of this technique is to write down an effective Hamiltonian that contains lowest order spin-waves interaction, truncated in the sector of one and two particles. This method was recently applied to the triangular lattice antiferromagnet [294], showing good agreement both with DMRG simulations and with neutron scattering experiments.
We organize the Holstein–Primakoff expansion by powers of $\sqrt{S}$,

$$H = S^2 E_{\rm cl} + S\, H_{\rm SW} + \sqrt{S}\, H^{(3)} + H^{(4)}, \tag{7.18}$$

with $H_{\rm SW}$ the linear spin-wave Hamiltonian, already diagonalized in terms of Bogoljubov modes b_α of energy ω_α, and $H^{(3)}$, $H^{(4)}$ the cubic and quartic interactions generated at the next orders. Both survive here because the glass is non-collinear, while, in a collinear magnet the cubic terms vanish, and spontaneous magnon decay is absent. Collecting the three-boson terms and grouping them by their operator content, the cubic Hamiltonian reads

$$H^{(3)} = \sum_{ij} \Big(C^1_{ij}\, a_i^\dagger a_i a_j + C^2_{ij}\, a_i^\dagger a_i a_j^\dagger + C^3_{ij}\, a_i a_j^\dagger a_j + C^4_{ij}\, a_i^\dagger a_j^\dagger a_j \Big), \tag{7.19}$$

with the bond coefficients

$$C^{1,2}_{ij} = \frac{J_{ij}}{2\sqrt{2}} \big(-\mathcal{R}^{zx}_{ij} \pm i\, \mathcal{R}^{zy}_{ij} \big), \qquad C^{3,4}_{ij} = \frac{J_{ij}}{2\sqrt{2}} \big(-\mathcal{R}^{xz}_{ij} \pm i\, \mathcal{R}^{yz}_{ij} \big). \tag{7.20}$$

Each term describes a density fluctuation on one site of a bond accompanied by the creation or annihilation of a single boson on the other, and correspond to a magnon splitting into two or two magnons merging into one. Expanding the bosons over the Bogoljubov modes, $a_i = \sum_\alpha \left(X^t_{i\alpha} b_\alpha + Y^\dagger_{i\alpha} b^\dagger_\alpha \right)$, and restricting to the space $\mathcal{H} = \mathcal{H}_1 \oplus \mathcal{H}_2$ of one and two magnons, the terms of $H^{(3)}$ that connect the two sectors fall into three channels,

$$O^{(1)}_{\alpha\beta\gamma} = b^\dagger_\alpha b^\dagger_\beta b_\gamma, \qquad O^{(2)}_{\alpha\beta\gamma} = b^\dagger_\alpha b_\beta b^\dagger_\gamma, \qquad O^{(3)}_{\alpha\beta\gamma} = b_\alpha b^\dagger_\beta b^\dagger_\gamma, \tag{7.21}$$

so that $H^{(3)}_{1\to 2} = \sum_\mu \sum_{\alpha\beta\gamma} V^{(\mu)}_{\alpha\beta\gamma} O^{(\mu)}_{\alpha\beta\gamma}$, with the vertices

$$V^{(1)}_{\alpha\beta\gamma} = \sum_{ij} \Big(C^1_{ij} X^\dagger_{i\alpha} Y^\dagger_{i\beta} X^t_{j\gamma} + C^2_{ij} X^\dagger_{i\alpha} Y^\dagger_{i\beta} Y^t_{j\gamma} + C^3_{ij} Y^\dagger_{i\alpha} X^\dagger_{j\beta} X^t_{j\gamma} + C^4_{ij} X^\dagger_{i\alpha} X^\dagger_{j\beta} X^t_{j\gamma} \Big), \tag{7.22a}$$

$$V^{(2)}_{\alpha\beta\gamma} = \sum_{ij} \Big(C^1_{ij} X^\dagger_{i\alpha} X^t_{i\beta} Y^\dagger_{j\gamma} + C^2_{ij} X^\dagger_{i\alpha} X^t_{i\beta} X^\dagger_{j\gamma} + C^3_{ij} Y^\dagger_{i\alpha} Y^t_{j\beta} Y^\dagger_{j\gamma} + C^4_{ij} X^\dagger_{i\alpha} Y^t_{j\beta} Y^\dagger_{j\gamma} \Big), \tag{7.22b}$$

$$V^{(3)}_{\alpha\beta\gamma} = \sum_{ij} \Big(C^1_{ij} Y^t_{i\alpha} Y^\dagger_{i\beta} Y^\dagger_{j\gamma} + C^2_{ij} Y^t_{i\alpha} Y^\dagger_{i\beta} X^\dagger_{j\gamma} + C^3_{ij} X^t_{i\alpha} X^\dagger_{j\beta} Y^\dagger_{j\gamma} + C^4_{ij} Y^t_{i\alpha} X^\dagger_{j\beta} Y^\dagger_{j\gamma} \Big). \tag{7.22c}$$

The structure of these vertices reflects the physics we care about. High energy modes are exponentially localized and the vertex connecting three modes is itself exponentially small in their separation, $V_{\alpha\beta\gamma} \sim e^{-|\mathbf{r}_\alpha - \mathbf{r}_\beta|/\xi}$. The quartic block is built in the same way: its vertices $W^{(\mu)}_{\alpha\beta\gamma\delta}$, and the matrix elements of all channels on the basis states, are collected in Appendix 7.8.4. Physically the quartic block plays a double role: its diagonal part renormalizes the single-magnon energies, while its off-diagonal is a two-magnon elastic scattering term.

The full Hamiltonian of the truncated space then takes the block form

$$H = \begin{pmatrix} H_{\mathrm{SW}} & \left(H^{(3)}_{1\to 2}\right)^\dagger \\ H^{(3)}_{1\to 2} & H^{(4)} \end{pmatrix}, \tag{7.23}$$

whose diagonal blocks hold the free one- and two-magnon energies. The size of the problem is set by the dimension $N(N+1)/2+N$ of the $1\oplus 2$ magnon sector, so that the Hamiltonian is a sparse matrix of linear size of order N^2. Diagonalizing (7.23) sums the interaction to all orders within the truncated space, and it does so on exactly the footing the disordered problem demands, treating the localized excitation and the pairs into which it can decay as a single quantum-mechanical problem. An excitation is then no longer a stationary magnon but a single magnon hybridized with the continuum of pairs into which it can decay, and the interacting spectral function shows at once which of the two scenarios of Sec. 7.5 is realized: a peak that survives, merely shifted and slightly broadened, describes an excitation that remains trapped and non-ergodic, whereas a peak that dissolves into the two-magnon continuum describes one that has decayed and thermalized.
Another useful diagnostic is to compute the measurement of the spin-spin correlator

$$C_{ij}(t) = \langle \vec{S}_i(t)\, \vec{S}_j \rangle \,, \tag{7.24}$$

whose relaxation, or persistence, is the direct signature of restored, or broken, ergodicity.
Also the dynamical structure factor

$$S(\omega) = \int dt e^{-i\omega t} \sum_{ij} C_{ij}(t) \,, \tag{7.25}$$

and in particular its behavior for low frequencies gives important information on the excitation content of the theory. We plan to benchmark the THED approach against density matrix renormalization group simulation. The advantage of performing DMRG, with respect to neural quantum states simulations, is the possibility to construct low

energy excitation without paying a very large additional cost in bond dimension. The complexity of the algorithm is then ruled by the bond dimension required to find the ground state, which is in general a hard problem for two dimensional problems, but we believe that the structure of this particular system makes the task reachable.

7.7. Discussion

In this chapter we have investigated the spin-wave excitations of the two–dimensional Heisenberg spin-glass model through a semiclassical expansion around classical equilibrium states. Our motivation was to clarify how disorder affects their dynamics and, in particular, to assess the conditions under which hydrodynamic descriptions of spin glasses may emerge despite the strong tendency toward Anderson localization in low dimensions.

At leading order in the $1/S$ expansion we obtained a quadratic spin-wave Hamiltonian whose structure reflects the correlations encoded in the underlying classical state. We showed that these correlations qualitatively modify the localization properties of the excitations with respect to those expected from uncorrelated random-matrix ensembles in the same AZ symmetry class. In the FM and AFM phases we find that the low-energy spin waves remain delocalized even in the presence of disorder, while higher-energy excitations become localized, giving rise to a mobility edge in the spectrum. In contrast, in the SG phase the correlations inherited from the classical background are RG-irrelevant and the entire spin-wave spectrum is weakly localized, consistently with the expectations for class D systems in two dimensions.

These results have important implications for the dynamical properties of the model. In particular, localization of the non-interacting spin waves prevents from a straightforward identification of the Goldstone excitations with hydrodynamic modes in the SG phase. We have argued that it is the interactions among spin waves that provide a natural mechanism to restore ergodic dynamics and a path to thermodynamics. Because the localization length of the low-energy modes grows rapidly as the energy decreases, interactions allow localized excitations to decay by emitting low energy, delocalized modes (spin waves), ultimately coupling the system to an extended low-energy sector and recovering hydrodynamic behavior at sufficiently long times.

Let us also comment on the separation of length scales that underlies our interpretation of the weak-disorder magnetically ordered regimes. As discussed above, in two dimensions an arbitrarily small density of defects may eventually destabilize FM order through the accumulation of dipolar distortions. However, the corresponding length

scale ξ_{mag} is expected to be exponentially large at small disorder concentration, of the form $\xi_{mag}(p) \sim e^{c/p^2}$, for some constant $c = O(1)$ [277]. This is true if the dipoles do not end up screening themselves [295]. Therefore, for weak disorder, the magnetization has an exceptionally slow flow with the system size. This should be contrasted with the behavior of the localization probes, ϕ and D, which display a much faster finite-size flow and allow one to identify localized and delocalized regions already on the system sizes accessible numerically. The mobility edge extracted in this way may therefore be a property of the pre-asymptotic, but physically relevant, magnetized regime where $\xi_{loc}(\omega, p) \ll L \ll \xi_{mag}(p)$, where ξ_{loc} is the localization length of a spin-wave mode at frequency ω. In this window of system sizes, the system behaves as magnetically ordered for all practical purposes: the magnetization is finite and changes only very slowly with L, while the localization properties of the spin waves are in the asymptotic, finite-size scaling regime. In $d = 3$, where Anderson transitions are allowed in the AZ class D, one may expect a genuine localization–delocalization transition already at the non-interacting level, also in the SG phase.

7.8. Appendix of Chapter 7

7.8.1. The action of the oscillators

In order to compute numerically the quantity $R_\alpha(i)^2$ defined in Eq. (7.4), we express it in terms of the eigenstates components X and Y, see Eqs. (5.46). Let us compute the following expectation value:

$$\begin{aligned}\langle\alpha|\hat{a}_i^\dagger\hat{a}_i|\alpha\rangle &= \sum_{\beta\gamma}\langle\alpha|(Y^t_{i\beta}\hat{b}_\beta + X^\dagger_{i\beta}\hat{b}^\dagger_\beta)(X^t_{i\gamma}\hat{b}_\gamma + Y^\dagger_{i\gamma}\hat{b}^\dagger_\gamma)|\alpha\rangle \\ &= \sum_{\beta\gamma} Y^t_{i\beta}Y^\dagger_{i\gamma}(\langle 0|\hat{b}_\alpha\hat{b}_\beta\hat{b}^\dagger_\gamma\hat{b}^\dagger_\alpha|0\rangle) + X^\dagger_{i\beta}X^t_{i\gamma}(\langle 0|\hat{b}_\alpha\hat{b}^\dagger_\gamma\hat{b}_\beta\hat{b}^\dagger_\alpha|0\rangle) \\ &= |Y_{\alpha i}|^2 + |X_{\alpha i}|^2 + \sum_\beta Y^t_{i\beta}Y_{i\beta}\ .\end{aligned} \tag{7.26}$$

In the second line, we retain only the zero charge four-point functions, which are the only non-vanishing ones, and then we take the Wick contractions. Now, since $\sum_\beta Y^t_{i\beta}Y_{i\beta} = \langle 0|\hat{a}_i^\dagger\hat{a}_i|0\rangle$ (see, e.g., the Supplemental Material of [4]), we have:

$$\langle\alpha|\hat{a}_i^\dagger\hat{a}_i|\alpha\rangle - \langle 0|\hat{a}_i^\dagger\hat{a}_i|0\rangle = |Y_{\alpha i}|^2 + |X_{\alpha i}|^2\ . \tag{7.27}$$

Therefore, we identify the quantity $R_\alpha(i)^2$ with

$$R_\alpha(i)^2 = \mathcal{R}_\alpha^{-1}\left(|Y_{\alpha i}|^2 + |X_{\alpha i}|^2\right)\ , \tag{7.28}$$

where $\mathcal{R}_\alpha$ is a proper normalization constant. Notice that $\sum_i |Y_{\alpha i}|^2 + |X_{\alpha i}|^2$ is not the normalization of the Bogoljubov mode α, since in the bosonic case Bogoljubov modes are normalized with respect to the metric η, see Eq. (5.42), which gives $\sum_i |Y_{\alpha i}|^2 - |X_{\alpha i}|^2$.

We refer to $R_\alpha(i)^2$ as an *action* increase of the harmonic oscillator on site i. The reason why this quantity is indeed an action becomes clear if one expresses it in terms of position and momentum variables: $\hat{x}_i \equiv \hat{S}^x_i/\sqrt{S}$ and $\hat{p}_i = \hat{S}^y_i/\sqrt{S}$. Since $\hat{a}_i^\dagger = \frac{1}{\sqrt{2}}(\hat{x}_i - i\hat{p}_i)$ and $\hat{a}_i = \frac{1}{\sqrt{2}}(\hat{x}_i + i\hat{p}_i)$, we have

$$\hat{a}_i^\dagger\hat{a}_i = \frac{\hat{x}_i^2 + \hat{p}_i^2}{2} - \frac{1}{2}\ . \tag{7.29}$$

Hence, $R_\alpha(i)^2$ is the phase space volume projected on the state α, reduced by the the same quantity projected on the vacuum state.

7.8.2. Mobility edge in the FM and AFM phases

In this section we provide further information on the mobility edge for values of p closer to the clean FM/AFM states. Let us briefly comment that, in this regime, finding the classical ground state is relatively easier compared to moderate values of p, allowing to push the numerics to larger system sizes; however, most of the spectrum is delocalized (we are considering a small deformation of a classically ordered state), so performing a finite size scaling analysis is not always possible. In Fig. 7.10 we show the rescaled $r-$parameter ϕ for $p \in \{0.04, 0.06, 0.94, 0.96\}$, computed over the largest energies of the Bogoljubov spectrum, where the crossing is expected. The phase diagram of Fig 7.2 is built from the estimated values of $\omega_c(p)$.

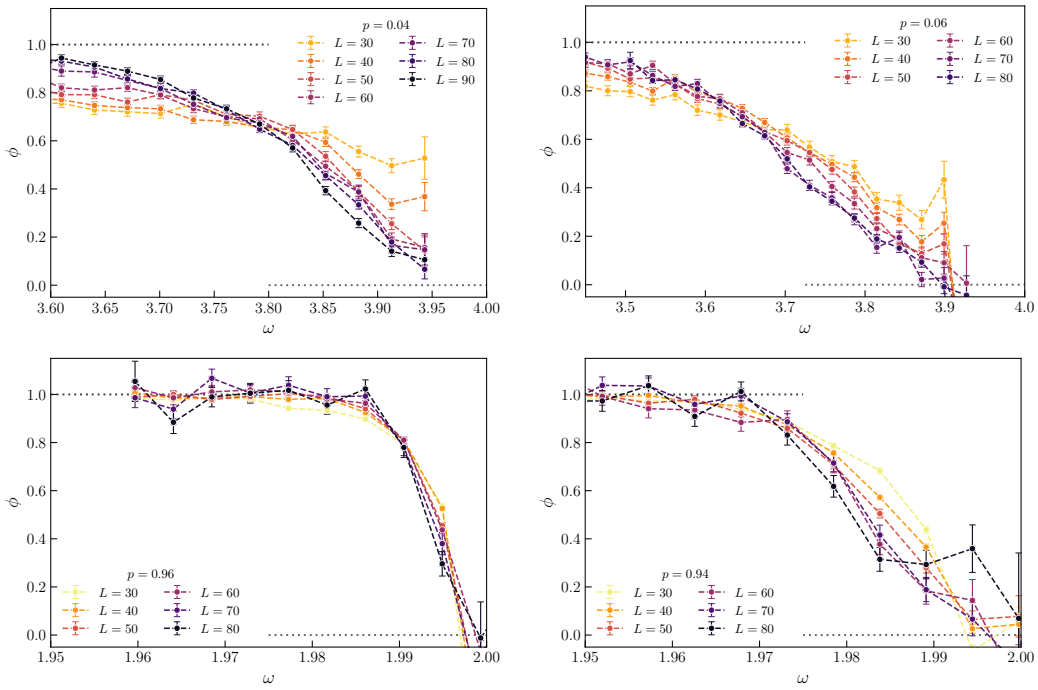

Figure 7.10.: Rescaled r-parameter for values of the antiferromagnetic bond concentration $p \in \{0.04, 0.06, 0.96, 0.94\}$. For increasing value of p and of $(1-p)$ the crossing shifts towards smaller energies: $\omega_c(p = 0.04) \simeq 3.8$, $\omega_c(p = 0.06) \simeq 3.65$, $\omega_c(p = 0.96) \simeq 1.99$, $\omega_c(p = 0.94) \simeq 1.97$ signaling the progressive localization of the whole spectrum moving away from the clean cases.

We have also computed the fractal dimension as the discrete derivative of the participation entropy for $p = 0.1$. Fig. 7.11 shows D for energy values close to the mobility edge, while the inset presents a data collapse using the values of (ω_c, ν) obtained from the scaling variable ϕ (see main text). The collapse is consistent, lending further support to our procedure. From this analysis, we estimate the fractal dimension at the critical point to be $D_c \simeq 0.75$.

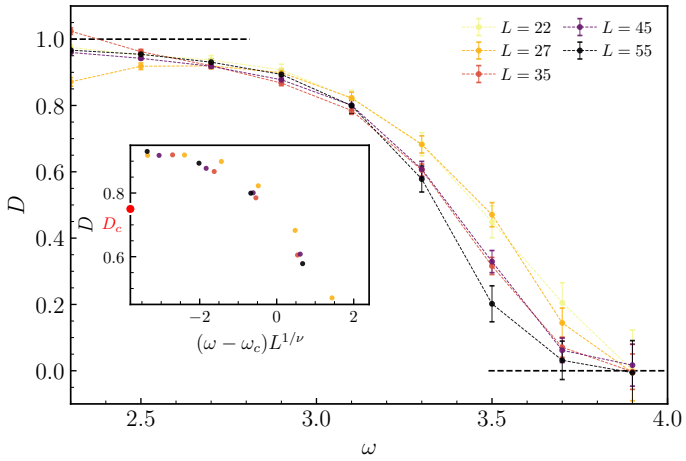

Figure 7.11.: Fractal dimension D for $p = 0.1$, as a function of the energy ω close to the mobility edge. In the inset data are collapsed with $\omega_c = 3.2,\ \nu = 2.1$, as in Fig. 7.6. This fit yields a value $D_c \simeq 0.75$.

7.8.3. Finite size scaling of the fractal dimension in the SG phase

We now describe in detail the procedure used to compute the fractal dimension D and its associated β function. The dominant source of uncertainty in the fractal dimension does not arise from the finite number of disorder realizations, but rather from sampling system sizes linearly instead of logarithmically. For this reason, it is important to consider and benchmark different methods for extracting the fractal dimension.

We first partition the participation entropy data into blocks containing n_B system sizes. Within each block, we perform a linear fit of the form

$$S(\omega, L) = D(\omega, L(n_B)) \ln L^2 + c(\omega, L(n_B)), \tag{7.30}$$

where $L(n_B)$ denotes the geometric mean of the system sizes within the block. We have verified that the fractal dimension value extracted as the coefficient of the linear terms depends only weakly on the choice of n_B. Consequently, this procedure primarily smooths the data and reduces the associated uncertainty, compared to estimating D via discrete derivatives of S.

Although this approach yields cleaner data for the fractal dimension (see Fig. 7.5 in the main text), it may introduce a systematic bias. In particular, a linear fit neglects the contribution of the β function, which enters at second order and is expected to be negative. To account for this effect, we have generalized the procedure by using a

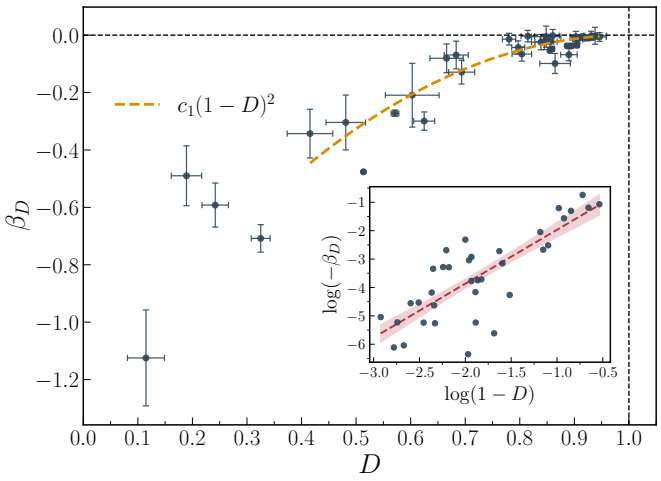

Figure 7.12.: Parametric plot of the β_D function as a function of the fractal dimension D, obtained from the quadratic fit in Eq. (7.31) with $n_B = 4$. The analysis is restricted to system sizes $L \geq 22$ in order to reduce finite-size effects. The inset shows the same data on a log-log scale for small values of $1 - D$, together with a fit to the form $\beta_D \simeq -c_1(1-D)^{\alpha_D}$, yielding an exponent $\alpha_D = 1.9(2)$ (with the shaded region indicating the 1σ confidence interval). The yellow dashed line in the main panel corresponds instead to the phenomenological assumption $\alpha_D = 2$, from which we extract $c_1 = 1.3(1)$.

quadratic fit of the form

$$S(\omega, L) = S_0 + D(\omega, L)\left(\ln L^2 - \ln L^2_{min}\right) + \frac{1}{2}\beta_D(\omega, L)D(\omega, L)\left(\ln L^2 - \ln L^2_{min}\right)^2 , \tag{7.31}$$

where L_{min} is the smallest system size in the block. While this approach leads to noisier estimates of the fractal dimension, it allows for a direct extraction of the β_D function from the coefficient of the quadratic term. In turn, this provides a check that the scaling relation $\alpha_D = 2$ is consistent with our data. In Fig. 7.12, we report the corresponding parametric plot $\beta(D)$. In the inset we extract the exponent α_D from a log-log fit of β_D vs D, yielding a value of $\alpha_D = 1.9(2)$, indeed compatible with 2.

7.8.4. Quartic interactions

By proceeding in a similar way as to build $H^{(3)}$, we consider all the terms producing a four body coupling in the a's and compute $H^{(4)}$. These terms arise from products of the rotated spin components xx, yy, zz, xy and yx:

$$\frac{J_{ij}}{2}\mathcal{R}^{xx}_{ij}\Sigma^x_i\Sigma^x_j = -\frac{J_{ij}}{2}\mathcal{R}^{xx}_{ij}\frac{1}{8}\left[(a_i + a_i^\dagger)(a_j^\dagger a_j a_j + a_j^\dagger a_j^\dagger a_j) + (a_i^\dagger a_i a_i + a_i^\dagger a_i^\dagger a_i)(a_j + a_j^\dagger)\right] \tag{7.32a}$$

$$\frac{J_{ij}}{2}\mathcal{R}_{ij}^{yy}\Sigma_i^y\Sigma_j^y = \frac{J_{ij}}{2}\mathcal{R}_{ij}^{yy}\frac{1}{8}\left[(a_i - a_i^\dagger)(a_j^\dagger a_j a_j - a_j^\dagger a_j^\dagger a_j) + (a_i^\dagger a_i a_i - a_i^\dagger a_i^\dagger a_i)(a_j - a_j^\dagger)\right] \tag{7.32b}$$

$$\frac{J_{ij}}{2}\mathcal{R}_{ij}^{xy}\Sigma_i^x\Sigma_j^y = \frac{J_{ij}}{2}\mathcal{R}_{ij}^{xx}\frac{i}{8}\left[(a_i + a_i^\dagger)(a_j^\dagger a_j a_j - a_j^\dagger a_j^\dagger a_j) + (a_i^\dagger a_i a_i + a_i^\dagger a_i^\dagger a_i)(a_j - a_j^\dagger)\right] \tag{7.32c}$$

$$\frac{J_{ij}}{2}\mathcal{R}_{ij}^{yx}\Sigma_i^y\Sigma_j^x = \frac{J_{ij}}{2}\mathcal{R}_{ij}^{yx}\frac{i}{8}\left[(a_i - a_i^\dagger)(a_j^\dagger a_j a_j + a_j^\dagger a_j^\dagger a_j) + (a_i^\dagger a_i a_i - a_i^\dagger a_i^\dagger a_i)(a_j + a_j^\dagger)\right] \tag{7.32d}$$

$$\frac{J_{ij}}{2}\mathcal{R}_{ij}^{zz}\Sigma_i^z\Sigma_j^z = \frac{J_{ij}}{2}\mathcal{R}_{ij}^{zz}a_i^\dagger a_i a_j^\dagger a_j \tag{7.32e}$$

By collecting similar terms, we find

$$H^{(4)} = H_{zz}^{(4)} + H_\perp^{(4)} \ , \tag{7.33}$$

where

$$H_{zz}^{(4)} = \sum_{ij} D_{ij} a_i^\dagger a_i a_j^\dagger a_j \ , \tag{7.34}$$

and

$$\begin{aligned} H_\perp^{(4)} = \sum_{ij} \Big[& F_{ij}(a_i a_j^\dagger a_j a_j + a_i^\dagger a_i a_i a_j) + F_{ij}^*(a_i^\dagger a_j^\dagger a_j^\dagger a_j + a_i^\dagger a_i^\dagger a_i a_j^\dagger) \\ & G_{ij}(a_i^\dagger a_j^\dagger a_j a_j + a_i^\dagger a_i^\dagger a_i a_j) + G_{ij}^*(a_i a_j^\dagger a_j^\dagger a_j + a_i^\dagger a_i a_i a_j^\dagger)\Big] \end{aligned} \tag{7.35}$$

with the coefficients defined as:

$$D_{ij} = \frac{J_{ij}}{2}\mathcal{R}_{ij}^{zz} \tag{7.36}$$

and

$$F_{ij} = \frac{J_{ij}}{16}\left[-\mathcal{R}_{ij}^{xx} + \mathcal{R}_{ij}^{yy} + i\left(\mathcal{R}_{ij}^{xy} + \mathcal{R}_{ij}^{yx}\right)\right] \tag{7.37a}$$

$$G_{ij} = \frac{J_{ij}}{16}\left[-\mathcal{R}_{ij}^{xx} - \mathcal{R}_{ij}^{yy} + i\left(\mathcal{R}_{ij}^{xy} - \mathcal{R}_{ij}^{yx}\right)\right] \tag{7.37b}$$

Now, we have to express $H^{(4)}$ in terms of the Bogoljubov modes b. Terms which are non-vanishing in the truncated 2-magnon Hilbert space must contain the same number of dagger and non-dagger operators. Therefore, of the 8 possible combinations of *bbbb* (16 with their daggers), we only retain the following 3 (6 with their daggers):

$$O_{\alpha\beta\gamma\delta}^{(1)} = b_\alpha^\dagger b_\beta^\dagger b_\gamma b_\delta \quad O_{\alpha\beta\gamma\delta}^{(2)} = b_\alpha^\dagger b_\beta b_\gamma^\dagger b_\delta \quad O_{\alpha\beta\gamma\delta}^{(3)} = b_\alpha^\dagger b_\beta b_\gamma b_\delta^\dagger \tag{7.38}$$

These terms will build the upper triangular matrix $H^{(4)}$, their daggers will enter the lower triangular; and, finally, the diagonal of $H^{(4)}$ will host the sum of the energies of

two magnons in each of the 2-magnon basis states:

$$H^{(4)} = \sum_{\mu=1}^{3} \sum_{\alpha\beta\gamma\delta} W^{(\mu)}_{\alpha\beta\gamma\delta} O^{(\mu)}_{\alpha\beta\gamma\delta} + \text{h.c.}\ , \tag{7.39}$$

where the 4-magnon vertex coefficients $W^{(\mu)}_{\alpha\beta\gamma\delta}$ have the following expressions:

$$\begin{aligned} W^{(1)}_{\alpha\beta\gamma\delta} = \sum_{ij} & D_{ij} X^{\dagger}_{i,\alpha} Y^{\dagger}_{i,\beta} X^{t}_{j,\delta} Y^{t}_{j,\gamma} + \\ & F_{ij} \left(Y^{\dagger}_{i,\alpha} X^{\dagger}_{j,\beta} X^{t}_{j,\gamma} X^{t}_{j,\delta} + X^{\dagger}_{i,\alpha} Y^{\dagger}_{i,\beta} X^{t}_{i,\gamma} X^{t}_{j,\delta} \right) + \\ & F^{*}_{ij} \left(X^{\dagger}_{i,\alpha} X^{\dagger}_{j,\beta} Y^{t}_{j,\gamma} X^{t}_{j,\delta} + X^{\dagger}_{i,\alpha} X^{\dagger}_{i,\beta} X^{t}_{i,\gamma} Y^{t}_{j,\delta} \right) + \\ & G_{ij} \left(X^{\dagger}_{i,\alpha} X^{\dagger}_{i,\beta} X^{t}_{i,\gamma} X^{t}_{j,\delta} + X^{\dagger}_{i,\alpha} X^{\dagger}_{j,\beta} X^{t}_{j,\gamma} X^{t}_{j,\delta} \right) + \\ & G^{*}_{ij} \left(Y^{\dagger}_{i,\alpha} X^{\dagger}_{j,\beta} Y^{t}_{j,\gamma} X^{t}_{j,\delta} + X^{\dagger}_{i,\alpha} Y^{\dagger}_{i,\beta} X^{t}_{i,\gamma} Y^{t}_{j,\delta} \right) \end{aligned} \tag{7.40a}$$

$$\begin{aligned} W^{(2)}_{\alpha\beta\gamma\delta} = \sum_{ij} & D_{ij} X^{\dagger}_{i,\alpha} X^{t}_{i,\beta} X^{\dagger}_{j,\gamma} X^{t}_{j,\delta} + \\ & F_{ij} \left(X^{\dagger}_{i,\alpha} X^{t}_{i,\beta} Y^{\dagger}_{i,\gamma} X^{t}_{j,\delta} + Y^{\dagger}_{i,\alpha} Y^{t}_{j,\beta} Y^{\dagger}_{j,\gamma} X^{t}_{j,\delta} \right) + \\ & F^{*}_{ij} \left(X^{\dagger}_{i,\alpha} Y^{t}_{j,\beta} X^{\dagger}_{j,\gamma} X^{t}_{j,\delta} + X^{\dagger}_{i,\alpha} Y^{t}_{i,\beta} Y^{\dagger}_{i,\gamma} Y^{t}_{j,\delta} \right) + \\ & G_{ij} \left(X^{\dagger}_{i,\alpha} Y^{t}_{i,\beta} Y^{\dagger}_{i,\gamma} X^{t}_{j,\delta} + X^{\dagger}_{i,\alpha} Y^{t}_{j,\beta} Y^{\dagger}_{j,\gamma} X^{t}_{j,\delta} \right) + \\ & G^{*}_{ij} \left(Y^{\dagger}_{i,\alpha} Y^{t}_{j,\beta} X^{\dagger}_{j,\gamma} X^{t}_{j,\delta} + X^{\dagger}_{i,\alpha} X^{t}_{i,\beta} Y^{\dagger}_{i,\gamma} Y^{t}_{j,\delta} \right) \end{aligned} \tag{7.40b}$$

$$\begin{aligned} W^{(3)}_{\alpha\beta\gamma\delta} = \sum_{ij} & D_{ij} X^{\dagger}_{i,\alpha} X^{t}_{i,\beta} Y^{\dagger}_{j,\delta} Y^{t}_{j,\gamma} + \\ & F_{ij} \left(X^{\dagger}_{i,\alpha} X^{t}_{i,\beta} X^{t}_{i,\gamma} Y^{\dagger}_{j,\delta} + Y^{\dagger}_{i,\alpha} Y^{t}_{j,\beta} X^{t}_{j,\gamma} Y^{\dagger}_{j,\delta} \right) + \\ & F^{*}_{ij} \left(X^{\dagger}_{i,\alpha} Y^{t}_{i,\beta} X^{t}_{i,\gamma} X^{\dagger}_{j,\delta} + X^{\dagger}_{i,\alpha} Y^{t}_{j,\beta} Y^{t}_{j,\gamma} Y^{\dagger}_{j,\delta} \right) + \\ & G_{ij} \left(X^{\dagger}_{i,\alpha} Y^{t}_{i,\beta} Y^{\dagger}_{j,\delta} X^{t}_{i,\gamma} + X^{\dagger}_{i,\alpha} Y^{t}_{j,\beta} X^{t}_{j,\gamma} Y^{\dagger}_{j,\delta} \right) + \\ & G^{*}_{ij} \left(X^{\dagger}_{i,\alpha} X^{t}_{i,\beta} X^{t}_{i,\gamma} X^{\dagger}_{j,\delta} + Y^{\dagger}_{i,\alpha} Y^{t}_{j,\beta} Y^{t}_{j,\gamma} Y^{\dagger}_{j,\delta} \right) \end{aligned} \tag{7.40c}$$

8. Weakly disordered ferromagnets

In this chapter we analyze the weakly disordered Heisenberg spin model. We find evidence of an abundance of low energy modes, compared to the clean ferromagnetic case, that modify the dispersion relation. We present a field theoretical derivation, that has its roots in the numerical reconstruction of the spin-stiffness correlations, that aims to explain the dynamical exponent increase.

8.1. Introduction

In the previous chapter we focused on the disordered Heisenberg model at concentration $p \simeq 1/2$ of antiferromagnetic bonds, where the competition between ferromagnetic and antiferromagnetic exchange is maximal and the classical ground state is a quantum spin glass. We now turn to the opposite regime, $p \ll 1/2$, in which the vast majority of bonds remain ferromagnetic and the classical ground state is, at least locally, magnetized. This regime is far from trivial: as we show in this chapter, an arbitrarily small density of antiferromagnetic bonds is enough to qualitatively change the long-wavelength dynamics of the two-dimensional ferromagnet, even though it does not change the presence of a magnetized ground state on any accessible scale.

The model is the same one introduced in the previous chapter, the $T = 0$ disordered Heisenberg model on the square lattice, and we rewrite here the Hamiltonian for clarity:

$$H = \sum_{\langle i,j \rangle} J_{ij} \vec{S}_i \cdot \vec{S}_j \,, \tag{8.1}$$

with $\vec{S}_i$ an $SU(2)$ spin operator in representation s (or, in the classical limit $s \to \infty$, a unit vector on the sphere), and nearest-neighbor couplings J_{ij} drawn independently from the binary distribution

$$P(J) = (1-p)\,\delta(J+1) + p\,\delta(J-1)\,, \tag{8.2}$$

where p is the concentration of antiferromagnetic bonds. As p is tuned from 0 to 1 the ground state interpolates between the ferromagnet (FM) and the antiferromagnet

(AFM), passing through the spin-glass region discussed previously. Here we restrict to $p \ll 1/2$, where the classical ground-state configurations remain magnetized and are only weakly canted by the antiferromagnetic bonds.

Two-dimensional magnetism is a natural setting in which to ask how robust this magnetized state is to disorder. On the clean side, the Mermin–Wagner theorem [82] forbids the spontaneous breaking of a continuous symmetry at any $T > 0$; at $T = 0$, however, a magnetized ground state is compatible with the theorem, and the low-energy physics is controlled by the Goldstone (spin-wave) modes, whose quadratic dispersion is set by the spin-stiffness constant ρ_s. The conventional expectation is that weak bond disorder simply renormalizes ρ_s to a new, finite value, without altering the hydrodynamic, quadratic form of the magnon dispersion [267, 268]. Renewed interest in two-dimensional magnetic materials [296–306], together with the prospect of realizing frustrated spin Hamiltonians on quantum simulators (Rydberg arrays, trapped ions, superconducting qubits) [307–309], makes it worth revisiting this expectation carefully.

In fact, our own numerical study of the disordered Heisenberg model (that we discussed in the previous chapters) which combined machine-learning variational states with a semiclassical treatment of the ground state, left an anomaly unexplained: for $p \ll 1/2$, where the classical ground states are spontaneously magnetized on all accessible scales, the smallest spin-wave eigenvalues were nevertheless found to scale anomalously with the system size, with an effective dynamical exponent $z > 2$ rather than the clean-ferromagnet value $z = 2$ [2]. This chapter is devoted to identifying the mechanism responsible for this anomaly and to characterizing it quantitatively.

The chapter is organized as follows. Section 8.2 presents the numerical evidence for the anomalous dynamical exponent, obtained from exact diagonalization of the semiclassical spin-wave Hamiltonian. Section 8.3 develops a real-space, dipole picture à la Villain of how a dilute set of antiferromagnetic bonds deforms the magnetization pattern, and asks whether this deformation is enough, by itself, to destabilize long-range order at any $p > 0$. Then we set the basis for a field theoretical calculation that describes the observation made numerically.

8.2. The dynamical critical exponent

To probe the low-energy excitations of Eq. (8.1) we perform a semiclassical (large-s) expansion around the classical ground-state configurations, following the same procedure used in the previous chapters. The classical minima are located with an over-relaxation gradient-descent algorithm and the quadratic fluctuations around each min-

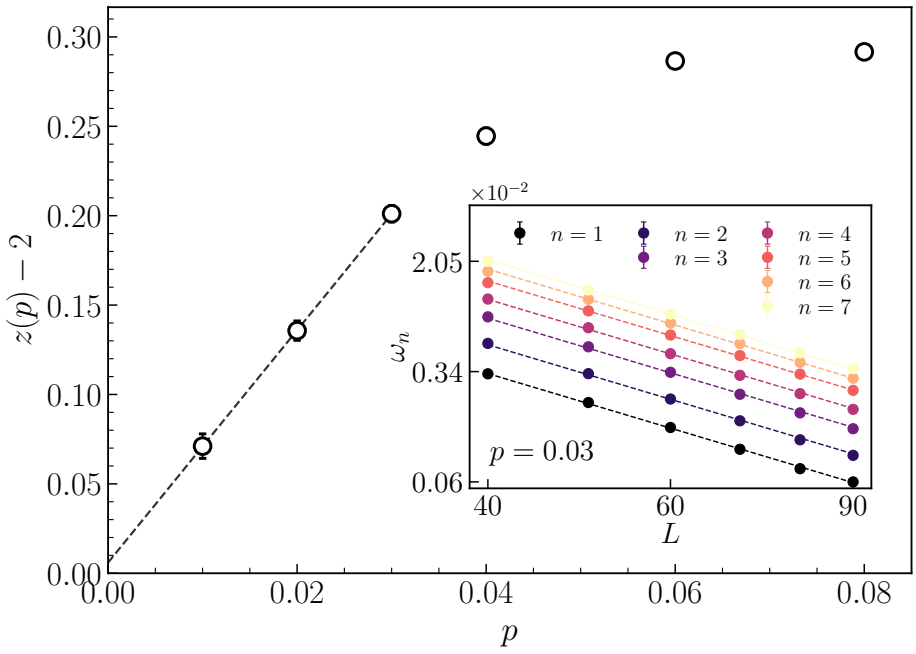

Figure 8.1.: Growth of the dynamical exponent z away from the clean ferromagnetic value $z = 2$, as a function of the antiferromagnetic bond concentration p. The dashed line is a linear fit, consistent with the expected behavior as $p \to 0$. *Inset*: finite-size scaling of the n-th spin-wave eigenvalue (disorder-averaged) with the linear system size L, for $p = 0.03$.

imum define the spin-wave (SW) problem in Bogoljubov form Eq. (5.37), that we discussed in detail throughout this thesis. For $p \ll 1/2$, where the classical reference state is spontaneously magnetized, the low-energy spin-wave modes are completely delocalized, so it is meaningful to assume a dispersion relation $\omega \sim k^z$ at small wavenumber k, with z the dynamical exponent. The density of states then follows the standard relation $\varrho(\omega) \sim \omega^{d/z-1}$ in spatial dimension d. In the clean limit ($p = 0$), the matrix A –containing magnon hopping terms– reduces to (minus) the discrete lattice Laplacian, and the matrix B– containing anomalous terms– is exactly zero. The dispersion is the familiar $\omega \sim k^2$, i.e., $z = 2$, with a flat density of states $\varrho(\omega) \sim \omega^0$ at low ω.

Once a small concentration of antiferromagnetic bonds is switched on, the low-energy spectrum shows an *excess* of slow modes compared to the clean case: the density of states develops a singularity at $\omega \to 0$, signaling a dispersion softer than quadratic. To quantify this without relying on the binning used to construct $\varrho(\omega)$, we instead track the finite-size scaling of the lowest positive spin-wave frequencies directly. For each of the ten lowest modes ($n \leq 10$) we fit $\omega_n \sim L^{-z}$, averaged over disorder realizations. As shown in Fig. 8.1, the extracted exponents are, within error bars, independent of the mode index n – supporting the existence of a single, common dynamical exponent – and are systematically larger than the clean value $z = 2$. Moreover, z grows monotonically

with the antiferromagnetic bond concentration p, roughly linearly as $p \to 0$.

This is the central numerical fact that the rest of the chapter sets out to explain: bond disorder that leaves the classical ground state magnetized on all accessible scales nevertheless produces an accumulation of anomalously soft magnon modes, i.e., a dynamical exponent $z > 2$ and a singular low-energy density of states. We note, as an aside, that at the larger concentrations and system sizes accessible numerically ($L \lesssim 90$), the measured $z - 2$ appears to saturate to a roughly constant value rather than continuing to grow with p. This is expected, since it likely signals the breakdown of the weak-disorder (small-p) expansion rather than a genuinely new regime. Let us also briefly comment that, in this disorder regime, we reach with more confidence larger system sizes. Indeed the complexity in the system is very small, compared to the spin glass case (see Fig.7.1) and the global minimum can be reached with more probability. However, in this case, it is crucial to select the correct one because, opposite to the spin glass phase, we conjecture that higher energy minima may have drastically different statistical behavior.

8.3. The dipole approximation

We now ask how a small deformation of the exchange couplings modifies the ground state of the clean ferromagnet. The simplest defect is a single modified bond,

$$H = H_0 + V_{ab} \,, \qquad V_{ab} = (J' - J)\, \vec{S}_a \cdot \vec{S}_b \,, \tag{8.3}$$

with $J' > 0$. As shown by Parker and Saslow [295], such a bond leaves the collinear ground state of H_0 undistorted unless its strength exceeds the clean coupling, $J' > 1$: below this threshold the neighboring spins do not cant and the order is locally undisturbed. In the following we consider the case of a defect with the same strength as the other couplings, i.e. $|J| = 1$. A finite distortion of the ground state therefore requires composite defects, the simplest being two adjacent modified bonds. If the concentration of antiferromagnetic bonds in the system is p, the most relevant defect that alters the magnetization is $\mathcal{O}(p^2)$. Let us now focus on the case where we have a finite concentration of composite defects.

When the defects are dilute and well separated, the relevant configurations are slow spatial variations of the local order and are described by a continuous theory [279],

$$H = J \sum_{ij} (\vec{m}_i - \vec{m}_j)^2 \sim \int d^2 r \sum_{\alpha=\{x,y,z\}} (\nabla m^\alpha)^2 \,, \tag{8.4}$$

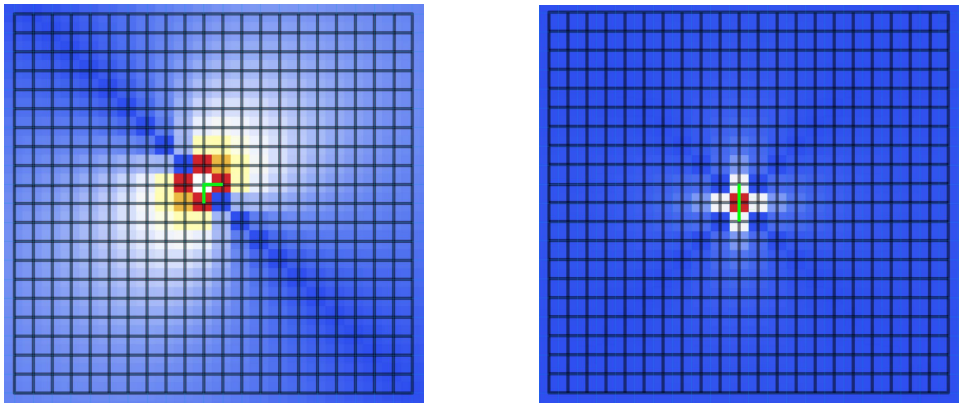

Figure 8.2.: Amplitude of the local magnetic fluctuation $|\vec{m}|$ in the plane orthogonal to the spin orientation of a ferromagnetic state perturbed by a single defect placed at the center of a 120×120 sample (the figure shows the central 20×20 patch of the lattice). The L-shaped defect on the left clearly displays a dipole solution, while the linear defect on the right displays a quadrupole one.

where $\vec{m} = (m_i^x, m_i^y, m_i^z)$, $|\vec{m}| = 1$, is the local magnetization direction. In the ordered background $m_i^z \simeq 1$, and for a small number of defects the transverse components stay small, $|m_i^{x,y}| \ll 1$. To this order the two transverse fields are free, and in any region away from a defect the ground-state configuration obeys Laplace's equation

$$\nabla^2 m^\alpha = 0 \,, \qquad \alpha = \{x, y\}. \tag{8.5}$$

A localized defect acts as a source for the transverse field, and the distortion it induces is the corresponding solution of Eq. (8.5) in two dimensions, that is, a multipole field whose leading nonvanishing term is set by the symmetry of the defect. The lowest multipole a defect can carry is a dipole,

$$m^\alpha(\vec{r}) = \frac{\vec{r} \cdot \vec{\mu}^\alpha}{r^2} \,, \tag{8.6}$$

which decays as $1/r$, with $\vec{\mu}^\alpha$ the dipole vectors. Inspecting individual defects, we find that the less symmetric ones carry a nonzero dipole moment while the more symmetric ones do not. The L-shaped pair of modified bonds is dipolar and produces the $1/r$ field, whereas the collinear (I-shaped) pair has vanishing dipole and generates a weaker, quadrupolar distortion decaying as $1/r^2$ (Figs. 8.2). This distinction is what matters in the following, since only the slowly decaying dipole fields accumulate over the sample.

Consider now a finite density of dipolar defects at random positions $\vec{x}_i$. As long as the transverse distortion remains small, the total field is the superposition of the

individual dipole solutions,

$$m^{\alpha}(\vec{r}) = \sum_{i \in \text{defects}} \frac{(\vec{r} - \vec{x}_i) \cdot \vec{\mu}_i^{\alpha}}{|\vec{r} - \vec{x}_i|^2} \ . \tag{8.7}$$

The reduction of the order parameter is controlled by the variance $|\vec{m}(\vec{r})|^2$, and its estimate requires an assumption about how the defects are correlated. We proceed under a non-screening hypothesis: the dipole moments $\vec{\mu}_i$ are quenched by the local defect geometry, randomly oriented and mutually uncorrelated, so that the defects neither align nor rearrange to screen one another. This is the counterpart, for fixed quenched sources, of an unscreened gas of electrostatic dipoles, and it is the assumption on which the conclusion below rests. Squaring the field,

$$\left(m^{\alpha}(\vec{r})\right)^2 = \sum_{ij} \mu_{i,\beta}^{\alpha} M_{ij}^{\beta\gamma} \mu_{j,\gamma}^{\alpha} \qquad M_{ij}^{\beta\gamma} = \frac{(\vec{r} - \vec{x}_i)^{\beta} (\vec{r} - \vec{x}_j)^{\gamma}}{|\vec{r} - \vec{x}_i|^2 |\vec{r} - \vec{x}_j|^2} \ , \tag{8.8}$$

the cross terms $i \neq j$ carry the uncorrelated moments and average to zero, so that only the diagonal, self-interaction terms survive. Replacing the sum by an integral over a density $\rho(\vec{x})$,

$$\begin{aligned} \left(m^{\alpha}(\vec{r})\right)^2 &\simeq \int d^2x \ \rho(\vec{x}) \ \mu_{\beta}^{\alpha}(\vec{x}) M^{\beta\gamma}(\vec{x}) \mu_{\gamma}^{\alpha}(\vec{x}) \\ &\simeq \mu_{\beta}^{\alpha} \mu_{\gamma}^{\alpha} \int d^2x \ \rho(\vec{x}) \ \frac{y^{\beta} y^{\gamma}}{y^4} \ , \end{aligned} \tag{8.9}$$

with $\vec{y} = \vec{r} - \vec{x}$ and the dipole vectors taken spatially uniform. Using rotational invariance, $y^{\beta} y^{\gamma} / y^4 = \frac{1}{2} \delta^{\beta\gamma} / y^2$, this reduces to

$$\left(m^{\alpha}(\vec{r})\right)^2 \simeq \frac{\left(\mu^{\alpha}\right)^2}{2} \int d^2x \ \rho(\vec{x}) \ \frac{1}{|\vec{r} - \vec{x}|^2} \ . \tag{8.10}$$

For a uniform density $\rho(\vec{x}) = \rho = N/S$ on a sample taken to be a disk of radius R and area $S = \pi R^2$, and cutting the integral off at the lattice spacing a, below which the continuum dipole field is not defined,

$$|\vec{m}(\vec{r})|^2 \simeq 2\pi \, |\vec{\mu}|^2 \rho \int_a^R \frac{dx}{x} \ , \tag{8.11}$$

one obtains a logarithmic growth,

$$|\vec{m}|^2 \sim 2\pi \, |\vec{\mu}|^2 \rho \, \ln\!\left(\frac{R}{a}\right) \ . \tag{8.12}$$

The variance of the transverse distortion therefore does not saturate but increases

without bound with the system size. This is the point at which the starting hypothesis of small fluctuations ceases to be self-consistent: for any finite density ρ, however small, there is a scale

$$R^* \sim a\ e^{\frac{1}{2\pi|\vec{\mu}|^2\rho}} \tag{8.13}$$

beyond which the accumulated distortion reaches order one, $|\vec{m}|^2 \sim 1$, and the linearized description breaks down. Within this argument, the ordered ground state at $T = 0$ is thus unstable against any finite concentration of dipolar defects.

Taking $\mu^2 \sim 1$ and estimating the density of L-shaped defects as $\rho \simeq 4p^2$, with p the concentration of antiferromagnetic bonds [1], the crossover scale becomes

$$R^* \sim a\ e^{\frac{c}{p^2}}\ . \tag{8.14}$$

The exponential largeness of R^* at weak disorder means that the region appears ferromagnetic, or antiferromagnetic, for any practically accessible size, while asymptotically the transverse order is destroyed. In Villain's terminology [279] a state ordered along a given direction z but disordered in the perpendicular plane is a semi spin glass; here it arises at its critical point, with a magnetization m^z that decreases only logarithmically with the system size.
Let us notice that, since the interaction graph is bipartite, a staggered rotation maps the dilute antiferromagnetic-bond problem at concentration p onto the same problem at $1-p$, so the argument applies unchanged to the dirty Heisenberg antiferromagnet.

8.4. Renormalization group approach to the weakly disordered ferromagnet

In order to make analytic progress, we should take two limits: first the long-wavelength limit, for the low-energy modes of Eq.(5.37), and second the small p approximation, in which the distance between the microscopic defects is $l \sim 1/p \gg 1$. The matrices A, B, defining the spin wave Hamiltonian, are correlated random matrices, which can be computed only after the classical minimum has been found. In the small p limit, and long wavelength limit $1 \ll 1/p \ll L$ one can reason phenomenologically to derive an effective field theory which does not depend explicitly on the lattice constant. Because of the global symmetry A, B must be proportional to a discrete

[1] The probability of placing an antiferromagnetic bond is p, then the second bond that constitutes the L-shaped defect can be placed with probability p in 4 different ways, hence the $4p^2$.

Laplacian term:

$$\begin{aligned} H_{SW} &= \textstyle\sum_i \rho_i^{(0)} (\nabla a^\dagger)_i (\nabla a)_i \\ &+ \textstyle\sum_i \frac{\theta_i^{(0)*}}{2} (\nabla a^\dagger)_i (\nabla a^\dagger)_i \\ &+ \textstyle\sum_i \frac{\theta_i^{(0)}}{2} (\nabla a)_i (\nabla a)_i \ , \end{aligned} \tag{8.15}$$

where $(\nabla a^\dagger)_i \cdot (\nabla a)_i = (a^\dagger_{i+e_x} - a_i)(a^\dagger_{i+e_x} - a_i) + (a^\dagger_{i+e_y} - a_i)(a^\dagger_{i+e_y} - a_i)$. Passing to Fourier transform, in the limit in which $\rho_i^{(0)}, \theta_i$ are constant we have

$$H_{SW} = \sum_{\vec{k}} \epsilon_k \rho^{(0)} a^\dagger_{\vec{k}} a_{\vec{k}} + \frac{\theta^*}{2} a^\dagger_{\vec{k}} a^\dagger_{\vec{k}} + \frac{\theta}{2} a_{\vec{k}} a_{\vec{k}} \ , \tag{8.16}$$

where $\epsilon_k = 2 - \cos(k_x) - \cos(k_y)$ are the eigenvalues of the Laplacian on the square lattice (with $a = 1$).

For $\theta \ll \rho$, which means $B \ll A$, which we verified numerically for small p, one can rotate to Bogoljubov bosons and get

$$H_{SW} = \sum_k \rho \ \epsilon_k b^\dagger_{\vec{k}} b_{\vec{k}} \ , \tag{8.17}$$

with $\rho = \sqrt{\rho^{(0)\,2} - |\theta|^2}$. We can now pass to the continuum and re-introduce a smooth dependence of ρ on $\vec{x}$, let ϕ be the continuum limit of the Bogoljubov boson b and $\epsilon_k \sim \frac{k^2}{2}$. In this way we recover the Hamiltonian equivalent of (8.18).

At long wavelengths, we have a complex scalar magnon field $\phi = \phi(\vec{x}, t)$, with action:

$$S[\phi, \rho_s] = s \int d^2x dt \left(i\phi^* \partial_t \phi - \rho_s(\vec{x}) |\nabla \phi|^2 \right) \ , \tag{8.18}$$

where $\rho_s(\vec{x})$ is the local spin-stiffness, and $s \sim 1/\hbar$ is the spin representation (we set $s = 1$ in the following). In the weak-disorder regime, the leading effect of the antiferromagnetic bonds is to promote the stiffness constant to a quenched, slowly-varying random field $\rho_s \to \rho_s(\vec{x})$. This field can be thought of as the cost of twisting the spins away from their equilibrium position, in a region of space around the point $\vec{x}$ and must be computed for any classical disorder realization. In order to gain insight into its nature, we have developed an *ad hoc* numerical technique [2].

After having found the classical ground state, we select a square patch and impose a twist of magnitude θ on the spins along its upper and right boundaries, while those

[2] The *global* spin stiffness, also referred to as the helicity modulus [310, 311], is usually measured from the free-energy cost associated with an imposed twist of boundary conditions. For a small twist angle θ, we write $F(\theta) - F(0) = \rho_s \theta^2 + O(\theta^4)$. At $T = 0$, the free energy coincides with the energy $F(\theta) = E(\theta)$.

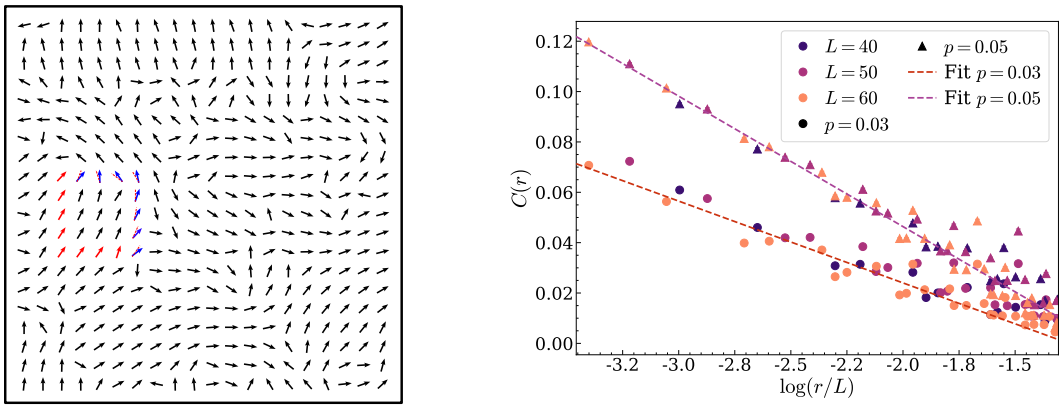

Figure 8.3.: Left panel: A square patch on a classical ground state spin-configuration, used to measure the *local* spin stiffness. The spin vectors are three-dimensional, even though they are drawn as planar arrows for clarity. The boundary red spins are kept fixed, while the boundary blue spins are rotated by a uniform angle $\theta = \pi/10$. Then, all spins on the boundary of the patch are held fixed, while the remaining spins in the system are relaxed to minimize the energy. The value of the stiffness of the clean FM in this protocol is $\rho_s^{(0)} \simeq 3.5$ in an arbitrary scale. **Right panel**: Spin stiffness correlations as a function of the distance. From the linear fit, we find $\Delta \simeq 0.2$ for $p = 0.03$ (for which $\rho_s = 2.4$) and $\Delta \sim 0.3$ for $p = 0.05$ (for which $\rho_s = 2.1$).

along the lower and left boundaries are kept fixed at their original orientations, as illustrated in Fig. 8.3. Then, the energy is minimized once again keeping the patch boundaries fixed. The local stiffness associated with a given patch centered in $\vec{x}$ is then measured as $\rho_s(\vec{x}) = \Delta E(\vec{x})/\theta^2$, where $\Delta E(\vec{x})$ is the energy increase due to the imposed twist. We used $(L/2)^2$ overlapping 10×10 patches in such a way to densely sampling the whole lattice.

We then measure the spatial correlations of $\rho_s(\vec{x})$ separating an average and a fluctuating part $\rho_s(\vec{x}) = \rho_s + \delta\rho(\vec{x})$, with $\delta\rho(\vec{x})$ zero averaged and correlated over disorder realizations. In the right panel of Fig. 8.3 we show that the correlation at fixed distance r is well fitted to decay logarithmically with the distance:

$$C(\vec{x}, \vec{x}') \simeq -\frac{\Delta}{2\pi} \ln\left(\mu|\vec{x} - \vec{x}'|\right) \ , \quad \mu \sim L^{-1} \ , \tag{8.19}$$

with an amplitude Δ increasing with p. This measure reveals that spatially uncorrelated bond disorder generates long-range, logarithmically correlated fluctuations of the spin stiffness. As we show below, this is precisely the marginal form of stiffness disorder capable of modifying the infrared magnon dynamics in two dimensions.

8.4.1. Effective field theory

The spin stiffness is a positive random function with long-range correlated fluctuations. We, however do not know its distribution. The purpose of this section is to set-up a field theory framework in which the distribution of $\rho_s(\vec{x})$ is found in a self-consistent way. The action (8.18) can be written as a magnon action [82, 268] and an interaction term between magnons and the static random field $\rho_s(\vec{x})$.

If we isolate an average value $\rho_s = \langle \rho_s(x) \rangle$, the bare magnon propagator is

$$\begin{aligned} G(\vec{x},t|\vec{x}',t') &= \langle \phi(\vec{x},t)\phi^*(\vec{x}',t') \rangle \\ &= \int \frac{d^2q d\omega}{(2\pi)^3} \frac{e^{i\vec{q}\cdot(\vec{x}-\vec{x}')-i\omega(t-t')}}{\omega - \rho_s q^2} \ , \end{aligned} \tag{8.20}$$

where $\langle (\cdot) \rangle$ denotes the average over the measure $\mathcal{D}\phi$. The density of states is related to the averaged propagator as:

$$\varrho(\omega) = \mathbb{E}\left[\frac{1}{\pi} \Re \int \frac{d^2k}{(2\pi)^2} G(k,\omega) \right] \ , \tag{8.21}$$

and its scaling properties can be read from the pole of G at the appropriate wavenumber k.

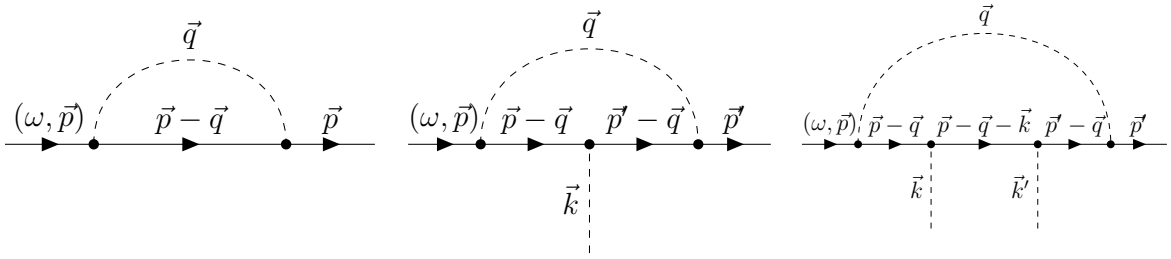

Figure 8.4.: One loop corrections to the model with random stiffness. The ϕ_a field is the continuous line, the σ field is the fluctuations of the stiffness. The ϕ_a field carries frequency ω and momentum $\vec{p}$. The frequency is conserved along the continuous line and we have indicated it only on the leftmost leg of the diagram.

To compute disorder-averaged correlation functions, we use the replica trick [60, 74]. For the propagator, one has:

$$\mathbb{E}[G(k,\omega)] = \mathbb{E}\left[\langle \phi_1(\vec{k},\omega)\phi_1^*(\vec{k},\omega) \rangle \right]_{n\to 0} \ , \tag{8.22}$$

where n is the number of replicas, eventually sent to zero.

We now define a reference, Gaussian random field $\sigma(\vec{x})$ such that the stiffness $\rho_s(\vec{x})$ is obtained as a function $f(\sigma(\vec{x}))$. In this way, if ρ_s is a Gaussian random field itself,

$f = \rho_s + g\sigma$, while, if the map is more complicated, for example to preserve the condition $\rho_s(\vec{x}) \geq 0$, the function f does the trick.

We can rewrite the two averages in (8.22) (over quantum fluctuations and over disorder) to be almost on the same footing by defining:

$$\mathbb{E}[\langle(\cdot)\rangle] = \int \mathcal{D}\phi\mathcal{D}\sigma \; e^{iS_n[\phi,\sigma]}(\cdot) \; , \tag{8.23}$$

in terms of a replicated action

$$\begin{aligned} S_n[\phi,\sigma] = i \int d^2x \frac{1}{2}(\nabla\sigma)^2 \\ + \int d^2x dt \sum_{a=1}^{n} \left[i\phi_a^* \partial_t \phi_a \, - \, f(\sigma)|\nabla\phi_a|^2 \right] \; . \end{aligned} \tag{8.24}$$

We included in the action the necessary term to reproduce the numerical observation (8.19). In fact, the σ correlator is:

$$\langle\sigma(\vec{x})\sigma(\vec{x}')\rangle = \int \frac{d^2q}{(2\pi)^2} \frac{e^{i\vec{q}\cdot(\vec{x}-\vec{x}')}}{q^2+\mu^2} \; , \tag{8.25}$$

where $\mu \sim L^{-1}$ acts as an infrared regulator, independent of f, courtesy of the limit $n \to 0$ (the magnon field does not feed back on the σ field). This expression reduces to (8.19) for $|\vec{x} - \vec{x}'| \ll 1/\mu \sim L$, and, therefore, $\Delta = g^2$ connects the effective field theory to our numerical evidence on the microscopic model.

By expanding $f(\sigma) = \rho_s + g_1\sigma + g_2\sigma^2 + ...$ in powers of σ, we notice that with a logarithmically correlated disorder all g_n's are dimensionless. Indeed, for this lagrangian, the bare scaling dimensions in momentum units are: $[x] = -1$, $[t] = -2$, $[\phi] = 1$, $[\sigma] = 0$, $[f] = 0$ so for all n, $[g_n] = 0$. [3]. The logarithmically correlated stiffness disorder numerically observed in Fig. 8.3 is instead marginal at the bare level, and its effect on the infrared theory must be determined beyond power counting.

8.4.2. One loop RG flow

The structure of divergences is independent of ω. This can be seen at one loop easily for example looking at the amplitude of the self-energy (see appendix 8.6). The divergence being logarithmic, the divergent part can be computed by setting $\omega = 0$ from the beginning. This is the same for every divergent diagram, which dresses all the couplings g_n.

[3] More generally, power-law correlations $C(r) \sim \Delta r^{-\alpha}$ would require $[\sigma] = -\alpha/2$ and all g_n, $n > 0$ are again irrelevant for any $\alpha > 0$.

All the logarithmic divergences therefore are the same ones as the theory

$$S_{div} = \int d^2x \left[\frac{i}{2}(\nabla\sigma)^2 - f(\sigma) \sum_{a=1}^{n} |\nabla\phi_a|^2 \right] . \tag{8.26}$$

By writing the complex field $\phi_a = \chi_a + i\psi_a$ and then collecting the fields σ, χ, ϕ into a $2n+1$-dimensional real field Φ_α, we can write this action as a non-linear sigma model (NLSM) on the target space $\mathbb{R}^{2n+1}$, and Euclidean weight e^{-S_E} with:

$$S_E \equiv -iS_{div} = \frac{1}{2} \int d^2x \, g_{\alpha\beta}(\sigma) \nabla\Phi^\alpha \cdot \nabla\Phi^\beta . \tag{8.27}$$

Following the usual treatment for the NLSM, we extract the $(2n+1)$-dimensional target space metric $g_{\alpha\beta}$:

$$g_{00} = 1 , \qquad g_{\alpha\beta} = -if(\sigma, \ell)\delta_{\alpha\beta} , \tag{8.28}$$

where the second equation is valid for any $\alpha, \beta > 0$ (0 being the index of the field σ). The function f has acquired a scale dependence which we wrote as $f(\sigma, \ell)$ and the microscopic, initial condition, is $f(\sigma, 0)$. Notice that the target space metric for the replica fields is purely imaginary due to the e^{iS} convention, but this is not an obstacle in the calculations.

We can then apply Friedan's solution of the one-loop RG [312] for the NLSM and write:

$$\frac{\partial g_{\alpha\beta}}{\partial \ell} = -\frac{1}{2\pi} R_{\alpha\beta} , \tag{8.29}$$

where $\ell = \ln(\mu_0/\mu)$ is the logarithmic RG scale, and $R_{\alpha\beta}$ is the Ricci tensor of the target manifold. Computing the Ricci tensor is easy (only a handful of terms are non-zero), after we realize this is an example of a $2n+1$-dimensional Friedmann-Robertson-Walker (FRW) metric and that moreover in the $n \to 0$ limit there is no feedback on the σ part of the metric. We are then left with a *functional* RG (FRG) equation for the function $f(\sigma, \ell)$

$$\frac{\partial f}{\partial \ell} = \frac{1}{4\pi} \left[f'' - \frac{(f')^2}{f} \right] . \tag{8.30}$$

This contains the evolution of all the couplings of the theory at the one-loop level. It is worth noticing that, passing to $h = \ln f$ this is nothing but the heat equation

$$\frac{\partial h}{\partial \ell} = \frac{1}{4\pi} \frac{\partial^2 h}{\partial \sigma^2} . \tag{8.31}$$

The couplings can be defined as the derivatives of $f(\sigma, \ell)$. It is straightforward to see that the solution of Eq. (8.31) with an initial condition $f(\sigma, 0) = \rho_s + g\sigma$ is in general complex, due to the branch cut of $h = \ln f$. This is due to the fact that for $g\sigma < -\rho_s$, the $|\nabla\phi|^2$ term in the action becomes negative, and this signals an instability of the theory. This is an artifact of the choice of f. Of course, if the classical configuration has to be a minimum the function $f(\sigma, 0)$ is ≥ 0 for every configuration of disorder $\sigma(\vec{x})$, so our choice of a linear function is poor. Starting from an $f(\sigma, 0) \geq 0$, under the FRG all these functions will converge to the fixed points of the FRG flow.

The fixed points of the FRG form a two-parameters family

$$h_\infty(\sigma) = a + b\sigma \ , \tag{8.32}$$

which means

$$f_\infty(\sigma) = e^{a+b\sigma} \ . \tag{8.33}$$

It is also possible to see that a linear h_∞ is also the fixed point of the *2-loop FRG equation* (see appendix 8.6). We conjecture then that it is the *exact solution* of the all-loop FRG equations, a conformal field theory (CFT) which we write now for completeness

$$\begin{aligned} S_\lambda = &\int d^2x \frac{i}{2}(\nabla\sigma)^2 \\ &+ \int d^2x\, dt \sum_{a=1}^{n} \left[i\phi_a^* \partial_t \phi_a - e^{a+b\,\sigma} |\nabla\phi_a|^2 \right] \ . \end{aligned} \tag{8.34}$$

The subscript λ identifies the free parameter of the CFT which we now define. Since σ is the Gaussian random function, the coefficient $f(\sigma)$ is *a log-normal random variable*. This remarkable, exact result allows us to explain the observed numerics. First of all, notice that since σ is Gaussian, a standard result in CFT guarantees a vanishing spin stiffness:

$$\langle f(\sigma, \ell) \rangle = \exp\left(a + \frac{b^2}{2} \langle \sigma(\vec{x})^2 \rangle \right) = e^a L^\lambda \ , \tag{8.35}$$

where $\langle \sigma(\vec{x})^2 \rangle \simeq \frac{1}{2\pi} \ln(L)$ follows from (8.25) and (8.19) and $\lambda = b^2/4\pi$.

Since this quantity represents the energy change in the boundary conditions it must be $O(1)$. So we must choose $e^a = L^{-\lambda}$ as a normalization and the stiffness is $\rho_s = f(0, \ell) = L^{-\lambda}$.

Now, since we have seen that at no order is $\phi^* \partial_t \phi$ renormalized, the dispersion at $k \sim 1/L$ keeps the form:

$$\omega(k) = \rho_s(k) k^2 \to k^{2+\lambda} \ , \tag{8.36}$$

where the running coupling ρ_s is computed at the inverse momentum scale, $\ell \simeq -\ln k$,

of the modes we are looking at. Eq. (8.36) yields our main result: a relation between the scale-dependent dynamical exponent z and the dimensionless coupling λ:

$$z = 2 + \lambda > 2 \, . \tag{8.37}$$

The identification of the coupling λ with the measured $z - 2$ is now in principle possible, since λ is a free parameter of the CFT, and it can be extracted from the numerics. It is worth noticing that the measured values of $\lambda = z - 2$ for $L \leq 90$ plateau at around 0.3 upon increasing p . It is possible that the theory for $\lambda > \lambda_c \simeq 0.3$ is unstable toward a spin glass state.

8.5. Conclusion

Although, at the present time, the prediction of the field theory does not match quantitatively the numerical results, they still provide a clear picture on the physical mechanism governing the increase of the dynamical exponent due to the presence of weak disorder. This mismatch could be due to the presence of large irrelevant corrections in the microscopic model that prevents us from identifying correctly the low energy behavior, or, on the other hand, to the fact that the theory flows very slowly toward the disordered phase. We are more inclined toward the first scenario, but additional confirmations are needed.
A finite order parameter coexisting with a vanishing stiffness has analogues in other systems, the amplitude of the order parameter and the associated rigidity being logically independent quantities. In strongly disordered superconducting films, the pairing amplitude survives locally while the superfluid stiffness is suppressed and drives the superconductor-insulator transition [313, 314]; in two-dimensional melting, unbinding dislocations drive the renormalized shear modulus to zero while local crystalline order persists [315–317]; in pinned flux lattices, quasi-long-range order coexists with anomalous, scale-dependent elasticity [318, 319]. In the superconducting case, however, the loss of rigidity requires strong disorder; here the stiffness flows to zero for arbitrarily weak disorder, as a consequence of the double marginality of two dimensions: the stiffness is dimensionless, and the emergent logarithmically correlated disorder is exactly marginal. The same mechanism should operate in any two-dimensional system with a continuous order parameter and dilute local frustration.

Our result should also be reminiscent of that of S. Chakravarty [320], who, motivated by the analogy with the scale-free conductance fluctuations found by Altshuler, Kravtsov, and Lerner [321], considered a clean two-dimensional Heisenberg ferromag-

net at $T > 0$, on scales smaller than the correlation length. By integrating out the high-energy magnons, Chakravarty found, at one loop, a reduction of the global spin stiffness and a growth of its fluctuations. The reduction found here is similar, but instead of flowing to the paramagnet (the fixed point of the clean ferromagnet at $T > 0$), our model flows to a phase with zero stiffness, reminiscent of a weakly ordered Griffiths phase [322–325].

It is worth mentioning that our results, being confined to the quadratic magnon Hamiltonian, are valid both for the quantum and the *classical* Heisenberg model. In fact, while the eigenstates are different, the spectrum of the Bogoljubov Hamiltonian is the same as the dynamical matrix of the classical model. Since the $s = 1/2$ case will contain $1/s$ corrections that correspond to magnon interactions, we know from studies of many-body localization [269, 271] that interactions might destroy localization and restore hydrodynamics. Our work poses the basis for the study of the interacting, small-s model as well.

8.6. Appendix of Chapter 8

8.6.1. One-loop self-energy and vertex computation

We evaluate the one-loop corrections to the stiffness ρ_s and the coupling g, from the corresponding diagrams in Fig. 8.4. For this one-loop computation, we adopt a UV cutoff regularization scheme. The self-energy can then be computed as:

$$\begin{aligned}\Sigma_1(p,\omega) = (-ig)^2 \int^{\Lambda} \frac{d^2q}{(2\pi)^2} \frac{1}{q^2+\mu^2} \\ \times \frac{i(\vec{p}\cdot(\vec{p}-\vec{q}))^2}{\omega - \rho_s(\vec{p}-\vec{q})^2} ,\end{aligned} \tag{8.38}$$

where Λ is the UV cutoff. By extracting the UV divergent part of the integral, we find the following expression:

$$\Sigma_1(p,\omega) = \frac{ig^2}{4\pi\rho_s} \ln\left(\frac{\Lambda}{\mu}\right) p^2 + \text{finite} , \tag{8.39}$$

which is independent of ω, meaning that the time derivative part of the action is not renormalized at one loop. All 1PR (*one particle reducible*) diagrams of this kind appearing at higher orders in the perturbative expansion can be resummed through the Dyson equation. Eventually, the one-loop renormalized magnon propagator has the following expression:

$$G_{\Lambda,\mu}(q,\omega) = \frac{i}{\omega - \rho_s\left(1 - \frac{g^2}{4\pi\rho_s^2}\ln(\Lambda/\mu)\right)q^2} , \tag{8.40}$$

from which we extract the one-loop correction to the stiffness:

$$\rho_s \to \rho_s - \frac{g^2}{4\pi\rho_s}\ln\frac{\Lambda}{\mu} . \tag{8.41}$$

The coupling g receives corrections from the following one-loop integral:

$$\begin{aligned}A_{\Lambda,\mu}(\vec{p},\vec{p}',\omega) = (-ig)^3 \int^{\Lambda} \frac{d^2q}{(2\pi)^2} \frac{1}{q^2+\mu^2} \\ \times \frac{i^2\vec{p}\cdot(\vec{p}-\vec{q})(\vec{p}-\vec{q})\cdot(\vec{p}'-\vec{q})(\vec{p}'-\vec{q})\cdot\vec{p}'}{(\omega-\rho_s(\vec{p}-\vec{q})^2)(\omega-\rho_s(\vec{p}'-\vec{q}')^2)} ,\end{aligned} \tag{8.42}$$

from which we extract the UV divergent part:

$$A_{\Lambda,\mu}(\vec{p},\vec{p}',\omega) = -\frac{ig^3}{4\pi\rho_s^2}\ln\left(\frac{\Lambda}{\mu}\right)(\vec{p}\cdot\vec{p}') + \text{finite} . \tag{8.43}$$

Since the vertex function structure is $-igs(\vec{p}\cdot\vec{p}')$, the disorder coupling g is corrected as:

$$g \to g + \frac{g^3}{4\pi\rho_s^2}\ln\frac{\Lambda}{\mu}\ . \tag{8.44}$$

8.6.2. Exact solution of the NLSM

The exact one-loop FRG flow equation for the metric tensor of the target space manifold is (8.29). We need to compute the Ricci tensor for the metric defined in (8.28). For a generic metric $g_{\alpha\beta}$, the Ricci tensor is given by

$$R_{\alpha\beta} = \partial_\gamma\Gamma^\gamma_{\alpha\beta} - \partial_\beta\Gamma^\gamma_{\alpha\gamma} + \Gamma^\gamma_{\gamma\delta}\Gamma^\delta_{\alpha\beta} - \Gamma^\gamma_{\beta\delta}\Gamma^\delta_{\alpha\gamma}\ , \tag{8.45}$$

in terms of the Christoffel symbols

$$\Gamma^\gamma_{\alpha\beta} = \frac{1}{2}g^{\gamma\delta}(\partial_\alpha g_{\delta\beta} + \partial_\beta g_{\alpha\delta} - \partial_\delta g_{\alpha\beta})\ . \tag{8.46}$$

Since the metric is diagonal, it is easy to find that the only non-vanishing Christoffel symbols are for $\alpha,\beta > 0$:

$$\Gamma^0_{\alpha\beta} = -\frac{1}{2}F'(\sigma)\delta_{\alpha\beta} \tag{8.47}$$

$$\Gamma^\alpha_{0\beta} = \Gamma^\alpha_{\beta 0} = \frac{F'(\sigma)}{2F(\sigma)}\delta^\alpha_\beta\ , \tag{8.48}$$

where $F(\sigma) = -if(\sigma)$, and the prime denotes the derivative with respect to σ. Then, we compute the Ricci tensor components:

$$R_{00} = -n\frac{F''}{F} + \frac{n}{2}\frac{(F')^2}{F^2} \tag{8.49}$$

$$R_{\alpha\beta} = \left[-\frac{1}{2}F'' + \frac{1-n}{2}\frac{(F')^2}{F}\right]\delta_{\alpha\beta}\ , \tag{8.50}$$

while the mixed components vanish: $R_{0\alpha} = R_{\alpha 0} = 0$. By plugging these expressions into Friedan's equation (8.29), substituting back f and canceling the i prefactors from both sides of the equation, we find

$$\frac{\partial f(\sigma,\ell)}{\partial\ell} = \frac{1}{4\pi}\left[f''(\sigma,\ell) - (1-n)\frac{(f'(\sigma,\ell))^2}{f(\sigma,\ell)}\right]\ , \tag{8.51}$$

which reduces to (8.30) in the limit $n \to 0$. The heat equation (8.31) follows by replacing $f = e^h$.

Expanding f in powers of σ gives the one-loop RG equations for the couplings of

the theory. One can easily see that, at order σ, by writing $f(\sigma) = \rho_s + g\sigma + O(\sigma^2)$, one finds the same RG equations for ρ_s and g, which can be obtained from the UV divergences of diagrams in Fig. 8.4:

$$\frac{\partial \rho_s}{\partial \ell} = -\frac{g^2}{4\pi\rho_s} , \tag{8.52}$$

$$\frac{\partial g}{\partial \ell} = \frac{g^3}{4\pi\rho_s^2} . \tag{8.53}$$

The two-loop FRG flow is described by Friedan's equation [312]:

$$\frac{\partial g_{\alpha\beta}}{\partial \ell} = -\frac{1}{2\pi} R_{\alpha\beta} - \frac{1}{8\pi^2} T_{\alpha\beta} , \tag{8.54}$$

where $T_{\alpha\beta} = R_{\alpha\gamma\delta\eta} R_{\beta}^{\gamma\delta\eta}$ and $R_{\alpha\gamma\delta\eta}$ is the Riemann tensor, which is defined as

$$R_{\alpha\beta\gamma\delta} = g_{\alpha\eta} \left(\partial_\gamma \Gamma^\eta_{\beta\delta} - \partial_\delta \Gamma^\eta_{\beta\gamma} + \Gamma^\eta_{\gamma\zeta} \Gamma^\zeta_{\beta\delta} - \Gamma^\eta_{\delta\zeta} \Gamma^\zeta_{\beta\gamma} \right) . \tag{8.55}$$

After computing $R_{\alpha\beta\gamma\delta}$ and its contractions for the metric (8.28), we obtain the following equation for the function $f(\sigma, \ell)$ in the limit $n \to 0$:

$$\frac{\partial f}{\partial \ell} = \frac{1}{4\pi} \left(f'' - \frac{(f')^2}{f} \right) \left[1 - \frac{1}{4\pi} \frac{f''}{f} \right] , \tag{8.56}$$

and in terms of the function $h = \ln f$:

$$\frac{\partial h}{\partial l} = \frac{1}{4\pi} \frac{\partial^2 h}{\partial \sigma^2} \left[1 - \frac{1}{4\pi} \left(\frac{\partial^2 h}{\partial \sigma^2} + \left(\frac{\partial h}{\partial \sigma} \right)^2 \right) \right] . \tag{8.57}$$

9. Conclusions and future directions

In the last Chapter of this thesis, we summarize the results obtained and discuss possible outlooks. In the first part of the work, we studied the renormalization group scaling theory of the many body localization transition. We presented an extended and comprehensive discussion on the possible scenarios that appear when investigating the scaling theory of localization. The single-particle Anderson transition is described by a single-parameter scaling scenario, where the renormalization group flow follows a single equation and the critical fixed point is deformed by a single RG-relevant operator. Interestingly, this scenario must be modified when the model is defined on a random regular graph, which is the lattice proxy for infinite dimensions, and where the connectivity of a node scales exponentially, as opposed to a finite dimensional geometry. In this case the renormalization group flow is described by a family of coupled equations that depend on two parameters. The critical point is localized and sits at the end of a line of localized points, each one being an attractive fixed point for the RG dynamics. By means of exact diagonalization, we investigated the scaling theory of two models where the interplay between localization and interactions is very relevant. First, we considered the case of the random-field spin-1/2 Heisenberg chain, a prototypical model for many body localization. In this case, we showed that a two-parameter scaling describes well the numerical data, which are restricted to small system sizes, due to the intrinsic difficulty of the problem and the absence of reliable numerical methods that allow one to circumvent this. Although we cannot locate the critical point with great accuracy, we argued that a two-parameter ansatz describes much better the finite size scaling compared to the one-parameter scaling. This analysis has two remarkable physical consequences: first, this result points toward the formal analogy between the single-particle Anderson model on a tree-like graph and interacting disordered fermions in one dimension; and second, the two-parameter scaling scenario was already conjectured in a series of recent works that considered a phenomenological, strong-disordered renormalization group approach to describe the many body localization phase transition, and our work set the ground for a microscopical derivation of the same phenomenology.

Then, we considered the case of the quantum random energy model, an interacting

disordered spin chain where energy correlations are artificially suppressed and substituted with gaussian distributed random values. This system, which retains many of the interesting physical properties both of localization and of spin glasses, has a peculiar dynamical phase diagram: at zero energy density the system is ergodic for any value of the disorder strength. We showed that at finite energy the scaling of the model is well described by the two-parameter scenario and, upon an appropriate rescaling of the couplings in the Hamiltonian, it is possible to induce a localization transition even at zero energy, described by the same scaling theory. This result adds more confirmation to the scenario where the universality class of the random regular graph describes the many body localization transitions. We believe that this universal picture that we partially unveiled is indeed very solid and could provide a unified framework to tackle the many body localization problem. Future directions comprise the application of this analysis tool to other models, such as the quasiperiodic Heisenberg chain and the disordered Floquet Ising chain. More importantly, we plan to develop a field theoretical renormalization group analysis of the Anderson model on the Bethe lattice: by exploiting the supersymmetric formulation of the problem, we aim to see if the two-parameter scaling can be recovered also in this case. This result would strengthen our understanding of the problem considerably and provide a bridge between numerical observations and theoretical understanding.

In the second part of the thesis, we investigated the rich physics of two dimensional disordered quantum spin models. First, we studied the zero-temperature, quantum phase diagram of the bond disordered Heisenberg quantum spin 1/2 model, resorting to a neural quantum states variational method. This state-of-the-art technique allowed us to consider system sizes unreachable by any other numerical scheme and showed the presence of an extended parameter region hosting a zero temperature quantum spin glass phase. Parallel to this, we investigated the model by means of a spin-wave expansion starting from the minimum energy states of the analogous classical problems, where, in the absence of thermal fluctuations, the system is (trivially) a spin glass. This effective, semiclassical theory allows one to compute the quantum correction to the classical order parameter, its strength given by the inverse spin representation. Remarkably, extrapolating the large S expansion to $S = 1/2$, we obtain a value of the spin glass order parameter that is in excellent agreement with the neural quantum state result. This strengthens our findings a lot, since the two methods rely on completely different formulations and allow us to confidently claim the existence of a quantum spin glass phase in the model.
The spin-wave Hamiltonian governing the semiclassical expansion is itself very inter-

esting to analyze. We studied the localization properties, finding that the dynamical phase diagram of the system is governed by the presence of magnetic order. For low enough disorder, low energy excitations are extended and separated from localized, high energy excitations, while in the spin glass phase the entire spectrum is weakly localized. This posed a conceptual problem, since in a glassy, symmetry-broken state we expect Goldstone modes and transport. However, we claimed that this picture is immediately recovered, and ergodicity restored, by the addition of interactions, which correspond to higher order terms in the expansion. We are currently working on two parallel directions to investigate the dynamics of the quantum Heisenberg spin glass: on one hand we plan to implement a density matrix renormalization group simulation to study the exact dynamics of low energy excitations, and on the other hand we aim to develop in more detail (and test its limits) the truncated Hilbert space method, which we discussed in Chapter 7, that allows one to incorporate higher order interactions into an effective Hamiltonian. In the future, we plan to extend this study to the disordered, two-dimensional XY model, which is highly relevant to the physics of disordered superconductors. We also plan to investigate in greater detail the classical problem, which has received little attention in the past. Although this class of models is fragile against thermal fluctuations, its zero-temperature energy landscape is nonetheless of great interest, since it supports an exponential number of states. This gives rise to highly non-trivial phenomena, governed by the complexity of the problem and the scaling of the barriers, which we plan to study further, both numerically and analytically.

Lastly, we focused on the study of the Heisenberg model in the low-disorder regime, where it can be treated as a perturbation of the clean ferromagnet. The main effect of the disorder is to produce an abundance of low energy modes, that modify the dynamical exponent of the theory. We developed a field theoretical approach, physically motivated by numerically measuring the spin-stiffness correlations, that yields a description of this phenomenon.

Bibliography

[1] J. Niedda, A. Coraggio, G. Bracci-Testasecca, and A. Scardicchio, Vanishing spin stiffness in weakly disordered two-dimensional heisenberg ferromagnets, (2026), arXiv:2607.20036 [cond-mat.dis-nn] .

[2] G. Bracci-Testasecca, J. Niedda, A. Coraggio, R. Moessner, and A. Scardicchio, Semiclassical picture of the heisenberg spin glass in two dimensions: from weak localization to hydrodynamics, (2026), arXiv:2603.22077 [cond-mat.dis-nn] .

[3] J. Niedda, G. Bracci Testasecca, G. Magnifico, F. Balducci, C. Vanoni, and A. Scardicchio, *Renormalization group analysis of the many-body localization transition in the random-field xxz chain,* Phys. Rev. B **112**, 144201 (2025).

[4] L. L. Viteritti, R. Rende, G. Bracci-Testasecca, J. Niedda, R. Moessner, G. Carleo, and A. Scardicchio, *Quantum spin glass in the two-dimensional disordered Heisenberg model via foundation neural-network quantum states,* arXiv:2507.05073 (2024).

[5] F. Balducci, G. Bracci-Testasecca, J. Niedda, A. Scardicchio, and C. Vanoni, *Scaling analysis and renormalization group on the mobility edge in the quantum random energy model,* Phys. Rev. B **111**, 214206 (2025).

[6] G. D. Birkhoff, *Proof of the ergodic theorem,* Proceedings of the National Academy of Sciences **17**, 656 (1931).

[7] J. von Neumann, *Proof of the quasi-ergodic hypothesis,* Proceedings of the National Academy of Sciences **18**, 70 (1932).

[8] V. I. Arnold and A. Avez, *Ergodic Problems of Classical Mechanics* (W. A. Benjamin, New York, 1968).

[9] J. M. Deutsch, *Eigenstate thermalization hypothesis,* Reports on Progress in Physics **81**, 082001 (2018).

[10] M. Srednicki, *Chaos and quantum thermalization,* Physical review e **50**, 888 (1994).

[11] J. von Neumann, *Beweis des ergodensatzes und des H-theorems in der neuen Mechanik,* Zeitschrift für Physik **57**, 30 (1929).

[12] S. Goldstein, J. L. Lebowitz, R. Tumulka, and N. Zanghì, *Long-time behavior of macroscopic quantum systems: Commentary accompanying the english translation of john von neumann's 1929 article on the quantum ergodic theorem,* European Physical Journal H **35**, 173 (2010).

[13] E. P. Wigner, *Characteristic vectors of bordered matrices with infinite dimensions,* Annals of Mathematics **62**, 548 (1955).

[14] F. J. Dyson, *The threefold way. algebraic structure of symmetry groups and ensembles in quantum mechanics,* Journal of Mathematical Physics **3**, 1199 (1962).

[15] O. Bohigas, M. J. Giannoni, and C. Schmit, *Characterization of chaotic quantum spectra and universality of level fluctuation laws,* Physical Review Letters **52**, 1 (1984).

[16] J. M. Deutsch, *Quantum statistical mechanics in a closed system,* Physical Review A **43**, 2046 (1991).

[17] M. Srednicki, *Chaos and quantum thermalization,* Physical Review E **50**, 888 (1994).

[18] L. D'Alessio, Y. Kafri, A. Polkovnikov, and M. Rigol, *From quantum chaos and eigenstate thermalization to statistical mechanics and thermodynamics,* Advances in Physics **65**, 239 (2016).

[19] M. Rigol, V. Dunjko, and M. Olshanii, *Thermalization and its mechanism for generic isolated quantum systems,* Nature **452**, 854 (2008).

[20] H. Bernien, S. Schwartz, A. Keesling, H. Levine, A. Omran, H. Pichler, S. Choi, A. S. Zibrov, M. Endres, M. Greiner, V. Vuletić, and M. D. Lukin, *Probing many-body dynamics on a 51-atom quantum simulator,* Nature **551**, 579 (2017).

[21] C. J. Turner, A. A. Michailidis, D. A. Abanin, M. Serbyn, and Z. Papić, *Weak ergodicity breaking from quantum many-body scars,* Nature Physics **14**, 745 (2018).

[22] P. W. Anderson, *Absence of Diffusion in Certain Random Lattices,* Phys. Rev. **109**, 1492 (1958).

[23] N. F. Mott, *Electrons in disordered structures,* Advances in Physics **16**, 49 (1967).

[24] E. Abrahams, P. W. Anderson, D. C. Licciardello, and T. V. Ramakrishnan, *Scaling Theory of Localization: Absence of Quantum Diffusion in Two Dimensions,* Phys. Rev. Lett. **42**, 673 (1979).

[25] J. T. Chalker and G. J. Daniel, *Scaling, Diffusion, and the Integer Quantized Hall Effect ,* Phys. Rev. Lett. **61**, 593 (1988).

[26] J. T. Chalker, *Scaling and eigenfunction correlations near a mobility edge ,* Physica A: Statistical Mechanics and its Applications **167**, 253 (1990).

[27] F. Evers and A. D. Mirlin, *Anderson transitions,* Reviews of Modern Physics **80**, 1355 (2008).

[28] J. T. Chalker, V. E. Kravtsov, and I. V. Lerner, *Spectral rigidity and eigenfunction correlations at the Anderson transition,* Journal of Experimental and Theoretical Physics Letters **64**, 386–392 (1996).

[29] B. L. Altshuler, V. E. Kravtsov, and I. V. Lerner, *Statistical properties of mesoscopic fluctuations and similarity theory,* JETP Lett. **43**, 441 (1986).

[30] B. L. Altshuler, V. E. Kravtsov, and I. V. Lerner, *Statistics of mesoscopic fluctuations and instability of one-parameter scaling,* Zh. Eksp. Teor. Fiz. **91**, 2276 (1986).

[31] B. L. Altshuler, V. E. Kravtsov, and I. V. Lerner, *Mesoscopic phenomena in solids* (Elsiever, 1991) p. 449.

[32] J. Billy *et al.*, *Direct observation of anderson localization of matter waves in a controlled disorder,* Nature **453**, 891 (2008).

[33] G. Roati *et al.*, *Anderson localization of a non-interacting bose-einstein condensate,* Nature **453**, 895 (2008).

[34] S. S. Kondov, W. R. McGehee, J. J. Zirbel, and B. DeMarco, *Three-dimensional anderson localization of ultracold matter,* Science **334**, 66 (2011).

[35] F. Jendrzejewski *et al.*, *Three-dimensional localization of ultracold atoms in an optical disordered potential,* Nature Physics **8**, 398 (2012).

[36] G. Semeghini *et al.*, *Measurement of the mobility edge for 3d anderson localization,* Nature Physics **11**, 554 (2015).

[37] M. White *et al.*, *Observation of two-dimensional anderson localisation of ultracold atoms,* Nature Communications **11**, 4942 (2020).

[38] A. Lagendijk, B. van Tiggelen, and D. S. Wiersma, *Fifty years of anderson localization,* Physics Today **62**, 24 (2009).

[39] L. Fleishman and P. W. Anderson, *Interactions and the Anderson transition,* Phys. Rev. B **21**, 2366 (1980).

[40] D. Basko, I. Aleiner, and B. Altshuler, *Metal–insulator transition in a weakly interacting many-electron system with localized single-particle states,* Ann. Phys. (Amsterdam) **321**, 1126 (2006).

[41] V. Oganesyan and D. A. Huse, *Localization of interacting fermions at high temperature,* Phys. Rev. B **75**, 155111 (2007).

[42] A. Pal and D. A. Huse, *Many-body localization phase transition,* Phys. Rev. B **82**, 174411 (2010).

[43] M. Serbyn, Z. Papić, and D. A. Abanin, *Local conservation laws and the structure of the many-body localized states,* Physical review letters **111**, 127201 (2013).

[44] D. A. Huse, R. Nandkishore, and V. Oganesyan, *Phenomenology of fully many-body-localized systems,* Phys. Rev. B **90**, 174202 (2014).

[45] V. Ros, M. Müller, and A. Scardicchio, *Integrals of motion in the many-body localized phase,* Nuclear Physics B **891**, 420 (2015).

[46] J. Z. Imbrie, V. Ros, and A. Scardicchio, *Local integrals of motion in many-body localized systems,* Ann. Phys. (Berlin) **529**, 1600278 (2017).

[47] M. Schreiber, S. S. Hodgman, P. Bordia, H. P. Lüschen, M. H. Fischer, R. Vosk, E. Altman, U. Schneider, and I. Bloch, *Observation of many-body localization of interacting fermions in a quasirandom optical lattice,* Science **349**, 842 (2015).

[48] J.-y. Choi, S. Hild, J. Zeiher, P. Schauß, A. Rubio-Abadal, T. Yefsah, V. Khemani, D. A. Huse, I. Bloch, and C. Gross, *Exploring the many-body localization transition in two dimensions,* Science **352**, 1547 (2016).

[49] J. Smith, A. Lee, P. Richerme, B. Neyenhuis, P. W. Hess, P. Hauke, M. Heyl, D. A. Huse, and C. Monroe, *Many-body localization in a quantum simulator with programmable random disorder,* Nature Physics **12**, 907 (2016).

[50] P. Roushan, C. Neill, J. Tangpanitanon, V. M. Bastidas, A. Megrant, R. Barends, Y. Chen, Z. Chen, B. Chiaro, A. Dunsworth, A. Fowler, B. Foxen, M. Giustina, E. Jeffrey, J. Kelly, E. Lucero, J. Mutus, M. Neeley, C. Quintana, D. Sank,

A. Vainsencher, J. Wenner, T. White, H. Neven, D. G. Angelakis, and J. Martinis, *Spectroscopic signatures of localization with interacting photons in superconducting qubits,* Science **358**, 1175 (2017).

[51] A. Lukin, M. Rispoli, R. Schittko, M. E. Tai, A. M. Kaufman, S. Choi, V. Khemani, J. Léonard, and M. Greiner, *Probing entanglement in a many-body-localized system,* Science **364**, 256 (2019).

[52] M. Rispoli, A. Lukin, R. Schittko, S. Kim, M. E. Tai, J. Léonard, and M. Greiner, *Quantum critical behaviour at the many-body localization transition,* Nature **573**, 385 (2019).

[53] W. D. Roeck, L. Giacomin, F. Huveneers, and O. Prosniak, Absence of normal heat conduction in strongly disordered interacting quantum chains, (2025), arXiv:2408.04338 [math-ph] .

[54] J. Šuntajs, J. Bonča, T. Prosen, and L. Vidmar, *Quantum chaos challenges many-body localization,* Phys. Rev. E **102**, 062144 (2020).

[55] D. Sels and A. Polkovnikov, *Dynamical obstruction to localization in a disordered spin chain,* Phys. Rev. E **104**, 054105 (2021).

[56] D. Sels and A. Polkovnikov, *Thermalization of dilute impurities in one-dimensional spin chains,* Phys. Rev. X **13**, 011041 (2023).

[57] W. De Roeck and F. Huveneers, *Stability and instability towards delocalization in many-body localization systems,* Phys. Rev. B **95**, 155129 (2017).

[58] T. Thiery, F. Huveneers, M. Müller, and W. De Roeck, *Many-body delocalization as a quantum avalanche,* Phys. Rev. Lett. **121**, 140601 (2018).

[59] J. Léonard, S. Kim, M. Rispoli, A. Lukin, R. Schittko, J. Kwan, E. Demler, D. Sels, and M. Greiner, *Probing the onset of quantum avalanches in a many-body localized system,* Nature Physics **19**, 481 (2023).

[60] M. Mézard, G. Parisi, and M. A. Virasoro, *Spin glass theory and beyond: An Introduction to the Replica Method and Its Applications*, Vol. 9 (World Scientific Publishing Company, 1987).

[61] J. A. Mydosh, *Spin Glasses: an Experimental Introduction* (CRC Press, 1993).

[62] G. Parisi, *Nobel lecture: Multiple equilibria,* Reviews of Modern Physics **95**, 030501 (2023).

[63] S. F. Edwards and P. W. Anderson, *Theory of spin glasses,* Journal of Physics F: Metal Physics **5**, 965 (1975).

[64] J. A. Mydosh, *Spin Glasses: An Experimental Introduction* (Taylor & Francis, 1993).

[65] J. Vannimenus and G. Toulouse, *Theory of the frustration effect. ii. ising spins on a square lattice,* Journal of Physics C: Solid State Physics **10**, L537 (1977).

[66] E. Vincent, J. Hammann, M. Ocio, J.-P. Bouchaud, and L. F. Cugliandolo, *Slow dynamics and aging in spin glasses,* Complex Behaviour of Glassy Systems (1997).

[67] K. Jonason, E. Vincent, J. Hammann, J. P. Bouchaud, and P. Nordblad, *Memory and chaos effects in spin glasses,* Phys. Rev. Lett. **81**, 3243 (1998).

[68] G. Parisi, *Toward a mean field theory for spin glasses,* Phys. Lett. A **73**, 203 (1979).

[69] G. Parisi, *A sequence of approximated solutions to the S-K model for spin glasses,* J. Phys. A: Math. Gen. **13**, L115 (1980).

[70] G. Parisi, *The order parameter for spin glasses: a function on the interval 0-1,* J. Phys. A: Math. Gen. **13**, 1101 (1980).

[71] A. J. Bray and M. A. Moore, *Replica theory of quantum spin glasses,* Journal of Physics C: Solid State Physics **13**, L655 (1980).

[72] M. Mézard, G. Parisi, N. Sourlas, G. Toulouse, and M. Virasoro, *Nature of the spin-glass phase,* Phys. Rev. Lett. **52**, 1156 (1984).

[73] D. Sherrington and S. Kirkpatrick, *Solvable model of a spin-glass,* Phys. Rev. Lett. **35**, 1792 (1975).

[74] K. Efetov, *Supersymmetry in Disorder and Chaos* (Cambridge University Press, 1996).

[75] D. S. Fisher and D. A. Huse, *Ordered phase of short-range ising spin-glasses,* Phys. Rev. Lett. **56**, 1601 (1986).

[76] D. S. Fisher and D. A. Huse, *Equilibrium behavior of the spin-glass ordered phase,* Phys. Rev. B **38**, 386 (1988).

[77] M. A. Moore, *The stability of the replica-symmetric state in finite-dimensional spin glasses,* Journal of Physics A: Mathematical and General **38**, L783 (2005).

[78] C. D. Dominicis and I. Giardina, *Random Fields and Spin Glasses: a Field Theory Approach* (Cambridge University Press, Hardback, 2006).

[79] M. A. Moore and A. J. Bray, *Disappearance of the de almeida-thouless line in six dimensions,* Phys. Rev. B **83**, 224408 (2011).

[80] J. J. Ruiz-Lorenzo, *Nature of the Spin Glass Phase in Finite Dimensional (Ising) Spin Glasses,* in *Order, Disorder and Criticality. Advanced Problems of Phase Transition Theory. Volume 6*, edited by Y. Holovatch (World Scientific Connect, 2020) Chap. 1.

[81] M. C. Angelini, C. Lucibello, G. Parisi, G. Perrupato, F. Ricci-Tersenghi, and T. Rizzo, *Unexpected upper critical dimension for spin glass models in a field predicted by the loop expansion around the Bethe solution at zero temperature,* Phys. Rev. Lett. **128**, 075702 (2022).

[82] A. Auerbach, *Interacting Electrons and Quantum Magnetism* (Springer, New York, NY, 1994).

[83] S. Sachdev, *Quantum Phase Transitions*, 2nd ed. (Cambridge University Press, 2011).

[84] R. Moessner and A. P. Ramirez, *Geometrical frustration,* Physics Today **59**, 24 (2006).

[85] N. Read and S. Sachdev, *Valence-bond and spin-peierls ground states of low-dimensional quantum antiferromagnets,* Physical Review Letters **62**, 1694 (1989).

[86] D. S. Rokhsar and S. A. Kivelson, *Superconductivity and the quantum hard-core dimer gas,* Phys. Rev. Lett. **61**, 2376 (1988).

[87] R. Moessner and S. L. Sondhi, *Resonating valence bond phase in the triangular lattice quantum dimer model,* Phys. Rev. Lett. **86**, 1881 (2001).

[88] F. Becca and S. Sorella, *Quantum Monte Carlo Approaches for Correlated Systems* (Cambridge University Press, 2017).

[89] P. W. Anderson, *Resonating valence bonds: A new kind of insulator?* Materials Research Bulletin **8**, 153 (1973).

[90] L. Balents, *Spin liquids in frustrated magnets,* Nature **464**, 199 (2010).

[91] L. Savary and L. Balents, *Quantum spin liquids: a review,* Reports on Progress in Physics **80**, 016502 (2017).

[92] Y. Zhou, K. Kanoda, and T.-K. Ng, *Quantum spin liquid states,* Reviews of Modern Physics **89**, 025003 (2017).

[93] J. Knolle and R. Moessner, *A field guide to spin liquids,* Annual Review of Condensed Matter Physics **10**, 451 (2019).

[94] Y. Iqbal, F. Becca, S. Sorella, and D. Poilblanc, *Gapless spin-liquid phase in the kagome spin-$\frac{1}{2}$ heisenberg antiferromagnet,* Phys. Rev. B **87**, 060405(R) (2013).

[95] W.-J. Hu, F. Becca, A. Parola, and S. Sorella, *Direct evidence for a gapless z_2 spin liquid by frustrating néel antiferromagnetism,* Phys. Rev. B **88**, 060402(R) (2013).

[96] Y. Iqbal, W.-J. Hu, R. Thomale, D. Poilblanc, and F. Becca, *Spin liquid nature in the heisenberg j_1–j_2 triangular antiferromagnet,* Phys. Rev. B **93**, 144411 (2016).

[97] F. Ferrari and F. Becca, *Dynamical structure factor of the j_1–j_2 heisenberg model on the triangular lattice: Magnons, spinons, and gauge fields,* Phys. Rev. X **9**, 031026 (2019).

[98] C. Broholm, R. J. Cava, S. A. Kivelson, D. G. Nocera, M. R. Norman, and T. Senthil, *Quantum spin liquids,* Science **367**, eaay0668 (2020).

[99] Y. Matsuda, T. Shibauchi, and H.-Y. Kee, *Kitaev quantum spin liquids,* Rev. Mod. Phys. **97**, 045003 (2025), 2501.05608 .

[100] G. Semeghini, H. Levine, A. Keesling, S. Ebadi, T. T. Wang, D. Bluvstein, R. Verresen, H. Pichler, M. Kalinowski, R. Samajdar, A. Omran, S. Sachdev, A. Vishwanath, M. Greiner, V. Vuletić, and M. D. Lukin, *Probing topological spin liquids on a programmable quantum simulator,* Science **374**, 1242 (2021).

[101] P. Charbonneau, E. Marinari, M. Mézard, G. Parisi, F. Ricci-Tersenghi, G. Sicuro, and F. Zamponi, *Spin glass theory and far beyond. replica symmetry breaking after 40 years,* in *Spin Glass Theory and Far Beyond. Replica Symmetry Breaking After 40 Years*, edited by P. Charbonneau, E. Marinari, M. Mézard, G. Parisi, F. Ricci-Tersenghi, G. Sicuro, and F. Zamponi (World Scientific Connect, 2023) Chap. 18.

[102] D. H. Reich, B. Ellman, J. Yang, T. F. Rosenbaum, G. Aeppli, and D. P. Belanger, *Dipolar magnets and glasses: Neutron-scattering, dynamical, and calorimetric studies of randomly distributed ising spins,* Phys. Rev. B **42**, 4631 (1990).

[103] W. Wu, B. Ellman, T. F. Rosenbaum, G. Aeppli, and D. H. Reich, *From antiferromagnet to spin glass: A magnetic phase diagram of heisenberg spin glass,* Physical Review Letters **67**, 2076 (1991).

[104] W. Wu, D. Bitko, T. F. Rosenbaum, and G. Aeppli, *Quenching of the nonlinear susceptibility at a t=0 spin glass transition,* Phys. Rev. Lett. **71**, 1919 (1993).

[105] C. Ancona-Torres, D. M. Silevitch, G. Aeppli, and T. F. Rosenbaum, *Quantum and classical glass transitions in* $LiHo_xY_{1-x}F_4$, Phys. Rev. Lett. **101**, 057201 (2008).

[106] J. Brooke, D. Bitko, T. F. Rosenbaum, and G. Aeppli, *Quantum annealing of a disordered magnet,* Science **284**, 779 (1999).

[107] S. Ghosh, R. Parthasarathy, T. F. Rosenbaum, and G. Aeppli, *Coherent spin oscillations in a disordered magnet,* Science **296**, 2195 (2002).

[108] S. Ghosh, T. F. Rosenbaum, G. Aeppli, and S. N. Coppersmith, *Entangled quantum state of magnetic dipoles,* Nature **425**, 48 (2003).

[109] P. E. Jönsson, R. Mathieu, W. Wernsdorfer, A. M. Tkachuk, and B. Barbara, *Absence of conventional spin-glass transition in the ising dipolar system* $LiHo_xY_{1-x}F_4$, Phys. Rev. Lett. **98**, 256403 (2007).

[110] J. A. Quilliam, S. Meng, C. G. A. Mugford, and J. B. Kycia, *Evidence of spin glass ordering in the dilute dipolar ising magnet* $LiHo_xY_{1-x}F_4$, Phys. Rev. Lett. **101**, 187204 (2008).

[111] S. M. A. Tabei, M. J. P. Gingras, Y.-J. Kao, P. Stasiak, and J.-Y. Fortin, *Induced random fields in the* $LiHo_xY_{1-x}F_4$ *quantum ising magnet in a transverse magnetic field,* Phys. Rev. Lett. **97**, 237203 (2006).

[112] M. J. P. Gingras and P. Henelius, *Collective phenomena in the* $LiHo_xY_{1-x}F_4$ *quantum ising magnet: Recent progress and open questions,* J. Phys.: Conf. Ser. **320**, 012001 (2011).

[113] L. F. Cugliandolo and G. Lozano, *Real-time nonequilibrium dynamics of quantum glassy systems,* Phys. Rev. B **59**, 915 (1999).

[114] M. P. Kennett, C. Chamon, and J. Ye, *Aging dynamics of quantum spin glasses of rotors,* Phys. Rev. B **64**, 224408 (2001).

[115] M. P. Kennett and C. Chamon, *Time reparametrization group and the long time behavior in quantum glassy systems,* Phys. Rev. Lett. **86**, 1622 (2001).

[116] G. E. Santoro, R. Martoňák, E. Tosatti, and R. Car, *Theory of quantum annealing of an Ising spin glass,* Science **295**, 2427 (2002), https://www.science.org/doi/pdf/10.1126/science.1068774 .

[117] C. Laumann, R. Moessner, and A. Scardicchio, *Quantum adiabatic algorithm and scaling of gaps at first-order quantum phase transitions,* Physical review letters **109**, 030502 (2012).

[118] C. R. Laumann, R. Moessner, A. Scardicchio, and S. L. Sondhi, *Quantum annealing: The fastest route to quantum computation?* The European Physical Journal Special Topics **224**, 75 (2015).

[119] V. Martin-Mayor and I. Hen, *Unraveling quantum annealers using classical hardness,* Scientific Reports **5**, 15324 (2015).

[120] H. G. Katzgraber, F. Hamze, Z. Zhu, A. J. Ochoa, and H. Munoz-Bauza, *Seeking quantum speedup through spin glasses: The good, the bad, and the ugly,* Phys. Rev. X **5**, 031026 (2015).

[121] A. J. Bray and M. A. Moore, *Replica theory of quantum spin glasses,* J. Phys. C: Solid State Phys. **13**, L655 (1980).

[122] Y. Y. Goldschmidt and P.-Y. Lai, *Ising spin glass in a transverse field: Replica-symmetry-breaking solution,* Phys. Rev. Lett. **64**, 2467 (1990).

[123] J. Miller and D. A. Huse, *Zero-temperature critical behavior of the infinite-range quantum ising spin glass,* Phys. Rev. Lett. **70**, 3147 (1993).

[124] N. Read, S. Sachdev, and J. Ye, *Landau theory of quantum spin glasses of rotors and ising spins,* Phys. Rev. B **52**, 384 (1995).

[125] S. Sachdev and J. Ye, *Gapless spin-fluid ground state in a random quantum Heisenberg magnet,* Physical review letters **70**, 3339 (1993).

[126] D. Chowdhury, A. Georges, O. Parcollet, and S. Sachdev, *Sachdev-ye-kitaev models and beyond: Window into non-fermi liquids,* Rev. Mod. Phys. **94**, 035004 (2022).

[127] A. Georges, O. Parcollet, and S. Sachdev, *Mean field theory of a quantum heisenberg spin glass,* Phys. Rev. Lett. **85**, 840 (2000).

[128] A. Georges, O. Parcollet, and S. Sachdev, *Quantum fluctuations of a nearly critical heisenberg spin glass,* Phys. Rev. B **63**, 134406 (2001).

[129] M. Christos, F. M. Haehl, and S. Sachdev, *Spin liquid to spin glass crossover in the random quantum heisenberg magnet,* Phys. Rev. B **105**, 085120 (2022).

[130] N. Kavokine, M. Müller, A. Georges, and O. Parcollet, *Exact numerical solution of the fully connected classical and quantum heisenberg spin glass,* Phys. Rev. Lett. **133**, 016501 (2024).

[131] H. Rieger and A. P. Young, *Zero-temperature quantum phase transition of a two-dimensional ising spin glass,* Phys. Rev. Lett. **72**, 4141 (1994).

[132] J. Choi and S. K. Baek, *Finite-size scaling analysis of the two-dimensional random transverse-field Ising ferromagnet,* Phys. Rev. B **108**, 144204 (2023).

[133] C. Krämer, J. A. Koziol, A. Langheld, M. Hörmann, and K. P. Schmidt, *Quantum-critical properties of the one- and two-dimensional random transverse-field Ising model from large-scale quantum monte carlo simulations,* SciPost Physics **17** (2024).

[134] M. Bernaschi, I. González-Adalid Pemartín, V. Martín-Mayor, and G. Parisi, *The quantum transition of the two-dimensional ising spin glass,* Nature **631**, 749 (2024).

[135] G. Parisi, *Infinite number of order parameters for spin-glasses,* Phys. Rev. Lett. **43**, 1754 (1979).

[136] G. Parisi, *A sequence of approximated solutions to the SK model for spin glasses,* J. Phys. A: Math. Gen. **13**, L115 (1980).

[137] M. Mézard, G. Parisi, and M. A. Virasoro, *Spin Glass Theory and Beyond* (World Scientific, 1987).

[138] L. F. Cugliandolo and J. Kurchan, *Analytical solution of the off-equilibrium dynamics of a long-range spin-glass model,* Phys. Rev. Lett. **71**, 173 (1993).

[139] L. F. Cugliandolo and J. Kurchan, *On the out-of-equilibrium relaxation of the Sherrington–Kirkpatrick model,* J. Phys. A: Math. Gen. **27**, 5749 (1994).

[140] L. Lundgren, P. Svedlindh, P. Nordblad, and O. Beckman, *Dynamics of the relaxation-time spectrum in a CuMn spin glass,* Phys. Rev. Lett. **51**, 911 (1983).

[141] L. F. Cugliandolo, J. Kurchan, and L. Peliti, *Energy flow, partial equilibration, and effective temperatures in systems with slow dynamics,* Phys. Rev. E **55**, 3898 (1997).

[142] L. F. Cugliandolo and G. Lozano, *Quantum aging in mean-field models,* Phys. Rev. Lett. **80**, 4979 (1998).

[143] L. F. Cugliandolo and G. Lozano, *Real-time nonequilibrium dynamics of quantum glassy systems,* Phys. Rev. B **59**, 915 (1999).

[144] P. Sierant, M. Lewenstein, A. Scardicchio, L. Vidmar, and J. Zakrzewski, *Many-body localization in the age of classical computing,* Reports on Progress in Physics **88**, 026502 (2025).

[145] C. R. Laumann, A. Pal, and A. Scardicchio, *Many-Body Mobility Edge in a Mean-Field Quantum Spin Glass,* Phys. Rev. Lett. **113**, 200405 (2014).

[146] C. L. Baldwin, C. R. Laumann, A. Pal, and A. Scardicchio, *The many-body localized phase of the quantum random energy model,* Physical Review B **93**, 024202 (2016).

[147] C. Vanoni, B. L. Altshuler, V. E. Kravtsov, and A. Scardicchio, *Renormalization group analysis of the Anderson model on random regular graphs,* Proceedings of the National Academy of Sciences **121** (2024).

[148] B. L. Altshuler, V. E. Kravtsov, A. Scardicchio, P. Sierant, and C. Vanoni, *Renormalization group for anderson localization on high-dimensional lattices,* Proceedings of the National Academy of Sciences **122**, e2423763122 (2025).

[149] J. Cardy, ed., *Finite-Size Scaling*, 2 (North Holland, 1988).

[150] A. Pelissetto and E. Vicari, *Critical phenomena and renormalization-group theory,* Physics Reports **368**, 549 (2002).

[151] B. L. Altshuler, V. E. Kravtsov, A. Scardicchio, P. Sierant, and C. Vanoni, *Renormalization group for Anderson localization on high-dimensional lattices,* arXiv:2403.01974 (2024).

[152] J. Cardy, *Scaling and Renormalization in Statistical Physics*, Cambridge Lecture Notes in Physics (Cambridge University Press, 1996).

[153] S.-K. Ma, C. Dasgupta, and C.-K. Hu, *Random Antiferromagnetic Chain,* Phys. Rev. Lett. **43**, 1434 (1979).

[154] C. Dasgupta and S.-K. Ma, *Low-temperature properties of the random Heisenberg antiferromagnetic chain,* Phys. Rev. B **22**, 1305 (1980).

[155] D. S. Fisher, *Random transverse field Ising spin chains,* Phys. Rev. Lett. **69**, 534 (1992).

[156] D. S. Fisher, *Random antiferromagnetic quantum spin chains,* Phys. Rev. B **50**, 3799 (1994).

[157] D. S. Fisher, *Critical behavior of random transverse-field Ising spin chains,* Phys. Rev. B **51**, 6411 (1995).

[158] R. Vosk and E. Altman, *Many-Body Localization in One Dimension as a Dynamical Renormalization Group Fixed Point,* Phys. Rev. Lett. **110**, 067204 (2013).

[159] D. Pekker, G. Refael, E. Altman, E. Demler, and V. Oganesyan, *Hilbert-Glass Transition: New Universality of Temperature-Tuned Many-Body Dynamical Quantum Criticality,* Phys. Rev. X **4**, 011052 (2014).

[160] A. C. Potter, R. Vasseur, and S. A. Parameswaran, *Universal Properties of Many-Body Delocalization Transitions,* Phys. Rev. X **5**, 031033 (2015).

[161] L. Zhang, B. Zhao, T. Devakul, and D. A. Huse, *Many-body localization phase transition: A simplified strong-randomness approximate renormalization group,* Phys. Rev. B **93**, 224201 (2016).

[162] T. Thiery, M. Müller, and W. De Roeck, A microscopically motivated renormalization scheme for the MBL/ETH transition, (2017), arXiv:1711.09880 .

[163] A. Goremykina, R. Vasseur, and M. Serbyn, *Analytically Solvable Renormalization Group for the Many-Body Localization Transition,* Phys. Rev. Lett. **122**, 040601 (2019).

[164] P. T. Dumitrescu, A. Goremykina, S. A. Parameswaran, M. Serbyn, and R. Vasseur, *Kosterlitz-Thouless scaling at many-body localization phase transitions,* Phys. Rev. B **99**, 094205 (2019).

[165] A. Morningstar and D. A. Huse, *Renormalization-group study of the many-body localization transition in one dimension,* Phys. Rev. B **99**, 224205 (2019).

[166] A. Morningstar, D. A. Huse, and J. Z. Imbrie, *Many-body localization near the critical point,* Phys. Rev. B **102**, 125134 (2020).

[167] R. Vosk, D. A. Huse, and E. Altman, *Theory of the Many-Body Localization Transition in One-Dimensional Systems,* Phys. Rev. X **5**, 031032 (2015).

[168] V. L. Berezinskii, *Destruction of long-range order in one-dimensional and two-dimensional systems having a continuous symmetry group I. Classical systems,* Sov. Phys. JETP **32**, 493 (1971).

[169] J. M. Kosterlitz and D. J. Thouless, *Ordering, metastability and phase transitions in two-dimensional systems,* J. Phys. C: Solid State Physics **6**, 1181 (1973).

[170] A. Kutlin and C. Vanoni, *Investigating finite-size effects in random matrices by counting resonances,* arXiv:2402.10271 (2024).

[171] M. Žnidarič, T. Prosen, and P. Prelovšek, *Many-body localization in the Heisenberg XXZ magnet in a random field,* Phys. Rev. B **77**, 064426 (2008).

[172] M. Žnidarič, A. Scardicchio, and V. K. Varma, *Diffusive and Subdiffusive Spin Transport in the Ergodic Phase of a Many-Body Localizable System,* Phys. Rev. Lett. **117**, 040601 (2016).

[173] E. V. H. Doggen, F. Schindler, K. S. Tikhonov, A. D. Mirlin, T. Neupert, D. G. Polyakov, and I. V. Gornyi, *Many-body localization and delocalization in large quantum chains,* Phys. Rev. B **98**, 174202 (2018).

[174] J. Z. Imbrie, *Diagonalization and Many-Body Localization for a Disordered Quantum Spin Chain,* Phys. Rev. Lett. **117**, 027201 (2016).

[175] J. Z. Imbrie, *On Many-Body Localization for Quantum Spin Chains,* J. Stat. Phys. **163**, 998 (2016).

[176] T. Thiery, F. Huveneers, M. Müller, and W. De Roeck, *Many-Body Delocalization as a Quantum Avalanche,* Phys. Rev. Lett. **121**, 140601 (2018).

[177] H. Ha, A. Morningstar, and D. A. Huse, *Many-Body Resonances in the Avalanche Instability of Many-Body Localization,* Phys. Rev. Lett. **130**, 250405 (2023).

[178] A. Morningstar, L. Colmenarez, V. Khemani, D. J. Luitz, and D. A. Huse, *Avalanches and many-body resonances in many-body localized systems,* Phys. Rev. B **105**, 174205 (2022).

[179] A. Chandran, C. R. Laumann, and V. Oganesyan, Finite size scaling bounds on many-body localized phase transitions, (2015), arXiv:1509.04285 .

[180] R. K. Panda, A. Scardicchio, M. Schulz, S. R. Taylor, and M. Žnidarič, *Can we study the many-body localisation transition?* EPL (Europhysics Letters) **128**, 67003 (2020).

[181] D. Abanin, J. Bardarson, G. De Tomasi, S. Gopalakrishnan, V. Khemani, S. Parameswaran, F. Pollmann, A. Potter, M. Serbyn, and R. Vasseur, *Distinguishing localization from chaos: Challenges in finite-size systems,* Ann. Phys. (Amsterdam) **427**, 168415 (2021).

[182] P. Sierant and J. Zakrzewski, *Challenges to observation of many-body localization,* Phys. Rev. B **105**, 224203 (2022).

[183] J. Šuntajs, T. Prosen, and L. Vidmar, *Spectral properties of three-dimensional Anderson model,* Annals of Physics **435**, 168469 (2021), special issue on Philip W. Anderson.

[184] D. Sels and A. Polkovnikov, *Dynamical obstruction to localization in a disordered spin chain,* Phys. Rev. E **104**, 054105 (2021).

[185] P. J. D. Crowley and A. Chandran, *A constructive theory of the numerically accessible many-body localized to thermal crossover,* SciPost Phys. **12**, 201 (2022).

[186] V. Oganesyan and D. A. Huse, *Localization of interacting fermions at high temperature,* Phys. Rev. B **75**, 155111 (2007).

[187] F. Pietracaprina, N. Macé, D. J. Luitz, and F. Alet, *Shift-invert diagonalization of large many-body localizing spin chains,* SciPost Phys. **5**, 045 (2018).

[188] P. Sierant, M. Lewenstein, and A. Scardicchio, *Universality in Anderson localization on random graphs with varying connectivity,* SciPost Phys. **15**, 045 (2023).

[189] D. J. Luitz, N. Laflorencie, and F. Alet, *Many-body localization edge in the random-field Heisenberg chain,* Phys. Rev. B **91**, 081103 (2015).

[190] A. B. Harris, *Effect of random defects on the critical behaviour of Ising models,* J. Phys. C **7**, 1671 (1974).

[191] R. Abou-Chacra, D. J. Thouless, and P. W. Anderson, *A selfconsistent theory of localization,* J. Phys. C **6**, 1734 (1973).

[192] G. Parisi, S. Pascazio, F. Pietracaprina, V. Ros, and A. Scardicchio, *Anderson transition on the bethe lattice: an approach with real energies,* Journal of Physics A: Mathematical and Theoretical **53**, 014003 (2019).

[193] B. L. Altshuler, Y. Gefen, A. Kamenev, and L. S. Levitov, *Quasiparticle Lifetime in a Finite System: A Nonperturbative Approach,* Phys. Rev. Lett. **78**, 2803 (1997).

[194] A. De Luca, B. Altshuler, V. Kravtsov, and A. Scardicchio, *Anderson localization on the bethe lattice: Nonergodicity of extended states,* Physical review letters **113**, 046806 (2014).

[195] E. Bogomolny, O. Giraud, and C. Schmit, *Integrable random matrix ensembles,* Nonlinearity **24**, 3179–3213 (2011).

[196] W. De Roeck, F. Huveneers, M. Müller, and M. Schiulaz, *Absence of many-body mobility edges,* Phys. Rev. B **93**, 014203 (2016).

[197] P. Ponte, C. Laumann, D. A. Huse, and A. Chandran, *Thermal inclusions: how one spin can destroy a many-body localized phase,* Philosophical Transactions of the Royal Society A: Mathematical, Physical and Engineering Sciences **375**, 20160428 (2017).

[198] J. Šuntajs and L. Vidmar, *Ergodicity breaking transition in zero dimensions,* Phys. Rev. Lett. **129**, 060602 (2022).

[199] P. Crowley and A. Chandran, *Partial thermalisation of a two-state system coupled to a finite quantum bath,* SciPost Physics **12**, 103 (2022).

[200] V. Hernandez, J. E. Roman, and V. Vidal, *SLEPc: A scalable and flexible toolkit for the solution of eigenvalue problems,* ACM Trans. Math. Softw. **31**, 351–362 (2005).

[201] S. Balay, S. Abhyankar, M. F. Adams, *et al.*, PETSc Web page, `https://petsc.org/` (2024).

[202] A. D. Luca and A. Scardicchio, *Ergodicity breaking in a model showing many-body localization,* Europhys. Lett. **101**, 37003 (2013).

[203] B. Derrida, *Random-Energy Model: Limit of a Family of Disordered Models,* Phys. Rev. Lett. **45**, 79 (1980).

[204] D. Gross and M. Mezard, *The simplest spin glass,* Nucl. Phys. B **240**, 431 (1984).

[205] Y. Y. Goldschmidt, *Solvable model of the quantum spin glass in a transverse field,* Phys. Rev. B **41**, 4858 (1990).

[206] C. Manai and S. Warzel, *Phase Diagram of the Quantum Random Energy Model,* J. Stat. Phys. **180**, 654 (2020).

[207] C. Manai and S. Warzel, *Spectral Analysis of the Quantum Random Energy Model,* Commun. Math. Phys. **402**, 1259 (2023).

[208] G. Biroli, D. Facoetti, M. Schiró, M. Tarzia, and P. Vivo, *Out-of-equilibrium phase diagram of the quantum random energy model,* Phys. Rev. B **103**, 014204 (2021).

[209] T. Scoquart, I. V. Gornyi, and A. D. Mirlin, *Role of Fock-space correlations in many-body localization,* Phys. Rev. B **109**, 214203 (2024).

[210] F. Pietracaprina, V. Ros, and A. Scardicchio, *Forward approximation as a mean-field approximation for the Anderson and many-body localization transitions,* Phys. Rev. B **93**, 054201 (2016).

[211] M. Pino, V. E. Kravtsov, B. L. Altshuler, and L. B. Ioffe, *Multifractal metal in a disordered Josephson junctions array,* Phys. Rev. B **96**, 214205 (2017).

[212] M. Kac, Foundations of Kinetic Theory, in *Volume 3 Proceedings of the Third Berkeley Symposium on Mathematical Statistics and Probability, Volume III*, edited by J. Neyman (University of California Press, Berkeley, 1956) pp. 173–200.

[213] A. Campa, T. Dauxois, D. Fanelli, and S. Ruffo, *Physics of Long-Range Interacting Systems* (Oxford University Press, 2014).

[214] P. W. Anderson, *An approximate quantum theory of the antiferromagnetic ground state,* Phys. Rev. **86**, 694 (1952).

[215] A. W. Sandvik, *Finite-size scaling of the ground-state parameters of the two-dimensional Heisenberg model,* Phys. Rev. B **56**, 11678 (1997).

[216] N. N. Bogoljubov, *On the theory of superfluidity,* Journal of Physics (USSR) **11**, 23 (1947).

[217] J.-P. Blaizot and G. Ripka, *Quantum Theory of Finite Systems* (MIT Press, Cambridge, Massachusetts, 1986).

[218] V. Gurarie and J. T. Chalker, *Bosonic excitations in random media,* Phys. Rev. B **68**, 134207 (2003).

[219] J. Colpa, *Diagonalization of the quadratic boson hamiltonian,* Physica A: Statistical Mechanics and its Applications **93**, 327 (1978).

[220] J. Goldstone, A. Salam, and S. Weinberg, *Broken symmetries,* Physical Review **127**, 965 (1962).

[221] H. Nielsen and S. Chadha, *On how to count goldstone bosons,* Nuclear Physics B **105**, 445 (1976).

[222] H. Watanabe and T. c. v. Brauner, *Number of nambu-goldstone bosons and its relation to charge densities,* Phys. Rev. D **84**, 125013 (2011).

[223] H. Watanabe and H. Murayama, *Unified description of nambu-goldstone bosons without lorentz invariance,* Phys. Rev. Lett. **108**, 251602 (2012).

[224] A. Aharony, R. J. Birgeneau, A. Coniglio, M. A. Kastner, and H. E. Stanley, *Magnetic phase diagram and magnetic pairing in doped* $\mathrm{la_2cuo_4}$*,* Phys. Rev. Lett. **60**, 1330 (1988).

[225] A. Aharony, R. Birgeneau, A. Coniglio, M. Kastner, and H. Stanley, *Magnetic phases and possible magnetic pairing in doped lanthanum cuprate,* Physica C: Superconductivity **153-155**, 1211 (1988), proceedings of the International Conference on High Temperature Superconductors and Materials and Mechanisms of Superconductivity Part II.

[226] M. Frachet, I. Vinograd, R. Zhou, S. Benhabib, S. Wu, H. Mayaffre, S. Krämer, S. K. Ramakrishna, A. P. Reyes, J. Debray, T. Kurosawa, N. Momono, M. Oda, S. Komiya, S. Ono, M. Horio, J. Chang, C. Proust, D. LeBoeuf, and M.-H. Julien, *Hidden magnetism at the pseudogap critical point of a cuprate superconductor,* Nature Physics **16**, 1064–1068 (2020).

[227] J. Oitmaa and O. P. Sushkov, *Two-dimensional randomly frustrated spin-1/2 Heisenberg model.* Physical review letters **87 16**, 167206 (2001).

[228] L. Arrachea and M. J. Rozenberg, *Dynamical response of quantum spin-glass models at* $T = 0$*,* Phys. Rev. Lett. **86**, 5172 (2001).

[229] J. P. Rodriguez, J. Bonča, and J. Ferrer, *Random frustration in a two-dimensional spin-1/2 Heisenberg antiferromagnet,* Phys. Rev. B **51**, 3616 (1995).

[230] K. Uematsu and H. Kawamura, *Randomness-induced quantum spin liquid behavior in the $s = \frac{1}{2}$ random J_1-J_2 Heisenberg antiferromagnet on the square lattice,* Phys. Rev. B **98**, 134427 (2018).

[231] D. Wu, F. Yang, and G. Carleo, Unveiling nonmagnetic phase and many-body entanglement in two-dimensional random quantum magnets $\mathrm{sr_2cute_{1-x}w_xo_6}$, (2024), arXiv:2407.05917 [cond-mat.str-el] .

[232] H.-D. Ren, T.-Y. Xiong, H.-Q. Wu, D. N. Sheng, and S.-S. Gong, *Characterizing random-singlet state in two-dimensional frustrated quantum magnets and implications for the double perovskite* $\mathrm{sr_2cute_{1-x}w_xo_6}$, Phys. Rev. B **107**, L020407 (2023).

[233] E. Stoudenmire and S. R. White, *Studying two-dimensional systems with the density matrix renormalization group,* Annual Review of Condensed Matter Physics **3**, 111–128 (2012).

[234] R. Rende, L. L. Viteritti, F. Becca, A. Scardicchio, A. Laio, and G. Carleo, Foundation neural-network quantum states, (2025), arXiv:2502.09488 [quant-ph] .

[235] J. F. Fernandez, *Isotropic Heisenberg spin-glass order in two dimensions,* Journal of Physics C: Solid State Physics **10**, L441 (1977).

[236] H. Kawamura and H. Yonehara, *Ordering of the Heisenberg spin glass in two dimensions,* Journal of Physics A: Mathematical and General **36**, 10867–10880 (2003).

[237] M. Calandra Buonaura and S. Sorella, *Numerical study of the two-dimensional Heisenberg model using a green function monte carlo technique with a fixed number of walkers,* Phys. Rev. B **57**, 11446 (1998).

[238] A. W. Sandvik, *Numerical study of a two-dimensional quantum antiferromagnet with random ferromagnetic bonds,* Phys. Rev. B **50**, 15803 (1994).

[239] A. W. Sandvik, *Classical percolation transition in the diluted two-dimensional $s = \frac{1}{2}$ Heisenberg antiferromagnet,* Phys. Rev. B **66**, 024418 (2002).

[240] M. Fava, J. L. Jacobsen, and A. Nahum, *Heisenberg spin chain with random-sign couplings,* Proceedings of the National Academy of Sciences **121**, e2401292121 (2024), https://www.pnas.org/doi/pdf/10.1073/pnas.2401292121 .

[241] S. Li, H. Shao, and A. W. Sandvik, *Ground state of the $s = 1/2$ Heisenberg spin chain with random ferromagnetic and antiferromagnetic couplings,* Phys. Rev. Lett. **134**, 086501 (2025).

[242] N. Kavokine, M. Müller, A. Georges, and O. Parcollet, *Exact numerical solution of the fully connected classical and quantum Heisenberg spin glass,* Physical Review Letters **133**, 016501 (2024).

[243] F. Becca and S. Sorella, *Quantum Monte Carlo Approaches for Correlated Systems* (Cambridge University Press, 2017).

[244] L. L. Viteritti, R. Rende, and F. Becca, *Transformer variational wave functions for frustrated quantum spin systems,* Phys. Rev. Lett. **130**, 236401 (2023).

[245] L. L. Viteritti, R. Rende, A. Parola, S. Goldt, and F. Becca, *Transformer wave function for two dimensional frustrated magnets: Emergence of a spin-liquid phase in the shastry-sutherland model,* Phys. Rev. B **111**, 134411 (2025).

[246] R. Rende, S. Goldt, F. Becca, and L. L. Viteritti, *Fine-tuning neural network quantum states,* Phys. Rev. Res. **6**, 043280 (2024).

[247] K. Sprague and S. Czischek, *Variational monte carlo with large patched transformers,* Communications Physics **7**, 90 (2024).

[248] R. Rende, L. L. Viteritti, L. Bardone, F. Becca, and S. Goldt, *A simple linear algebra identity to optimize large-scale neural network quantum states,* Communications Physics **7** (2024).

[249] M. Baity-Jesi and G. Parisi, *Inherent structures in m-component spin glasses,* Physical Review B **91**, 134203 (2015).

[250] D. Sherrington, *Spin waves in a mattis random magnet,* Journal of Physics C: Solid State Physics **10**, L7 (1977).

[251] H. Takayama, *A contribution to the theory of spin waves in a metallic spin glass,* Journal of Physics F: Metal Physics **8**, 2417 (1978).

[252] W. Y. Ching, D. L. Huber, and K. M. Leung, *Numerical studies of spin-wave dynamics in heisenberg spin-glasses,* Phys. Rev. B **23**, 6126 (1981).

[253] S. E. Barnes, *Electron-spin-resonance modes and the edwards-anderson theory of the spin-glass state,* Phys. Rev. Lett. **47**, 1613 (1981).

[254] A. J. Bray and M. A. Moore, *Metastable states, internal field distributions and magnetic excitations in spin glasses,* Journal of Physics C: Solid State Physics **14**, 2629 (1981).

[255] T. Cea, D. Bucheli, G. Seibold, L. Benfatto, J. Lorenzana, and C. Castellani, *Optical excitation of phase modes in strongly disordered superconductors,* Phys. Rev. B **89**, 174506 (2014).

[256] R. Menu and T. Roscilde, *Anomalous diffusion and localization in a positionally disordered quantum spin array,* Phys. Rev. Lett. **124**, 130604 (2020).

[257] Y. Nomura and M. Imada, *Dirac-type nodal spin liquid revealed by refined quantum many-body solver using neural-network wave function, correlation ratio, and level spectroscopy,* Phys. Rev. X **11**, 031034 (2021).

[258] W.-J. Hu, F. Becca, A. Parola, and S. Sorella, *Direct evidence for a gapless Z_2 spin liquid by frustrating néel antiferromagnetism,* Phys. Rev. B **88**, 060402 (2013).

[259] A. W. Sandvik, *Computational studies of quantum spin systems,* AIP Conference Proceedings **1297**, 135 (2010).

[260] G. Carleo and M. Troyer, *Solving the quantum many-body problem with artificial neural networks,* Science **355**, 602 (2017).

[261] H. Lange, A. Van de Walle, A. Abedinnia, and A. Bohrdt, *From architectures to applications: a review of neural quantum states,* Quantum Science and Technology **9**, 040501 (2024).

[262] S. Sorella, *Green function monte carlo with stochastic reconfiguration,* Phys. Rev. Lett. **80**, 4558 (1998).

[263] S. Sorella, *Wave function optimization in the variational monte carlo method,* Phys. Rev. B **71**, 241103 (2005).

[264] A. Chen and M. Heyl, *Empowering deep neural quantum states through efficient optimization,* Nature Physics **20**, 1476 (2024).

[265] L. Capriotti and S. Sorella, *Spontaneous plaquette dimerization in the $j_1 - -j_2$ heisenberg model,* Phys. Rev. Lett. **84**, 3173 (2000).

[266] S.-S. Gong, W. Zhu, D. N. Sheng, O. I. Motrunich, and M. P. A. Fisher, *Plaquette ordered phase and quantum phase diagram in the spin-$\frac{1}{2}$ J_1-J_2 square heisenberg model,* Phys. Rev. Lett. **113**, 027201 (2014).

[267] B. I. Halperin and W. M. Saslow, *Hydrodynamic theory of spin waves in spin glasses and other systems with noncollinear spin orientations,* Phys. Rev. B **16**, 2154 (1977).

[268] B. I. Halperin and P. C. Hohenberg, *Hydrodynamic theory of spin waves,* Phys. Rev. **188**, 898 (1969).

[269] D. M. Basko, I. L. Aleiner, and B. L. Altshuler, *Metal–insulator transition in a weakly interacting many-electron system with localized single-particle states,* Annals of physics **321**, 1126 (2006).

[270] F. Evers and A. D. Mirlin, *Anderson transitions,* Rev. Mod. Phys. **80**, 1355 (2008).

[271] P. Sierant, M. Lewenstein, A. Scardicchio, L. Vidmar, and J. Zakrzewski, *Many-body localization in the age of classical computing*,* Reports on Progress in Physics **88**, 026502 (2025).

[272] P. W. Anderson, *An approximate quantum theory of the antiferromagnetic ground state,* Phys. Rev. **86**, 694 (1952).

[273] T. Oguchi, *Theory of spin-wave interactions in ferro- and antiferromagnetism,* Phys. Rev. **117**, 117 (1960).

[274] G. E. Castilla and S. Chakravarty, *Spin-wave expansion of the staggered magnetization of a square-lattice heisenberg antiferromagnet at t=0,* Phys. Rev. B **43**, 13687 (1991).

[275] A. Altland and M. R. Zirnbauer, *Nonstandard symmetry classes in mesoscopic normal-superconducting hybrid structures,* Phys. Rev. B **55**, 1142 (1997).

[276] M. Baity-Jesi, V. Martín-Mayor, G. Parisi, and S. Perez-Gaviro, *Soft modes, localization, and two-level systems in spin glasses,* Phys. Rev. Lett. **115**, 267205 (2015).

[277] A. Coraggio, J. Niedda, G. Bracci-Testasecca, and A. Scardicchio, *Analysis of the energy landscape of the two-dimensional heisenberg spin glass, in preparation* (2026).

[278] M. Cieplak and M. Cieplak, *Scaling stiffness and correlations in the spin-glass-ferromagnet transition: evidence for the mixed phase,* Journal of Physics C: Solid State Physics **18**, 1481 (1985).

[279] J. Villain, *Insulating spin glasses,* Zeitschrift für Physik B Condensed Matter **33**, 31 (1979).

[280] K. Binder and A. P. Young, *Spin glasses: Experimental facts, theoretical concepts, and open questions,* Rev. Mod. Phys. **58**, 801 (1986).

[281] L. D. Landau and E. M. Lifshitz, *Statistical Physics, Part 1, Course of Theoretical Physics, Vol. 5* (Pergamon Press, 1980).

[282] G. Seibold, L. Benfatto, C. Castellani, and J. Lorenzana, *Superfluid density and phase relaxation in superconductors with strong disorder,* Phys. Rev. Lett. **108**, 207004 (2012).

[283] G. Seibold, L. Benfatto, C. Castellani, and J. Lorenzana, *Amplitude, density, and current correlations of strongly disordered superconductors,* Phys. Rev. B **92**, 064512 (2015).

[284] Q.-R. Xu, V. P. Flynn, A. Alase, E. Cobanera, L. Viola, and G. Ortiz, *Squaring the fermion: The threefold way and the fate of zero modes,* Phys. Rev. B **102**, 125127 (2020).

[285] M. L. Mehta, *Random Matrices*, 3rd ed. (Elsevier, 2004).

[286] J. Canisius and J. L. van Hemmen, *Spin waves in a disordered medium: A simple model with a mobility edge,* Phys. Rev. Lett. **46**, 1487 (1981).

[287] Y. Y. Atas, E. Bogomolny, O. Giraud, and G. Roux, *Distribution of the ratio of consecutive level spacings in random matrix ensembles,* Phys. Rev. Lett. **110**, 084101 (2013).

[288] S. Jiricek, M. Hopjan, V. Kravtsov, B. Altshuler, and L. Vidmar, *Universal relation between spectral and wavefunction properties at criticality,* Proceedings of the National Academy of Sciences of the United States of America **123**, e2518027123 (2026).

[289] W. De Roeck, L. Giacomin, F. Huveneers, and O. Prosniak, *Absence of normal heat conduction in strongly disordered interacting quantum chains,* arXiv:2408.04338 (2024).

[290] S. John, H. Sompolinsky, and M. J. Stephen, *Localization in a disordered elastic medium near two dimensions,* Phys. Rev. B **27**, 5592 (1983).

[291] W. De Roeck, F. Huveneers, M. Müller, and M. Schiulaz, *Absence of many-body mobility edges,* Physical Review B **93**, 014203 (2016).

[292] A. Chandran, A. Pal, C. Laumann, and A. Scardicchio, *Many-body localization beyond eigenstates in all dimensions,* Physical Review B **94**, 144203 (2016).

[293] W. Eisenmenger and A. A. Kaplianskiĭ, *Nonequilibrium phonons in nonmetallic crystals.*, Modern problems in condensed matter sciences. v.16. (North-Holland, Amsterdam, 1986).

[294] H. Zhang, T. Huang, A. O. Scheie, M. Zhu, T. Xie, N. Murai, S. Ohira-Kawamura, A. Zheludev, A. M. Läuchli, and C. D. Batista, Nonperturbative semiclassical spin dynamics for ordered quantum magnets, (2025), arXiv:2508.21142 [cond-mat.str-el] .

[295] G. N. Parker and W. M. Saslow, *Defect interactions and canting in ferromagnets.* Physical review. B, Condensed matter **38 16**, 11718 (1988).

[296] S. Yan, D. A. Huse, and S. R. White, *Spin-liquid ground state of the s = 1/2 kagome heisenberg antiferromagnet,* Science **332**, 1173–1176 (2011).

[297] I. Kimchi, A. Nahum, and T. Senthil, *Valence bonds in random quantum magnets: Theory and application to ybmggao4",* Physical Review X **8** (2018).

[298] L. Liu, H. Shao, Y.-C. Lin, W. Guo, and A. W. Sandvik, *Random-singlet phase in disordered two-dimensional quantum magnets,* Phys. Rev. X **8**, 041040 (2018).

[299] S. Dey, E. C. Andrade, and M. Vojta, *Destruction of long-range order in noncollinear two-dimensional antiferromagnets by random-bond disorder,* Phys. Rev. B **101**, 020411(R) (2020).

[300] C. Gong *et al.*, *Discovery of intrinsic ferromagnetism in two-dimensional van der waals crystals,* Nature **546**, 265 (2017).

[301] B. Huang *et al.*, *Layer-dependent ferromagnetism in a van der waals crystal down to the monolayer limit,* Nature **546**, 270 (2017).

[302] A. Bedoya-Pinto *et al.*, *Intrinsic 2d-xy ferromagnetism in a van der waals monolayer,* Science **374**, 616 (2021).

[303] J. Cenker *et al.*, *Direct observation of two-dimensional magnons in atomically thin CrI_3,* Nature Physics **17**, 20 (2021).

[304] S. Jenkins, L. Rózsa, U. Atxitia, R. F. L. Evans, K. S. Novoselov, and E. J. G. Santos, *Breaking through the mermin-wagner limit in 2d van der waals magnets,* Nature Communications **13**, 6917 (2022).

[305] Y. J. Bae *et al.*, *Exciton-coupled coherent magnons in a 2d semiconductor,* Nature **609**, 282 (2022).

[306] B. Pal *et al.*, *Realization of a spin glass in a two-dimensional van der waals material,* Science **392**, 624 (2026).

[307] S. Ebadi, T. T. Wang, H. Levine, A. Keesling, G. Semeghini, A. Omran, D. Bluvstein, R. Samajdar, H. Pichler, W. W. Ho, *et al.*, *Quantum phases of matter on a 256-atom programmable quantum simulator,* Nature **595**, 227 (2021).

[308] P. Scholl, M. Schuler, H. J. Williams, A. A. Eberharter, D. Barredo, K.-N. Schymik, V. Lienhard, L.-P. Henry, T. C. Lang, T. Lahaye, *et al.*, *Quantum simulation of 2d antiferromagnets with hundreds of rydberg atoms,* Nature **595**, 233 (2021).

[309] C. Chen, G. Bornet, M. Bintz, G. Emperauger, L. Leclerc, V. S. Liu, P. Scholl, D. Barredo, J. Hauschild, S. Chatterjee, *et al.*, *Continuous symmetry breaking in a two-dimensional rydberg array,* Nature **616**, 691 (2023).

[310] B. S. Shastry and B. Sutherland, *Twisted boundary conditions and effective mass in heisenberg-ising and hubbard rings,* Phys. Rev. Lett. **65**, 243 (1990).

[311] J. Bonča, J. P. Rodriguez, J. Ferrer, and K. S. Bedell, *Direct calculation of spin stiffness for spin-1/2 heisenberg models,* Phys. Rev. B **50**, 3415 (1994).

[312] D. Friedan, *Nonlinear models in $2+\epsilon$ dimensions,* Phys. Rev. Lett. **45**, 1057 (1980).

[313] V. J. Emery and S. A. Kivelson, *Importance of phase fluctuations in superconductors with small superfluid density,* Nature **374**, 434 (1995).

[314] A. Ghosal, M. Randeria, and N. Trivedi, *Inhomogeneous pairing in highly disordered s-wave superconductors,* Phys. Rev. B **65**, 014501 (2001).

[315] B. I. Halperin and D. R. Nelson, *Theory of two-dimensional melting,* Phys. Rev. Lett. **41**, 121 (1978).

[316] D. R. Nelson and B. I. Halperin, *Dislocation-mediated melting in two dimensions,* Phys. Rev. B **19**, 2457 (1979).

[317] A. P. Young, *Melting and the vector coulomb gas in two dimensions,* Phys. Rev. B **19**, 1855 (1979).

[318] J. L. Cardy and S. Ostlund, *Random symmetry-breaking fields and the* XY *model,* Phys. Rev. B **25**, 6899 (1982).

[319] T. Giamarchi and P. Le Doussal, *Elastic theory of flux lattices in the presence of weak disorder,* Phys. Rev. B **52**, 1242 (1995).

[320] S. Chakravarty, *Scale-independent fluctuations of spin stiffness in the heisenberg model and its relationship to universal conductance fluctuations,* Phys. Rev. Lett. **66**, 481 (1991).

[321] B. Altshuler, V. Kravtsov, and I. Lerner, *Statistics of mesoscopic fluctuations and instability of one-parameter scaling,* Zh. Eksp. Teor. Fiz **91**, 2276 (1986).

[322] T. Vojta and J. Schmalian, *Quantum griffiths effects in itinerant heisenberg magnets,* Physical Review B—Condensed Matter and Materials Physics **72**, 045438 (2005).

[323] P. Mohan, R. Narayanan, and T. Vojta, *Infinite randomness and quantum griffiths effects in a classical system: the randomly layered heisenberg magnet,* Physical Review B—Condensed Matter and Materials Physics **81**, 144407 (2010).

[324] T. Vojta, *Rare region effects at classical, quantum and nonequilibrium phase transitions,* Journal of Physics A: Mathematical and General **39**, R143 (2006).

[325] C. Laumann, A. Scardicchio, and S. L. Sondhi, *Griffiths-mccoy singularities, lee-yang zeros, and the cavity method in a solvable diluted ferromagnet,* Phys. Rev. E **77**, 061139 (2008).